**The Dissertation Committee for Wan Wei Certifies that this is the approved version of the following dissertation:**

# Numerical Modeling of Matrix Acidizing in Carbonate and Sandstone Reservoirs

**Committee:**

Kamy Sepehrnoori, Supervisor

Matthew T. Balhoff

Lee Chin

Mojdeh Delshad

Kishore K. Mohanty

# Numerical Modeling of Matrix Acidizing in Carbonate and Sandstone Reservoirs

**by**

**Wan Wei**

**Dissertation**

Presented to the Faculty of the Graduate School of

The University of Texas at Austin

in Partial Fulfillment

of the Requirements

for the Degree of

**Doctor of Philosophy**

**The University of Texas at Austin**

**May 2020**

# Dedication

To my parents, Li Yang and Shaoxiang Wei,

for their love, patience, support and encouragement.

# Acknowledgements

I would like to thank all those people who made the completion of this dissertation possible and provided support and assistance to me continuously. First, and most of all, I would like to express my sincerest gratitude to my supervisor, Dr. Kamy Sepehrnoori, for his valuable guidance, patience, support and encouragement from my first day studying in The University of Texas at Austin. He taught me fundamentals of conducting scientific research and inspired me with his passionate and hardworking attitude. I would also like to thank my committee members: Dr. Matthew Balhoff, Dr. Lee Chin, Dr. Mojdeh Delshad, and Dr. Kishore Mohanty for their time and effort reviewing my dissertation and for providing valuable comments, feedback, and guidance through my research.

I greatly appreciate Dr. Chowdhury Mamun for his patient review and comments on my dissertation. I would like to express special thanks to Dr. Abdoljalil Varavei, for a lot of helpful discussions with him and for resolving my technical problems throughout my research. I greatly appreciate Dr. Alireza Sanaei for his help and suggestions in technical and programming details. I would also like to thank Dr. Bruno Fernandes, Dr. Wei Yu, Youguang Chen, and Fabio Rego for their help in different parts of this dissertation.

I would like to acknowledge the staff of the Hildebrand Department of Petroleum and Geosystems Engineering, Frankie Hart, Amy Stewart, John Cassibry, Jessica Yeager, Diane Landeros, and Glen Baum.

I would like to thank my great officemates for their companion and support during the whole period of my Ph.D. study. Many thanks go to my officemates, Adi

Junira, Ali Goudarzi, Esmail Eltahan, Hamza Rawahi, Jia He, Mahdi Haddad, Mauricio Fiallos, Mehran Mehrabi, Yujing Du, Yanli Pei, and many others I didn't enumerate here. I would also like to thank all my friends for wonderful time spending with them.

I express my gratitude to company members of Reservoir Simulation Joint Industry Project (RSJIP) in The University of Texas at Austin for their financial support for my research.

Finally, I would like to thank my parents for their understanding, support and encouragement on every decision I have made. Their unconditional love and support helped me accomplish goals in every stage of my life.

# Abstract

## Numerical Modeling of Matrix Acidizing in Carbonate and Sandstone Reservoirs

Wan Wei, Ph.D.

The University of Texas at Austin, 2020

Supervisor: Kamy Sepehrnoori

Matrix acidizing is a stimulation technique to improve productivity/injectivity in the near-wellbore region in carbonate and sandstone reservoirs. Carbonate reservoir is heterogeneous in mineralogy, primary porosity, and secondary porosity such as fractures. Optimally through acidizing treatment, wormholes are generated in carbonate reservoirs to improve the permeability and bypass the damaged zone.

A two-scale continuum model is implemented in a radial coordinate system to simulate acidizing process in the near-wellbore geometry. The model is extended from single-phase to two-phase by considering mobility change due to water-oil displacement and defining a new criterion for acidizing breakthrough applicable to two-phase flow. The requirement of acid consumption is lower with the existence of oil prior to acidizing treatment. This indicates that for field treatment, maintaining a higher oil saturation can enhance acidizing efficiency.

To consider varying mineral compositions in carbonates, the acidizing model is implemented in the UTCOMP-IPhreeqc coupled software to model homogeneous and heterogeneous reactions among acid and minerals. Different acid pore volumes are

predicted for limestone, dolostone, and partially dolomitized formation due to the difference in reaction rate and dissolution structures generated.

To consider fracture effect in carbonates, the acidizing model in UTCOMP-IPhreeqc is extended to consider reactions on the fracture surface with the aid of EDFM (Embedded Discrete Fracture Model). The fracture with a high conductivity will receive most acid and slow down the wormhole propagation in the matrix.

To improve computational efficiency, the acidizing model is also implemented in the semi-parallel version of UTCOMP-IPhreeqc, with the parallelized geochemical calculation. Besides, speedup techniques through defining a tolerance on the relative amount change of geochemical elements to reduce IPhreeqc calls are also applied. Parallel computing saves up to 85% of the total computational time when using 16 processors. And speedup techniques obtain about 50% improvement for the wormhole pattern.

The acidizing model in UTCOMP-IPhreeqc is also extended to simulate acidizing process in sandstone reservoirs through modifying IPhreeqc database to include primary and secondary reactions. A largest possible injection rate is recommended to achieve best performance mitigating formation damage caused by precipitation.

# Table of Contents

# List of Tables

# List of Figures

# CHAPTER 1: INTRODUCTION

In this dissertation, a reactive transport model for acidizing process is developed based on a two-scale continuum model. The two-scale continuum model incorporates Darcy-scale model and pore-scale correlations. The Darcy-scale model describes convection, dispersion, and reaction, while pore-scale correlations relate Darcy-scale parameters with pore structure evolution. First, the model is implemented in radial coordinates, considering two-phase flow (water and oil). A breakthrough criterion for acidizing simulation is proposed to consider the overall mobility change in the computational domain. Second, the model is implemented into UTCOMP (a 3D reservoir simulator) considering homogeneous and heterogeneous reactions through the coupled UTCOMP-IPhreeqc model. IPhreeqc is an open-source program that performs a wide variety of geochemical calculations. IPhreeqc is capable of simulating a wide range of equilibrium reactions provided in the IPhreeqc database. It also provides a general kinetic formulation which allows users to modify or supplement modeling of non-equilibrium mineral dissolution and precipitation. Third, the UTCOMP-IPhreeqc model is extended to consider reactions on the fracture surface for fractured reservoirs on the basis of EDFM (Embedded Discrete Fracture Model). In addition, the model is also implemented into UTCOMP with parallelized IPhreeqc to improve the computational efficiency. Also, two types of speedup methods are used to reduce IPhreeqc calls through defining a tolerance for the relative amount change of geochemical components.

This chapter introduces background, literature review, research objectives, and organization of this dissertation.

## 1.1 BACKGROUND

The poor performance of production or injection wells can be diagnosed for different reasons. One possible reason is low inherent reservoir quality. Other causes may be formation damage, which receives most blame for the underperforming wells. Formation damage receives more attention as people face more challenges when exploiting tighter, deeper, and more depleted reservoirs. Formation damage may occur at any time during the entire life of a well since well operations may change the properties of the formation through different mechanisms, including mechanical mechanism, chemical mechanism, biological mechanism, and thermal mechanism (Bennion 2002). Different stimulation techniques can be utilized to improve the fluid flow from the reservoir into the wellbore, including hydraulic fracturing, matrix acidizing, and acid fracturing. Matrix acidizing is an economic method to improve production by removing formation damage or creating new pathways within several inches to a foot or two around the wellbore. The earliest recorded acid treatments were performed in 1895 (Williams et al. 1979). The earliest matrix acidizing was used for limestone in 1895 by the Ohio Oil Company (Crowe et al. 1992). From then on, hydrochloric acid was used to dissolve limestone and dolomite, which are predominant mineral compositions in carbonate formations.

Acids are efficacious because of their ability to dissolve formation minerals and foreign materials such as drilling mud. In general, acidizing techniques include three categories: acid washing, matrix acidizing, and acid fracturing. Acid washing is a process to remove acid-soluble scales in the wellbore or to open perforations. Matrix acidizing is a stimulation technique in which acid is injected through the well into the formation below formation fracture pressure. In acid fracturing operation, acid is injected into the

formation at a pressure high enough to fracture the formation or to open existing fractures.

Matrix acidizing aims at improving formation permeability or bypassing damaged zone in both carbonate reservoirs and sandstone reservoirs. Carbonate reservoirs are often treated with hydrochloric acid (HCl). Under various conditions of reaction and injection rates, different dissolution types can be generated in carbonate formations. For sandstone formations, mud acid which is a mixture of hydrofluoric acid (HF) and hydrochloric acid (HCl) or organic acid is usually applied.

### 1.1.1 Carbonate acidizing

Estimation indicates that more than 60% of oil reserves and 40% of gas reserves are deposited in carbonate reservoirs (Schlumberger 2007). Compared with sandstone reservoirs, carbonate exploration is more difficult due to intrinsic heterogeneities at all scales. Carbonate heterogeneities include pore structure, lithology, mineralogy, and sedimentary facies due to geological and diagenesis processes (Fitch 2011).

Carbonate reservoirs present spatial variability in petrophysical properties, such as porosity and permeability. Permeability can be related to primary porosity and secondary porosity. Primary porosity refers to the small-scale pore type from original deposition. Secondary porosity is often attributed to the larger-scale features, such as channels, vugs, and fractures. A feature of importance in carbonates is the existence of natural fractures. Fractures widely exist in carbonates because of their brittle nature, compared with ductile siliciclastics (Moore and Wade 2013).

Carbonate rocks exhibit heterogeneity in pore network because of local deposition. Usually, the grains that comprise carbonate sediments deposit close to the place where they are generated and then undergo diagenesis process which changes the

rock structure. Alteration of rock structure leads to changing of rock properties such as porosity and permeability (Schlumberger 2007). Heterogeneity is a key factor that initiates wormhole formation in carbonate acidizing. Different dissolution patterns can be generated under different conditions. Under the optimum condition, with least acid consumption, wormholes are generated in the formation.

Carbonate rocks also exhibit heterogeneity in mineral compositions. There are two major types of carbonate rocks: limestone and dolostone. Limestone is mainly composed of calcite ($CaCO_3$), while dolostone is mainly composed of dolomite ($CaMg(CO_3)_2$). Many dolomites form by replacement of a precursor limestone through dolomitization. Dolomitization is a process of recrystallization in which magnesium substitutes for calcium. The diagenesis process can be described as

$$2CaCO_3 + Mg^{2+} = CaMg\left(CO_3\right)_2 + Ca^{2+}. \quad (1.1)$$

Original limestone textures are preserved in such dolomites to various degrees, ranging from virtually not replaced to totally replaced. This means that at different locations in carbonate reservoirs, a mixture of calcite and dolomite may exist with different proportions.

Different heterogeneities need to be considered during carbonate acidizing. The two main kinetic reactions between HCl and calcite or dolomite can be expressed as

$$CaCO_3 + 2HCl = CaCl_2 + CO_2 + H_2O, \quad (1.2)$$

$$CaMg(CO_3)_2 + 4HCl = CaCl_2 + MgCl_2 + 2CO_2 + 2H_2O. \quad (1.3)$$

### 1.1.2 Sandstone acidizing

The goal of a matrix treatment is different in sandstones than in carbonates. In sandstones, matrix treatment is to restore or improve formation permeability around the wellbore by removing formation damage. In carbonates, matrix stimulation creates new

highly conductive channels. During matrix acidizing in carbonate formations, acid can react with the entire matrix. However, in sandstone acidizing, the acid only reacts with the soluble substances in the formation matrix to enlarge the pore spaces.

Sandstone is a sedimentary rock mainly composed of quartz. It also contains significant amounts of feldspar, sometimes silt and clay. The overall chemical formula of quartz is $SiO_2$. Feldspars ($KAlSi_3O_8$-$NaAlSi_3O_8$-$CaAl_2Si_2O_8$) are a group of tectosilicate minerals. Most clay minerals are described as hydrous aluminosilicates. Sandstone acidizing mainly aims at removing siliceous particles, such as formation clay, feldspar and quartz fines which block pore throats.

For sandstone acidizing, reactions are more complex compared with carbonate acidizing. The commonly used acid system in sandstone acidizing is mud acid, which is composed of HCl and HF (Yang et al. 2012). Different HCl/HF ratios have been applied to dissolve clays, feldspars, and silica to improve well productivity or injectivity (Smith and Hendrickson 1965; Gidley 1985; Shuchart 1995; Thomas et al. 2001; Hartman et al. 2003). Traditional mud acid has a few limitations: rapid spending, high corrosion rate, and incompatibility with sensitive clays (Al-harbi et al. 2012). To overcome these limitations, organic/HF acid mixtures have been used instead of HCl/HF system to improve the effectiveness of sandstone acidizing. Among organic acids, formic acid and acetic acid are most frequently used to substitute for HCl (Yang et al. 2012). Standard treatments include pre-flush and/or post-flush stages of HCl to minimize the potential for calcium fluoride ($CaF_2$) and other secondary precipitations. The reaction with calcite is more rapid than with silicate minerals (clay or feldspar), which, in turn, is more rapid than the reaction with silica ($SiO_2$) (Hill et al. 1981).

The reaction between HF and $SiO_2$ can be described as (Shafiq et al. 2013):

$$4HF + SiO_2 \rightarrow SiF_4 + 2H_2O \,. \tag{1.4}$$

The most common damaging precipitates generated in sandstone acidizing are calcium fluoride ($CaF_2$), silica gel ($Si(OH)_4$), ferric hydroxide ($Fe(OH)_3$), and asphaltene sludges (Mohammed 2016).

The reaction between calcite and HF can form calcium fluoride (Yang et al. 2012) as follows:

$$CaCO_3 + 2HF \rightarrow CaF_2 + H_2O + CO_2 . \quad (1.5)$$

The injected HF reacts with aluminosilicates to bring about precipitation of reaction products. There are primary, secondary, and tertiary reactions (Gdanski 1996; Gdanski 1999; Gdanski 2000). The primary reaction of HF with aluminosilicates is

$$(5+x)HF + MAlSi + (3-x+1)H^+ \rightarrow HSiF_5 + AlF_x^{(3-x)+} + M^+ + H_2O . \quad (1.6)$$

The reaction is rapid and generates fluoride complexes of silicon and aluminum, other cations, and water. M represents all other cations, such as Na and Fe(II).

The secondary reaction is between fluosilicic acid and aluminosilicates and can be expressed as:

$$x/5HSiF_5 + MAlSi + (3-x+1)H^+ + H_2O \rightarrow AlF_x^{(3-x)+} + M^+ + silicagel . \quad (1.7)$$

The tertiary reaction was first reported by Shuchart and Buster (1995) and can be expressed in the general form:

$$yAlF_x^{(3-x)+} + (x-y)AlSi + 3(x-y)H^+ \rightarrow xAlF_y^{(3-y)+} + (x-y)silicagel . \quad (1.8)$$

Sources of iron include equipment from surface, subsurface, and formation minerals, such as chlorite, smectite and siderite (Al-Harbi et al. 2012). There are two states of iron: Fe(II) and Fe(III). Ferric hydroxide ($Fe(OH)_3$) and ferrous hydroxide ($Fe(OH)_2$) precipitate in spent acid under different pH conditions. Ferric hydroxide precipitates when pH is above around 1, while ferrous hydroxide precipitates when pH is above around 6. The reactions can be expressed as

$$Fe^{3+} + 3OH^- \leftrightarrow Fe(OH)_3 \cdot mH_2O \ (pH > 1), \quad (1.9)$$

$$Fe^{2+} + 2OH^- \leftrightarrow Fe(OH)_2 \cdot nH_2O \ (pH > 6). \quad (1.10)$$

According to pH conditions of the two reactions, ferric hydroxide is a potential precipitate in acid treatments.

## 1.2 LITERATURE REVIEW

### 1.2.1 Review of experimental work in carbonate acidizing

Researchers have obtained initial understanding on dissolution structures through experiments. 2D radial experiments were conducted by injecting pure water into plaster porous media (Daccord 1987). Final dissolution patterns at different flow rates were obtained by injecting Wood's metal (a low-melting-point alloy) into the dried plaster sample. The results showed that the branches were broader and the number of ramifications was smaller at lower flow rates. Linear coreflood experiments (Hoefner and Fogler 1988) were designed using limestone and dolomite, which represent two limiting regimes based on reaction rates: mass-transfer limited regime and reaction-limited regime. The channel structure (branch size and degree of branching) was controlled by fluid velocity and reaction rate, which can be described by the Damkohler number. More knowledge on dissolution patterns has been gained by subsequent experiments. Wang et al. (1993) conducted linear corefloods using limestone and dolomite. They discovered an optimum injection rate for reaching breakthrough corresponding to a minimum acid volume for limestone. At the optimum rate, a single wormhole penetrated the core. Fredd and Fogler (1999) conducted experiments on linear limestone cores. The reactant solutions included acetic acid (HAc), HCl, and chelating agents. They found a common dependence of the dissolution phenomenon on the Damkohler number and the existence of an optimum Damkohler number corresponding to the least acid consumption. Bazin (2001) did experimental work using limestone cores and two types of acid: HCl and acid-

in-diesel emulsion. They discovered that the optimum injection rate increased with acid concentration, temperature, and limestone permeability. In comparison between straight acid and emulsion acid, emulsion acid was more effective with less acid volume required and deeper penetration, especially at lower injection rates. McDuff et al. (2010) developed a methodology to conduct experiments on larger-scale carbonate rock samples up to 14 $ft^3$ in volume and utilized advanced CT imaging to visualize the intricacies of wormholes. Dong et al. (2017) conducted acidizing experiments to test the prediction from their semi-empirical model which take into account effects of rock lithology, acid concentration, temperature, and pore-size distribution. Dong et al. (2018) did experimental study using dolomite rock samples from Silurian formation. They visualized wormhole structures in dolomite and concluded dolomite generally requires larger acid volumes compared with limestone. Fredd (2000) summarized from previous experiments (Hoefner and Fogler 1988; Fredd and Fogler 1998; Fredd and Fogler 1999) the five main patterns of dissolution structures: face dissolution pattern, conical wormhole pattern, dominant wormhole pattern, ramified wormhole pattern, and uniform pattern.

### 1.2.2 Review of theoretical models in carbonate acidizing

The dissolution phenomenon and the existence of an optimum Damkohler number can be substantiated by different theoretical models: semi-analytical model, capillary tube model, network model, and two-scale continuum model.

Gong and El-Rabaa (1999) presented a quantitative wormhole model to predict wormhole growth, breakthrough volume and optimum injection rate. Before applying the model, experiments have to be conducted to determine the coefficients in the model for specific formation. Buijse (1997) derived an approximate expression of acid spending

profiles for reaction-controlled and diffusion-controlled regimes that fit the numerical results. Buijse and Glasbergen (2005) proposed a semi-empirical model to predict the average wormhole growth rate as a function of injection rate. The effects of parameters, such as permeability, temperature, acid type and acid concentration, were incorporated by fitting the model to experimental results. Talbot and Gdanski (2008) analyzed many experiments where plain HCl was used. The experiments varied in temperature, acid concentration, core aspect ratio, porosity, and permeability. Based on all the experimental data, they proposed a global function to fit all the data to generate a master curve. The curve can be used to predict the optimum injection rate given a set of experimental conditions. Baghel and Pravesh (2016) presented a semi-empirical model for chelating agents based on published experimental data.

In capillary tube model, a wormhole is assumed as a cylindrical pipe in which chemical kinetics and fluid hydrodynamics are considered. Nierode and Williams (1971) obtained a mathematical model considering acid reaction kinetics at the limestone surface, acid transfer rate to the surface, and fluid loss rate from the wormhole to the matrix on the premise wormhole geometry is known. They discovered that for HCl and limestone, fluid loss from the wormhole was a limiting step but reaction was not. Hung et al. (1989) developed a mathematical model to describe growth and competition of multiple wormholes. They characterized heterogeneity using the distribution of largest pores. Wormhole characteristics (size, length, and distribution) were controlled by injection, diffusion and fluid loss rate.

Network model (Fredd and Fogler 1998; Tansey 2014) is a pore-scale model, made up of nodes connected by cylindrical tubes called bonds. The nodes serve as pore space while the bonds represent pore throats. Hoefner and Fogler (1988) developed a triangular network model to study channeling. Fluid flow is simulated in bonds while

mixing is in nodes. The rate of bond growth is controlled by the reaction rate in the bond. The model can predict channel structures and the rate of channel propagation as a function of fluid flow rate, reaction rate, acid concentration, original permeability, and heterogeneity of the porous media. Tansey and Balhoff (2016) presented a pore-network model that included pore-scale mass transfer coefficient and pore-merging criterion. The simulation work based on the finite element method was able to describe permeability increase and reproduce different dissolution patterns. Gray et al. (2018) developed a pore-scale model to simulate carbonate acidizing and compared with experiments. They pointed out some challenges that prohibited comparison between simulation and experimental profiles, including unreliability in the micro-CT image with too much noise.

At a larger scale, two-scale continuum model is able to capture different types of dissolution patterns observed in experiments and can be used to simulate the core-scale samples. Darcy-scale model and pore-scale correlations constitute two-scale continuum model. Darcy-scale model describes convection, dispersion, and reaction. Pore-scale correlations relate Darcy-scale parameters to pore structure evolution. Panga et al. (2005) developed a two-scale continuum model on a 2D domain in a Cartesian coordinate system. They investigated the influence of different parameters including dispersion, heterogeneity, acid strength, and pore-scale mass transfer on wormhole formation. Kalia and Balakotaiah (2007) extended linear model to radial model (r-θ coordinate system) to simulate near wellbore flow geometry. They simulated three main dissolution types: compact dissolution, wormhole dissolution, and uniform dissolution. They studied the effects of heterogeneity magnitude and aspect ratio on dissolution behavior. Maheshwari et al. (2013) presented 3D simulation work in a Cartesian coordinate system to analyze the effects of acid injection rate, dissolution rate, and rock properties on wormhole formation. Liu et al. (2013) improved the model by considering invaded and compressed

zones. They investigated the effects of compressed zone and the distance of two layers on wormhole propagation. They also proposed that normally distributed porosity gives a better match with experiments than uniform porosity distribution. Qiu et al. (2014) investigated the effect of $CO_2$ on wormholing phenomena by conducting experiments to compare diffusion coefficients under different pressures. They coupled a new set of kinetics parameters obtained from the experiment with a 3D hydrodynamic numerical model. Compared with 1000 psi condition, under 3000 psi condition, wormholes were narrower and propagated faster, pore volumes to breakthrough were smaller and optimum injection rate was smaller. Ghommem et al. (2015) combined initial porosity distribution obtained from CT scanning and measured reaction kinetics to simulate 3D core-scale samples in a Cartesian coordinate system. Ghommem and Brady (2016) extended 2D radial model to 3D cylindrical model and analyzed the 3D carbonate acidizing process. They investigated the effect of rock heterogeneity on the wormhole initiation and propagation and captured wormhole patterns from compact dissolution, conical wormhole dissolution, dominant wormhole dissolution, to ramified wormhole dissolution. Tansey (2016) developed a two-scale continuum model with the hybrid technique. The mass transfer coefficients and the pore-scale correlations were provided by a pore network model. The model was accurate for high injection rates.

Recent studies which have focused on modeling matrix acidizing with in-situ gelled acids showed that gelled acids lead to more branched wormholes and more uniform stimulation by diversion (Ratnakar et al. 2013). Gelled acid is essential to stimulation for horizontal wells or vertical wells with long target zones, since high acid viscosity can improve acid diversion (Taylor and Nasi-El-Din 2003). MaGee et al. (1997) described the use of in-situ crosslinked acid (ICA) for fluid diversion during matrix acidizing in carbonate reservoirs. ICA treatments were successfully performed in the Idd

El Shargi field with final skin values of -3 to -4. Lynn and Nasr-El-Din (2001) compared reaction characteristics of diesel emulsified acid (DEA) and self-diverting polymer/HCl (in-situ gelled acid or GA) using reservoir condition corefloods. The results showed that GA formulations enhanced the permeability more than DEA. However, GA required larger volumes of acid to achieve the same penetration depth as DEA. GA left a residual of polymeric material in the wormholes while DEA left no residual. Chang et al. (2001) developed a self-diverting-acid (SDA) using a viscoelastic surfactant (VES). The viscosity of the solution increased with an increase in $Ca^{2+}$ and pH due to reaction. The new material left no residual once it had broken. Multi-core flood testing showed that SDA successfully diverted acid from high permeability section into low permeability section. Gomaa et al. (2010) studied the diversion ability of in-situ gelled acids using parallel corefloods. Experimental results showed that diversion was needed for nearly all acid treatments. For a high permeability contrast, lower injection rate was required to build enough pressure forcing the regular acid into the low permeability core. Ratnakar et al. (2012) developed a semi-empirical rheological model based on experimental data to investigate carbonate acidizing with gelled acids. They incorporated the rheological model into the two-scale continuum model to describe the reactive flow of gelling acids in carbonate reservoirs. They discovered that the amount of diversion strongly depended on rheological properties and injection rate.

### 1.2.3 Review of experimental work in sandstone acidizing

Besides widely-used mud acid, different acid systems have been applied in sandstone acidizing to achieve optimal acidizing performance or facilitate diversion between layers with different permeability ranges. Hill et al. (1981) conducted a series of coreflood experiments using an acid mixture of 3% HF and 12% HCl. They used Berea

sandstone with mineral compositions of quartz, dolomite, siderite, chlorite, illite, and feldspar. They measured HF effluent curves for comparison and validation with their theoretical model. Kunze and Shaughnessy (1983) conducted sandstone coreflood experiments to compare acidizing performance using fluoboric acid ($HBF_4$) and HF under formation conditions. They concluded that no evidence was observed on permeability response and effluent chemistry analysis for increased penetration distance using $HBF_4$ compared with HF under formation temperature. Hsi et al. (1993) conducted acidizing experiments using sandstone cores with different injection rates and different concentrations. They measured effluent HF to validate the theoretical model by Bryant (1991). Parlar et al. (1995) did acidizing studies using Berea sandstone through single-core and dual-core experiments. They investigated foam diversion by investigating sensitivities of surfactant types, surfactant concentrations, foam and post-foam injection rates, permeability, temperature, and presence of oil. They discovered that the critical parameters for foam diversion were surfactant type, pre-flush and foam slug sizes. Mahmoud et al. (2011) conducted acidizing experiments using a chelating agent. They used Berea sandstone with 8% of clays and glutami-N,N-diacetic acid (GLDA). The effects of injection rate, injection volume, temperature, pH of the chelating agent were investigated on the acidizing process. Ji et al. (2014) investigated the retardation effect of $AlCl_3$ using Berea sandstone core plugs and acid system with a combination of HCl, HF, and $AlCl_3$. They conducted solubility tests for clay minerals and coreflood tests for sandstones to prove the retardation effect of $AlCl_3$. Legemah et al. (2015) designed injection processes to treat sandstone or limestone formations with high bottomhole pressure using polycarboxylic (PC) or amino-polycarboxylic (APC) acid. Garcia et al. (2016) conducted sandstone acidizing experiments using APC with 1 to 1.5% HF. They concluded using an APC chelating agent expanded application regarding the temperature

range and mineral types. Shafiq et al. (2017) conducted sandstone acidizing experiments using a combination of acetic acid ($CH_3COOH$) and HCl in the pre-flush stage. Compared with experiments only using HCl in the pre-flush stage, the acid combination resulted in more significant effect on the porosity and removed positive ions more efficiently.

### 1.2.4 Review of theoretical models in sandstone acidizing

Theoretical models in sandstone acidizing have been developed and improved since 1960s (Leong et al. 2018). Williams and Whiteley (1971) developed a procedure to predict porosity changes during sandstone acidizing using HF. They used a lumped reaction rate obtained from experiments to represent heterogeneous reactions between acid and sandstone minerals. Hill et al. (1981) developed a capillary model to predict the effluent acid concentration and the model fitted well with experimental data. In the kinetic model, they lumped all the clays and feldspars into one average parameter. Taha et al. (1986) developed a numerical simulator to study sandstone acidizing. They used a two-parameter model to characterize reactions between HF and sandstone minerals. The first parameter incorporates reactions with all silicate minerals. The second parameter describes reaction with quartz. They investigated the effect of injection rates on acid penetration depth and diversion efficiency of a diverting agent on non-communicating layers. Bryant (1991) presented an improved chemistry model between mud acid and sandstone, considering a secondary dissolution/precipitation. The author took into consideration the reactivity of fluosilicic acid ($H_2SiF_6$) and precipitation of amorphous silica. Lea et al. (1992) developed a mathematical model to describe single-phase flow around a single perforation during sandstone acidizing. They assumed perforation was ellipsoidal and the sandstone was composed of two pseudo-chemical minerals with

different dissolution rates. Sevougian et al. (1995) developed a simulator KGEOFLOW with detailed chemistry characterization. The simulator has the capability of modeling sandstone acidizing considering any number of kinetic and equilibrium reactions. The geochemical simulator was used to predict optimal injection rate based on mineral dissolution and precipitation. Leong et al. (2019) built a simulation model using COMSOL (a commercial software of computational fluid dynamics) to study sandstone acidizing using $HBF_4$. They investigated the capability of $HBF_4$ on porosity/permeability improvement and the effect of temperature. Mou et al. (2019) developed a two-acid three-mineral numerical model for radial acid flooding. They took into consideration mineralogy heterogeneity and porosity/permeability heterogeneity. They investigated the effect of heterogeneity on acidizing performance.

### 1.2.5 Review of PHREEQC and IPhreeqc

PHREEQC (pH-REdox-EQuilibrium in C programing language) is a free, open-source geochemical package of the U.S. Geological Survey (Parkhurst and Appelo 1999; 2013). It is a very general and flexible tool for modeling reactive-transport studies with rich databases. This geochemical package has the capability of equilibrium calculations that include aqueous, mineral, gas, solid-solution, surface-complexation, and ion-exchange equilibria. It also has the capabilities of speciation and saturation index calculation, batch-reaction and one-dimensional transport, reversible and irreversible reactions, kinetic reaction, mixing solutions, and inverse modeling in which temperature and pressure effects are included.

If PHREEEQC is coupled with a reservoir simulator, the geochemical capabilities can be applied to comprehensively model reaction-related problems in the oil industry (Korrani 2014). There are two kinds of coupling approaches: soft coupling and hard

coupling. Soft coupling is easier to implement. In soft coupling, reservoir simulator writes the input file for PHREEQC, then PHREEQC is run externally to do equilibrium calculation for all gridblocks and provides the output file for reservoir simulator to read. Because of the repeated writing and reading, soft coupling is computationally slow. For hard coupling, PHREEQC source code needs to be modified to transfer data through computer memory. Hard coupling is difficult to program since data structures and data dependencies between the structures are complicated (Charlton and Parkhurst 2011). IPhreeqc is a free and open-source module of the PHREEQC designed to be used in scripting languages and integrated into C++, C, and Fortran programs. "I" stands for "Interface" in IPhreeqc. It means IPhreeqc provides an interface through which a simulator can easily communicate with PHREEQC geochemical package. Coupling with IPhreeqc makes simulation runs about an order of magnitude faster compared with soft coupling with PHREEQC (Muller et al. 2011). The speedup is due to several aspects: the first, data transfer between reservoir simulator and IPhreeqc is achieved using a well-defined set of methods skipping the process of writing and reading files; the second, IPhreeqc loads the database only once throughout the entire simulation; the third is that IPhreeqc performs the solution speciation only once at the first time step and later modifies it instead of recalculation. Muller et al. (2011) compared computational time for different coupling methods. CPU time of soft coupling with PHREEQC is 8.3 times that of using IPhreeqc as a dynamically linked library (DLL) to client software, 11.8 times that of coupling IPhreeqc with the client software written in the C++ programming language.

### 1.2.6 Review of research work in acidizing considering fractures

Accurately predicting the recovery from carbonate reservoirs is a challenging task because of both complexity and heterogeneity. Most carbonate reservoirs contain natural fractures that range from isolated microscopic fissures to "fracture swarms" which are kilometer-wide collections (Schlumberger 2008). This also poses difficulty in modeling acidizing process in carbonate reservoirs. Most researchers characterize heterogeneity of carbonates through initial porosity (or permeability) field in their simulation work. The porosity field is a family of random numbers within a certain range. Based on the porosity field, permeability distribution is calculated using pore-scale correlations. Some of them use uniform distribution (Maheshwari et al. 2013) while others use normal distribution to represent initial porosity field (Liu et al. 2013).

When acid is injected into a naturally fractured carbonate formation under formation fracture pressure, the acidizing process will be different from either a matrix treatment or an acid fracturing treatment (Dong et al. 1999). In matrix acidizing without considering natural fractures, acid usually generates wormholes at the optimal condition. In acid fracturing treatment, acid flows through wide fractures leading to relatively uniform etching of the fracture walls. However, during acidizing in naturally fractured reservoirs, different etching patterns in the fracture can be generated, depending on the width of the natural fracture. The widths of natural fractures range from $1\times10^{-3}$ cm to $5\times10^{-2}$ cm for reservoirs with depths less than 1000 m, and $1\times10^{-5}$ cm to $1\times10^{-2}$ cm for reservoirs with depths between 1500 m and 1700 m (Nelson 1979; 2001). In formations with low to medium permeability, the average hydraulic fracture width is between 0.3 cm and 1 cm (Economides and Nolte 1989).

Dong et al. (1999) conducted experiments to study the influence of natural fractures on the acid etching patterns using two closely contacted rock samples. The

fracture widths varied from $1\times10^{-3}$ cm to $9\times10^{-3}$ cm. The resulting etching patterns were strongly dependent on the width of the natural fracture. Broader and longer channels were generated with larger fracture width, while narrower and shorter channels form with smaller fracture width. Dong et al. (2001) presented a model to predict acid propagation along natural fracture networks and the etching of the fracture walls. They assumed the natural fracture network as a system of intersecting fractures forming a main pathway for acid transport and dissolution. Acid penetration estimate from this model was deeper than the model considering only matrix flow. Dong et al. (2002) developed a mathematical model to describe transport and dissolution in a single natural fracture. The model included the change of fracture width due to reaction and acid leak-off. They observed three different etching patterns: wormhole pattern, channel pattern, and uniform pattern. The patterns depended on initial fracture width and surface roughness of the fracture wall. The acid leak-off had little effect on etching patterns but created wormholes perpendicular to the fracture walls. However, these models only considered reactive transport in the fractures neglecting flow in the matrix around the fractures. Salimi et al. (2014) used Computational Fluid Dynamics (CFD) scheme to simulate fluid flow in the fracture and in the matrix for naturally fractured reservoirs. The model coupled Darcy's law, reaction flow equation, and fracture growth equation. The effects of fracture geometry, acid properties, fracture width, and matrix permeability were analyzed during matrix acidizing process. Xiong (1994) developed a simulation model to investigate matrix acidizing in naturally fractured carbonates. He used a network model to represent arbitrarily distributed fractures. The model was used to predict the effective acid penetration distance and the requirement on the acid volume. In the model, the flow in the matrix was eliminated and the parameter distribution in every fracture was not obtained since the natural fracture distribution was simplified in the network model. Liu

et al. (2017) used a continuum model with explicit fractures to examine wormhole propagation in matrices with single and multiple fractures. The fluid flow and acid transport were modeled both in the matrix and in the fracture, but the reaction on the fracture wall was neglected.

### 1.2.7 Review of EDFM (Embedded Discrete Fracture Model)

There are three different approaches to simulate fractured reservoirs: dual porosity and dual permeability (DPDP) approach; discrete fracture model (DFM) approach; embedded discrete fracture model (EDFM) approach. DPDP approach is computationally efficient and has been successfully applied to many real field studies. However, due to the simplification in the model, they are only adequate for reservoirs with a large number of inter-connected small-scale fractures. In addition, it is not an explicit method to simulate fractures. It means during acidizing, etching patterns in the fractures cannot be simulated through DPDP approach. DFM method is more accurate in modeling of large-scale fractures and fracture geometry can be detailed. However, DFM method requires complex gridding and large computational time. As a compromise, EDFM method has been developed to keep the accuracy of DFM approach using structured gridding (Xu 2015).

In EDFM method, the reservoir is discretized using Cartesian grids, while additional grids are introduced for the fractures. Lee et al. (2001) described a hierarchical approach to model flow in naturally fractured formation. They classified fractures into three groups: short fractures, medium-length fractures, and long fractures. The fractures were computed in a hierarchical manner. For short fractures, an analytical expression has been derived to calculate their permeability contribution. The effective matrix permeability with medium-length fractures was numerically solved using a boundary

element method. The long fractures were modeled explicitly as major fluid conduits. Li and Lee (2008) proposed a hybrid finite volume method to simulate multiphase flow in a field-scale naturally fractured reservoir. They introduced a simple, systematic way to calculate transport parameters between fracture networks and discretized, homogenized media. Also, they devised an efficient numerical algorithm to solve the dual system of fracture network and finite volume grid. Hajibeygi et al. (2011) devised an iterative multiscale finite volume method to simulate multiphase flow in fractured reservoir under a hierarchical fracture framework. Moinfar et al. (2014) extended the EDFM to 3D and implemented in GPAS, a fully-implicit in-house compositional simulator developed at The University of Texas at Austin. The model was compatible with existing finite difference discretization. Fractures can have arbitrary orientations in the model. Shakiba (2014) implemented EDFM in UTCOMP (a compositional simulator) and UTGEL (a compositional-chemical simulator). Xu et al. (2016) described a method to introduce EDFM into reservoir simulators with Cartesian grids. The model can handle fractures with nonplanar shape and variable aperture. They demonstrated the accuracy and efficiency of the EDFM by comparison with LGR (local grid refinement) method and a semi-analytical solution. They successfully applied EDFM in a hydraulically fractured reservoir with natural fractures.

### 1.3 RESEARCH OBJECTIVES

The primary objective of this dissertation is to develop a numerical acidizing model for carbonate and sandstone reservoirs. Complex reactions between acid and different mineral compositions during acidizing need to be considered. Different aspects of heterogeneity in carbonates need to be taken into consideration, including porosity heterogeneity, mineralogy heterogeneity, and natural fractures.

The following are the specific objectives of this dissertation:

- Develop a reactive transport simulator for acidizing in radial coordinates considering water and oil two-phase flow; propose a breakthrough criteria for acidizing simulation considering overall mobility change.
- Implement acidizing module into UTCOMP-IPhreeqc to consider simultaneously occurring reactions during acidizing, including kinetic reactions between acid and mineral compositions, and equilibrium reactions among aqueous species.
- Implement acidizing module into UTCOMP-IPhreeqc-EDFM to consider mineral dissolution on the fracture surface due to reaction in fractured carbonates.
- Implement acidizing module into UTCOMP with parallelized IPhreeqc and utilize two types of speedup methods to improve computational efficiency for matrix acidizing.
- Supplement IPhreeqc database with kinetic reactions between HF and minerals in sandstone and apply UTCOMP-IPhreeqc in sandstone acidizing.

## 1.4 ORGANIZATION OF THE DISSERTATION

The dissertation is divided into nine chapters. Following this chapter, Chapter 2 introduces the two-scale continuum model in radial coordinates considering water and oil two-phase flow and the model validation.

In Chapter 3, simulation cases using the two-scale continuum model in radial coordinates are analyzed, and the effects of rock wettability, oil viscosity, and initial oil saturation on wormhole propagation and acidizing efficiency are investigated.

In Chapter 4, the acidizing model in UTCOMP-IPhreeqc is introduced and the validation case is presented.

In Chapter 5, simulation cases using UTCOMP-IPhreeqc considering complex mineral compositions in carbonates are analyzed and the effect of mineralogy heterogeneity is investigated on wormhole propagation and acidizing efficiency.

In Chapter 6, the acidizing model in UTCOMP-IPhreeqc-EDFM is introduced; simulation cases with consideration of fractures are presented. The effects of fracture existence in homogeneous and heterogeneous matrices are analyzed on wormhole propagation and acidizing efficiency.

In Chapter 7, parallel performance using UTCOMP with parallelized geochemical calculation is evaluated. Two types of speedup methods, used for reducing IPhreeqc calls to improve computational efficiency, are introduced. The computational efficiency for different dissolution patterns is analyzed using the speedup methods.

In Chapter 8, IPhreeqc database is modified to include kinetic reactions between acid and minerals in sandstone; simulation cases for sandstone acidizing are presented.

In Chapter 9, summary, conclusions, and future work are introduced.

# CHAPTER 2: MODELING AND VALIDATION OF ACIDIZING PROCESS IN RADIAL COORDINATES[1]

Matrix acidizing is a stimulation technique aiming at either improving formation permeability or bypassing damaged zone. In this process, acid is injected through the well into the vicinity of wellbore to dissolve the rock. For either production or injection wells, the formation may contain multiple phases (water and oil) near the wellbore region when acid treatment begins. In this chapter, a two-phase two-scale continuum model is developed to simulate wormhole propagation in radial coordinates. The model describes mechanisms of convection, dispersion, and reaction in two-phase flow during matrix acidizing. We have validated the simulation model using two methods: one is to compare with the previous simulation results; the other is to compare with the analytical solution. In addition, we have proposed a new criterion for acid breakthrough since the pressure response is not only affected by reaction, but also by overall mobility change in the formation. The traditional criterion for single-phase model is no longer applicable to the current two-phase model.

## 2.1 INTRODUCTION

Matrix acidizing can be used in different production stages. When used at initial time, it is a method to maximize the productivity of new wells. When applied in the middle of production, the objective is to restore productivity of aging wells.

Recent studies focused on modeling matrix acidizing with in-situ gelled acids showed that gelled acids lead to more branched wormholes and more uniform stimulation

[1] The content of this chapter was published as: Wei, W., Varavei, A., and Sepehrnoori, K. 2017. Modeling and analysis on the effect of two-phase flow on wormhole propagation in carbonate acidizing. SPE Journal 22(06): 2067-2083. https://doi.org/10.2118/186111-PA. Kamy Sepehrnoori supervised the research, provided technical support, and revised the manuscript. Abdoljalil Varavei provided technical support and revised the manuscript.

by diversion. Acid diversion is essential to stimulation for horizontal wells or vertical wells with long target zones; high acid viscosity can improve acid diversion (Taylor and Nasi-El-Din 2003). Gomaa et al. (2010) studied the diversion ability of in-situ gelled acids using parallel corefloods. Ratnakar et al. (2012) developed a semi-empirical rheological model to investigate carbonate acidizing with gelled acids. These studies indicate that decreasing the mobility of injecting acids contributes to more uniform stimulation. However, deep penetration using minimum amount of acid is also important, especially when stimulating single layer formation.

Previous two-scale continuum models focused on single-phase flow. However, acidizing may involve two-phase flow since acid treatment can be applied at any stage of production wells. If acid treatment is applied in the middle of oil production to restore productivity of old wells, any oil saturation condition may exist when acidizing begins. Even if acid stimulation is applied on wells immediately after completion, any oil saturation is possible, but it is highly possible that the near wellbore region is saturated with water with residual oil saturation or oil with irreducible water saturation. It depends on whether drilling fluid is water based or oil based. As mentioned in the previous work (Golfier et al. 2002), channeling phenomenon in chemical dissolution is similar to viscous fingering in miscible or immiscible floods. Both of these processes are unstable due to the heterogeneity of the porous media. In single-phase dissolution, water preferentially flows into the path where fluid has the largest mobility corresponding to the least resistance. Similarly, in two-phase displacement process, water saturation is larger in high permeability regions than in the surroundings. The superposition of these two similar mechanisms can reduce fluid loss from main paths and improve acidizing efficiency.

In this chapter, a two-scale continuum model is developed including water and oil two-phase flow in radial coordinates. A new criterion that has been used to define acid breakthrough is proposed taking overall mobility change into consideration.

## 2.2 METHODOLOGY

### 2.2.1 Assumptions

In this study, two phases of water and oil are considered and acid only exists in the water phase. Reservoir rock, water and oil are incompressible. Reaction is irreversible with a single step following the rule of first-order reaction and 100% of the rock can react with acid. The process is isothermal which means that heat generated during reaction is neglected. Capillary pressure and gravity are neglected in the current implementation.

### 2.2.2 Darcy-scale model

There are two sets of continuity equations for water and oil. Continuity equation ensures mass conservation and is used to describe transport of either phase. Continuity equations for water and oil phases in radial coordinates are

$$\frac{\partial (S_w \varphi)}{\partial t} + \nabla \cdot \mathbf{U_w} = 0, \tag{2.1}$$

$$\frac{\partial (S_o \varphi)}{\partial t} + \nabla \cdot \mathbf{U_o} = 0, \tag{2.2}$$

where $S_w$ and $S_o$ are water and oil saturation, respectively; $\varphi$ is the porosity of the matrix; $t$ is time; $r$, $\theta$, and $z$ represent independent variables in cylindrical coordinates; $\mathbf{U_w} = (u_w, v_w, w_w)$ is the Darcy velocity vector for water; $\mathbf{U_o} = (u_o, v_o, w_o)$ is the Darcy velocity vector for oil; $u_w$ and $u_o$ are components of Darcy velocity in $r$ direction for water and oil, respectively; $v_w$ and $v_o$ are components of Darcy velocity in

$\theta$ direction for water and oil, respectively; $w_w$ and $w_o$ are components of Darcy velocity in $z$ direction for water and oil, respectively.

Darcy's law relates phase velocity with pressure gradient and can be inserted into continuity equation. Darcy's law can be expressed as

$$u_w = -\frac{KK_{rw}}{\mu_w}\frac{\partial p}{\partial r}, v_w = -\frac{KK_{rw}}{\mu_w}\frac{1}{r}\frac{\partial p}{\partial \theta}, w_w = -\frac{KK_{rw}}{\mu_w}\frac{\partial p}{\partial z}, \tag{2.3}$$

$$u_o = -\frac{KK_{ro}}{\mu_o}\frac{\partial p}{\partial r}, v_o = -\frac{KK_{ro}}{\mu_o}\frac{1}{r}\frac{\partial p}{\partial \theta}, w_o = -\frac{KK_{ro}}{\mu_o}\frac{\partial p}{\partial z}, \tag{2.4}$$

where $K$ is the permeability of the matrix; $K_{rw}$ and $K_{ro}$ are water and oil relative permeabilities, respectively; $\mu_w$ and $\mu_o$ are water and oil viscosities, respectively; $p$ is pressure.

Combined equations of continuity equation and Darcy's law are used to solve pressure and phase saturation and can be written as

$$\frac{\partial (S_w \varphi)}{\partial t} - \frac{1}{r}\frac{\partial}{\partial r}\left( r\frac{KK_{rw}}{\mu_w}\frac{\partial p}{\partial r}\right) - \frac{1}{r}\frac{\partial}{\partial \theta}\left(\frac{KK_{rw}}{\mu_w}\frac{1}{r}\frac{\partial p}{\partial \theta}\right) - \frac{\partial}{\partial z}\left(\frac{KK_{rw}}{\mu_w}\frac{\partial p}{\partial z}\right) = 0, \tag{2.5}$$

$$\frac{\partial (S_o \varphi)}{\partial t} - \frac{1}{r}\frac{\partial}{\partial r}\left( r\frac{KK_{ro}}{\mu_o}\frac{\partial p}{\partial r}\right) - \frac{1}{r}\frac{\partial}{\partial \theta}\left(\frac{KK_{ro}}{\mu_o}\frac{1}{r}\frac{\partial p}{\partial \theta}\right) - \frac{\partial}{\partial z}\left(\frac{KK_{ro}}{\mu_o}\frac{\partial p}{\partial z}\right) = 0. \tag{2.6}$$

Generalized Corey correlation is used to calculate relative permeability to water and oil. The equations are as follows:

$$K_{rw} = (K_{rw})_{S_{or}}\left(\frac{S_w - S_{wc}}{1 - S_{wc} - S_{or}}\right)^{n_w}, \tag{2.7}$$

$$K_{ro} = (K_{ro})_{S_{wc}}\left(\frac{1 - S_w - S_{or}}{1 - S_{wc} - S_{or}}\right)^{n_o}, \tag{2.8}$$

where $(K_{rw})_{S_{or}}$ is the water relative permeability at residual oil saturation; $(K_{ro})_{S_{wc}}$ is the oil relative permeability at connate water saturation; $S_{or}$ is the residual oil saturation; $S_{wc}$ is the connate water saturation; $n_w$ and $n_o$ are exponents on relative permeability curves for water and oil, respectively.

Acid concentration in water phase can be solved using acid species conservation equation. There are three mechanisms included in the equation: convection, dispersion and reaction. The equation is as follows:

$$\frac{\partial\left(\varphi S_w C_f\right)}{\partial t}+\nabla\cdot(\mathbf{U_w}C_f)=\nabla\cdot(\varphi S_w\mathbf{D_e}\cdot\nabla C_f)-k_c a_{vw}\left(C_f-C_s\right), \tag{2.9}$$

where $C_f$ is the average concentration of acid in water phase; $\mathbf{D_e}$ is the effective dispersion tensor in water phase; $k_c$ is the mass transfer coefficient from water phase to rock surface; $a_v$ is the matrix interfacial area, that is fluid-rock interfacial area per unit matrix volume; $a_{vw}$ is the interfacial area which is available to the water phase, $a_{vw}=a_v f$, $f$ is the water-solid contacting efficiency; $C_s$ is the acid concentration at fluid-rock surface.

El-Hisnawi et al. (1982) proposed two forms of correlations for the external contacting efficiency of porous packing trickle-bed reactors. One form is based on Reynolds number and Galileo number, while the other form relates the external contacting efficiency with dynamic liquid saturation. In this work, the water-solid contacting efficiency is described by the following correlation (El-Hisnawi et al. 1982):

$$f=aS_w^{\,b}, \tag{2.10}$$

where $a=1.02$, $b=0.244$.

The above correlation was obtained through experiments using trickle-bed reactors with concurrent gas and liquid flow (El-Hisnawi et al. 1982). We may investigate more using different correlations to calculate wetting efficiency for rocks with different wettability in future work.

The convection term can be expanded as

$$\nabla\cdot(\mathbf{U_w}C_f)=\frac{1}{r}\frac{\partial}{\partial r}\left(ru_wC_f\right)+\frac{1}{r}\frac{\partial}{\partial\theta}\left(v_wC_f\right)+\frac{\partial}{\partial z}\left(w_wC_f\right). \tag{2.11}$$

Each dispersion coefficient consists of two parts: one is molecular diffusion, the other is mechanical dispersion. Hence, the value of each element in the effective dispersion tensor is dependent on molecular diffusion, pore geometry, and water phase velocity. The effective dispersion tensor in cylindrical coordinates can be expressed as

$$\mathbf{D_e} = \begin{bmatrix} D_{err} & D_{er\theta} & D_{erz} \\ D_{e\theta r} & D_{e\theta\theta} & D_{e\theta z} \\ D_{ezr} & D_{ez\theta} & D_{ezz} \end{bmatrix}. \tag{2.12}$$

Thus, the dispersion term can be expanded as

$$\nabla \cdot (\varphi S_w \mathbf{D_e} \cdot \nabla C_f) = \xi_r + \xi_\theta + \xi_z, \tag{2.13}$$

$$\xi_r = \frac{1}{r}\frac{\partial}{\partial r}\left[\varphi S_w (D_{err} r \frac{\partial C_f}{\partial r} + D_{er\theta} \frac{\partial C_f}{\partial \theta} + D_{erz} r \frac{\partial C_f}{\partial z})\right], \tag{2.14}$$

$$\xi_\theta = \frac{1}{r}\frac{\partial}{\partial \theta}\left[\varphi S_w (D_{e\theta r} \frac{\partial C_f}{\partial r} + \frac{D_{e\theta\theta}}{r} \frac{\partial C_f}{\partial \theta} + D_{e\theta z} \frac{\partial C_f}{\partial z})\right], \tag{2.15}$$

$$\xi_z = \frac{\partial}{\partial z}\left[\varphi S_w (D_{ezr} \frac{\partial C_f}{\partial r} + \frac{D_{ez\theta}}{r} \frac{\partial C_f}{\partial \theta} + D_{ezz} \frac{\partial C_f}{\partial z})\right]. \tag{2.16}$$

In an acidizing process, acid reacts with rock to increase porosity. Based on first-order reaction, reaction rate is linearly proportional to acid concentration at fluid-rock surface. The rate of porosity increase depends on reaction rate, acid dissolving power, rock density, and matrix interfacial area. Porosity change due to reaction is as follows:

$$\frac{\partial \varphi}{\partial t} = \frac{R(C_s)\alpha a_{vw}}{\rho_s}, \tag{2.17}$$

$$R(C_s) = k_s C_s, \tag{2.18}$$

where $k_s$ is the reaction rate constant based on surface area; $\alpha$ is the acid dissolving power; $\rho_s$ is the solid density.

As dissolution proceeds, acid transfers from water phase to fluid-solid surface. The amount of acid transferred is equal to that reacted with surface rock. The relationship

can be used to correlate acid concentration in water phase with that at fluid-solid surface, and can be expressed as

$$k_c\left(C_f - C_s\right) = R\left(C_s\right). \tag{2.19}$$

### 2.2.3 Pore-scale correlations

Dissolution of rock not only increases the porosity, but also changes the structure of the matrix, leading to an increase in permeability and average pore radius and a decrease in interfacial area. A modified Carman-Kozeny (Carman 1956) correlation can be used to relate the change of other parameters with the change of porosity. Maheshwari and Balakotaiah (2013) proposed an improved structure-property correlation that takes into consideration both pore-broadening and pore-connectivity effects. Here, this new two parameter correlation is used as follows:

$$\frac{K}{K_0} = \left(\frac{\varphi}{\varphi_0}\right)^{\gamma}\left(\frac{\varphi\left(1-\varphi_0\right)}{\varphi_0\left(1-\varphi\right)}\right)^{2\beta}, \tag{2.20}$$

$$\frac{r_p}{r_{p0}} = \left(\frac{\varphi\left(1-\varphi_0\right)}{\varphi_0\left(1-\varphi\right)}\right)^{\beta}, \tag{2.21}$$

$$\frac{a_v}{a_{v0}} = \frac{\varphi}{\varphi_0}\left(\frac{\varphi\left(1-\varphi_0\right)}{\varphi_0\left(1-\varphi\right)}\right)^{-\beta}, \tag{2.22}$$

where $\varphi_0$ is the initial average porosity, also used as the reference porosity; $r_p$ is the pore radius; $K_0$ is the reference permeability; $r_{p0}$ is the reference pore radius; $a_{v0}$ is the reference interfacial area; $\gamma$ is the pore-connectivity parameter; $\beta$ is the pore-broadening parameter.

The correlations (Maheshwari and Balakotaiah 2013) used to calculate absolute permeability, pore radius, and interfacial area have a common parameter $\beta$, this may cause additional limitations for comparison between simulation and experiments when

tuning empirical parameters. Schwalbert (2019) obtained better matching with experimental results through modifying these correlations by using different exponents.

A general functional form of Sherwood number is shown in Balakotaiah and West (2002). To consider incomplete wetting in two-phase flow, wetting efficiency is introduced into the correlation (Satterfield et al. 1978; Rao and Drinkenburg 1985; Saroha 2010). Correlations for calculation of effective dispersion coefficients are adopted from Kalia and Balakotaiah (2007). The effective dispersion tensor is considered by two components, the effective longitudinal dispersion coefficient $D_{eL}$, and the effective transverse dispersion coefficient $D_{eT}$. The equations can be expressed as

$$Sh = \frac{2k_c r_p}{D_m} = Sh_\infty + \frac{0.7}{m^{1/2}} Re_p^{1/2} Sc^{1/3}, \tag{2.23}$$

$$D_L = \frac{D_{eL}}{D_m} = \alpha_{os} + \frac{2\lambda_L \left|\mathbf{U_w}\right| r_p}{\varphi S_w D_m}, \tag{2.24}$$

$$D_T = \frac{D_{eT}}{D_m} = \alpha_{os} + \frac{2\lambda_T \left|\mathbf{U_w}\right| r_p}{\varphi S_w D_m}, \tag{2.25}$$

$$Re_p = \frac{2\left|\mathbf{U_w}\right| r_p}{\nu_w}, \tag{2.26}$$

$$Sc = \frac{\nu_w}{D_m}, \tag{2.27}$$

where $Sh$ is the Sherwood number that is defined as the ratio of the total rate of mass transfer to the rate of diffusion; $D_m$ is the effective molecular diffusivity of acid in water phase; $Sh_\infty$ is the asymptotic Sherwood number; $m$ is the ratio of pore length to pore diameter; $Re_p$ is the pore-scale Reynold's number which represents the ratio of inertial force to viscous force based on average pore radius; $Sc$ is the Schmidt number which is the ratio of momentum diffusivity and mass diffusivity; $\alpha_{os}$, $\lambda_L$ and $\lambda_T$ are numerical constants; $\left|\mathbf{U_w}\right|$ is the magnitude of water velocity; $\nu_w$ is the kinematic viscosity of water which can be expressed as $\frac{\mu_w}{\rho_w}$; $\mu_w$ is the dynamic viscosity of water.

### 2.2.4 Boundary and initial conditions

Darcy-scale model and pore-scale correlations need to be coupled to obtain fields of pressure, phase saturation, acid concentration and porosity at different times. In addition, initial conditions and boundary conditions are necessary to provide constraints to the above set of Darcy-scale differential equations.

Initial conditions include distributions of pressure, saturation, acid concentration, and porosity. The heterogeneity of carbonate rocks can be characterized using any form of porosity distribution, which can represent a family of random numbers within a certain range. This is essential to initiate wormholes in the matrix. Initial conditions can be expressed as

$$p = p_i, S_w = S_{wi}, C_f = C_{fi}, \varphi = \varphi_i, at\ t = 0\ , \tag{2.28}$$

where $p_i$ is the distribution of initial pressure; $S_{wi}$ is the distribution of initial water saturation; $C_{fi}$ is the distribution of initial acid concentration; $\varphi_i$ is the distribution of initial porosity.

Specifically, in the following cases, initial pressure is constant in the domain. It is assumed there is no acid present before water injection. Initial water saturation is also constant, but different values ranging from $S_{wc}$ to $1\text{-}S_{or}$ have been assigned in different cases.

There are four boundaries in the current model: inner boundary at $r = r_w$, outer boundary at $r = r_e$, upper boundary at $z = z_u$, and lower boundary at $z = z_l$. Generally, boundary conditions for 3D flow in cylindrical coordinates include periodic boundary condition, and Dirichlet condition or Neumann condition imposed on any of the four boundaries. Periodic boundary conditions for pressure and acid concentration can be expressed as

$$p(r,\theta,z) = p(r,\theta+2\pi,z), C_f(r,\theta,z) = C_f(r,\theta+2\pi,z)\ . \tag{2.29}$$

Based on different purposes, different boundary conditions can be used on any of the four boundaries. Among different sets of boundary conditions, two of them are used in the sensitivity studies and in the validation case, respectively.

***Radial flow boundary conditions***

At inner boundary, water injection with a constant rate and a constant acid concentration is imposed. At outer boundary, pressure is fixed as a constant value and Neumann boundary condition is used for acid concentration. Neumann boundary conditions with the derivatives equaling zero are applied on upper and lower boundaries representing no-flow boundaries.

$$u_w = -\frac{KK_{rw}}{\mu_w}\frac{\partial p}{\partial r} = u_0, u_o = 0, C_f = C_0, at\ r = r_w, \tag{2.30}$$

$$p = p_e, \frac{\partial C_f}{\partial r} = 0, at\ r = r_e, \tag{2.31}$$

$$w_w = -\frac{KK_{rw}}{\mu_w}\frac{\partial p}{\partial z} = 0, w_o = -\frac{KK_{ro}}{\mu_o}\frac{\partial p}{\partial z} = 0, \frac{\partial C_f}{\partial z} = 0, at\ z = z_u, \tag{2.32}$$

$$w_w = -\frac{KK_{rw}}{\mu_w}\frac{\partial p}{\partial z} = 0, w_o = -\frac{KK_{ro}}{\mu_o}\frac{\partial p}{\partial z} = 0, \frac{\partial C_f}{\partial z} = 0, at\ z = z_l, \tag{2.33}$$

where $u_0$ is the constant water injection velocity at inlet; $C_0$ is the acid concentration at inlet defined as number of moles per volume of water phase; $r_w$ is the inner radius of the domain; $p_e$ is the constant pressure at outer boundary; $r_e$ is the outer radius of the domain; $z_u$ and $z_l$ are positions of upper boundary and lower boundary of the domain, respectively.

***Linear flow boundary conditions***

To model linear flow in a cylindrical core, the flow is from one end of the cylindrical matrix to the other end in $z$ direction. For inner or outer boundary, Neumann boundary conditions are applied for pressure and acid concentration. For one end of the

cylindrical core, constant water flow rate and constant acid concentration are applied. For the other end of the core, pressure is fixed and second boundary condition for acid concentration is applied. Boundary conditions applied here can be expressed as

$$u_w = 0, u_o = 0, \frac{\partial C_f}{\partial r} = 0, at\ r = r_w, \tag{2.34}$$

$$u_w = 0, u_o = 0, \frac{\partial C_f}{\partial r} = 0, at\ r = r_e, \tag{2.35}$$

$$w_w = -\frac{KK_{rw}}{\mu}\frac{\partial p}{\partial z} = w_0, w_o = 0, C_f = C_0, at\ z = z_u, \tag{2.36}$$

$$p = p_e, \frac{\partial C_f}{\partial z} = 0, at\ z = z_l. \tag{2.37}$$

### 2.3 NEW CRITERION OF ACID BREAKTHROUGH FOR TWO-PHASE FLOW

The purpose of acidizing is to enhance permeability in well vicinity. In laboratory scale core, pressure is fixed at outer boundary. To increase average permeability in the domain to 100 times, the difference between bottomhole pressure and outer boundary pressure should decrease to 1/100 of initial value since average permeability is inversely correlated with the pressure difference. This can be obviously implied in ideal single-phase equation for steady-state radial flow as follows:

$$q = \frac{2\pi \bar{K} h \left( p_{bh} - p_e \right)}{\mu ln\left( r_e / r_w \right)}, \tag{2.38}$$

where $q$ is the fluid flow rate; $\bar{K}$ is the average permeability in the domain; $h$ is the thickness of the domain; $p_{bh}$ is the bottomhole pressure; $p_e$ is the pressure at outer boundary; $\mu$ is the fluid viscosity; $r_e$ is the outer radius of the domain; $r_w$ is the inner radius of the domain.

However, this criterion is not applicable to two-phase flow. In two-phase flow cases, both acid-rock reaction and mobility change due to water-oil displacement affect permeability. Water and oil flow equations can be respectively expressed as

$$q_w = \frac{2\pi \bar{K} h \left( p_{bh} - p_e \right)}{ln\left( r_e / r_w \right)} \frac{K_{rw}}{\mu_w}, \tag{2.39}$$

$$q_o = \frac{2\pi \bar{K} h \left( p_{bh} - p_e \right)}{ln\left( r_e / r_w \right)} \frac{K_{ro}}{\mu_o}, \tag{2.40}$$

where $q_w$ is the water flow rate; $K_{rw}$ is the water relative permeability; $\mu_w$ is the water viscosity; $q_o$ is the oil flow rate; $K_{ro}$ is the oil relative permeability; $\mu_o$ is the oil viscosity.

The total flow rate is the summation of the water flow rate and the oil flow rate:

$$q = \frac{2\pi \bar{K} h \left( p_{bh} - p_e \right)}{ln\left( r_e / r_w \right)} \left( M_{rw} + M_{ro} \right), \tag{2.41}$$

$$M_{rw} = \frac{K_{rw}}{\mu_w}, \tag{2.42}$$

$$M_{ro} = \frac{K_{ro}}{\mu_o}, \tag{2.43}$$

where $M_{rw}$ is the water relative mobility; $M_{ro}$ is the oil relative mobility.

In two-phase flow, pressure drop $\Delta p = p_{bh} - p_e$ is no longer inversely proportional to the average absolute permeability, since average mobility $\frac{K_{rw}}{\mu_w} + \frac{K_{ro}}{\mu_o}$ in the domain changes and depends on average water saturation in the domain (as water is injected, water saturation increases). To separate the effect of mobility ratio on bottomhole pressure, mobility has to be taken into consideration. At breakthrough time, water saturation almost reaches 1-$S_{or}$ in main flow paths. So, the new criterion is expressed as

$$p_{bhf} - p_e = \frac{1}{100}\left(p_{bhi} - p_e\right)\frac{\left(M_{rw} + M_{ro}\right)_{S_{wi}}}{\left(M_{rw} + M_{ro}\right)_{S_w = 1 - S_{or}}}, \tag{2.44}$$

where $p_{bhf}$ is the bottomhole pressure at breakthrough time; $p_{bhi}$ is the bottomhole pressure at initial time; $(M_{rw} + M_{ro})_{S_{wi}}$ is the summation of water relative mobility and oil relative mobility at initial water saturation; $(M_{rw} + M_{ro})_{S_w = 1 - S_{or}}$ is the summation of water relative mobility and oil relative mobility at residual oil saturation.

This criterion is consistent with previous criterion for single-phase flow. For single-phase of water, there is no residual oil saturation and water saturation is 1.0 from beginning to end. The same saturation condition guarantees the same overall mobility at breakthrough as before the acidizing treatment, which leads to the same value for the numerator and the denominator in Eq. 2.44.

## 2.4 VALIDATION

### 2.4.1 Comparison with previous work

To compare with simulation work from Kalia and Balakotaiah (2007) in radial coordinate system, radial flow boundary conditions are applied. At initial time, uniform distribution of porosity is selected to represent the heterogeneity of carbonates. Parameter values used are listed in Table 2.1.

| Parameter | Value | Parameter | Value | Parameter | Value |
|---|---|---|---|---|---|
| $\alpha_w$ | 0.20 | $N_{ac}$ | 0.1 | $\lambda_L$ | 0.5 |
| $\varphi_0$ | 0.20 | $Sc$ | 1,000 | $\lambda_T$ | 0.1 |
| $\Delta\varphi_0$ | ±0.15 | $Sh_\infty$ | 3.0 | $m$ | 1.0 |
| $\phi^2$ | 0.07 | $\eta$ | 0.000001 | $\gamma$ | 1.0 |
| $\Phi^2$ | 1,000,000 | $\alpha_{os}$ | 0.5 | $\beta$ | 1.0 |

Table 2.1: Parameter values in comparison with previous work.

Dimensionless variables used in Kalia and Balakotaiah (2007) are as follows:

$$\alpha_w = \frac{r_w}{r_e}, \phi^2 = \frac{2k_s r_{p0}}{D_m}, \Phi^2 = \frac{k_s a_{v0} r_e^2}{D_m}, N_{ac} = \frac{\alpha C_0}{\rho_s}, \eta = \frac{2r_{p0}}{r_e}, Da = \frac{k_s a_{v0} r_e}{u_0}, \quad (2.45)$$

where $\alpha_w$ is the aspect ratio; $\phi^2$ is the pore-scale Thiele modulus, which is defined as the ratio of reaction rate to diffusion rate based on reference pore radius; $\Phi^2$ is the macroscopic Thiele modulus; $N_{ac}$ is the acid capacity number; $\eta$ is the ratio of reference pore radius to external radius of the domain; $Da$ is the Damkohler number defined as the ratio of reaction rate to convection rate.

PVBT (pore volume breakthrough) represents how much pore volume is required when acidizing process reaches breakthrough. In this validation case with single-phase flow, breakthrough is defined as the time when pressure drop across the domain decreases to 1/100 of initial pressure drop, which is consistent with the new two-phase flow criterion mentioned above. Damkohler number used in the validation case is defined in Eq. 2.45, which is consistent with that used in Kalia and Balakotaiah (2007). This definition is similar to that defined in Fredd and Fogler (1998) for reaction rate limited dissolution. PVBT values corresponding to different Da numbers are listed in Table 2.2. The PVBT values are very close except for a slightly larger difference at Da=5.0. This is due to randomness of initial porosity distribution. The exact same distribution cannot be guaranteed.

| Da | PVBT of Kalia et al. | PVBT of current model |
|---|---|---|
| 50.0 | 4.30 | 4.48 |
| 33.33 | 4.54 | 4.53 |
| 20.0 | 5.62 | 5.51 |
| 10.0 | 9.00 | 8.73 |
| 5.0 | 12.62 | 11.59 |

Table 2.2: Comparison of PVBT values with work by Kalia and Balakotaiah (2007).

### 2.4.2 Comparison with analytical solution

Maheshwari et al. (2013) derived an analytical solution for 1D dissolution under single-phase flow condition. To validate simulation model, simulation model predictions are compared with the result calculated from analytical solution. To ensure the same flow condition with the analytical solution, linear flow boundary conditions need to be used. Here, the flow is from one end of the cylindrical matrix to the other end in $z$ direction.

To follow the assumptions made in derivation of analytical solution, mass transfer coefficient and dispersion coefficients are kept constant in the simulation, and porosity is constant in the matrix at initial time. Parameters used in this validation case are listed in Table 2.3.

| Parameter | Value | Unit | Parameter | Value | Unit |
|---|---|---|---|---|---|
| $r_e$ | 2.77 | in | $r_{p0}$ | 1.0 | μm |
| $r_w$ | 0.125 | in | $a_{v0}$ | 50.0 | $cm^{-1}$ |
| $h$ | 1.38 | in | $Sh_\infty$ | 3.66 | - |
| $\varphi_0$ | 0.20 | - | $D_m$ | $4\times10^{-10}$ | $m^2/s$ |
| $K_0$ | 10.0 | md | $\alpha_{os}$ | 0.5 | - |
| $p_i$ | 1500.0 | psi | $\lambda_L$ | 0.0 | - |
| $\mu_w$ | 1.0 | cp | $\lambda_T$ | 0.0 | - |
| $c_0$ | 0.1 | - | $\alpha$ | 50.0 | g/mol |
| $k_s$ | $1.4\times10^{-5}$ | m/s | - | - | - |

Table 2.3: Parameter values used in the validation case.

In Table 2.3, $c_0$ is acid mass concentration at inlet defined as mass of acid per mass of water phase. The relationship of $c_0$ and $C_0$ is as follows:

$$C_0 = \frac{c_0 \rho_w}{MW_{HCl}}, \tag{2.46}$$

where $MW_{HCl}$ is the molecular weight of HCl; $\rho_w$ is the water phase density; $C_0$ is the acid concentration at inlet defined as number of moles per volume of water phase.

The comparisons of simulation model predictions and analytical results are shown in Figure 2.1. The porosity and fluid velocity match well except for a small difference.

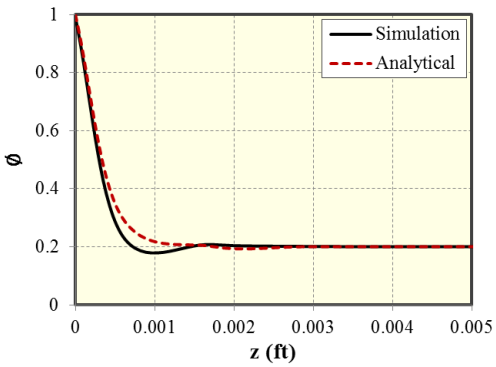


(a) Porosity

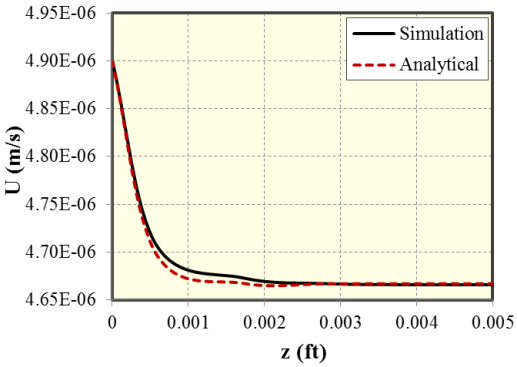


(b) Fluid velocity

Figure 2.1: Comparison of parameters between simulation model and analytical solution.

# CHAPTER 3: EFFECT OF TWO-PHASE FLOW ON WORMHOLE PROPAGATION IN CARBONATE ACIDIZING[2]

In this chapter, simulation results of a two-phase acidizing simulator in radial coordinates are presented and the key parameters influencing wormhole propagation in water-oil two-phase flow are analyzed. The parameters include rock wettability, oil viscosity, and initial water saturation. It is found that water-oil mobility ratio is a key factor that affects acidizing efficiency. The results show that adverse water-oil mobility ratio leads to a higher efficiency for wormhole breakthrough. In carbonate reservoirs with heterogeneity, water-oil displacement and wormhole propagation contribute to narrower, less branched channels. Through the two-phase acidizing model, it is possible to simulate formations with two phases (water and oil) during carbonate acidizing. The presented model improves our understanding in optimization of carbonate acidizing.

Various parameters used in simulation are listed in Table 3.1. The grid information is listed in Table 3.2. All of them are fixed unless otherwise stated. In these case studies, radial flow boundary conditions are used and a uniform distribution of porosity at initial time is applied. Some of the parameters are selected from radial core experiments (Tardy et al. 2007).

[2] The content of this chapter was published as: Wei, W., Varavei, A., and Sepehrnoori, K. 2017. Modeling and analysis on the effect of two-phase flow on wormhole propagation in carbonate acidizing. SPE Journal 22(06): 2067-2083. https://doi.org/10.2118/186111-PA. Kamy Sepehrnoori supervised the research, provided technical support, and revised the manuscript. Abdoljalil Varavei provided technical support and revised the manuscript.

| Parameter | Value | Unit | Parameter | Value | Unit |
|---|---|---|---|---|---|
| $r_e$ | 2.77 | in | $\gamma$ | 1.0 | - |
| $r_w$ | 0.125 | in | $\beta$ | 1.0 | - |
| $h$ | 2.25 | in | $r_{p0}$ | 1.0 | μm |
| $\varphi_0$ | 0.11 | - | $a_{v0}$ | 50.0 | $cm^{-1}$ |
| $\Delta\varphi_0$ | ±0.05 | - | $Sh_\infty$ | 3.0 | - |
| $K_0$ | 19.6 | md | $D_m$ | $3.6\times10^{-9}$ | $m^2/s$ |
| $p_i$ | 1500.0 | psi | $\alpha_{os}$ | 0.5 | - |
| $\mu_w$ | 1.2 | cp | $\lambda_L$ | 0.5 | - |
| $\mu_o$ | 1.2 | cp | $\lambda_T$ | 0.1 | - |
| $c_0$ | 0.15 | - | $\alpha$ | 50.0 | g/mol |
| $k_s$ | 0.005 | m/s | $m$ | 1.0 | - |

Table 3.1: Parameters used in the simulation.

| Parameter | | Value | Unit |
|---|---|---|---|
| No. of gridblocks | | 1600 (40×40) | - |
| $\Delta r$ | | 0.066 | in |
| $\Delta\theta$ | | 0.157 | rad |
| Permeability | $r$ direction | Heterogeneous | - |
| | $\theta$ direction | Heterogeneous | |
| Porosity | | Heterogeneous | - |

Table 3.2: Grid information in the simulation.

### 3.1 EFFECT OF WETTABILITY

About 80% of carbonate reservoirs are believed to have neutral to preferentially oil-wet conditions (Chabert et al. 2010). However, carbonate reservoirs with preferentially water-wet conditions also exist. Certain percent of carbonate reservoirs are naturally water-wet (Treiber and Owens 1972; Chilingar and Yen 1983). And researchers have been seeking different techniques to change carbonate reservoirs toward more water-wet to increase waterflood efficiency (Jarrahian et al. 2012). Wettability effect is

investigated in this study using two sets of relative permeability curves representing rocks with typical water-wet and typical oil-wet properties. These two curves are shown in Figure 3.1. They follow the shape of typical water-wet and oil-wet curves from Geffen et al. (1951). In the simulator, relative permeability curves are calculated using generalized Corey correlation, which was developed for a wider range of rock and wettability characteristics. The reference interfacial area available to the water phase for single-phase case and two-phase cases is assumed to be the same.

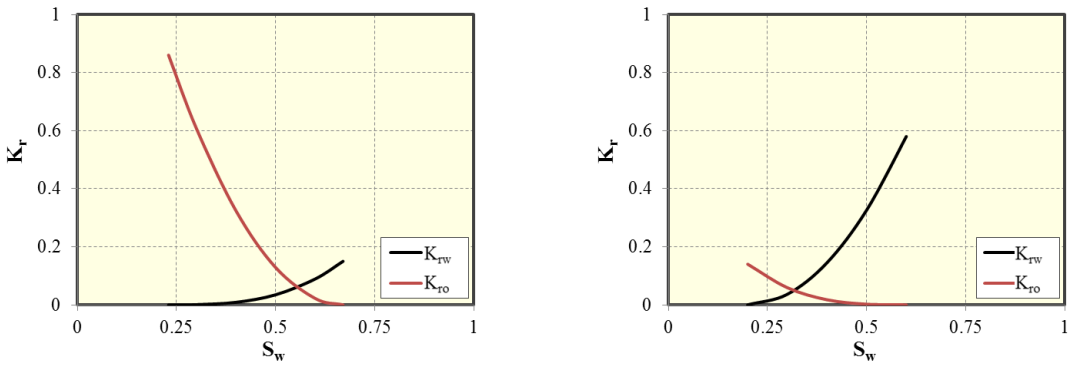


(a) Typical water-wet (b) Typical oil-wet

Figure 3.1: Effect of wettability on relative permeability curves.

There are three cases put into comparison. In Case 1, single-phase of water exists in the domain. In Case 2 and Case 3, the domain is saturated with oil with residual water at the time before acid injection. The difference between Case 2 and Case 3 is that relative permeability curves under water-wet condition are used in Case 2, while curves under oil-wet condition are used in Case 3. Acid breakthrough volume results corresponding to different Damkohler numbers for three cases are shown in Figure 3.2. Damkohler number used in sensitivity studies is defined in Eq. 2.45. As implied in Eq. 2.45, Damkohler number is negatively correlated with injection rate, which means higher

Damkohler number corresponds to lower injection rate while lower Damkohler number corresponds to higher injection rate. Either for single-phase case or two-phase cases, there is an optimal Damkohler number corresponding to smallest acid consumption. The optimal Damkohler number for these cases is 10 but different numbers may be obtained for different domain dimensions.

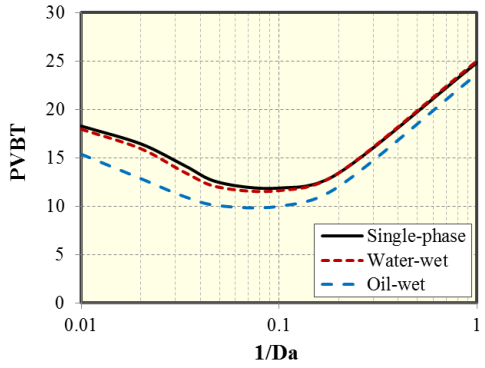


Figure 3.2: Effect of wettability on acid breakthrough curves.

Smaller volume of acid is required in either of the cases with two-phase flow although the water-wet case result is very similar to single-phase case, which implies that the presence of an immiscible phase prior to acid injection reduces acid consumption. This is consistent with the observations of experimental work (Shukla et al. 2006). As water flows into the domain, water will preferentially flow into the path with larger overall mobility, giving rise to larger water saturation in some higher permeability regions than surroundings. Preferential flow of water in these higher permeability regions means larger acid convection resulting in higher acid concentration in the water phase. Accordingly, rock dissolution rate is larger in high permeability regions than surroundings. In this way, main paths will be generated and main paths will have larger water saturation than surroundings. Relative permeability curves show that water relative

permeability is positively correlated with water saturation. It is harder for water to leak from main paths for two-phase flow compared with single-phase flow. The results suggest that higher efficiency with smaller amount of acid consumption can be achieved if oil exists with residual water before acid injection.

For two cases with rocks of different wettability conditions, oil-wet case has a larger efficiency in Figure 3.2. Water-oil mobility ratios after intersection points on relative permeability curves for these two cases are shown in Figure 3.3. In the comparison with water-wet case, mobility ratio of water and oil is much larger in the oil-wet case as water saturation increases from intersection point approaching residual oil condition. Adverse mobility ratio will facilitate water flow into regions with larger overall mobility compared with single-phase flow. And this effect is more severe in the oil-wet case than in the water-wet case, which can be seen obviously from the water saturation profiles at breakthrough in Figures 3.4 and 3.5. Compared with uniform water saturation in the whole region for water-wet case at breakthrough, water saturation is higher in main paths than surroundings in the oil-wet case, which has a compatible distribution with porosity and acid concentration, as shown in Figures 3.6 and 3.7. For water-wet case, from water saturation distributions either at breakthrough shown in Figure 3.4 or at early time shown in Figure 3.8, small water-oil mobility ratio leads to a stable water-oil displacement front. This can explain why water-wet case gives a result similar to single-phase case.

At initial time, water is at residual saturation where water has a smaller mobility than oil. However, at very early time, before injected water reaches 1.0 pore volume, water saturation in every part of the region reaches the intersection point on respective relative permeability curves, as shown for the water-wet case in Figure 3.8, and the oil-wet case in Figure 3.9. At this time, wormholes have not been generated or have just been

initiated, which can be seen in Figures 3.10 and 3.11. As long as water saturation reaches the intersection point, water has a larger mobility than oil in these cases (where water and oil have the same viscosity). Basically, during the entire stage of wormhole formation, water always has a larger mobility than oil, which is the adverse mobility ratio situation. On relative permeability curves under water-wet condition, the intersection point lies on $S_w$=0.55, and on relative permeability curves under oil-wet condition, intersection point lies on $S_w$=0.33. It should be mentioned that water chemistry may affect the rock wettability during acidizing process. There are two mechanisms: one is that water chemistry changes the charge on the rock surface; the other is that water chemistry dissolves rock minerals (Hiorth et al. 2010). These two mechanisms could occur simultaneously during acidizing treatment. However, wettability property of the rock is assumed stable in the current work. In a future work, wettability alteration may be considered.

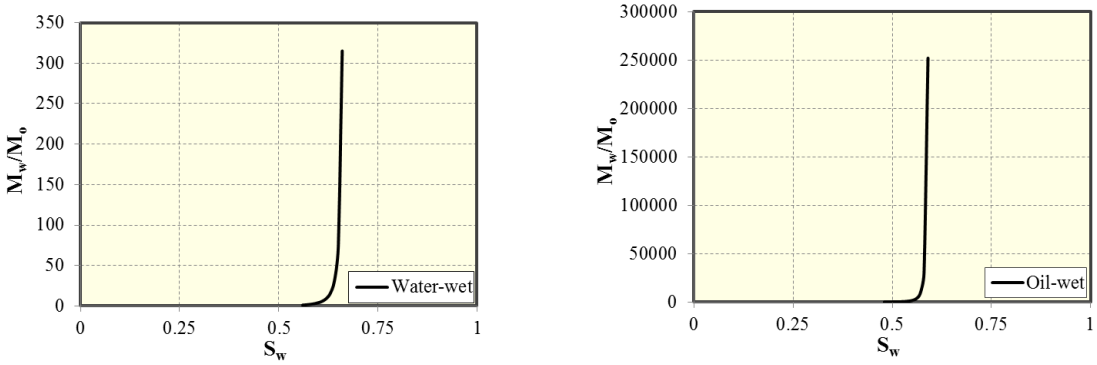


(a) Water-wet case (b) Oil-wet case

Figure 3.3: Water-oil mobility ratios.

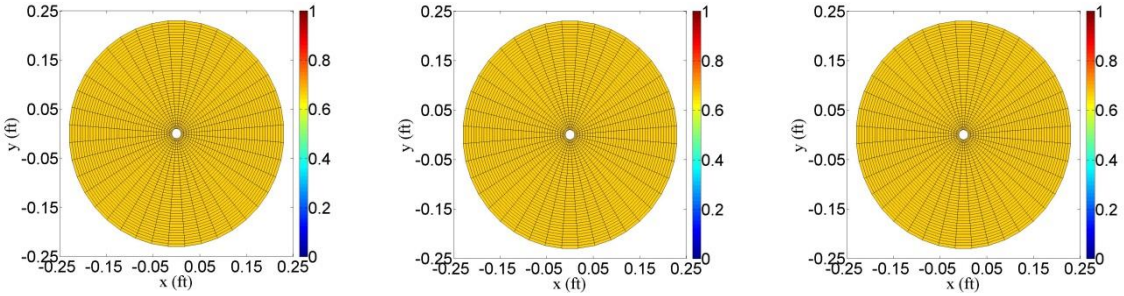


(a) Da=1.0 (b) Da=10.0 (c) Da=100.0

Figure 3.4: Water saturation distributions at breakthrough for water-wet case.

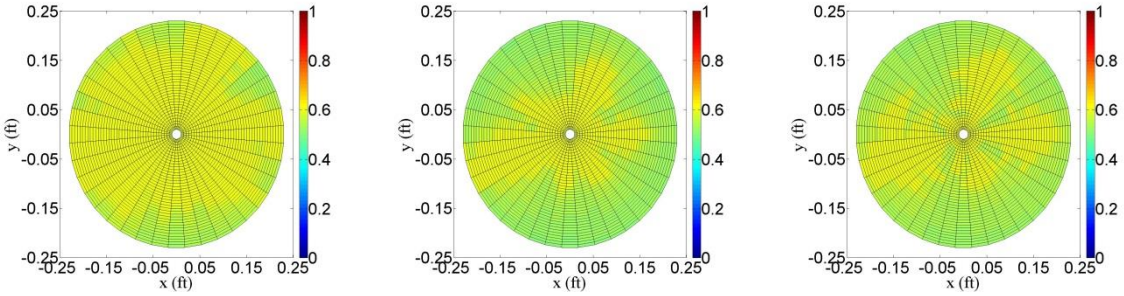


(a) Da=1.0 (b) Da=10.0 (c) Da=100.0

Figure 3.5: Water saturation distributions at breakthrough for oil-wet case.

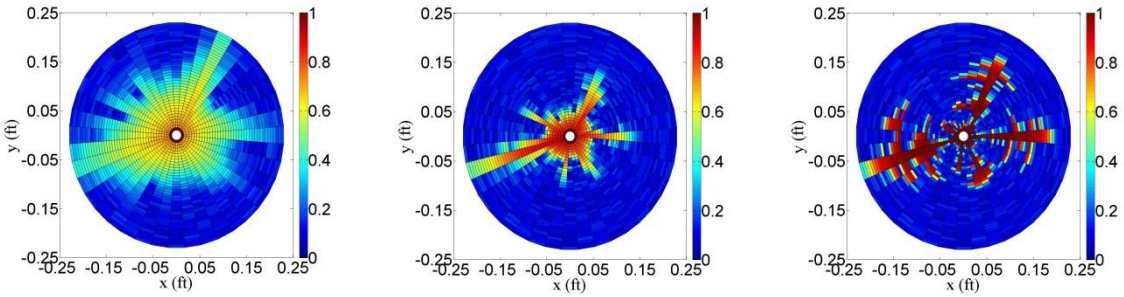


(a) Da=1.0 (b) Da=10.0 (c) Da=100.0

Figure 3.6: Porosity distributions at breakthrough for oil-wet case.

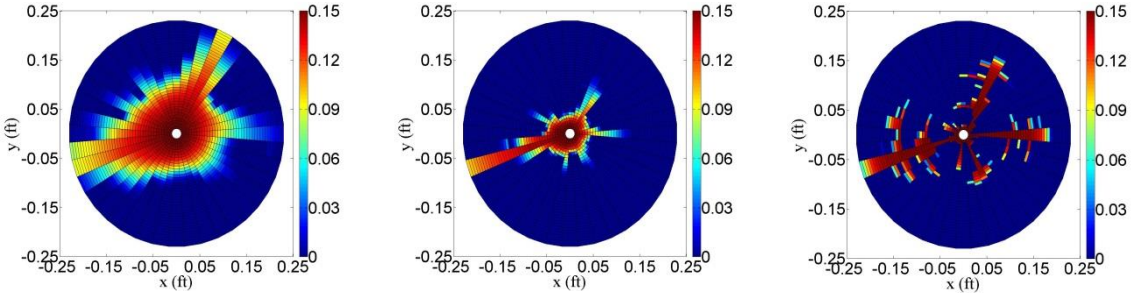


(a) Da=1.0 (b) Da=10.0 (c) Da=100.0

Figure 3.7: Acid concentration distributions at breakthrough for oil-wet case.

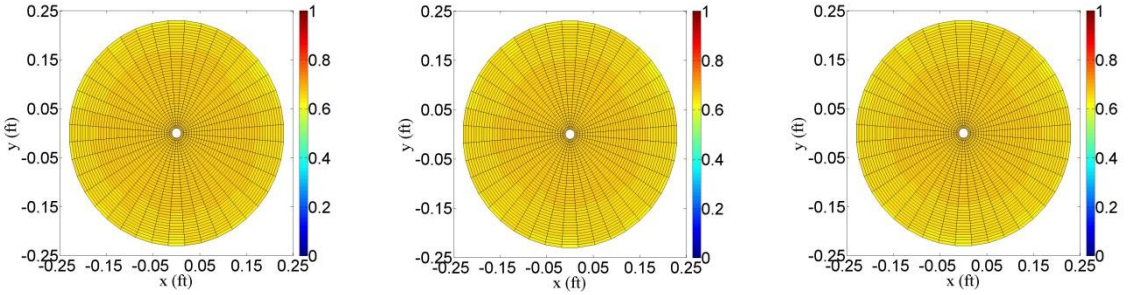


(a) Da=1.0 (b) Da=10.0 (c) Da=100.0

Figure 3.8: Water saturation distributions at PV=0.54 for water-wet case.

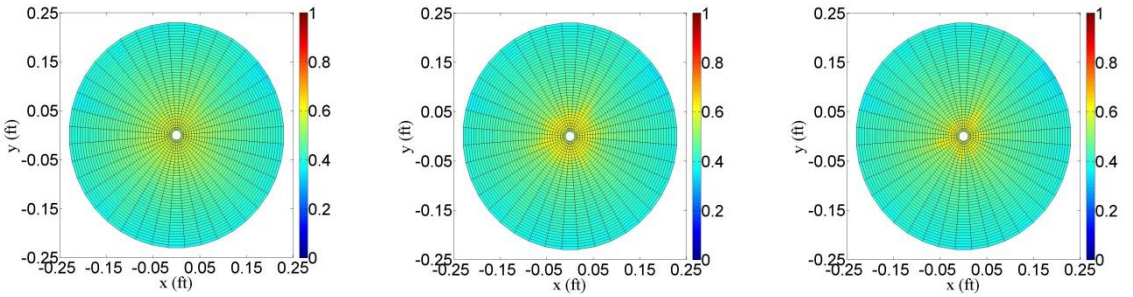


(a) Da=1.0 (b) Da=10.0 (c) Da=100.0

Figure 3.9: Water saturation distributions at PV=0.36 for oil-wet case.

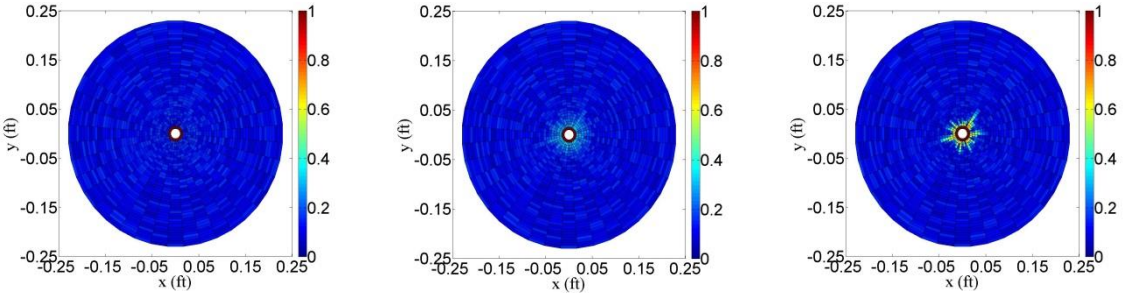


(a) Da=1.0 (b) Da=10.0 (c) Da=100.0

Figure 3.10: Porosity distributions at PV=0.54 for water-wet case.

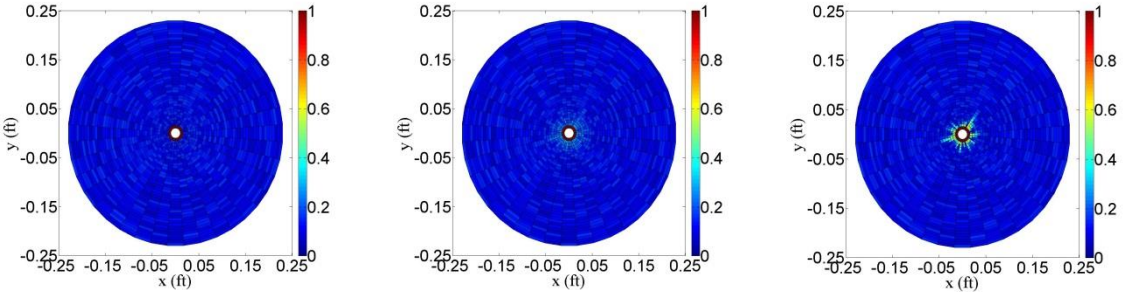


(a) Da=1.0 (b) Da=10.0 (c) Da=100.0

Figure 3.11: Porosity distributions at PV=0.36 for oil-wet case.

### 3.2 PRESSURE DROP ANALYSIS

Dimensionless pressure drop in radial flow is defined as

$$\Delta P = \frac{2\pi K_0 h\left(p_{bh} - p_e\right)}{\mu q_0 \ln\left(r_e / r_w\right)}, \tag{3.1}$$

where $q_0$ is the injection rate; $\mu$ is the fluid viscosity, water and oil are assumed to have the same viscosity.

Pore volume injected is expressed as

$$PV = \frac{q_0 t}{\pi\left(r_e^{\,2} - r_w^{\,2}\right) h\varphi_0}. \tag{3.2}$$

Taking Da=10.0 as an example, pressure drop curves for single-phase case, water-wet case, and oil-wet case are shown in Figure 3.12.

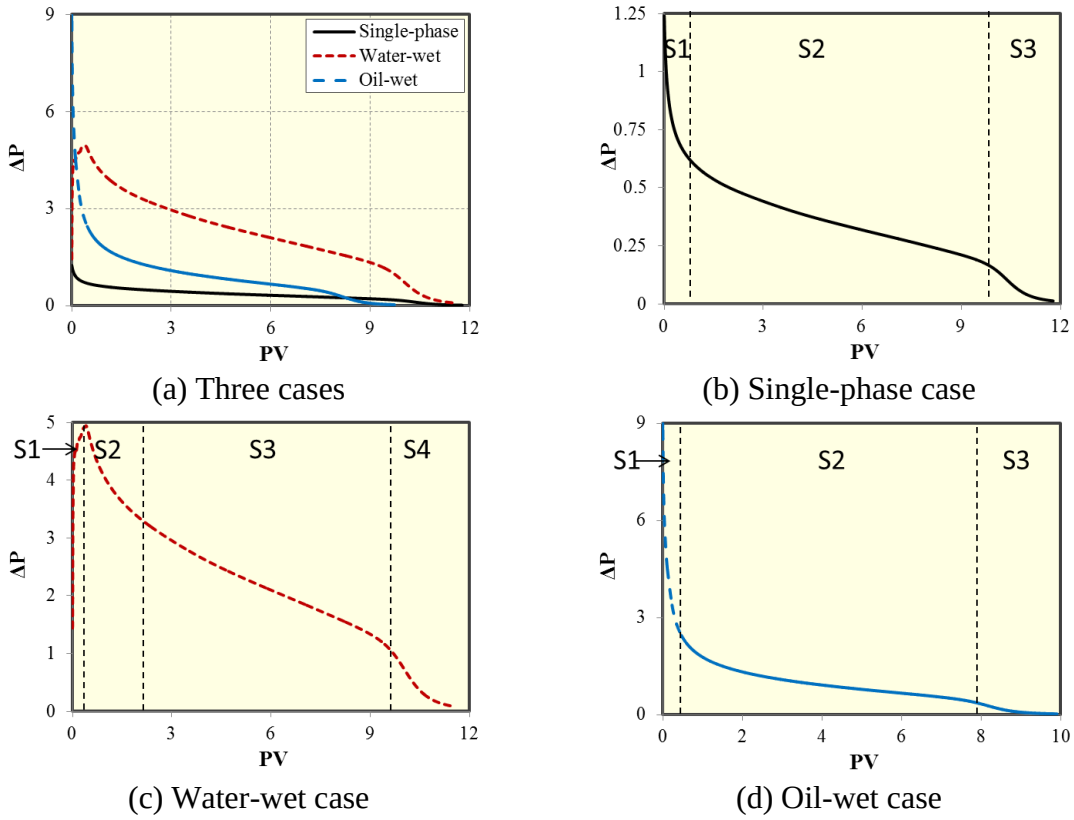


(a) Three cases (b) Single-phase case

(c) Water-wet case (d) Oil-wet case

Figure 3.12: Pressure drop curves plotted against pore volume injected at Da=10.0.

For single-phase flow, there are three stages on pressure decline curves: initiation region where wormholes start to form; wormhole propagation region where pressure declines steadily; end-zone region where pressure declines faster than in the wormhole propagation region. This is consistent with the pressure response analysis of Kalia and Balakotaiah (2007). For oil-wet case, there are also three stages, but pressure decline at the first stage is due to two reasons: one is that rock dissolution increases the absolute permeability; the other is that the overall relative mobility increases as water saturation increases, as shown in Figure 3.13(b). For water-wet case in Figure 3.12(c), there are four stages: displacement region, initiation region, wormhole propagation region, and end

region. In displacement region, the effect of overall relative permeability decrease is more pronounced than that of absolute permeability increase, leading to an increase of pressure drop. In initiation region, saturation condition is relatively stable in the domain, so rock dissolution begins to take effect. The last two stages are similar to that in the single-phase case.

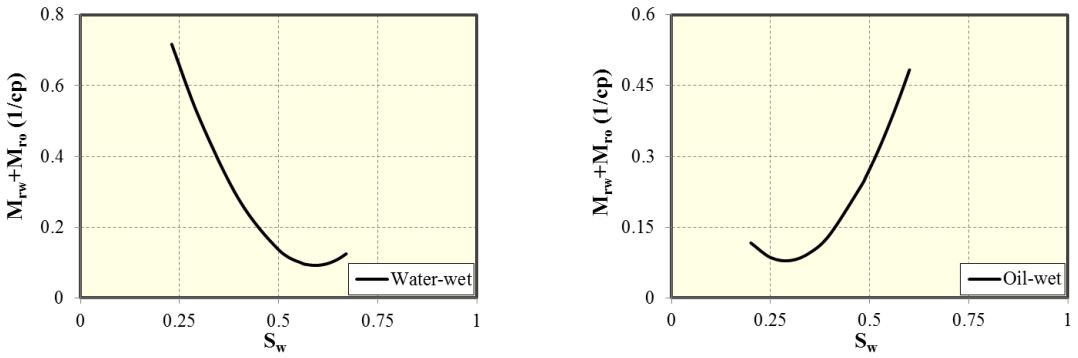


(a) Water-wet case (b) Oil-wet case

Figure 3.13: Overall relative mobility variation with water saturation.

### 3.3 EFFECT OF OIL VISCOSITY

The effect of oil viscosity is studied by simulating acidizing process with two-phase flow for different values of oil viscosity. At initial time, the domain is saturated with oil with residual water saturation and rock has preferentially water-wet condition. Acid breakthrough curves are compared in Figure 3.14. Less volume of acid is required for cases with larger oil viscosity. Larger oil viscosity makes water-oil mobility ratio even higher, which causes inefficient sweep in displacement of oil by water, as shown in Figure 3.17. However, in acidizing process, it is favorable that water mainly flows into some higher permeability regions and bypasses other lower permeability regions. Correspondingly, acid concentration has a compatible distribution as water saturation

distribution, as shown in Figure 3.18. Dissolution goes faster in higher permeability regions with higher acid concentration to increase the heterogeneity further, leading to early breakthrough. Comparison of water-oil mobility ratios is shown in Figure 3.15.

Porosity distributions at breakthrough for cases with different oil viscosities at Da=10.0 are shown in Figure 3.16. It is obvious that wormholes are thicker and more branched when oil has a smaller viscosity. On the contrary, wormholes are narrower and less branched for higher oil viscosity. When oil viscosity is 10 cp, there are six main wormholes and one of them reaches the outer boundary first. Similarly, when oil viscosity is 100 cp, there are six main wormholes, but except for the longest one, other five wormholes stop propagation earlier than that in the case with oil viscosity 10 cp. For the case with oil viscosity 1,000 cp, there are only four main wormholes and one of them develops much faster than the other three. This means that with large oil viscosity, most of the injected acid flows into one major wormhole that reaches the outer boundary finally. This can explain why larger oil viscosity gives higher acidizing efficiency with less acid consumed.

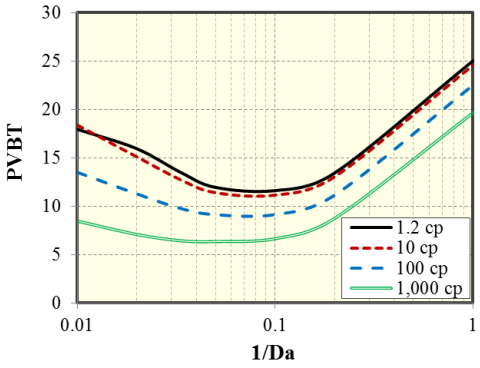


Figure 3.14: Effect of oil viscosity on acid breakthrough curves for water-wet cases.

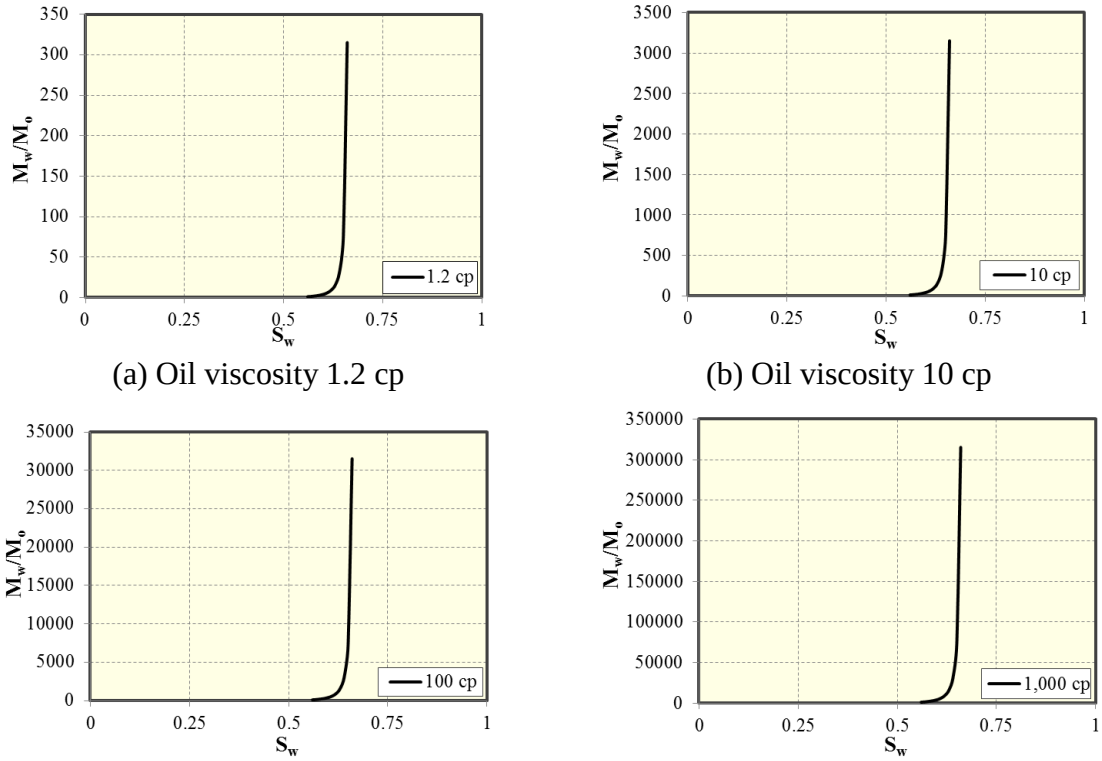


(a) Oil viscosity 1.2 cp (b) Oil viscosity 10 cp

(c) Oil viscosity 100 cp (d) Oil viscosity 1,000 cp

Figure 3.15: Effect of oil viscosity on water-oil mobility ratios.

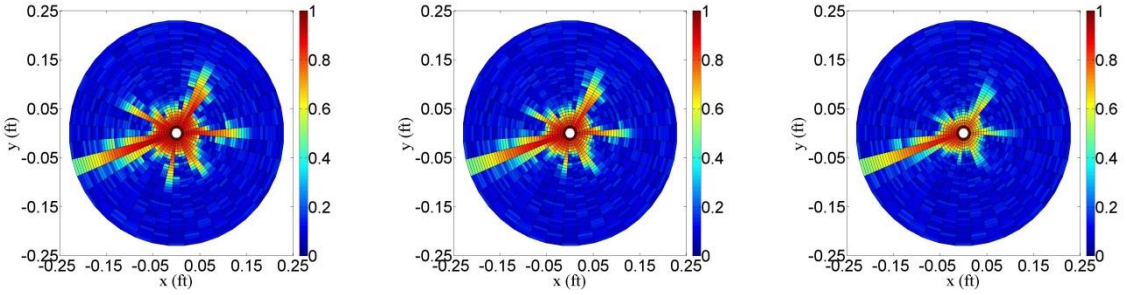


(a) Oil viscosity 10 cp (b) Oil viscosity 100 cp (c) Oil viscosity 1,000 cp

Figure 3.16: Porosity distributions of Da=10.0 at breakthrough time.

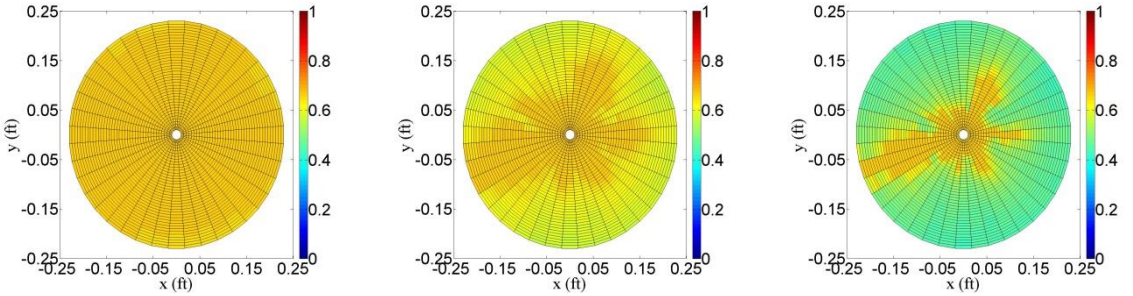


(a) Oil viscosity 10 cp (b) Oil viscosity 100 cp (c) Oil viscosity 1,000 cp

Figure 3.17: Water saturation distributions of Da=10.0 at breakthrough time.

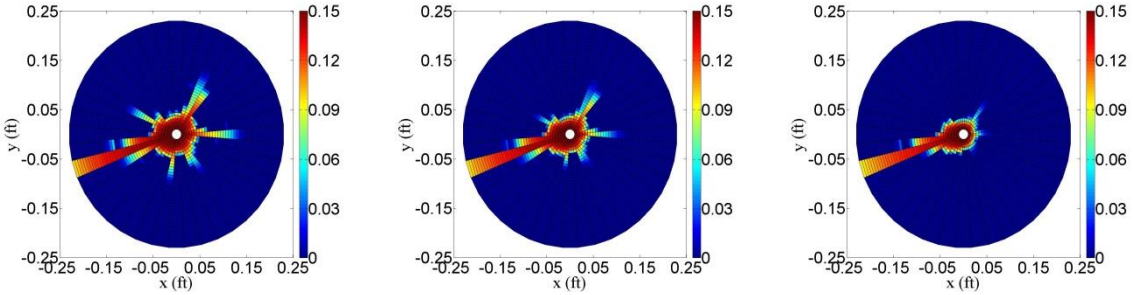


(a) Oil viscosity 10 cp (b) Oil viscosity 100 cp (c) Oil viscosity 1,000 cp

Figure 3.18: Acid concentration distributions of Da=10.0 at breakthrough time.

### 3.4 EFFECT OF INITIAL WATER SATURATION

There are different phase saturation conditions that may occur before the acidizing process. The effect of initial water saturation is investigated by assigning different values in the matrix at initial time. In these cases, rocks are assumed to have preferentially oil-wet condition; so relative permeability curves of typical oil-wet in Figure 3.1(b) are used. Connate water saturation is 0.20 and residual oil saturation is 0.40. Acid breakthrough curves for different initial water saturations are compared in Figure 3.19. $S_{wi}$=0.60 is the case when the domain is almost water with residual oil saturation. The acid volume required in this case is almost the same as the single-phase case. It means residual oil saturation has little effect on acidizing efficiency. The only

effect of residual oil is to decrease the relative permeability of water. In the process of acid injection, oil does not flow, as shown on relative permeability curves.

The cases with $S_{wi}$=0.40 and $S_{wi}$=0.20 need less acid volume to reach breakthrough. Taking Da=10.0 as an example, pore volume of acid is decreased from 11.86 to 9.98 for the case with $S_{wi}$=0.20, and to 10.01 for the case with $S_{wi}$=0.40, compared with single-phase case. These results further prove that the mobility ratio effect on two-phase flow can improve acidizing efficiency.

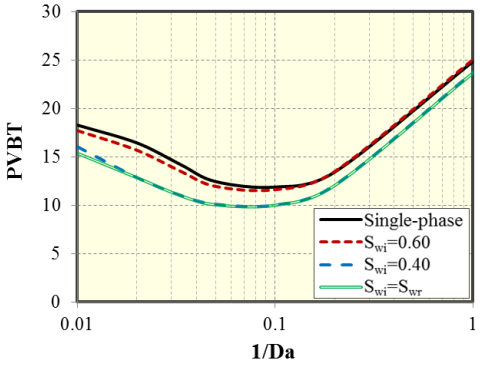


Figure 3.19: Effect of initial water saturation on acid breakthrough curves for oil-wet cases.

## 3.5 CONCLUSIONS

The main purpose of Chapter 2 and Chapter 3 is to extend single-phase two-scale continuum model to two-phase in radidal coordinates. In addition, a new criterion to determine acid breakthrough has been proposed for water-oil two-phase flow based on overall mobility variation in the domain. Based on pressure response analysis, pressure difference between bottomhole and outer boundary is affected by overall mobility; it changes with the variation of phase saturation in the domain. Based on the sensitivity studies, the following conclusions are presented:

- If rocks are preferentially oil-wet, higher efficiency can be obtained compared with water-wet rocks. It is due to the difference in relative permeability curves. In other words, adverse mobility ratio improves acidizing efficiency, and the larger water-oil mobility ratio is, the higher efficiency can be achieved.
- Higher oil viscosity leads to earlier acid breakthrough. The critical factor is also the effect of mobility ratio on water-oil displacement.
- A higher saturation of oil before acidizing treatment reduces acid volume consumption compared with the case with residual oil saturation.

This can give a hint for field acidizing treatment that maintaining a high saturation of oil can enhance acidizing efficiency at near or below optimal injection rate.

# CHAPTER 4: GEOCHEMICAL MODELING OF WORMHOLE PROPAGATION IN UTCOMP-IPHREEQC[3]

Carbonate rocks may contain different compositions due to precipitation and diagenesis, including calcite, dolomite, and other minerals. When acid is injected into the formation, reactions between acid and multiple minerals of carbonate rocks occur simultaneously. In this chapter, all aspects of a two-scale continuum model implemented in UTCOMP (a three-dimensional compositional reservoir simulator) coupled with IPhreeqc (generalized code of PHREEQC as a module) are discussed. PHREEQC is an open-source program which performs a wide variety of geochemical calculations. For the UTCOMP-IPhreeqc coupled model, the two-scale continuum model describes mechanisms of convection and dispersion, while IPhreeqc is used for the calculation of reactions among aqueous phase and minerals. We have validated the simulation model through comparison with the analytical solution. We also compared the UTCOMP-IPhreeqc coupled model with a simple-reaction model in which reaction is assumed as a first-order reaction between acid and calcite, by modifying the IPhreeqc database to obtain consistent results. This work contributes to simulating acidizing process with complex geochemical reactions considering chemistry of the aqueous solution interacting with minerals.

## 4.1 INTRODUCTION

Mineralogy heterogeneity has a significant impact on dissolution structure owing to different reaction kinetic parameters of calcite ($CaCO_3$) and dolomite ($CaMg(CO_3)_2$),

[3] The content of this chapter was published as: Wei, W., Varavei, A., Sanaei, A., and Sepehrnoori, K. 2019. Geochemical modeling of wormhole propagation in carbonate acidizing considering mineralogy heterogeneity. SPE Journal 24(05): 2163-2181. https://doi.org/10.2118/195593-PA. Kamy Sepehrnoori supervised the research, provided technical support, and revised the manuscript. Abdoljalil Varavei and Alireza Sanaei provided technical support and revised the manuscript.

which constitute two main minerals of carbonate reservoirs (Plummer et al. 1978; Busenberg and Plummer 1982). The carbonates which are originally precipitated may be almost pure calcite or pure dolomite. However, these two minerals are often intermingled. Limestones and dolomites may be interbedded. In addition, during diagenesis, calcium in calcite may be partially replaced by magnesium known as the dolomitization process. Based on the percentage of dolomite, the rock can be classified as calcareous dolomite or dolomitic limestone (Ham and Pray 1962).

The reaction rates of acid with limestone and dolomite differ by orders of magnitude depending on temperature. They can represent two reaction-rate limiting regimes at certain conditions. Limestone dissolution is mass-transfer limited above 0°C (Lund et al. 1973), while dolomite dissolution is reaction-limited below about 50°C (Lund et al. 1975). In previous experiments, limestone and dolomite exhibit different trends of acidizing efficiency as the injection rate increases, since the reaction rate of acid with dolomite is much slower than with limestone. Most of the experiments indicate that the effect of mineralogy heterogeneity is of great importance when modeling acidizing process in carbonate reservoirs with multiple rock types.

Most of simulation work on carbonate acidizing assumed a first-order irreversible reaction between HCl and $CaCO_3$, without including other mineral reactions. However, existence of multiple minerals leads to complex geochemical reactions with aqueous acid solution, and the kinetic parameters between HCl-$CaCO_3$ reaction and HCl-$CaMg(CO_3)_2$ reaction are quite different. Few of the previous simulation works took mineralogy heterogeneity into consideration, but they only modeled transport of hydrogen and assumed a single reaction between acid and each type of mineral. De Oliveira et al. (2012) performed simulation using a commercial CFD (computational fluid dynamics) package. They investigated the effect of porosity heterogeneity, as well as the influence

of different types of minerals by using different reaction rate constants for calcite and dolomite. They found that the presence of a second mineral has an impact on dissolution branching intensity and breakthrough time. Liang et al. (2015) studied mineralogy heterogeneity in detail by using different reaction formulas for different minerals. They found that wormhole pattern, breakthrough direction, wormhole propagation and PVBT are all affected by mineral heterogeneity. To realize complex reactions among the injected acid, multiple types of minerals, and different species in the aqueous phase; a geochemical model with full-speciation transportation is necessary. But very little work has been done towards geochemical modeling of matrix acidizing. Mahrous et al. (2017) realized full-speciation simulation for matrix acidizing using TOUGHREACT, which is a code for reactive modeling of multiphase flow of fluids. They modeled acidizing process considering geochemical reactions. The effects of the aqueous kinetics and the species other than hydrogen ions had been taken into consideration.

Different reaction models have been used previously in literature. For simplicity, many researchers (Kalia and Balakotaiah 2007; Maheshwari et al. 2013, 2016; Wei et al. 2017) assumed linear-kinetic reaction with a constant reaction rate. To more accurately model the reaction, Akanni and Nasi-El-Din (2016) utilized the kinetic equation from Schechter (1992) to model reaction between organic acid and carbonate. They considered dissociation equilibrium of acid in aqueous solution and fractional order of reaction. Akanni et al. (2017) introduced nonlinear kinetics in the reaction equation for considering more complex reactions between acidizing fluids and carbonates. Ali and Nasr-El-Din (2018) applied nonlinear reaction kinetics to their simulation model, and modified reaction rate and diffusion coefficient based on X-ray-fluorescence (XRF) results and effluent chemical analysis. With either linear or nonlinear kinetic reaction, only heterogeneous reaction between acid and rock is considered; all the homogeneous

reactions in the aqueous solution and transport of species other than hydrogen have been neglected. Mahrous et al. (2017) used reactive transport code "TOUGHREACT V3-OMP" to model one heterogeneous reaction and nine homogeneous reactions for an ideal HCl/limestone system. They considered transport of all the aqueous species. However, the model is limited to modeling reaction between HCl and pure calcite; if other reactions need consideration, more relationships between primary and secondary species need to be established, and more coding work need to be done. This method is more difficult to be generalized for different acid/rock systems compared with the model in this chapter. Table 4.1 summarizes reaction models mostly used in previous literature. UTCOMP-IPhreeqc model in this chapter is easy to be generalized to consider different acid/rock systems. IPhreeqc is able to model heterogeneous and homogeneous reactions for different acid/rock systems as long as the reaction is in the IPhreeqc database. Even if some reactions are not in the database, we can manually add the reaction model in the database without modifying the code.

| | |
|---|---|
| Linear-kinetics Reaction Single-species Transport (Kalia and Balakotaiah 2007; Maheshwari et al. 2013, 2016) | It's a simplified model only applicable to reaction between strong acid and single mineral. It only considers heterogeneous reaction, transport of hydrogen, neglecting homogeneous reactions and transport of other species. |
| Nonliear-kinetics Reaction Single-species Transport (Akanni and Nasi-El-Din 2016; Akanni et al. 2017; Ali and Nasr-El-Din 2018) | It extends application to reaction between weak acid and single mineral. It only considers heterogeneous reaction, transport of hydrogen, neglecting homogeneous reactions and transport of other species. |
| Full-species Transport Model (Mahrous et al. 2017) | It considers heterogeneous reaction, homogenous reaction, and full-species transport. But for every acid/rock system, extra modeling and coding work need to be done. |
| UTCOMP-IPhreeqc Model | It considers heterogeneous reaction, homogeneous reaction, and full-species transport. It is easy to be generalized for different acid/rock systems by modifying IPhreeqc input files or PHREEQC database. |

Table 4.1: Comparison of UTCOMP-IPhreeqc model with reaction models in previous literature.

Most previous two-scale continuum models only considered transport of hydrogen, and simple reaction between acid and each type of mineral. However, acidizing may involve complex geochemical reactions between aqueous acid solution and different types of minerals. In this chapter, a two-scale continuum model in Cartesian coordinates is implemented in UTCOMP coupled with IPhreeqc. PHREEQC is an open-source computer program developed by U.S. Geological Survey (USGS). The software is capable of simulating a variety of geochemical reactions including dissolution and precipitation of minerals interacting with the aqueous phase. IPhreeqc is an interface of

PHREEQC with the same modeling capability which is designed to be used in scripting languages (Charlton and Parkhurst 2011).

## 4.2 METHODOLOGY

### 4.2.1 Model description

In this study, a two-scale continuum model is coupled with IPhreeqc to realize the acidizing process. In the UTCOMP-IPhreeqc coupled model, the two-scale continuum model describes convection and dispersion, while IPhreeqc performs calculation for a variety of geochemical reactions among minerals and species in the aqueous phase. Two-scale continuum model consists of Darcy-scale model and pore-scale correlations. Darcy-scale model incorporates the pressure equation, the mass conservation equation of each element in the aqueous phase, and the pore evolution equation. Pore-scale correlations relate Darcy-scale parameters with the pore structure evolution. IPhreeqc is used for calculating dissolution or precipitation of minerals and the amount change of each geochemical species due to reactions.

### 4.2.2 Darcy-scale model

The pressure equation in UTCOMP is derived based on the assumption that the pore volume should be filled completely by the volume of the total fluids including an aqueous phase and the hydrocarbon phases (Chang 1990). The pore volume is a function of pressure while the volume of the total fluids depends on pressure and the total number of moles of each component:

$$V_t(p, \mathbf{N}) = V_p(p), \tag{4.1}$$

where $V_t$ is the volume of the total fluids; $p$ is the pressure; $\mathbf{N}$ is a vector including the total number of moles of each component $N_i$, the components here include all the hydrocarbon components and the water component; $V_p$ is the pore volume.

With the substitution of mass conservation equation of each component into Eq. 4.1, the pressure equation can be expressed as

$$V_b \frac{\partial \varphi}{\partial t} - \frac{\partial V_t}{\partial p}\frac{\partial p}{\partial t} - V_b \sum_{i=1}^{n_c+1} \overline{V_{ti}} \nabla \cdot \sum_{j=1}^{n_p} \mathbf{K} \lambda_{rj} \xi_j x_{ij} \nabla p =$$

$$V_b \sum_{i=1}^{n_c+1} \overline{V_{ti}} \nabla \cdot \sum_{j=1}^{n_p} \mathbf{K} \lambda_{rj} \xi_j x_{ij} \left( \nabla p_{c2j} - \gamma_j \nabla D \right) + V_b \sum_{i=1}^{n_c+1} \overline{V_{ti}} \nabla \cdot \sum_{j=1}^{n_p} \varphi \xi_j S_j \mathbf{D}_{\mathbf{e,ij}} \nabla x_{ij} + \sum_{i=1}^{n_c+1} \overline{V_{ti}} q_i \quad (4.2)$$

where $V_b$ is the bulk volume; $n_c$ is the number of hydrocarbon components; $n_p$ is the number of phases; $\mathbf{K}$ is the tensor of the absolute permeability; $\lambda_{rj}$ is the relative mobility of the phase $j$; $\xi_j$ is the molar density of the phase $j$; $x_{ij}$ is the mole fraction of the component $i$ in the phase $j$, and the unit is the mole of the component $i$ divided by the mole of the phase $j$; $p_{c2j}$ is the capillary pressure between the oil phase and phase $j$; $\gamma_j$ is the specific weight of the phase $j$; $D$ is the depth from the datum plane; $\varphi$ is the porosity; $S_j$ is the saturation of phase $j$; $\mathbf{D}_{\mathbf{e,ij}}$ is the effective dispersion tensor of component $i$ in phase $j$; $q_i$ is the molar flow rate of component $i$.

In Eq. 4.2, the partial derivative of the porosity with respect to time can be expanded into two terms: the first term is due to the compressibility of the formation based on the assumption that the formation is slightly compressible; the second term is due to the dissolution of the rock. In an acidizing process, rock dissolution makes much more contribution to the porosity change compared with the rock compressibility. IPhreeqc is responsible for the calculation of the second term. In IPhreeqc, the change in the amount of each mineral can be calculated through dissolution or precipitation. The porosity change equation is as follows:

$$\frac{\partial \varphi}{\partial t} = \varphi^0 c_f \frac{\partial p}{\partial t} - \frac{1}{V_b}\frac{\partial}{\partial t}\left(\sum_{k=1}^{n_s}\frac{n_k M w_k}{\rho_k}\right), \tag{4.3}$$

where $\varphi^0$ is the porosity at the reference pressure; $c_f$ is the formation compressibility; $n_s$ is the number of minerals; $n_k$ is the mole number of mineral $k$; $Mw_k$ is the molecular weight of mineral $k$; $\rho_k$ is the density of mineral $k$.

In Eq. 4.2, $\overline{V_{ti}}$ is the partial derivative of the total fluid volume with respect to the total moles of component $i$:

$$\overline{V_{ti}} = \left(\frac{\partial V_t}{\partial N_i}\right)_{p, N_{k(k\neq i)}}, i = 1, \cdots, n_c + 1. \tag{4.4}$$

The total number of moles of the component $i$ in the above equation can be expressed as

$$N_i = V_b \varphi \sum_{j=1}^{n_p} \xi_j S_j x_{ij}. \tag{4.5}$$

Different geochemical components exist in the aqueous phase upon injecting HCl into carbonate rocks. If carbonate rocks are composed of pure calcite, the geochemical components include C, Ca, Cl, H, and O. If carbonate rocks are composed of pure dolomite, the geochemical components include C, Ca, Cl, Mg, H, and O. The concentration of each geochemical component in the aqueous phase can be solved explicitly using their respective mass conservation equations. There are two mechanisms included in the equation: convection and dispersion. The consumption/production of each component through geochemical reactions is calculated in IPhreeqc. The mass conservation equation for each geochemical component is as follows:

$$\frac{\partial N_i^{'}}{\partial t} + V_b \sum_{j=1}^{n_p} \nabla \cdot \left(\rho_j x_{ij}^{'} \mathbf{u_j} - \varphi \rho_j S_j \mathbf{D_{e,ij}}^{'} \nabla x_{ij}^{'}\right) - q_i^{'} = 0, \tag{4.6}$$

where $N_i^{'}$ is the number of moles of geochemical component $i$; $\rho_j$ is the mass density of phase $j$; $x_{ij}^{'}$ is the concentration of geochemical component $i$ in phase $j$, and the

unit is the mole of geochemical component $i$ divided by the mass of phase $j$; $\mathbf{u}_j$ is the total flux of phase $j$, $\mathbf{u}_j = (u_j, v_j, w_j)$; $\mathbf{D}_{e,ij}'$ is the effective dispersion tensor of geochemical component $i$ in phase $j$; $q_i'$ is the molar flow rate of geochemical component $i$.

In current model, mass transfer coefficient is not included in Eq. 4.6. To consider mass transfer coefficient in the transport equation, iteration between transport and reaction calculations needs to be performed for each time step. In current model, UTCOMP-IPhreeqc coupled system is solved using a sequential non-iterative approach (SNIA). In the future work, the iteration between transport and reaction calculations needs to be implemented to consider mass transfer from the fluid phase to rock surface in the transport equation.

The number of moles of geochemical component $i$ can be expressed as

$$N_i' = V_b \varphi \sum_{j=1}^{n_p} \rho_j S_j x_{ij}' . \tag{4.7}$$

Despite the assumption that geochemical components only exist in the aqueous phase, the mass conservation equation is expressed in the full format including all the phases. Based on Darcy's law, the total flux of phase $j$ can be expressed as

$$\mathbf{u}_j = -\mathbf{K}\lambda_{rj}\left(\nabla p_j - \gamma_j \nabla D\right), \tag{4.8}$$

where $p_j$ is the pressure of phase $j$.

There are two parts in each element of the dispersion tensor, which are molecular diffusion and mechanical dispersion. So, the value of each element in the dispersion tensor is dependent on molecular diffusion, pore geometry, and phase velocity. The dispersion tensor in Cartesian coordinates can be expressed as

$$\mathbf{D}_{e,ij}' = \begin{bmatrix} D_{exx,ij}' & D_{exy,ij}' & D_{exz,ij}' \\ D_{eyx,ij}' & D_{eyy,ij}' & D_{eyz,ij}' \\ D_{ezx,ij}' & D_{ezy,ij}' & D_{ezz,ij}' \end{bmatrix}. \tag{4.9}$$

Substituting the dispersion tensor into the dispersion term, the following expression can be obtained:

$$\nabla \cdot (\varphi \rho_j S_j \mathbf{D_{eij}}' \nabla x_{ij}') = \xi_{x,ij} + \xi_{y,ij} + \xi_{z,ij}, \tag{4.10}$$

$$\xi_{x,ij} = \frac{\partial}{\partial x}\left[ \varphi \rho_j S_j (D_{exx,ij}' \frac{\partial x_{ij}'}{\partial x} + D_{exy,ij}' \frac{\partial x_{ij}'}{\partial y} + D_{exz,ij}' \frac{\partial x_{ij}'}{\partial z}) \right], \tag{4.11}$$

$$\xi_{y,ij} = \frac{\partial}{\partial y}\left[ \varphi \rho_j S_j (D_{eyx,ij}' \frac{\partial x_{ij}'}{\partial x} + D_{eyy,ij}' \frac{\partial x_{ij}'}{\partial y} + D_{eyz,ij}' \frac{\partial x_{ij}'}{\partial z}) \right], \tag{4.12}$$

$$\xi_{z,ij} = \frac{\partial}{\partial z}\left[ \varphi \rho_j S_j (D_{ezx,ij}' \frac{\partial x_{ij}'}{\partial x} + D_{ezy,ij}' \frac{\partial x_{ij}'}{\partial y} + D_{ezz,ij}' \frac{\partial x_{ij}'}{\partial z}) \right]. \tag{4.13}$$

### 4.2.3 Pore-scale correlations

Acid reacts with minerals in the rock increasing its porosity. At the same time, the pore structure of the matrix changes, leading to increases in permeability and average pore radius. A modified Carman-Kozeny (Carman 1956) correlation is employed to relate the change of other parameters with the change of porosity. Maheshwari and Balakotaiah (2013) proposed an improved structure-property correlation, which takes into consideration both pore-broadening and pore-connectivity effects. Here, the two-parameter correlation is used, as follows:

$$\frac{K}{K_0} = \left( \frac{\varphi}{\varphi_0} \right)^{\gamma} \left( \frac{\varphi (1-\varphi_0)}{\varphi_0 (1-\varphi)} \right)^{2\beta}, \tag{4.14}$$

$$\frac{r_p}{r_{p0}} = \left( \frac{\varphi (1-\varphi_0)}{\varphi_0 (1-\varphi)} \right)^{\beta}, \tag{4.15}$$

where $K$ is the element in the tensor of absolute permeability; $\varphi_0$ is the initial average porosity, also used as the reference porosity; $r_p$ is the pore radius; $K_0$ is the reference permeability; $r_{p0}$ is the reference pore radius; $\gamma$ is the pore-connectivity parameter; $\beta$ is the pore-broadening parameter.

Correlations for calculation of the effective dispersion coefficients are adopted from Kalia and Balakotaiah (2007). The effective dispersion tensor is considered by two components, the effective longitudinal dispersion coefficient $D_{eL}^{'}$, and the effective transverse dispersion coefficient $D_{eT}^{'}$. The equations can be expressed as

$$D_{L,ij}^{'} = \frac{D_{eL,ij}^{'}}{D_{m,ij}^{'}} = \alpha_{os} + \frac{2\lambda_L \left|\mathbf{u}_j\right| r_p}{\varphi S_j D_{m,ij}^{'}}, \tag{4.16}$$

$$D_{T,ij}^{'} = \frac{D_{eT,ij}^{'}}{D_{m,ij}^{'}} = \alpha_{os} + \frac{2\lambda_T \left|\mathbf{u}_j\right| r_p}{\varphi S_j D_{m,ij}^{'}}, \tag{4.17}$$

where $D_{m,ij}^{'}$ is the molecular diffusivity of geochemical component $i$ in phase $j$; $\alpha_{os}$, $\lambda_L$ and $\lambda_T$ are numerical constants; $\left|\mathbf{u}_j\right|$ is the magnitude of the phase velocity.

### 4.2.4 IPhreeqc

In the integrated model of UTCOMP-IPhreeqc, transport and reaction are calculated separately. IPhreeqc calculates all the reactions in the fluid/mineral system. At each time-step, once concentrations of different geochemical components are calculated in UTCOMP, the IPhreeqc input is accumulated in the computer memory. IPhreeqc will calculate new concentrations and moles of solid phases considering all involved reactions, and then transfer the results to UTCOMP (Korrani, 2014). The flowchart of the calculation in acidizing through the integrated model of UTCOMP-IPhreeqc is shown in Figure 4.1. The acidizing breakthrough is defined as when the pressure drop between inlet and outlet reaches 1/100 of the initial value.

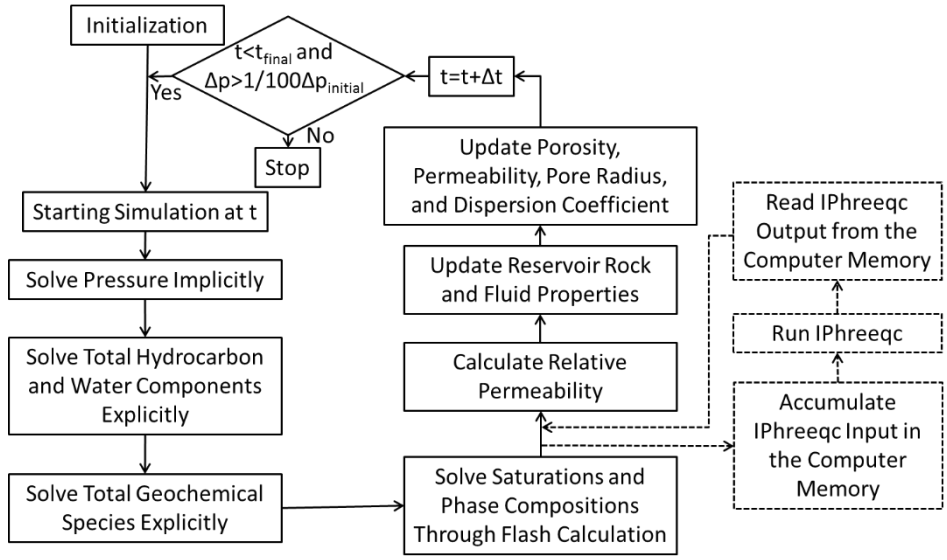


Figure 4.1: Flowchart of the computational algorithm in acidizing through the UTCOMP-IPhreeqc coupled model.

When injecting HCl into carbonate rocks, there are homogeneous and heterogeneous reactions occurring simultaneously in the fluid/mineral system. The reaction between the hydrogen ion and each mineral is the heterogeneous reaction which takes place on the surface of the rock. The reactions among different geochemical species in the aqueous phase are homogeneous reactions. If the rock is composed of pure calcite, the involved geochemical species include $H^+$, $OH^-$, $H_2O$, $CH_4$, $CO_2$, $HCO_3^-$, $CaHCO_3^+$, $CaCO_3$, $CO_3^{2-}$, $Ca^{2+}$, $CaOH^+$, $Cl^-$, $H_2$, and $O_2$. If the rock is composed of pure dolomite, the involved geochemical species include $H^+$, $OH^-$, $H_2O$, $CH_4$, $CO_2$, $HCO_3^-$, $CaHCO_3^+$, $MgHCO_3^+$, $CaCO_3$, $MgCO_3$, $CO_3^{2-}$, $Ca^{2+}$, $CaOH^+$, $Cl^-$, $H_2$, $Mg^{2+}$, $MgOH^+$, and $O_2$. All the reactions occurring in the HCl-$CaCO_3$ system and in the HCl-$MgCa(CO_3)_2$ system are listed in Table 4.2. All these geochemical species and reactions are defined in the IPhreeqc database.

| HCl-$CaCO_3$ System | HCl-$MgCa(CO_3)_2$ System |
|---|---|
| $CaCO_3 + H^+ \leftrightarrow Ca^{2+} + HCO_3^-$ | $CaMg(CO_3)_2 + 2H^+ \leftrightarrow Ca^{2+} + Mg^{2+} + 2HCO_3^-$ |
| $2H_2O \leftrightarrow O_2 + 4H^+ + 4e^-$ | $2H_2O \leftrightarrow O_2 + 4H^+ + 4e^-$ |
| $H^+ + HCO_3^- + H_2O \leftrightarrow CH_4 + 2O_2$ | $H^+ + HCO_3^- + H_2O \leftrightarrow CH_4 + 2O_2$ |
| $H_2O \leftrightarrow H_2 + 0.5O_2$ | $H_2O \leftrightarrow H_2 + 0.5O_2$ |
| $HCO_3^- + H^+ \leftrightarrow CO_2 + H_2O$ | $HCO_3^- + H^+ \leftrightarrow CO_2 + H_2O$ |
| $HCO_3^- \leftrightarrow CO_3^{2-} + H^+$ | $HCO_3^- \leftrightarrow CO_3^{2-} + H^+$ |
| $HCO_3^- + Ca^{2+} \leftrightarrow CaCO_3 + H^+$ | $HCO_3^- + Ca^{2+} \leftrightarrow CaCO_3 + H^+$ |
| $HCO_3^- + Ca^{2+} \leftrightarrow CaHCO_3^+$ | $HCO_3^- + Ca^{2+} \leftrightarrow CaHCO_3^+$ |
| $H_2O + Ca^{2+} \leftrightarrow CaOH^+ + H^+$ | $H_2O + Ca^{2+} \leftrightarrow CaOH^+ + H^+$ |
| $H^+ + Cl^- \leftrightarrow HCl$ | $H^+ + Cl^- \leftrightarrow HCl$ |
| $H_2O \leftrightarrow OH^- + H^+$ | $Mg^{2+} + HCO_3^- \leftrightarrow MgCO_3 + H^+$ |
| | $Mg^{2+} + HCO_3^- \leftrightarrow MgHCO_3^+$ |
| | $H_2O + Mg^{2+} \leftrightarrow MgOH^+ + H^+$ |
| | $H_2O \leftrightarrow OH^- + H^+$ |

Table 4.2: Geochemical reactions in the HCl-$CaCO_3$ system and in the HCl-$MgCa(CO_3)_2$ system.

The rate of calcite dissolution is estimated based on a rate expression from Plummer et al. (1978). The forward rate is given by the following equation:

$$R_f = k_1\left[H^+\right] + k_2\left[H_2CO_3^*\right] + k_3\left[H_2O\right], \tag{4.18}$$

where $R_f$ is the forward rate of the calcite-dissolution reaction; $k_1$, $k_2$, and $k_3$ are reaction-rate constants which are functions of temperature; $\left[H^+\right]$, $\left[H_2CO_3^*\right]$, and $\left[H_2O\right]$ are activities of $H^+$, $H_2CO_3^*$, and $H_2O$, respectively, $H_2CO_3^*$ includes $CO_{2(aq)}$ and $H_2CO_3$.

The dissolution rate of dolomite is estimated by means of a rate expression taken from Busenberg and Plummer (1982). The forward rate of the reaction is given by the following equation:

$$R_f^{'} = k_1^{'}\left[H^+\right]^n + k_2^{'}\left[H_2CO_3^*\right]^n + k_3^{'}\left[H_2O\right]^n, \quad (4.19)$$

where $R_f^{'}$ is the forward rate of the dolomite-dissolution reaction; $k_1^{'}$, $k_2^{'}$, and $k_3^{'}$ are reaction-rate constants which are functions of temperature; $n$ is the reaction order, $n = 0.5$ at temperatures below $45^{\circ}C$.

The temperature dependence of reaction-rate constants can be described by the following empirical expression:

$$\log k = a / T + b, \quad (4.20)$$

where $T$ is the temperature in Kelvin; $a$ and $b$ are constants which vary with different reaction-rate constants.

### 4.2.5 Boundary and initial conditions

Darcy-scale model, pore-scale correlations and IPhreeqc need to be coupled to obtain fields of pressure, phase saturation, concentration of each geochemical component and porosity at different times. In addition, initial conditions and boundary conditions are necessary to provide constraints to the above set of Darcy-scale differential equations.

Initial conditions include distributions of pressure, saturation, moles of components, moles of geochemical components and porosity. The heterogeneity of carbonate rocks can be characterized by using different forms of porosity distribution, which can represent a family of random numbers within a certain range. This is essential to initiate wormholes in the matrix. Initial conditions can be expressed as

$$p = p_i, S_j = S_{ji}, N_i = N_{ii}, N_i^{'} = N_{ii}^{'}, \varphi = \varphi_i, at\ t = 0, \quad (4.21)$$

where $p_i$ is the distribution of initial pressure; $S_{ji}$ is the distribution of initial phase saturation; $N_{ii}$ is the initial mole distribution of component $i$; $N_{ii}^{'}$ is the initial mole distribution of geochemical component $i$; $\varphi_i$ is the distribution of initial porosity.

In Cartesian coordinates, there are six boundaries in the model. Water is injected with a constant rate from one surface (at $x = 0$) and a constant HCl concentration in the aqueous phase is imposed. On the other end ($x = x_l$), pressure is fixed as a constant value and Neumann boundary condition is used for concentration of each element in the aqueous phase. Neumann boundary conditions with the derivatives equaling zero are applied on the other four boundaries representing no-flow boundaries.

$$u_1 = u_0, u_{j(j\neq 1)} = 0, x_{ij}^{'} = x_{ij0}^{'}, at\ x = 0, \tag{4.22}$$

$$p = p_e, \frac{\partial x_{ij}}{\partial x} = 0, \frac{\partial x_{ij}^{'}}{\partial x} = 0, at\ x = x_l, \tag{4.23}$$

$$v_j = 0, \frac{\partial x_{ij}}{\partial y} = 0, \frac{\partial x_{ij}^{'}}{\partial y} = 0, at\ y = 0, \tag{4.24}$$

$$v_j = 0, \frac{\partial x_{ij}}{\partial y} = 0, \frac{\partial x_{ij}^{'}}{\partial y} = 0, at\ y = y_l, \tag{4.25}$$

$$w_j = 0, \frac{\partial x_{ij}}{\partial z} = 0, \frac{\partial x_{ij}^{'}}{\partial z} = 0, at\ z = 0, \tag{4.26}$$

$$w_j = 0, \frac{\partial x_{ij}}{\partial z} = 0, \frac{\partial x_{ij}^{'}}{\partial z} = 0, at\ z = z_l, \tag{4.27}$$

where $u_1$ is the velocity of the aqueous phase in $x$ direction; $u_0$ is the water-injection velocity at the inlet surface; $u_j$ is the phase velocity in $x$ direction; $v_j$ is the phase velocity in $y$ direction; $w_j$ is the phase velocity in $z$ direction; $x_{ij0}^{'}$ is the concentration of geochemical component $i$ in phase $j$ at inlet; $p_e$ is the constant pressure at the outlet surface; $x_l$ is the dimension of the domain in $x$ direction in Cartesian coordinates; $y_l$ is the dimension of the domain in $y$ direction in Cartesian coordinates; $z_l$ is the dimension of the domain in $z$ direction in Cartesian coordinates.

## 4.3 VALIDATION

To validate the simulation model, we compared with an analytical solution. Also, we compared the UTCOMP-IPhreeqc coupled model with a simple-reaction model by

modifying the IPhreeqc database to obtain consistent results. There are several limitations hindering comparison with experimental results quantitatively. It was mentioned in many researchers' work (Kalia and Balakotaiah 2007; Maheshwari et al. 2013; Maheshwari et al. 2016) that further improvements on the simulation model are needed to quantitatively match with experiments. The first limitation is that initial pore structure of the core sample is unknown. The heterogeneity of the core sample is far more complex than the assumption of probability models (either uniform distribution or normal distribution). There even may be vugs or natural fractures which have not been considered in the simulation model. This leads to difficulty of quantitatively matching PVBT results corresponding to different injection rates. Different core samples are treated with different injection rates. Even though they come from the same source rocks of the same formation, they may have different heterogeneities. Even if the measured permeability is the same, they may have different pore structures that can affect dissolution structures significantly. The second limitation lies in the correlation relating Darcy-scale parameters to pore structure evolution. Different correlations lead to different PVBT results and different dissolution structures (Maheshwari et al. 2013). Besides, as dissolution changes the pore structure, parameters in pore-scale correlations are also expected to change. Based on the limitations, to quantitatively match with experiments, more detailed properties of the core sample need to be known, and more accurate structure-property relations or rigorous pore-scale models need to be established. Ali and Nasr-El-Din (2018) obtained initial distribution through CT scans, and modified simulation parameters based on experimental data to obtain reliable match of wormhole propagation and PVBT results. However, without appropriate experimental techniques and detailed measurement data, we have not been able to quantitatively match experimental results.

### 4.3.1 Comparison with analytical solution

Maheshwari et al. (2013) derived an analytical solution to the 1-D version of the Darcy-scale model with the first-order reaction assumption. To validate the simulation model, predictions of the simulation model coupled with the simple-reaction equation are compared with the results calculated from the analytical solution. To accommodate the assumptions made in derivation of the analytical solution, mass transfer coefficient and dispersion coefficients are kept constant in the simulation, and there is no heterogeneity in porosity in the matrix at initial time. Parameters used in the validation case are listed in Table 4.3.

| Parameter | Value | Unit | Parameter | Value | Unit |
|---|---|---|---|---|---|
| $x_l$ | 1.38 | in | $r_{p0}$ | 1.0 | μm |
| $y_l$ | 0.55 | in | $a_{v0}$ | 50.0 | $cm^{-1}$ |
| $z_l$ | 0.55 | in | $Sh_\infty$ | 3.66 | - |
| $\varphi_0$ | 0.20 | - | $D_m$ | $4\times10^{-10}$ | $m^2/s$ |
| $K_0$ | 10.0 | mD | $\alpha_{os}$ | 0.5 | - |
| $p_i$ | 14.7 | psi | $\lambda_L$ | 0.0 | - |
| $\mu_w$ | 1.0 | cp | $\lambda_T$ | 0.0 | - |
| $C_{a0}$ | 2.71 | mol/L | $\alpha$ | 50.0 | g/mol |
| $k_s$ | $1.4\times10^{-6}$ | m/s | - | - | - |

Table 4.3: Parameter values used in the validation case.

The comparisons of simulation model predictions and analytical results are shown in Figure 4.2. The porosity and acid concentration match well. In Figure 4.2, $x'$ is the dimensionless distance from the origin in $x$ direction, which is defined as $x/x_l$; $c_a$ is the acid mass concentration defined as the mass of acid divided by the mass of the aqueous phase. The relationship between $c_a$ and $C_a$ is as follows:

$$C_a = \frac{c_a \rho_w}{MW_a}, \tag{4.28}$$

where $C_a$ is the acid concentration defined as the number of moles divided by the volume of the aqueous phase; $\rho_w$ is the density of the aqueous phase; $MW_a$ is the molecular weight of the acid.

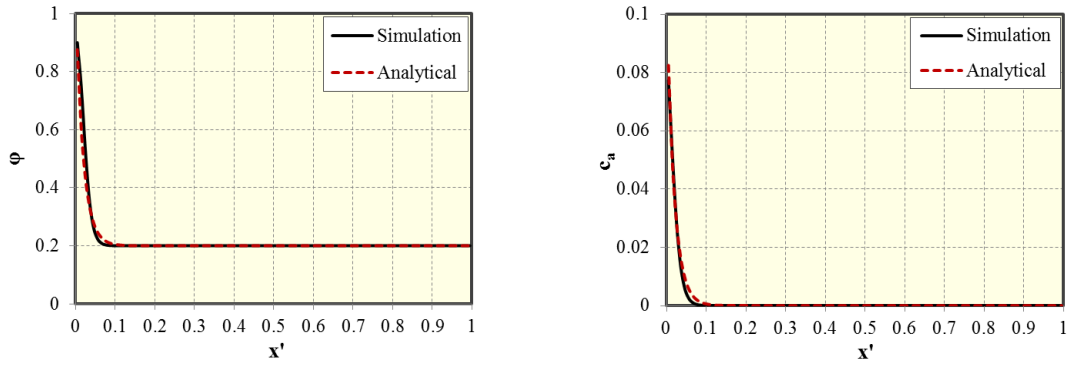


(a) Porosity (b) Acid concentration

Figure 4.2: Comparison of parameters between the simulation model and the analytical solution.

### 4.3.2 Comparison between the simple-reaction model and the IPhreeqc model

As mentioned above in Eqs. 4.18 and 4.19, the reaction rate between the pure mineral and the acid is dependent on the activity of $H^+$, $H_2CO_3^*$, $H_2O$, the reaction rate constant, and the reaction order. To validate the UTCOMP-IPhreeqc coupled model, the IPhreeqc database is modified using the first-order reaction equation which is the same as in the simple-reaction model. Another difference from the simple-reaction model is in the calculation of the interfacial area. In IPhreeqc database, the interfacial area is calculated based on the following equation:

$$\frac{a_v}{a_{v0}} = \left( \frac{M}{M_0} \right)^{\eta}, \tag{4.29}$$

where $a_v$ is the matrix interfacial area, which is defined as the fluid/rock interfacial area per unit of the matrix volume; $a_{v0}$ is the reference interfacial area; $M$ is current number of moles of the mineral; $M_0$ is the initial number of moles of the mineral; $\eta$ is the exponent.

To be consistent with the above equation, the calculation of the interfacial area in the simple-reaction model is modified using the following equivalent equation:

$$\frac{a_v}{a_{v0}} = \left( \frac{1-\varphi}{1-\varphi_0} \right)^{\eta} . \tag{4.30}$$

Parameters used in the comparison are listed in Table 4.4. Compared with the following simulation study cases, we used a smaller acid concentration of 1 mol/L in the comparison. Also, here we modified the IPhreeqc database to use a very small reaction rate of $5.89 \times 10^{-11}$ m/s, to ensure that porosity distribution and inlet pressure match well for a large pore volume of acid injection.

| Parameter | Value | Unit | Parameter | Value | Unit |
|---|---|---|---|---|---|
| $x_l$ | 1.97 | in | $\gamma$ | 1.0 | - |
| $y_l$ | 0.79 | in | $\beta$ | 1.0 | - |
| $z_l$ | 0.06 | in | $r_{p0}$ | 1.0 | μm |
| $\varphi_0$ | 0.20 | - | $a_{v0}$ | 50.0 | $cm^{-1}$ |
| $\Delta\varphi_0$ | ±0.15 | - | $\alpha$ | 50.0 | g/mol |
| $K_0$ | 1.0 | mD | $D_m$ | $3.6 \times 10^{-9}$ | $m^2/s$ |
| $p_i$ | 14.7 | psi | $\alpha_{os}$ | 0.5 | - |
| $\mu_w$ | 1.0 | cp | $\lambda_L$ | 0.5 | - |
| $C_{a0}$ | 1.0 | mol/L | $\lambda_T$ | 0.1 | - |
| $\eta$ | 1.0 | - | $T$ | 100 | °F |

Table 4.4: Parameters used in the comparison between the simple-reaction model and the UTCOMP-IPhreeqc model.

For a 1-D homogeneous case, porosity distribution is consistent between the simple-reaction model and the UTCOMP-IPhreeqc model at different times (1st day, 2nd day, 3rd day, 4th day and 5th day), as shown in Figure 4.3. For a 2-D heterogeneous case, the comparison of porosity distribution after 40 pore volumes of acid injection is shown in Figure 4.4. The comparison of the inlet pressure is shown in Figure 4.5. The dissolution structures are similar as shown in Figure 4.4, and the inlet pressure matches well as shown in Figure 4.5.

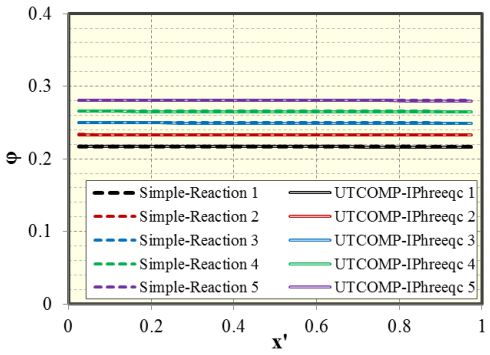


Figure 4.3: Comparison of porosity between the simple-reaction model and the UTCOMP-IPhreeqc model.

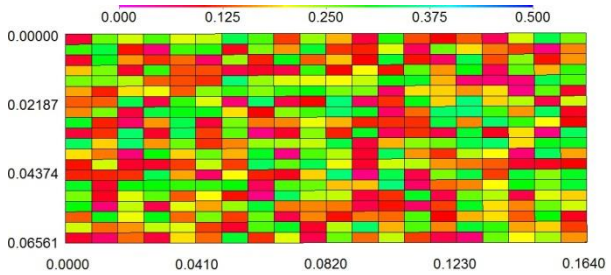


(a) Initial porosity distribution

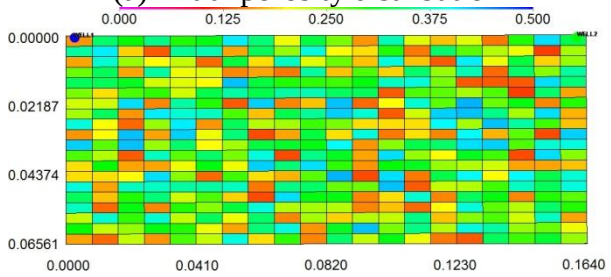


(b) Simple-reaction model

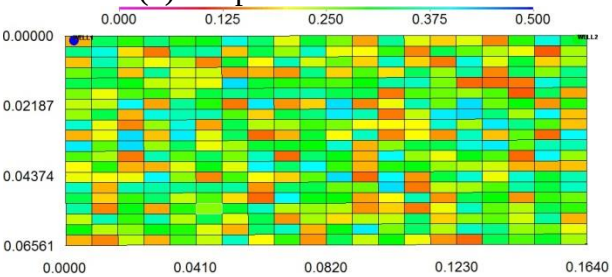


(c) UTCOMP-IPhreeqc model

Figure 4.4: Comparison of porosity distributions at 40 pore volumes between the simple-reaction model and the UTCOMP-IPhreeqc model.

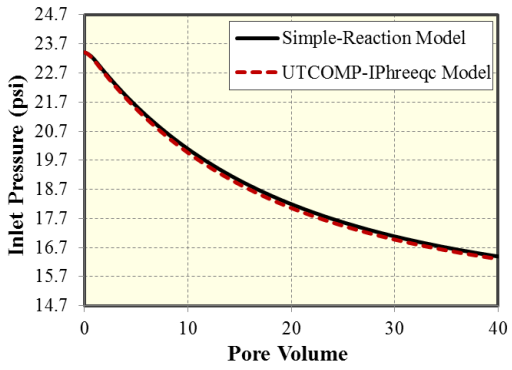


Figure 4.5: Inlet pressure comparison between the simple-reaction model and the UTCOMP-IPhreeqc model.

# CHAPTER 5: EFFECT OF MINERALOGY HETEROGENEITY IN CARBONATE ACIDIZING[4]

On the basis of UTCOMP-IPhreeqc coupled model in Chapter 4, in this chapter, the effects of mineral composition on wormhole propagation and acidizing efficiency are investigated and presented. It is found that mineralogy heterogeneity is a key factor affecting acidizing efficiency and dissolution structure. The parameters used in the simulation are the same as in the comparison case shown in Table 4.4, except that acid concentration at injection is 4.1mol/L. All of them are fixed unless otherwise stated. In these case studies, porosity heterogeneity at initial time is represented as a uniform distribution of porosity with the range of [0.05, 0.35]. The grid information in the simulation is listed in Table 5.1. We selected the mesh size based on the final PVBT values. We increased the grid number by 2 times in each direction (from 40×20 to 80×40), kept the same heterogeneity in the domain, and compared PVBT values corresponding to different injection rates to determine the level of grid refinement.

| Parameter | | Value | Unit |
|---|---|---|---|
| No. of gridblocks | | 3200 (80×40) | - |
| $\Delta x$ | | 0.0246 | in |
| $\Delta y$ | | 0.01975 | in |
| Permeability | $x$ direction | Heterogeneous | - |
| | $y$ direction | Heterogeneous | |
| Porosity | | Heterogeneous | - |

Table 5.1: Grid information in the simulation.

[4] The content of this chapter was published as: Wei, W., Varavei, A., Sanaei, A., and Sepehrnoori, K. 2019. Geochemical modeling of wormhole propagation in carbonate acidizing considering mineralogy heterogeneity. SPE Journal 24(05): 2163-2181. https://doi.org/10.2118/195593-PA. Kamy Sepehrnoori supervised the research, provided technical support, and revised the manuscript. Abdoljalil Varavei and Alireza Sanaei provided technical support and revised the manuscript.

## 5.1 PURE MINERAL

The reaction kinetic parameters are different for calcite and dolomite. Based on Eqs. 4.18 and 4.19, the difference is mainly in the reaction-rate constant and the reaction order. For calcite dissolution, the reaction is first order at temperatures between 5°C and 60°C (Plummer et al. 1978). For dolomite dissolution, the reaction order varies at different temperatures; it equals 0.5 below 45°C, and equals 0.6, 0.7 and 0.85 at 55°C, 65°C, 100°C, respectively (Busenberg and Plummer 1982). The comparisons of reaction-rate constants are shown in Figure 5.1 based on the empirical equation obtained through experiments of calcite dissolution by Plummer et al. (1978) and dolomite dissolution by Busenberg and Plummer (1982). As shown in Figure 5.1, the reaction-rate constant corresponding to $\left[H^+\right]$ for dolomite is smaller than calcite by 2 to 3 orders; the reaction-rate constant corresponding to $\left[H_2CO_3^*\right]$ is smaller than calcite by 1 to 2 orders; the reaction-rate constant corresponding to $[H_2O]$ is smaller than calcite by 1 to 2 orders. It's worth mentioning the reaction rate constant for $\left[H_2CO_3^*\right]$ is smaller by about 3 orders than that for $\left[H^+\right]$, and the reaction rate constant for $[H_2O]$ is smaller by about 6 orders than that for $\left[H^+\right]$. This indicates ignoring terms other than $\left[H^+\right]$ is a good approximation, and supports the assumption in Eq. 2.18 that the reaction between HCl and pure calcite is first-order and the reaction rate is only dependent on acid concentration.

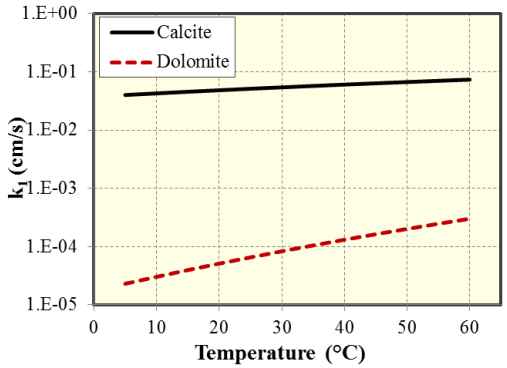


(a) Reaction rate constant with respect to $[H^+]$

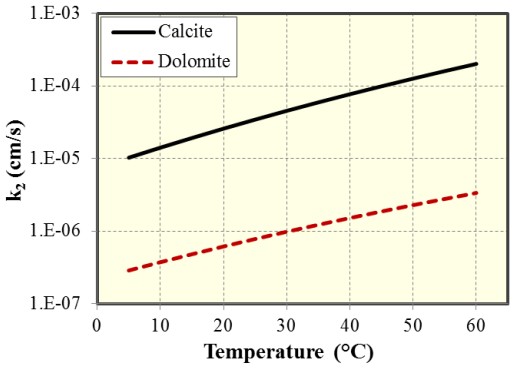


(b) Reaction rate constant with respect to $[H_2CO_3^*]$

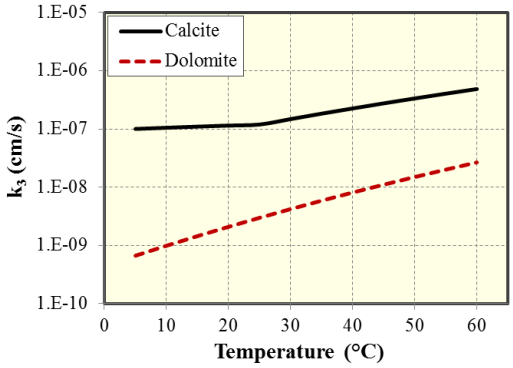


(c) Reaction rate constant with respect to $[H_2O]$

Figure 5.1: Comparison of reaction rate constants between calcite and dolomite.

PVBT results corresponding to different injection rates for pure calcite and pure dolomite are shown in Figure 5.2. For calcite, PVBT varies from 1.81 to 4.37, with the minimum value occurring at the injection rate of $1.0\times10^{-3}$ $cm^3$/min. For dolomite, within the same range of injection rates as calcite, no minimum PVBT can be obtained. As the injection rate increases, the acid consumption increases dramatically. The dissolution structures at the injection rate of $1.0\times10^{-5}$ $cm^3$/min are shown in Figure 5.3. The dissolution structure for dolomite is more ramified than that for calcite. Hence, the acid consumption is larger for dolomite than calcite. As the injection rate increases, the difference in the acid consumption between calcite and dolomite becomes larger and

larger. This can also be explained by the difference in their dissolution patterns. The dissolution structures at the injection rates of $1.0\times10^{-2}$ $cm^3$/min and $1.0\times10^{-1}$ $cm^3$/min are compared in Figure 5.4 and Figure 5.5, respectively. At the injection rate of $1.0\times10^{-2}$ $cm^3$/min, wormhole structure is generated for calcite, while uniform dissolution is created for dolomite. This is similar to the simulation work of Liang et al. (2015) in radial coordinates. Also, McDuff et al. (2010) drew the same conclusion through experiments using Indiana Limestone and Silurian Dolomite. As the injection rate increases to $1.0\times10^{-1}$ $cm^3$/min, dissolution structure is transitional between wormhole pattern and uniform pattern for calcite, while dissolution structure becomes more uniform for dolomite, compared with the injection rate of $1.0\times10^{-2}$ $cm^3$/min.

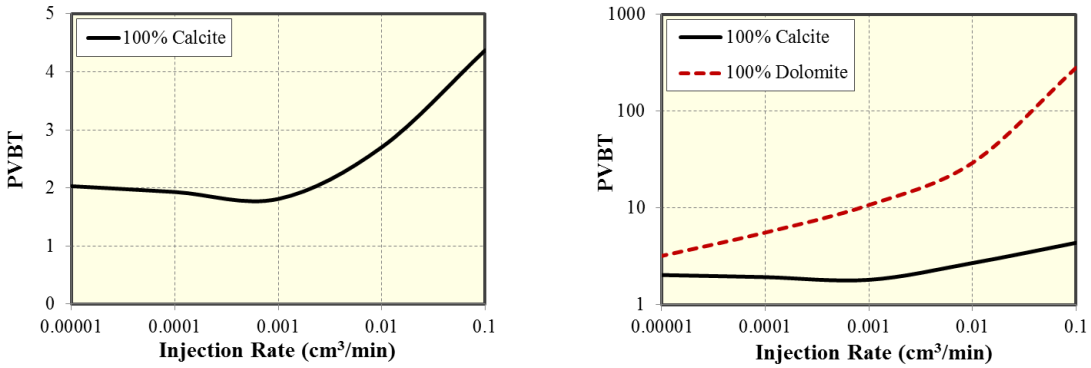


(a) Pure calcite (b) Pure calcite and pure dolomite

Figure 5.2: Effect of mineral type on acid breakthrough curves.

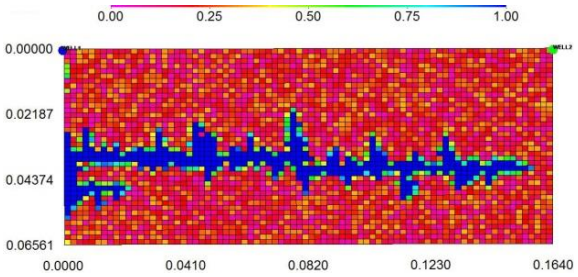


(a) Calcite

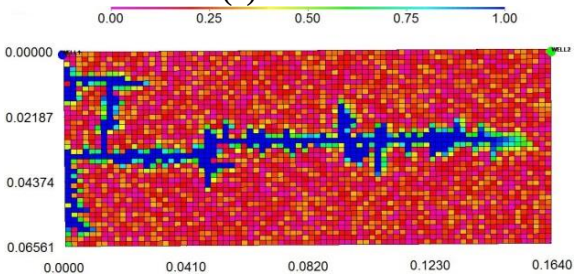


(b) Dolomite

Figure 5.3: Comparison of dissolution structures at breakthrough with $1.0\times10^{-5}$ $cm^3$/min.

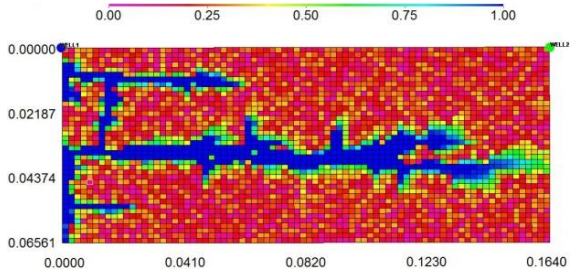


(a) Calcite

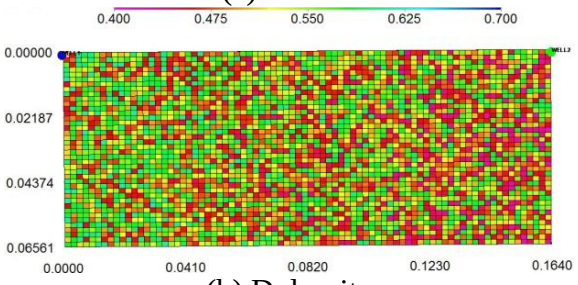


(b) Dolomite

Figure 5.4: Comparison of dissolution structures at breakthrough with $1.0\times10^{-2}$ $cm^3$/min.

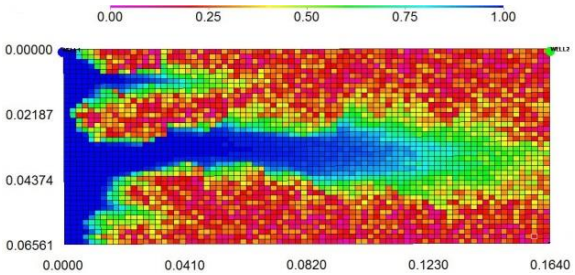


(a) Calcite

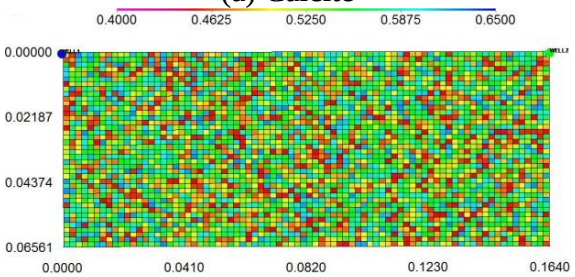


(b) Dolomite

Figure 5.5: Comparison of dissolution structures at breakthrough with $1.0\times10^{-1}$ $cm^3$/min.

## 5.2 MIXTURE OF CALCITE AND DOLOMITE

There are two major types of carbonate rocks: limestone and dolostone. Limestone is mainly composed of calcite, while dolostone is mainly composed of dolomite. Many dolomites are generated by replacement of a precursor limestone through dolomitization. Dolomitization is a process of recrystallization in which magnesium substitutes for calcium. The process can be described as

$$2CaCO_3 + Mg^{2+} = CaMg\left(CO_3\right)_2 + Ca^{2+}. \quad (5.1)$$

Original limestone textures are preserved in such dolomites to various degrees, ranging from virtually not replaced to totally replaced. In PHREEQC, a mixture of minerals can be defined for each grid block by adding fixed amounts of specified reactants using the keyword KINETICS. The keyword KINETICS is used to define kinetic reactions. The PVBT results for a mixture of calcite and dolomite (50% calcite and 50% dolomite) are shown in Figure 5.6. The acid consumption for the mixture is

between pure calcite and pure dolomite. In the range between $1.0\times10^{-5}$ $cm^3$/min and $1.0\times10^{-1}$ $cm^3$/min, there is no minimum value on the acid-breakthrough curve for the mixture. As the injection rate increases, the acid consumption increases, but not as much as dolomite. The comparisons of dissolution structures for pure calcite, pure dolomite, and mixture are shown in Figures 5.7-5.9. At the injection rate of $1.0\times10^{-1}$ $cm^3$/min, for the mixture, acid flows into and reacts with most parts of the matrix; the dissolution structure is between the wormhole structure for pure calcite and the uniform structure for pure dolomite. As a result, the amount of acid consumption is also between pure calcite and pure dolomite, as shown in Figure 5.6(b). At the injection rate of $1.0\times10^{-2}$ $cm^3$/min or $1.0\times10^{-3}$ $cm^3$/min, for the mixture, thicker wormhole is generated compared with pure calcite. It is because in the same grid block, calcite is consumed faster than dolomite due to faster reaction; when the amount of calcite becomes smaller, acid tends to flow into and react with nearby matrix where calcite has a larger proportion. Consequently, the wormhole is thicker and the porosity increases more slowly with the remaining dolomite compared with the case of pure calcite.

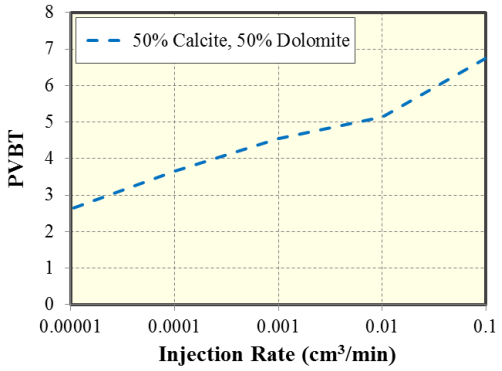


(a) Mixture (50% calcite and 50% dolomite)

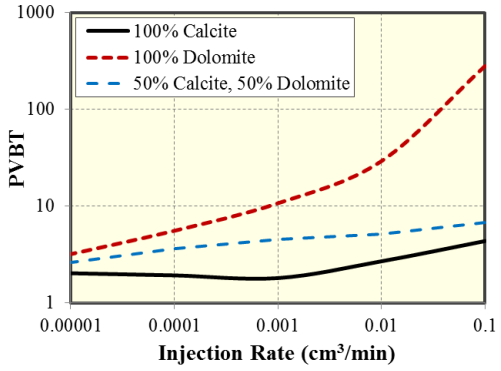


(b) Pure calcite, pure dolomite, mixture

Figure 5.6: Comparison of acid breakthrough curves for pure calcite, pure dolomite and mixture.

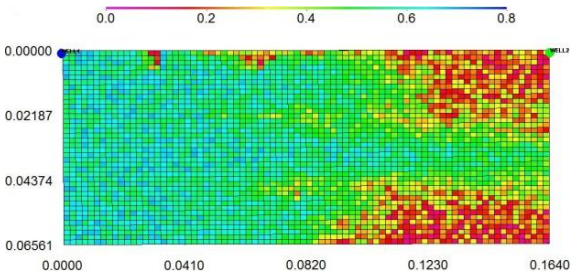


(a) Mixture (50% calcite and 50% dolomite)

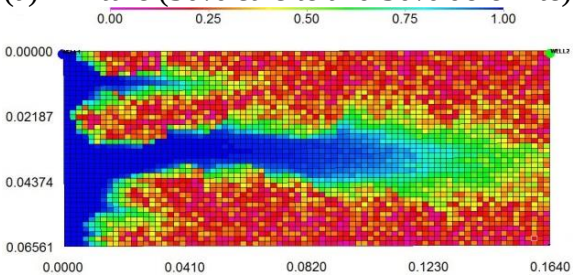


(b) Pure calcite

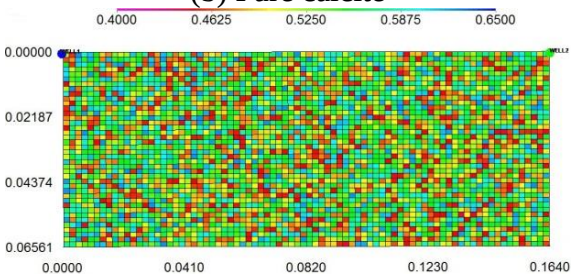


(c) Pure dolomite

Figure 5.7: Comparison of dissolution structures at breakthrough with $1.0\times10^{-1}$ $cm^3$/min.

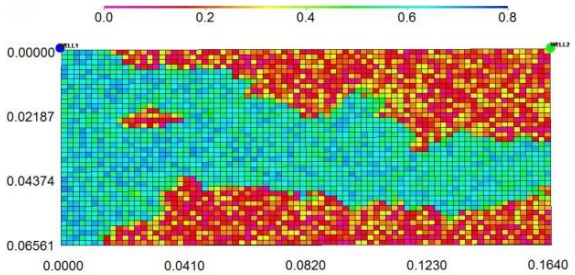


(a) Mixture (50% calcite and 50% dolomite)

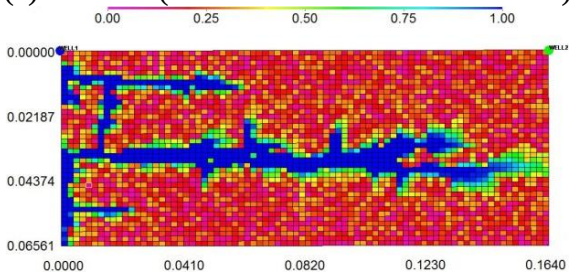


(b) Pure calcite

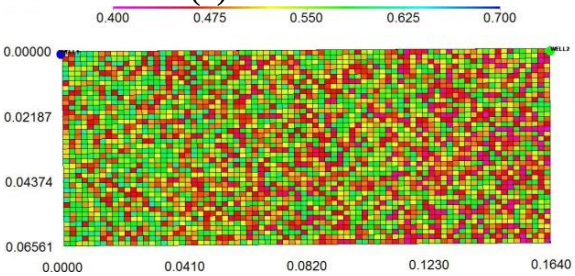


(c) Pure dolomite

Figure 5.8: Comparison of dissolution structures at breakthrough with $1.0\times10^{-2}$ $cm^3$/min.

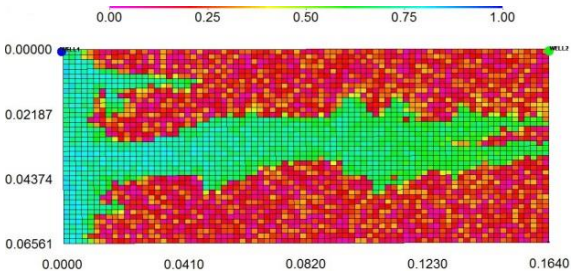


(a) Mixture (50% calcite and 50% dolomite)

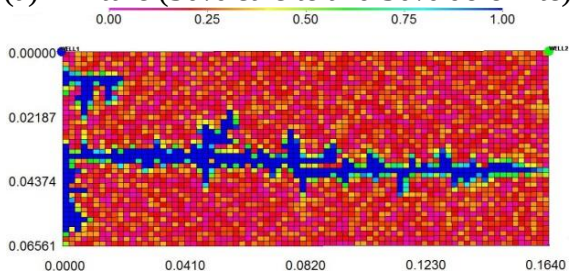


(b) Pure calcite

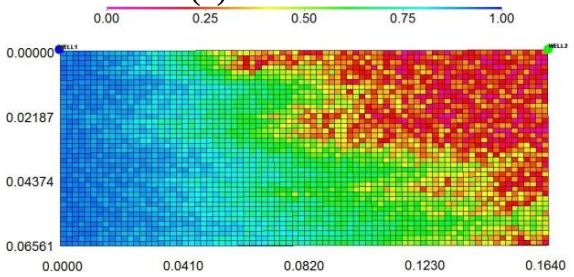


(c) Pure dolomite

Figure 5.9: Comparison of dissolution structures at breakthrough with $1.0\times10^{-3}$ $cm^3$/min.

### 5.3 PARTIALLY DOLOMITIZED CARBONATES

A large portion of dolomite is formed by replacement of calcite under different tectonic and geochemical conditions. Partially dolomitized carbonate rocks host large hydrocarbon reserves in producing areas, such as the Middle East or North America (Corbella et al. 2014). The dolomitization process occurs when original limestone interacts with fluids that trigger the dolomitizing reaction. The occurrence and distribution of burial dolostones have an impact on dissolution structures and acidizing efficiency. We assumed three cases with different proportion of dolomite assuming the dolomitizing fluids have been flooded from the left boundary of the domain. For Case 1,

12.5% of the whole domain consists of pure dolomite which is in the left-hand side; there is a transition zone with 50% of calcite and 50% of dolomite in the middle; the remaining part is composed of pure calcite which is in the right-hand side. For Case 2, 37.5% of the whole domain is made up of pure dolomite. For Case 3, 62.5% of the whole domain is composed of pure dolomite. The initial distribution of porosity is shown in Figure 5.10 with the mineral configurations for Case 1, Case 2, and Case 3. The degree of dolomitization increases from Case 1 to Case 3.

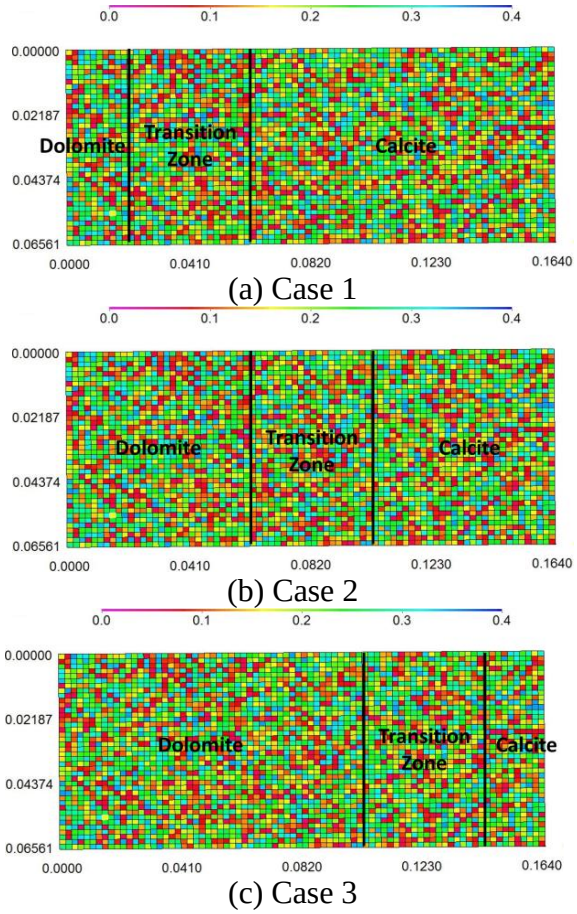


(a) Case 1

(b) Case 2

(c) Case 3

Figure 5.10: Initial porosity distributions with mineral configurations.

Acidizing breakthrough curves for Case 1, Case 2, and Case 3 are shown in Figure 5.11. As the degree of dolomitization increases, acidizing efficiency decreases with the larger volume of acid consumption. The reason lies in the difference of dissolution structures. The dissolution structures for these three cases are shown in Figures 5.12-5.16. The dissolution structures for the pure mineral are also shown for reference. At higher injection rates, such as $1.0\times10^{-1}$ $cm^3/min$ or $1.0\times10^{-2}$ $cm^3/min$, uniform dissolution is generated in pure dolomite, while wormhole dissolution is generated in pure calcite. As a result, when acid is injected from the left-hand side, at the beginning, uniform dissolution structure is generated; when the dissolution front moves to the transition zone in the middle, the dissolution becomes more uniform; finally, when dissolution front moves to pure calcite, wormhole structure is created. With a larger portion of dolomite, larger volume of acid is required since uniform dissolution consumes more acid. At the injection rate of $1.0\times10^{-3}$ $cm^3/min$, the dissolution structure in pure dolomite is between uniform and wormhole and this still requires more acid than pure calcite. At injection rate of $1.0\times10^{-4}$ $cm^3/min$, dissolution structure is consistent in pure calcite and in pure dolomite. However, as the dissolution front moves into pure calcite, the wormhole becomes thinner as shown in Figure 5.15. With the larger proportion of dolomite, thicker wormhole occupies the larger portion of the matrix which requires larger volume of acid. At injection rate of $1.0\times10^{-5}$ $cm^3/min$, wormhole structure in pure dolomite is more ramified than that in pure calcite. As the dissolution front moves into pure calcite, the wormhole becomes less ramified as shown in Figure 5.16. Consequently, within the range of injection rates investigated, as the degree of dolomitization increases, acidizing efficiency decreases.

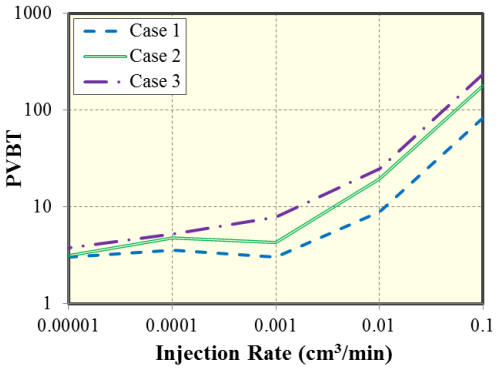


(a) Case 1-3

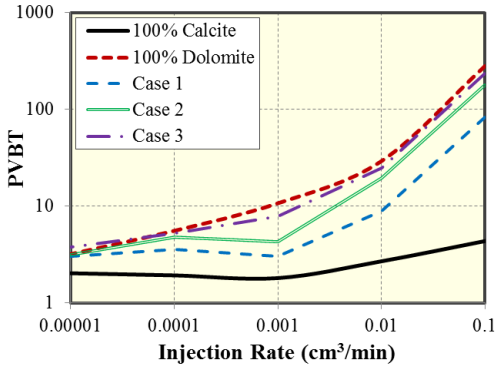


(b) Pure calcite, pure dolomite, Case 1-3

Figure 5.11: Acid breakthrough curves for pure calcite, pure dolomite, and Case 1-3.

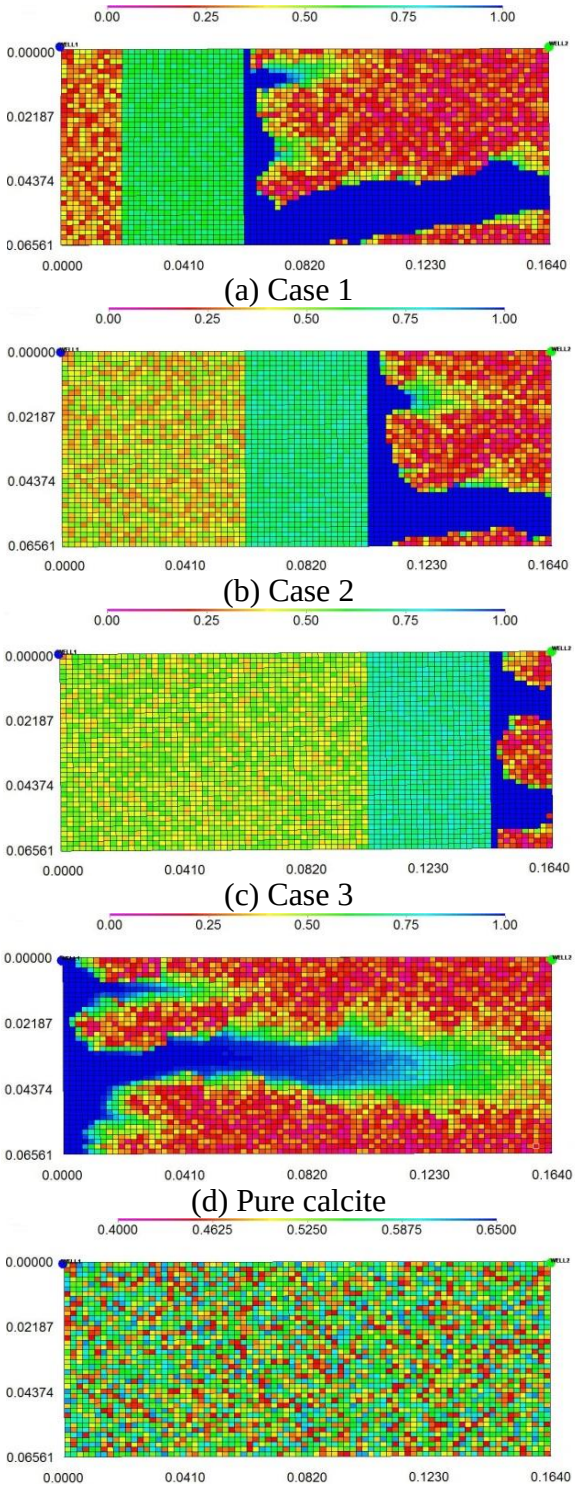


Figure 5.12: Comparison of dissolution structures at breakthrough with $1.0\times10^{-1}$ $cm^3$/min.

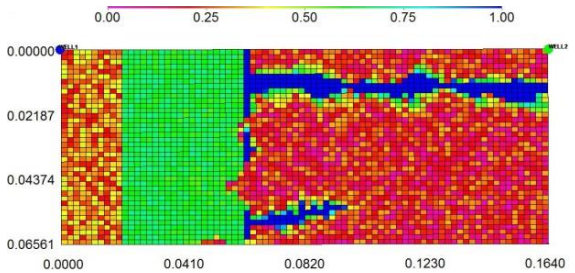


(a) Case 1

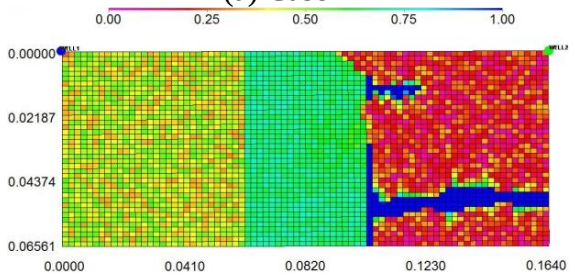


(b) Case 2

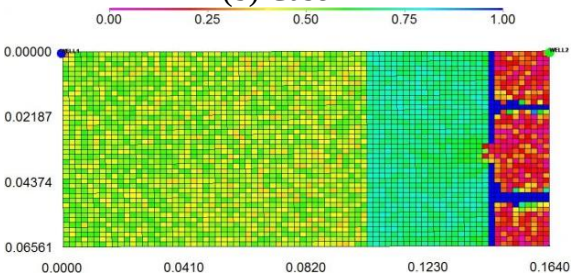


(c) Case 3

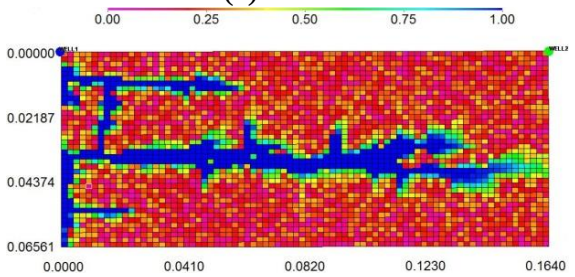


(d) Pure calcite

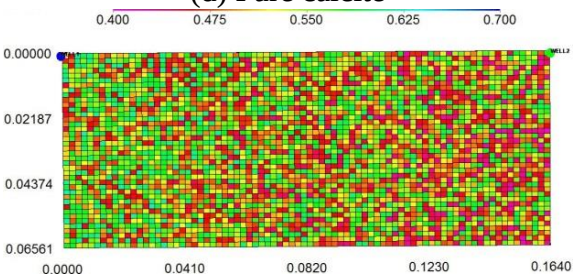


(e) Pure dolomite

Figure 5.13: Comparison of dissolution structures at breakthrough with $1.0\times10^{-2}$ $cm^3$/min.

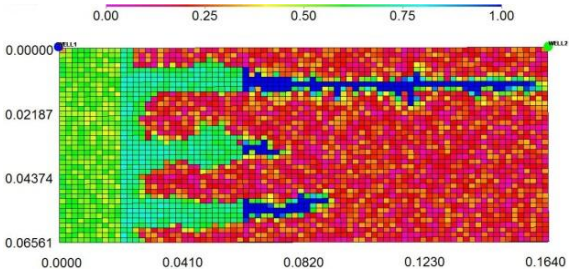


(a) Case 1

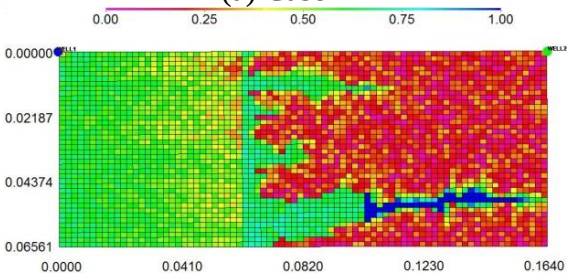


(b) Case 2

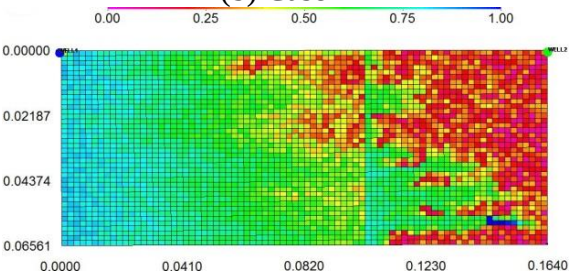


(c) Case 3

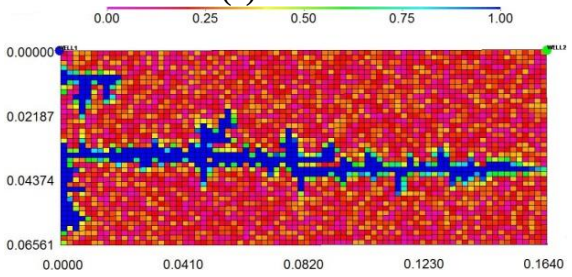


(d) Pure calcite

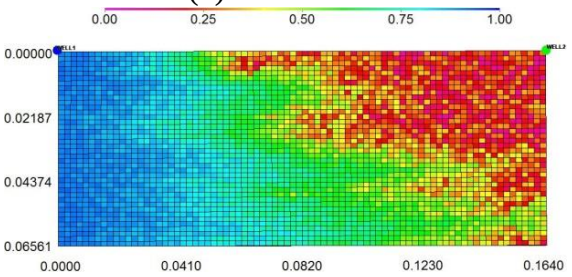


(e) Pure dolomite

Figure 5.14: Comparison of dissolution structures at breakthrough with $1.0\times10^{-3}$ $cm^3$/min.

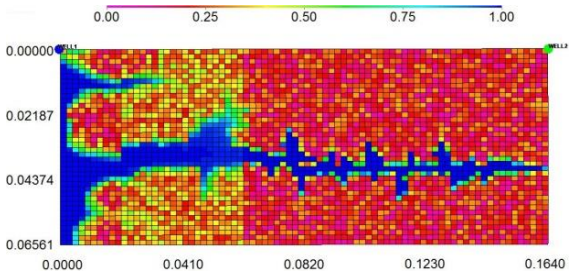


(a) Case 1

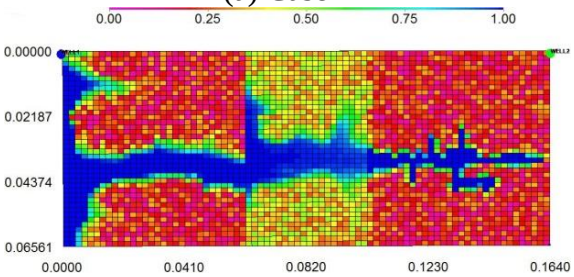


(b) Case 2

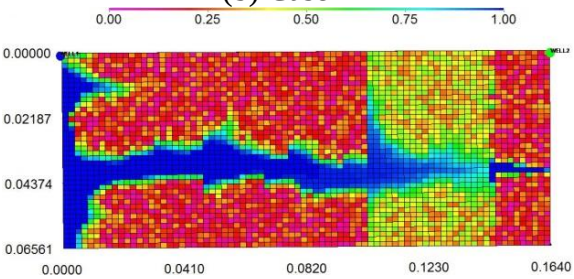


(c) Case 3

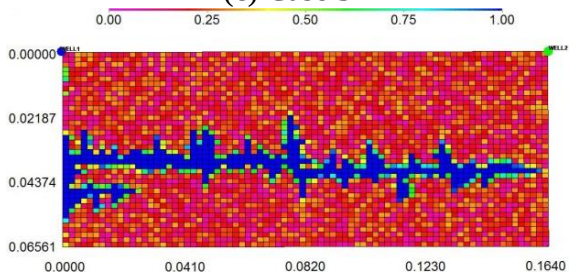


(d) Pure calcite

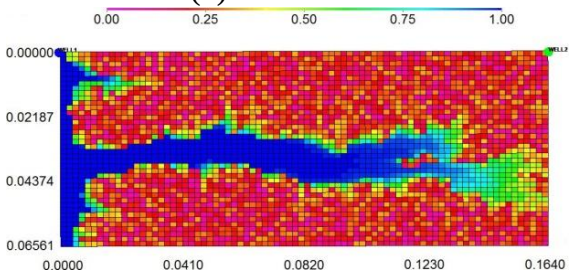


(e) Pure dolomite

Figure 5.15: Comparison of dissolution structures at breakthrough with $1.0\times10^{-4}$ $cm^3$/min.

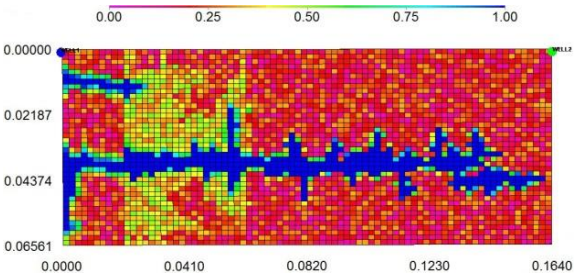


(a) Case 1

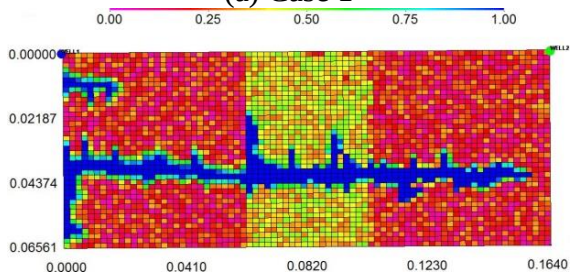


(b) Case 2

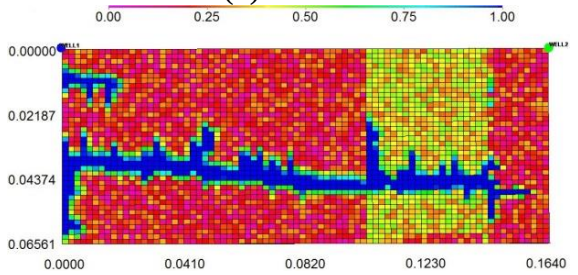


(c) Case 3

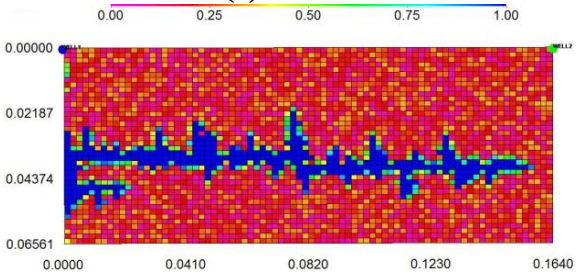


(d) Pure calcite

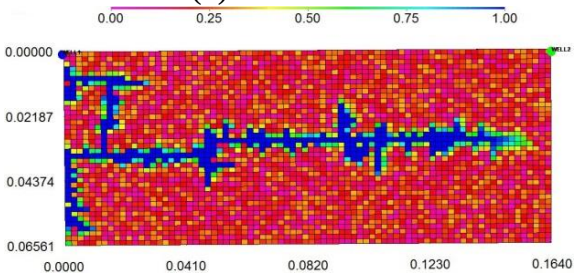


(e) Pure dolomite

Figure 5.16: Comparison of dissolution structures at breakthrough with $1.0\times10^{-5}$ $cm^3$/min.

Compared with the case of pure calcite, all these three cases have lower acidizing efficiency. However, when compared with the case of pure dolomite, the partially dolomitized matrix does not always have the higher acidizing efficiency. At lower injection rate, partially dolomitized matrix may require larger volume of acid compared with the case with pure dolomite, such as Case 2 and Case 3 at the injection rate of $1.0\times10^{-5}$ $cm^3$/min. This is due to the difference of dissolution structures between the transition zone and the pure mineral. In the transition zone, the reactions between acid and minerals not only generate an obvious wormhole, but also create uniform dissolution in the remaining part. However, in the pure mineral, the dissolution mostly occurs in the wormhole with the remaining part almost intact. This means the transition zone requires additional acid compared with the pure mineral.

## 5.4 CONCLUSIONS

The main purpose of chapter 4 and chapter 5 was to couple the two-scale continuum model with IPhreeqc, to realize acidizing process with complex geochemical reactions. The UTCOMP-IPhreeqc coupled model was validated through comparison with the analytical model, as well as with the simple-reaction model. With the aid of the UTCOMP-IPhreeqc coupled model, mineral compositions of carbonate rocks were taken into consideration. Based on the case studies, the following conclusions are presented:

- Pure dolomite requires larger amount of acid than pure calcite. The difference in acidizing efficiency between pure calcite and pure dolomite increases as the injection rate increases, which is due to the change of dissolution structures.
- Acidizing efficiency for the mixture of calcite and dolomite is smaller than pure calcite, but larger than pure dolomite. Compared with pure calcite, thicker

wormhole is generated for the mixture at certain injection rates which correspond to wormhole pattern.

- For partially dolomitized carbonate rocks, as the degree of dolomitization increases, acidizing efficiency decreases. At very low injection rates, larger amount of acid is required for partially dolomitized carbonates than pure dolomite.

# CHAPTER 6: GEOCHEMICAL MODELING OF WORMHOLE PROPAGATION DURING CARBONATE ACIDIZING WITH CONSIDERATION OF FRACTURES

Natural fractures exist in approximately 50% of carbonate reservoirs worldwide (Garland et al. 2018). In this chapter, a two-scale continuum model is implemented in UTCOMP-IPhreeqc with consideration of fractures using EDFM (Embedded Discrete Fracture Model). In the coupled model, the two-scale continuum model describes convection and dispersion while IPhreeqc is responsible for the dissolution calculation both in the matrix and on the fracture surface. We investigated the effects of fractures on acidizing efficiency and wormhole propagation. It is found that for homogeneous matrices where fractures can be present, wormhole in the matrix is generated along the fracture. For a heterogeneous matrix, the initiation of the wormhole is dependent on the permeability distribution in the matrix, but wormhole propagation after the initiation is dependent on the position of the nearest fracture tip and the fracture orientation. As a high-conductivity flow path, fracture retards wormhole propagation in the matrix by attracting most acid. As acid dissolves the minerals on the fracture surface, the fracture conductivity is increased and the fluid leak-off into the matrix is reduced. For a vertical fracture with a smaller height compared with the matrix thickness, wormhole propagation is slowed down for the entire matrix. Through the UTCOMP-EDFM coupled model, it is possible to simulate formations with hydraulic fractures or natural fractures during acidizing, with consideration of geochemical reactions among aqueous phase and different rock compositions through IPhreeqc.

## 6.1 INTRODUCTION

A feature of importance in carbonates is the existence of natural fractures. Fractures widely exist in carbonates because of their brittle nature, compared with ductile siliciclastics (Moore and Wade 2013). Some numerical models took into consideration of fractures during carbonate acidizing. Xiong (1994) developed a simulation model to investigate matrix acidizing in naturally fractured carbonates. He used a network model to represent arbitrarily distributed fractures. The model was used to predict the effective acid penetration distance and the requirement on the acid volume. In the model, the flow in the matrix was eliminated and the parameter distribution in every fracture was not obtained since the natural fracture distribution was simplified in the network model. Dong et al. (2002) modeled the natural fracture network as a main path consisting of a system of intersecting fractures. They considered acid transport in the main path, dissolution on the fracture wall, and leak-off both from the main path and from the intersecting tail of the fractures. The model was used to predict acid penetration in the natural fracture network and etching results on the fracture wall. The fluid flow and dissolution in the matrix were not considered. Liu et al. (2017) used a continuum model with explicit fractures to examine wormhole propagation in matrices with single and multiple fractures. The fluid flow and acid transport were modeled both in the matrix and in the fracture but the reaction on the fracture wall was neglected.

In this chapter, a two-scale continuum model considering reactive transport mechanisms both in the matrix and in the fracture is implemented in UTCOMP (a 3D compositional reservoir simulator) coupled with EDFM (Embedded Discrete Fracture Model). The convection and dispersion are calculated in the UTCOMP-EDFM model, while reactions are calculated through IPhreeqc. IPhreeqc is a set of modules designed specifically to allow easy integration of PHREEQC into other software (Charlton and

Parkhurst 2011). PHREEQC is a geochemical package capable of calculating a wide range of equilibrium reactions among geochemical species. It also has the capability of calculating kinetic reactions of non-equilibrium mineral dissolution and precipitation. IPhreeqc has all the capabilities of simulation and data-storage in PHREEQC. In this chapter, the effects of single fracture and multiple fractures on wormhole propagation and acidizing efficiency are investigated and presented.

## 6.2 METHODOLOGY

### 6.2.1 Model description

In this chapter, a two-scale continuum model is coupled with EDFM to realize acidizing process in carbonates with consideration of fractures. For the matrix acidizing model with no fractures, Darcy-scale model is used to model phase flow and solute transport while pore-scale correlations are used to relate Darcy-scale parameters with the pore structure variation. EDFM is used to describe fluid flow and solute transport related to fractures by considering additional transport relationships among fractures and matrices. UTCOMP-EDFM solves pressure equation and mass conservation equation while IPhreeqc is responsible for reaction calculation. IPhreeqc calculates the amount change of minerals both in the matrix and on the fracture surface. IPhreeqc calculations are performed based on homogeneous reactions among the geochemical species in the aqueous phase and heterogeneous reactions between hydrogen and minerals. The flow chart of the calculation is shown in Figure 6.1. The breakthrough in the model is when the pressure drop between inlet and outlet of the domain reaches 1/100 of its initial value.

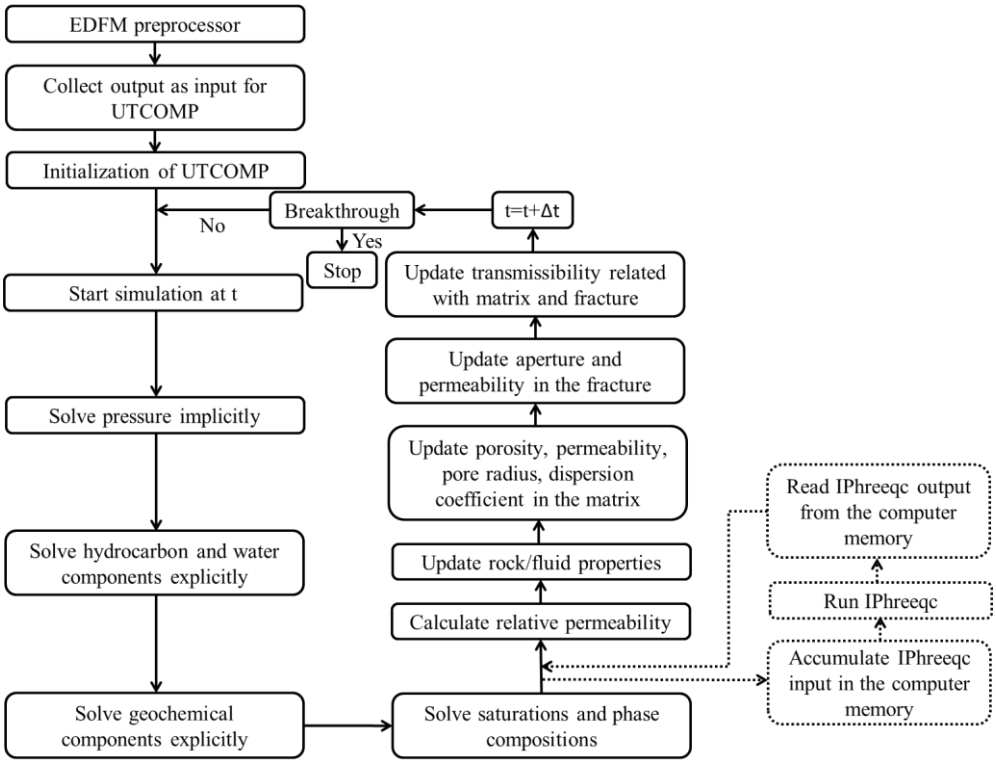


Figure 6.1: Flow chart of the computational algorithm in acidizing through the UTCOMP-EDFM model.

### 6.2.2 EDFM

EDFM was developed to honor the accuracy of Discrete Fracture Model (DFM) while maintaining the efficiency of structured grids (Moinfar et al. 2012; Moinfar 2013; Xu et al. 2017; Xu et al. 2019). EDFM was implemented in UTCOMP (Shakiba 2014) to model transport in the porous media in the presence of fractures. When a fracture penetrates a matrix grid, a fracture grid is created to represent the fracture segment bounded by the matrix grid. In EDFM, each fracture is divided into segments by boundaries of matrix grids and non-neighboring connections (NNCs) are created to calculate transport relationships involved with additional fracture grids. In UTCOMP-EDFM, the depth of the fracture grid is the centroid depth of the segment, and the pore

volume is defined as the product of the segment area and the fracture aperture. The effective porosity of the fracture segment is defined based on the pore volume:

$$\varphi_f = \frac{A_f w_f}{V_{bm}}, \tag{6.1}$$

where $\varphi_f$ is the effective porosity of the fracture segment; $A_f$ is the segment area perpendicular to the fracture aperture; $w_f$ is the fracture aperture; $V_{bm}$ is the bulk volume of the matrix grid corresponding to the fracture segment.

When acid flows into the fracture, acid dissolves the minerals on the fracture surface and increases the fracture aperture. The equation equating change in fracture aperture can be derived based on the change of the mineral amount due to reactions, similar as the second term in the porosity change equation for the matrix shown in Eq. 4.3. The porosity of the matrix near the fracture surface needs to be considered as follows:

$$\frac{\partial w_f}{\partial t} = -\frac{1}{A_f (1-\varphi_m)} \frac{\partial}{\partial t}\left( \sum_{k=1}^{n_s} \frac{n_k M w_k}{\rho_k} \right), \tag{6.2}$$

where $\varphi_m$ is the porosity of the matrix grid corresponding to the fracture segment.

The fracture permeability was found to be dependent on the fracture aperture and independent of stress history. The cubic law was proved to be valid for either open or closed fractures regardless of rock types (Witherspoon et al. 1980). The cubic law can be expressed in a simplified form as

$$\frac{Q}{\Delta h} = \frac{C}{f} w_f^{\,3}, \tag{6.3}$$

where $Q$ is the flow rate in the fracture; $\Delta h$ is the difference in hydraulic head; $C$ is a constant depending on the flow geometry and flow properties; $f$ is a flow reduction factor considering deviation of the fracture space from that between the ideal parallel plates.

The flow rate is proportional to the fracture conductivity which is defined as the product of the fracture permeability and the fracture aperture. From the cubic law relationship, the fracture permeability is proportional to the square of the fracture aperture. Therefore, the change of the fracture permeability due to mineral dissolution can be expressed as

$$\frac{K_f}{K_{f0}} = \left( \frac{w_f}{w_{f0}} \right)^2 , \tag{6.4}$$

where $K_f$ is the fracture permeability; $K_{f0}$ is the reference fracture permeability; $w_{f0}$ is the reference fracture aperture.

There are three types of NNCs in EDFM: type 1 is between a fracture segment and the corresponding matrix grid; type 2 is between fracture segments from the same fracture; type 3 is between fracture segments from two intersecting fractures. The transmissibility factor corresponding to NNC type 1 needs to be updated during acidizing since it's dependent on the matrix permeability which increases due to mineral dissolution. The transmissibility factor of NNC type 1 can be expressed as

$$T_{mf} = \frac{K_m A_f}{d_{mf}}, \tag{6.5}$$

where $T_{mf}$ is the transmissibility factor between the fracture segment and the corresponding matrix grid; $K_m$ is the matrix permeability component in the normal direction to the fracture plane; $d_{mf}$ is the average normal distance from the matrix grid to the fracture segment.

The transmissibility factor corresponding to NNC type 2 also changes during acidizing because it's related with the fracture permeability and the fracture aperture. The transmissibility factor of NNC type 2 can be written as follows, which is a simplified formulation similar to that in Karimi-Fard et al. (2003):

$$T_f = \frac{T_1 T_2}{T_1 + T_2}, \tag{6.6}$$

$$T_1 = \frac{K_f A_c}{d_1}, \tag{6.7}$$

$$T_2 = \frac{K_f A_c}{d_2}, \tag{6.8}$$

where $T_f$ is the transmissibility between the segments from the same fracture; $A_c$ is the common face area of the two neighboring segments from the same fracture; $d_1$ is the distance from the centroid of the segment 1 to the common face; $d_2$ is the distance from the centroid of the segment 2 to the common face.

The transmissibility factor corresponding to NNC type 3 is also dependent on the fracture permeability and the fracture aperture. The transmissibility factor of NNC type 3 can be expressed as follows:

$$T_{ff} = \frac{T_1' T_2'}{T_1' + T_2'}, \tag{6.9}$$

$$T_1' = \frac{K_{f1} w_{f1} L_{\text{int}}}{d_{f1}}, \tag{6.10}$$

$$T_2' = \frac{K_{f2} w_{f2} L_{\text{int}}}{d_{f2}}, \tag{6.11}$$

where $T_{ff}$ is the transmissibility factor between the segments from two intersecting fractures; $K_{f1}$ is the permeability of the fracture 1; $w_{f1}$ is the aperture of the fracture 1; $L_{\text{int}}$ is the length of the intersection line; $d_{f1}$ is the average normal distance from the sub-segment centroids of the segment 1 to the intersection line; $K_{f2}$ is the permeability of the fracture 2; $w_{f2}$ is the aperture of the fracture 2; $d_{f2}$ is the average normal distance from the sub-segment centroids of the segment 2 to the intersection line.

Except for the NNCs, if the well intersects the fracture segment, well index is also dependent on the fracture permeability and the fracture aperture. Moinfar et al. (2012)

derived the formulation similar to the Peaceman model (Peaceman 1983) to calculate the well index. The well index for the fracture segment which intersects the well can be expressed as

$$WI_f = \frac{2\pi K_f w_f}{\ln(r_e / r_w)}, \tag{6.12}$$

$$r_e = 0.14\sqrt{L^2 + W^2}, \tag{6.13}$$

where $L$ is the length of the fracture segment; $W$ is the height of the fracture segment.

## 6.3 VALIDATION

The UTCOMP-IPhreeqc model used for acidizing has been validated in the previous work (Wei et al. 2019), except for the effect of fractures. The simulation results were compared with an analytical solution derived for a 1D reactive transport model with the assumption of simple reaction. To validate the IPhreeqc calculation and the coupling between UTCOMP and IPhreeqc, the simulation results based on the UTCOMP/IPhreeeqc model were also compared with that based on the simple-reaction model. Through modifying the IPhreeqc database to use the same reaction equation as that used in the simple-reaction model, consistent results for a 1D homogeneous case and a 2D heterogeneous case were achieved. All of the validation results were presented in the previous work.

For the EDFM model, the EDFM results were compared with fine-grid simulation considering simple fractures using UTCOMP (Shakiba 2014). The author also compared UTCOMP-EDFM results with other simulation work (Moinfar 2013) using examples with randomly oriented vertical fractures and examples with dip-angled fractures. In addition, to validate the model with consideration of the well-fracture intersection, the EDFM results were compared against a semi-analytical solution of the diffusion equation

for unsteady state gas flow in unconventional reservoirs considering complex fracture networks, developed by Zhou et al. (2013) and Yu and Sepehrnoori (2014).

## 6.4 SIMULATION STUDIES ON CARBONATES WITH FRACTURES

In this section, simulation cases are presented for carbonate acidizing with consideration of fractures. Acid is injected from the left end of a homogeneous matrix or a heterogeneous matrix. The parameters used in the simulation are listed in Table 6.1.

| Parameter | Value | Unit | Parameter | Value | Unit |
|---|---|---|---|---|---|
| $x_l$ | 1.97 | in | $\gamma$ | 1.0 | - |
| $y_l$ | 0.79 | in | $\beta$ | 1.0 | - |
| $z_l$ | 0.06 | in | $r_{p0}$ | 1.0 | μm |
| $\varphi_0$ | 0.20 | - | $a_{v0}$ | 50.0 | $cm^{-1}$ |
| $\Delta\varphi_0$ | ±0.15 | - | $D_m$ | $3.6\times10^{-9}$ | $m^2/s$ |
| $K_0$ | 1.0 | mD | $\alpha_{os}$ | 0.5 | - |
| $p_i$ | 14.7 | psi | $\lambda_L$ | 0.5 | - |
| $\mu_w$ | 1.0 | cp | $\lambda_T$ | 0.1 | - |
| $C_{a0}$ | 4.1 | mol/L | $T$ | 100 | °F |
| $\eta$ | 1.0 | - | $w_{f0}$ | $1.0\times10^{-4}$ | m |
| $K_{f0}$ | 1000 | mD | - | - | - |

Table 6.1: Parameters used in the simulation.

### 6.4.1 Homogeneous matrix

The grid information in the simulation for a homogeneous matrix is listed in Table 6.2. For a homogeneous matrix, the dissolution front is supposed to be a planar surface propagating from left to right if there is no fracture. The dissolution structures for the homogeneous matrix with a single fracture are shown in Figure 6.2. The distributions

of the fracture aperture are also shown correspondingly in Figure 6.2. Acid preferentially flows into the fracture since the fracture provides a high-conductivity pathway. And due to the effect of fracture on the pressure field in the matrix, acid tends to flow towards the fracture wall, generating a wormhole along the fracture in the matrix. If the fracture is further away from the injection line as shown in Figure 6.2(b), the early-time dissolution structure is also influenced by the downstream fracture.

| Parameter | | Value | Unit |
|---|---|---|---|
| No. of gridblocks | | 800 (40×20) | - |
| $\Delta x$ | | 0.04925 | in |
| $\Delta y$ | | 0.0395 | in |
| Permeability | $x$ direction | 1.0 | mD |
| | $y$ direction | 1.0 | |
| Porosity | | 0.2 | - |

Table 6.2: Grid information in the simulation for a homogeneous matrix.

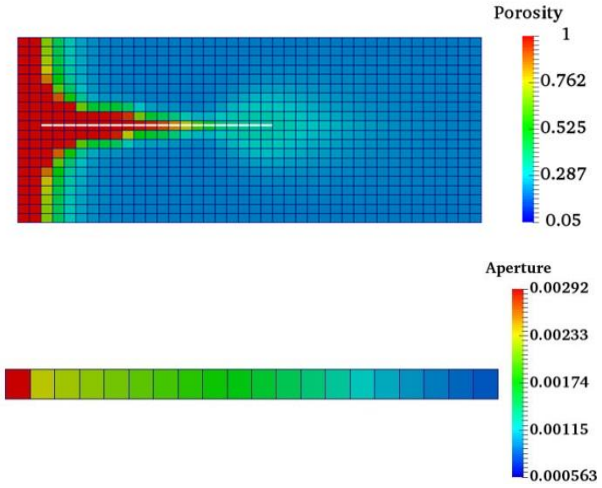


(a) Fracture near the injection line

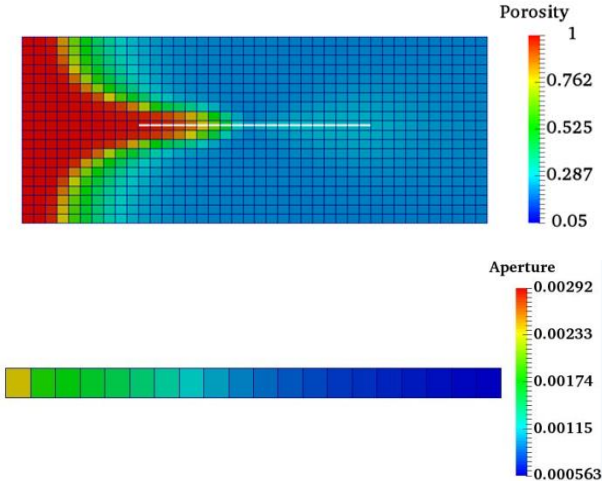


(b) Fracture in the middle

Figure 6.2: Dissolution structures in a homogeneous matrix with a single fracture.

Dissolution structures for a homogeneous matrix with two parallel fractures are shown in Figure 6.3. When two parallel fractures with the same conductivity are in a homogeneous matrix, two channels are generated symmetrically towards the entry points of the fractures, and the distributions of the fracture aperture are the same for the two fractures.

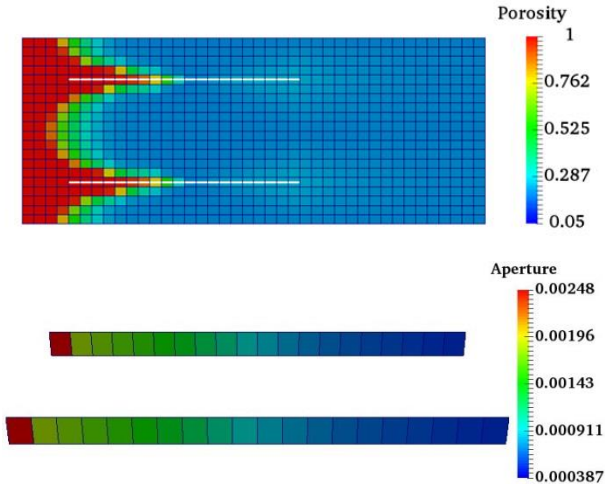


(a) Fractures near the injection line

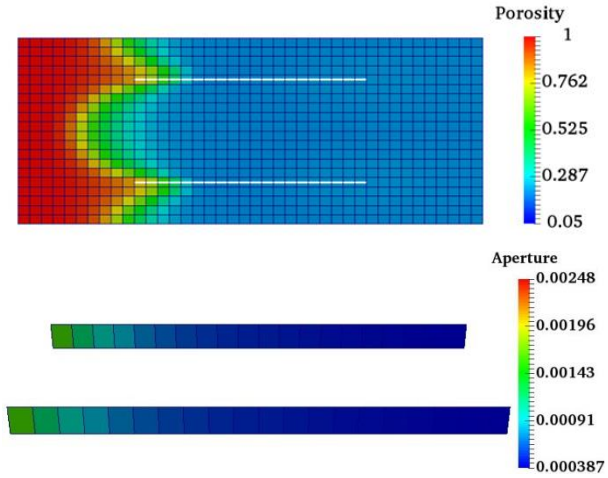


(b) Fractures in the middle

Figure 6.3: Dissolution structures in a homogeneous matrix with two parallel fractures.

### 6.4.2 Heterogeneous matrix

In the heterogeneous matrix, a uniform distribution of porosity with the range of [0.05, 0.35] is assumed and the permeability distribution is calculated based on the correlation in Eq. 4.14. The grid information in the simulation for a heterogeneous matrix is listed in Table 6.3. The dissolution structures for the heterogeneous matrix with no fractures and with a single fracture are compared in Figure 6.4. For the heterogeneous

matrix with no fractures, acid preferentially flows into the region with higher permeability, resulting in a dominant wormhole in the matrix. During carbonate acidizing, the wormhole pattern is the optimal dissolution structure with the least required acid consumption compared with other dissolution patterns. When there is a fracture in the heterogeneous matrix, the dissolution structure is not only affected by the distribution of the initial permeability, but also by the position of the fracture. The entry point of the fracture attracts the acid and changes the direction of the wormhole compared with the case with no fractures.

| Parameter | | Value | Unit |
|---|---|---|---|
| No. of gridblocks | | 800 (40×20) | - |
| $\Delta x$ | | 0.04925 | in |
| $\Delta y$ | | 0.0395 | in |
| Permeability | $x$ direction | Heterogeneous | - |
| | $y$ direction | Heterogeneous | |
| Porosity | | Heterogeneous | - |

Table 6.3: Grid information in the simulation for a heterogeneous matrix.

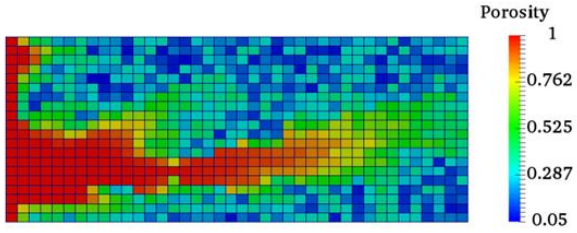


(a) No fractures

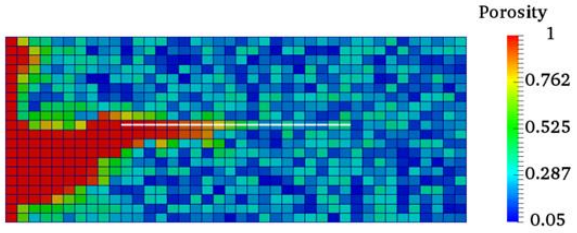


(b) Fracture in the middle

Figure 6.4: Dissolution structures in a heterogeneous matrix.

The dissolution structures in a heterogeneous matrix with two parallel fractures are shown in Figure 6.5. The initiation of the dissolution structure is dependent on the initial permeability distribution in the matrix. When the dominant channel reaches the entry point of one fracture, the channel will be propagating along the fracture in the matrix. One of the fractures attracts most of the acid with the other fracture almost no stimulation, especially for the case with the fractures further away from the injection line as shown in Figure 6.5(b).

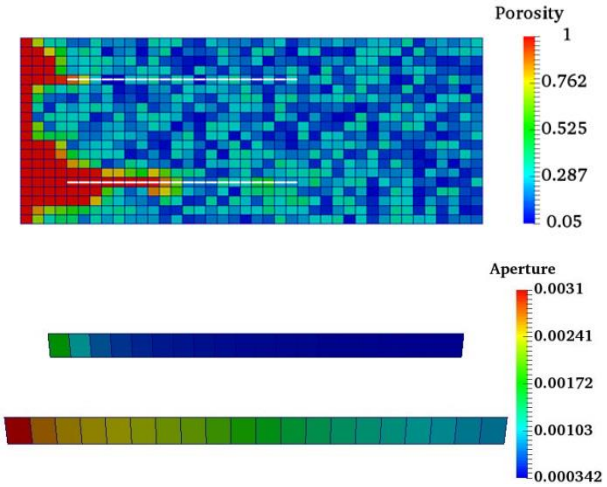


(a) Fractures near the injection line

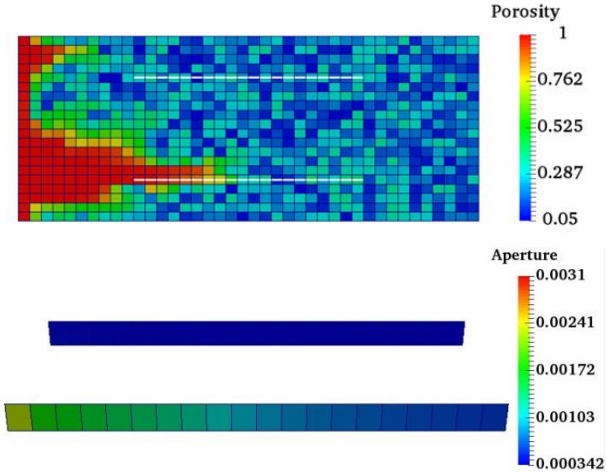


(b) Fractures in the middle

Figure 6.5: Dissolution structures in a heterogeneous matrix with two parallel fractures.

### 6.4.3 Fracture position

The fracture position has an influence on the dissolution structures in the matrix, and furthermore on acid consumption. Dissolution structures in Figure 6.4(a) indicate that there is a high-perm region in the lower part of the matrix near the injection line. Dissolution structures in a heterogeneous matrix with a fracture in different locations near the injection line are presented in Figure 6.6. Different dissolution structures have been generated with the fracture on top, in the middle, and on bottom. If the fracture is near the

high-perm region as shown in Figure 6.6(c), acid directly flows into the fracture without detouring since the wormhole is initiated in the lower part. If the fracture is in the middle, a little away from the high-perm region, as shown in Figure 6.6(b), acid sweeps the lower part of the matrix to reach the entry point of the fracture. If the fracture is on top as shown in Figure 6.6(a), further away from the high-perm region, acid sweeps almost the entire part of the matrix near the injection line to reach the entry point of the fracture.

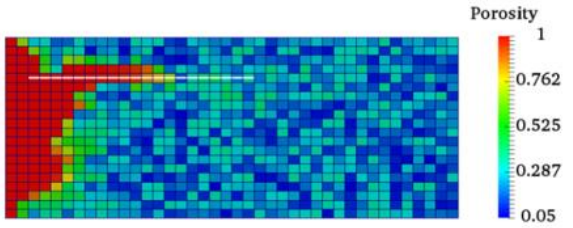


(a) Fracture on top

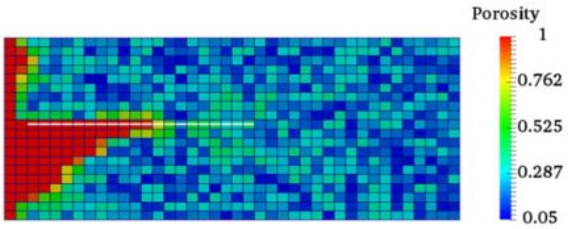


(b) Fracture in the middle

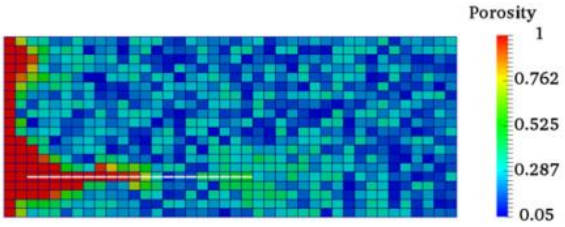


(c) Fracture on bottom

Figure 6.6: Dissolution structures in a heterogeneous matrix with a fracture near the injection line.

Dissolution structures in a heterogeneous matrix with a fracture in different locations in the middle are presented in Figure 6.7. When the fracture is away from the injection line, the early-time dissolution structures are similar for different cases. This also demonstrates that the initiation of the dissolution structures is largely dependent on the permeability distribution near the injection line. The wormholes propagate in different directions since the subsequent dissolution structures are determined by the fracture position, especially the location of the entry point.

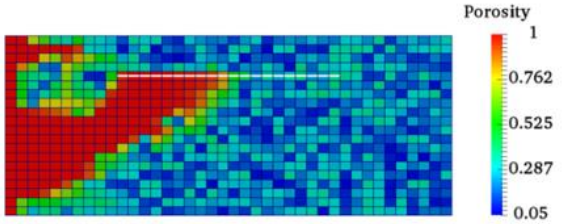


(a) Fracture on top

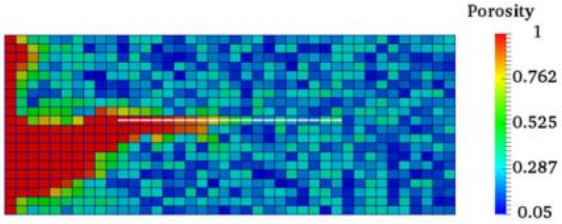


(b) Fracture in the middle

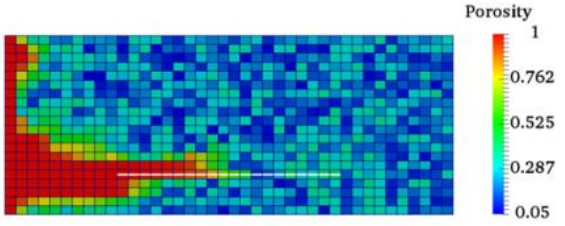


(c) Fracture on bottom

Figure 6.7: Dissolution structures in a heterogeneous matrix with a fracture in the middle region.

Dissolution structures in a heterogeneous matrix with a fracture in different locations near the right boundary are shown in Figure 6.8. When the fracture is near the right boundary of the domain, the early-stage period with no effect of fractures becomes longer. But finally, the dissolution structures are dependent on the fracture position as the wormhole propagates further into the matrix.

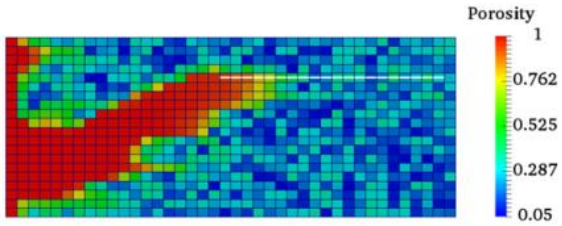


(a) Fracture on top

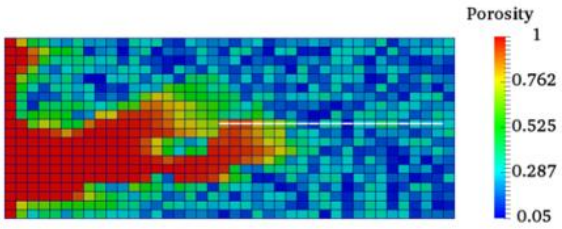


(b) Fracture in the middle

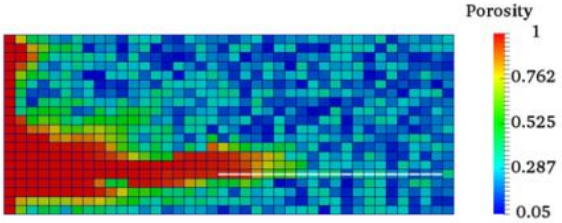


(c) Fracture on bottom

Figure 6.8: Dissolution structures in a heterogeneous matrix with a fracture near the right boundary.

### 6.4.4 Reaction on the fracture surface

Some previous work (Liu et al. 2017) focused on the effect of fracture conductivity on the wormhole propagation but neglected the reaction on the fracture surface. In this part, dissolution structures and the PVBT (Pore Volume Breakthrough) are compared between the cases with and without consideration of the reaction on the fracture surface. Dissolution structures when the fracture is in the middle are compared in Figure 6.9. The PVBT for the case without reaction on the fracture surface is 4.16. It is smaller than the case with no fractures in Figure 6.4(a), which requires 4.61 times of pore volume. This is because the fracture provides a high-conductivity path to connect the wormhole to the left and that to the right, reducing the acid consumption in the matrix near the fracture. For the case with consideration of the reaction on the fracture surface, when injecting 4.16 times of pore volume, the wormhole only propagates half way into the matrix. This is because acid flows into the fracture and reacts with minerals on the fracture wall, increasing the fracture conductivity. This leads to more difficulty for acid to leak-off from the fracture into the matrix, retarding wormhole propagation in the matrix.

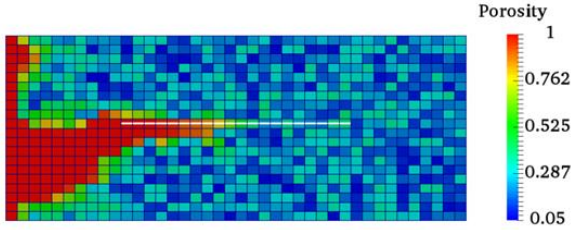


(a) Consider reaction on the fracture surface

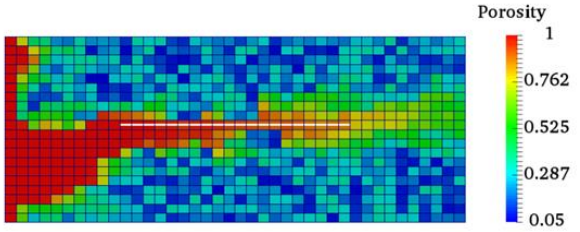


(b) Consider no reaction on the fracture surface

Figure 6.9: Comparison of dissolution structures for a heterogeneous matrix with a fracture in the middle.

Dissolution structures when the fracture is on bottom are compared in Figure 6.10. The PVBT for the case with no consideration of the reaction on the fracture surface is 4.11, smaller than that for the case when the fracture is in the middle. This is because the high-perm region is in the lower part of the matrix where the fracture is located. There is no necessity for the wormhole to detour to reach the entry point of the fracture. For the case considering the reaction on the fracture surface, the wormhole propagates much more slowly when injecting the same amount of acid.

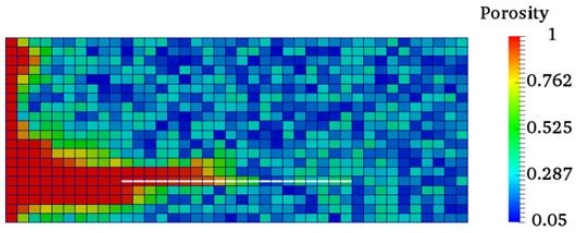


(a) Consider reaction on the fracture surface

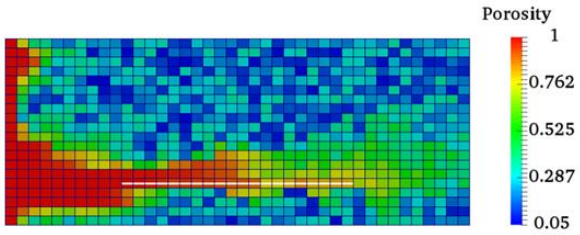


(b) Consider no reaction on the fracture surface

Figure 6.10: Comparison of dissolution structures for a heterogeneous matrix with a fracture on bottom.

Dissolution structures when the fracture is on top are compared in Figure 6.11. The PVBT for the case considering no reaction on the fracture surface is 5.38, larger than the case with no fracture in Figure 6.4(a). The reason is that the fracture is located far away from the high-perm region in the matrix. The wormhole is initiated depending on the permeability distribution near the injection line and then attracted by the entry point of the fracture. The wormhole propagation is deviated from the initial direction and acid needs to sweep a large volume of the matrix to get breakthrough, leading to more acid consumption compared with the case with no fractures. When considering the reaction on the fracture surface, the wormhole propagation is severely slowed down in the matrix.

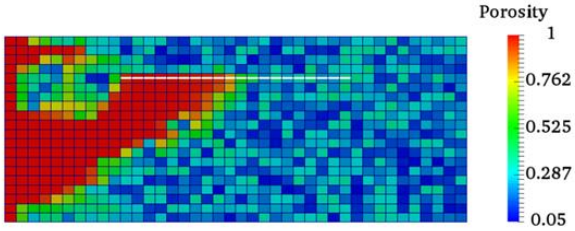


(a) Consider reaction on the fracture surface

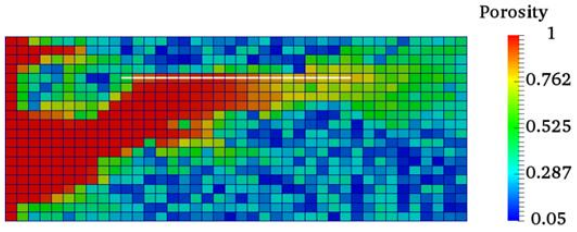


(b) Consider no reaction on the fracture surface

Figure 6.11: Comparison of dissolution structures for a heterogeneous matrix with a fracture on top.

### 6.4.5 Bottomhole pressure

One of the methods to define acidizing breakthrough in numerical modeling is monitoring the pressure drop between the inlet and the outlet of the domain. When the pressure drop decreases to 1/100 of the initial value, acid gets breakthrough. There are three stages on the dimensionless bottomhole pressure (BHP) curve when injecting acid into the matrix with no fractures, as shown in Figure 6.12, including initiation stage, wormhole propagation stage, and breakthrough stage. The dimensionless BHP curves when acidizing a heterogeneous matrix with a single fracture are presented in Figure 6.13, corresponding to the cases shown in Figure 6.6(b) and Figure 6.8(b). When the fracture is near the injection line as shown in Figure 6.6(b), in the initiation stage, the dimensionless BHP decreases and then levels out. This is because acid flows into the fracture during the initiation stage and acid is consumed to increase the fracture conductivity, leaving the downstream matrix almost intact with little stimulation. When

the fracture is near the right boundary as shown in Figure 6.8(b), the initiation stage is not affected by the fracture; during the wormhole propagation stage, the dimensionless BHP decreases and then levels out. This indicates that acid flows into the fracture during the wormhole propagation stage.

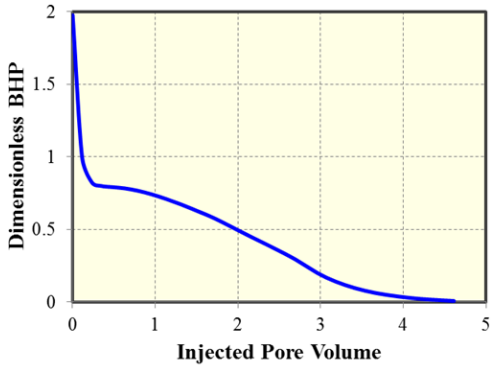


Figure 6.12: Dimensionless BHP when acidizing the matrix with no fractures.

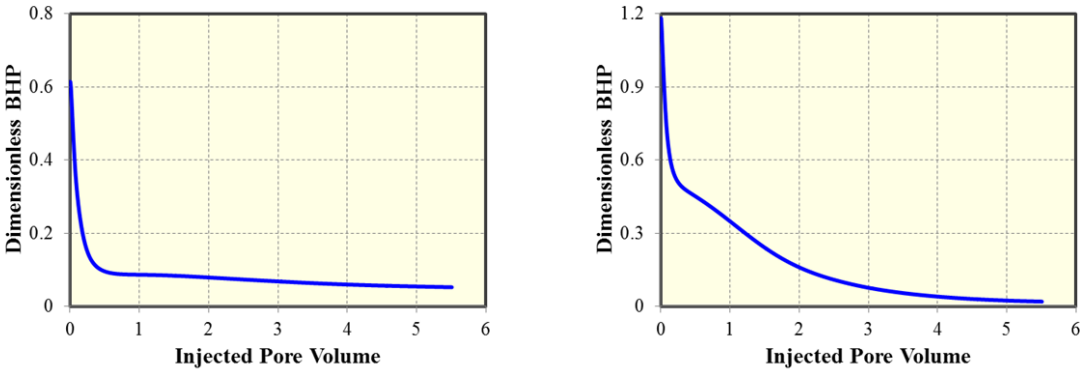


(a) Fracture near the injection line (b) Fracture near the right boundary

Figure 6.13: Dimensionless BHP curves when acidizing the matrix with a fracture.

### 6.4.6 Partially penetrated fractures

Fractures may not fully penetrate the matrix in the vertical direction. The 3D cases with three layers are investigated for a homogeneous matrix with a fracture penetrating in the top layer, in the middle layer, and in the bottom layer, as shown in

Figure 6.14. The grid information in the 3D simulation for a homogeneous matrix is listed in Table 6.4. The dissolution structures in the three layers are all affected by the fracture when the fracture partially penetrates the matrix in the vertical direction. Dissolution structures in different layers are presented in Figures 6.15-6.17 for the fracture penetrating in the top layer, in the middle layer, and in the bottom layer, respectively. Dissolution structures are similar in different layers no matter which part of the matrix is penetrated by the fracture in the vertical direction. This indicates that the wormhole propagation is retarded in the whole domain even though the fracture does not fully penetrate the matrix in the vertical direction.

| Parameter | | Value | Unit |
|---|---|---|---|
| No. of gridblocks | | 2400 (40×20×3) | - |
| $\Delta x$ | | 0.04925 | in |
| $\Delta y$ | | 0.0395 | in |
| $\Delta z$ | | 0.06 | in |
| Permeability | $x$ direction | 1.0 | mD |
| | $y$ direction | 1.0 | |
| | $z$ direction | 1.0 | |
| Porosity | | 0.2 | - |

Table 6.4: Grid information in the 3D simulation case for a homogeneous matrix.

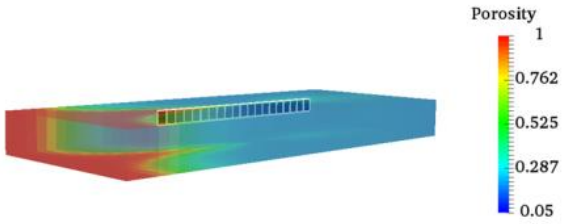


(a) Fracture on top

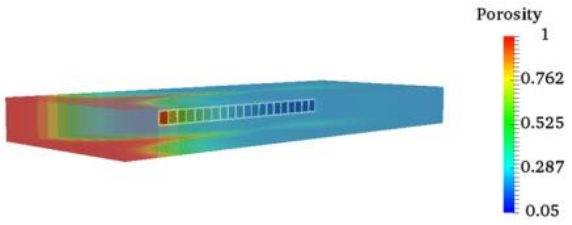


(b) Fracture in the middle

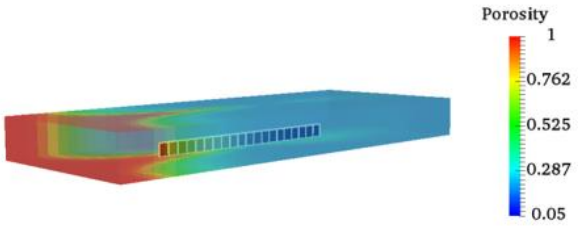


(c) Fracture on bottom

Figure 6.14: Homogeneous matrix with a partially penetrating fracture in the vertical direction.

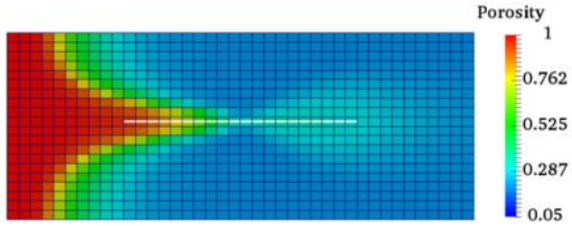


(a) Top layer

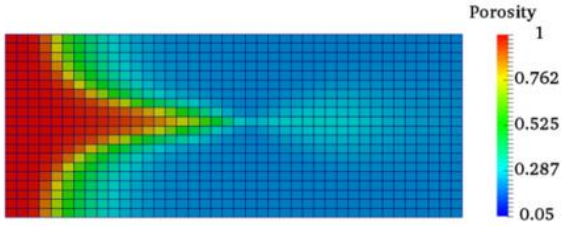


(b) Middle layer

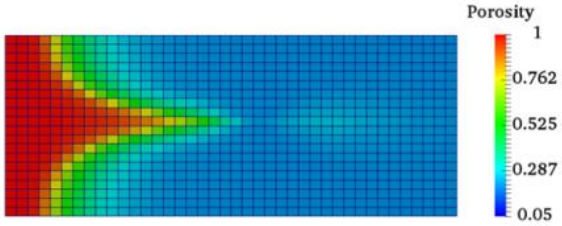


(c) Bottom layer

Figure 6.15: Dissolution structures in a homogeneous matrix with a fracture in the top layer.

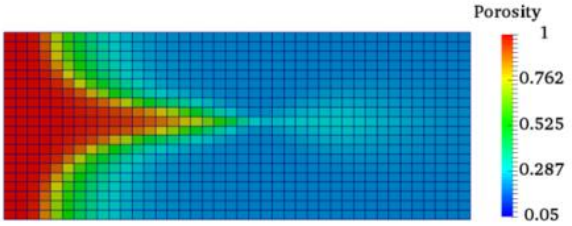


(a) Top layer

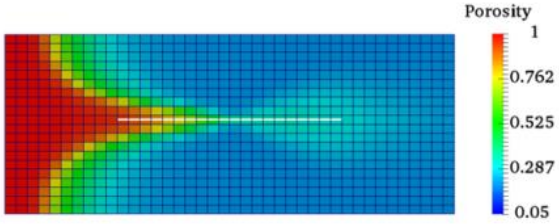


(b) Middle layer

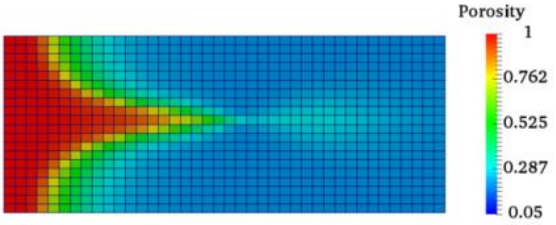


(c) Bottom layer

Figure 6.16: Dissolution structures in a homogeneous matrix with a fracture in the middle layer.

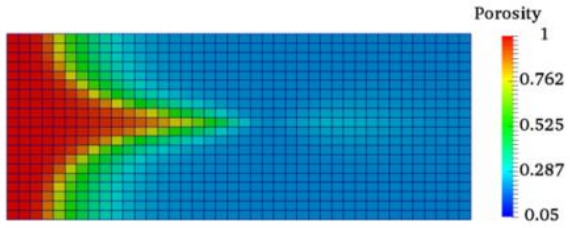


(a) Top layer

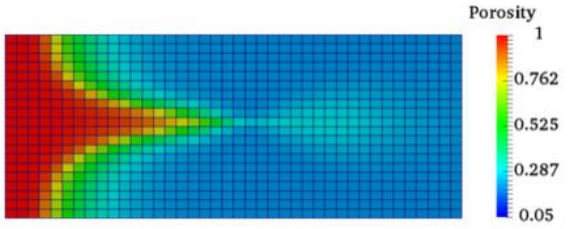


(b) Middle layer

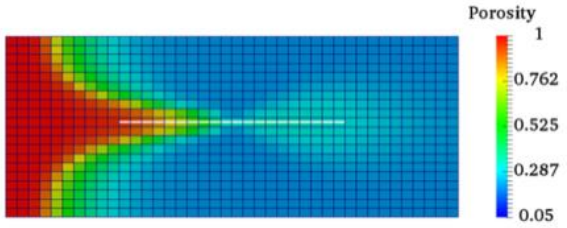


(c) Bottom layer

Figure 6.17: Dissolution structures in a homogeneous matrix with a fracture in the bottom layer.

The grid information in the 3D simulation for a heterogeneous matrix is listed in Table 6.5. Dissolution structures in a heterogeneous matrix with a partially penetrated fracture in the vertical direction are shown in Figure 6.18. Dissolution structures in the three layers are all affected by the fracture. Dissolution structures in different layers are presented in Figures 6.19-6.21 for the fracture penetrating in the top layer, in the middle layer, and in the bottom layer, respectively. Dissolution structures in different layers are different due to the difference in the permeability distribution. However, wormhole penetration depths are similar for the three layers. As the acid flows into the fracture,

most of the acid is consumed in the fracture, instead of in the matrix. Overall, the partially penetrating fracture in the vertical direction slows down the wormhole propagation in the matrix.

| Parameter | | Value | Unit |
|---|---|---|---|
| No. of gridblocks | | 2400 (40×20×3) | - |
| $\Delta x$ | | 0.04925 | in |
| $\Delta y$ | | 0.0395 | in |
| $\Delta z$ | | 0.06 | in |
| Permeability | $x$ direction | Heterogeneous | - |
| | $y$ direction | Heterogeneous | |
| | $z$ direction | Heterogeneous | |
| Porosity | | Heterogeneous | - |

Table 6.5: Grid information in the 3D simulation for a heterogeneous matrix.

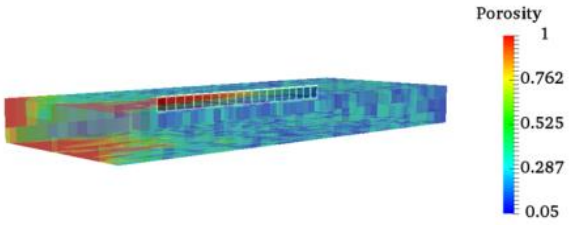


(a) Fracture on top

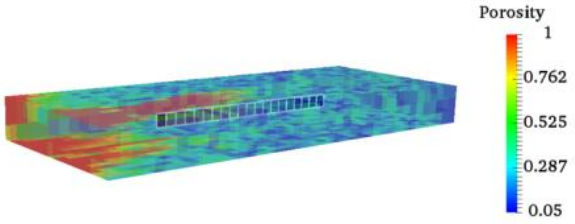


(b) Fracture in the middle

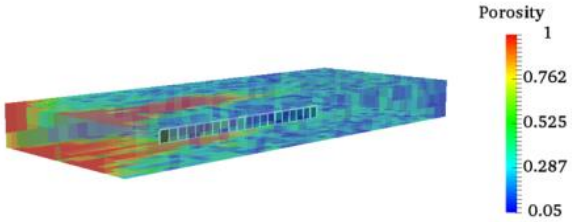


(c) Fracture on bottom

Figure 6.18: Heterogeneous matrix with a partially penetrating fracture in the vertical direction.

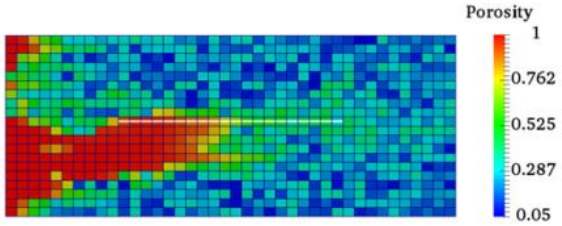


(a) Top layer

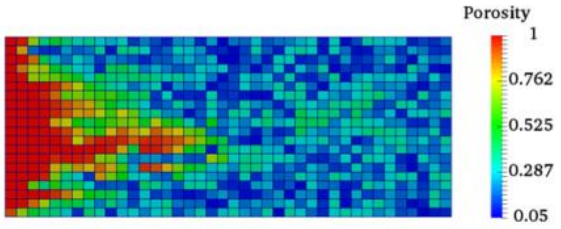


(b) Middle layer

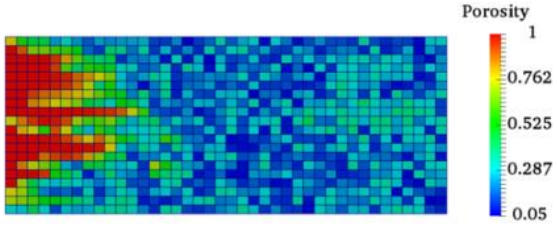


(c) Bottom layer

Figure 6.19: Dissolution structures in a heterogeneous matrix with a fracture in the top layer.

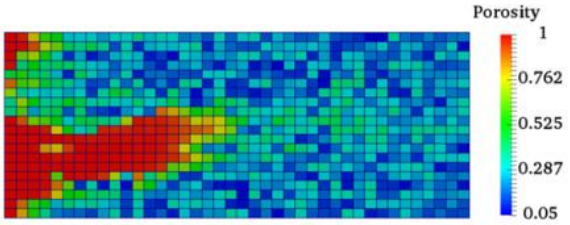


(a) Top layer

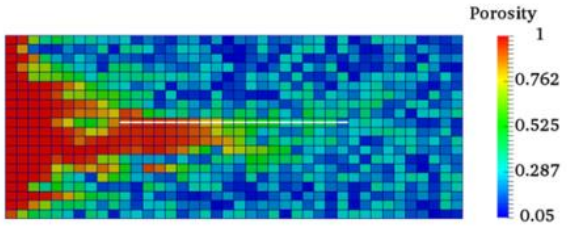


(b) Middle layer

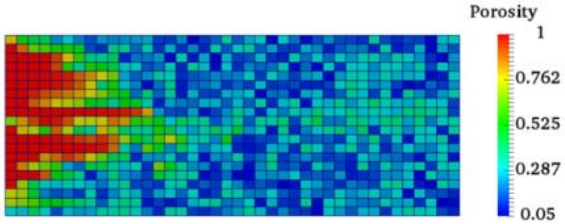


(c) Bottom layer

Figure 6.20: Dissolution structures in a heterogeneous matrix with a fracture in the middle layer.

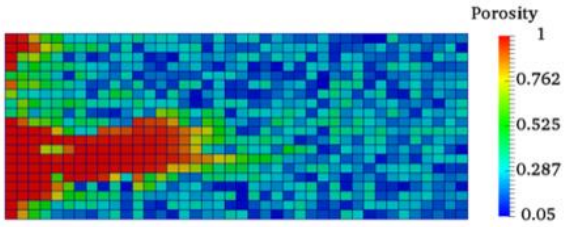


(a) Top layer

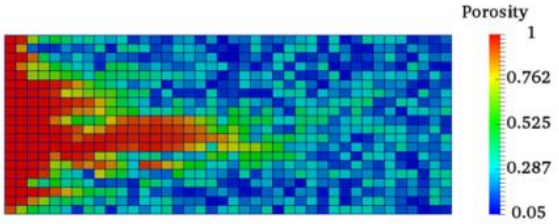


(b) Middle layer

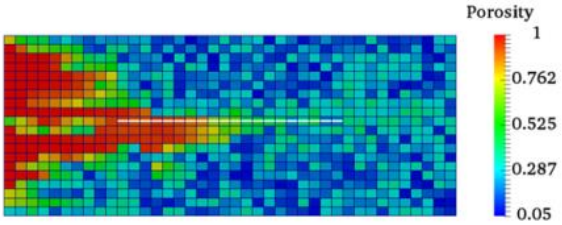


(c) Bottom layer

Figure 6.21: Dissolution structures in a heterogeneous matrix with a fracture in the bottom layer.

## 6.5 CONCLUSIONS

The main objective of this chapter is to couple the two-scale continuum model with EDFM to realize acidizing process with consideration of fractures. In this process, IPhreeqc is used to calculate all the reactions occurring in the matrix and in the fracture. All the transmissibility factors are modified during acidizing process based on the mineral dissolution results calculated from IPhreeqc. Based on the simulation studies, the following conclusions can be drawn:

- For a homogeneous matrix with a single fracture, the wormhole is generated along the fracture. For a homogeneous matrix with two parallel fractures, the

dissolution structure is symmetric with two wormholes propagating along the fractures.

- For a heterogeneous matrix with a single fracture, the initiation of the wormhole is dependent on the initial permeability distribution in the matrix, and the wormhole propagation is dependent on the fracture position. For a heterogeneous matrix with two parallel fractures, the dominant channel propagates along one of the fractures, while the other fracture receives much less acid.
- The presence of the fracture retards wormhole propagation in the matrix. For a partially penetrated fracture in the vertical direction, wormhole propagation is slowed down for the entire matrix.

# CHAPTER 7: HIGH PERFORMANCE COMPUTING AND SPEEDUP TECHNIQUES IN GEOCHEMICAL MODELING OF MATRIX ACIDIZING

Simulation of acidizing process is computationally expensive, especially for geochemical simulation which considers full-species transport and complex reactions. In Chapter 4, geochemical modeling of acidizing process is implemented in coupled UTCOMP-IPhreeqc model. Acidizing simulation through the coupled model UTCOMP-IPhreeqc is computationally expensive, and geochemical calculations through IPhreeqc are the computational bottleneck. To improve the computational efficiency, geochemical calculations, which take up the majority of the computational time, are parallelized. And speedup techniques are implemented to reduce the number of IPhreeqc calls by monitoring the amount change of geochemical species. We have validated the coupled model UTCOMP-IPhreeqc through comparison with the analytical solution in Chapter 4. Parallel performance is measured by comparing total CPU time, CPU time spent on geochemical calculations, and speedup ratios among simulation runs using different processor numbers. For heterogeneous matrix, different dissolution patterns are generated under different injection rates, and the computational time varies depending on the injection time until breakthrough and the average time-step size. Besides parallel computing, the speedup techniques also improve the computational efficiency, and obtain optimal performance for wormhole dissolution patterns in which most of the geochemical reactions occur in a localized volume. The computational time is reduced to 49.3% maintaining 95.9% accuracy compared with the case without using speedup techniques. The coupled model UTCOMP-IPhreeqc has the modeling ability of full-species transport and complex reactions. On this basis, the presented model significantly improves the

computational efficiency of UTCOMP-IPhreeqc through parallel computing and speedup techniques reducing the computational time of geochemical calculations.

## 7.1 INTRODUCTION

Acidizing simulations are computationally expensive and the requirements on computational time for different dissolution patterns are different. Uniform dissolution pattern or ramified wormhole pattern requires less computational time than dominant wormhole pattern, and face dissolution requires much more computational time than other dissolution patterns (Akanni and Nasr-El-Din 2016). Researchers applied different techniques to reduce the computational cost of acidizing simulation. Wu et al. (2015) developed the simulation model based on Darcy-Brinkman-Forchheimer (DBF) framework. They developed a parallel code with FORTRAN 90 and MPI to shorten the computational time. Ghommem et al. (2015) implemented the two-scale continuum model to simulate carbonate acidizing. The initial porosity of the core was obtained through CT scans and the reaction kinetics was measured to describe the acidizing process. They also used the library SAMG (algebraic multigrid methods for systems) to solve the discretized linear systems to reduce the computational cost. Akanni and Nasr-El-Din (2016) developed acidizing simulation model for acetic acid. They accounted for partially dissociated acid and fractional order reactions. They utilized parallel computing with a CFD software to reduce the computational time. They also pointed out that using Navier-Stokes momentum formulation improves the computational efficiency compared with using Darcy-Brinkman formulation. Dong et al. (2019) developed acidizing simulation model for fractured carbonate reservoirs using adaptive enriched Galerkin methods. They implemented adaptive mesh refinement around wormhole interfaces to speed up the simulation.

Reactive transport model is often implemented by coupling a hydrodynamical model with a geochemical model. The hydrodynamical model is responsible for fluid flow and solute transport while the geochemical model is responsible for reaction calculations. Geochemical simulations using the coupled model are computationally expensive and geochemical calculations are the bottleneck (Jatnieks et al. 2016). Many researchers work on improvement of the computational efficiency for the geochemical modeling. Hammond et al. (2014) introduced a geochemical transport code PFLOTRAN with its object-oriented design and numerical methods employed for parallel computing. They also demonstrated the parallel performance of PFLOTRAN through three realistic problem scenarios. Beisman et al. (2015) developed a parallel reactive transport model ParCrunchFlow through coupling a geochemical code with a hydrologic model. They conducted simulation work involving the biologically mediated reduction of nitrate in a floodplain aquifer to evaluate the parallel performance. Ahusborde et al. (2018) developed a parallel code coupling multiphase flow and geochemical interactions using the DUNE parallel library package based on MPI (Message Passing Interface). They investigated the parallel scalability using different grid resolutions for 3D simulations. He et al. (2015) coupled open-source software packages OpenGeoSys and IPhreeqc, and implemented a parallelization scheme based on MPI techniques. They presented parallel performance and result accuracy through 1D, 2D, and 3D examples.

To model detailed reactions between acid and multiple minerals, acidizing module is implemented into UTCOMP-IPhreeqc coupled software to simulate acidizing process (Wei et al. 2019). To reduce the computational time, the geochemistry module of the UTCOMP-IPhreeqc is parallelized using MPI (Message Passing Interface) (Korrani 2014) and two types of speedup methods are used to reduce IPhreeqc calls. The parallel performance is evaluated through comparison of total CPU time, CPU time spent on

geochemical calculations, and speedup ratios. The speedup performance using the two speedup methods is presented by comparing total CPU time and CPU time spent on geochemical calculations.

## 7.2 METHODOLOGY

### 7.2.1 Model description

In this chapter, a two-scale continuum model is implemented into UTCOMP with parallelized IPhreeqc to simulate acidizing process. The two-scale continuum model is composed of two parts: Darcy-scale model and pore-scale correlations. The Darcy-scale model is used to calculate pressure, phase saturation, and component concentration. The pore-scale correlations are relating Darcy-scale parameters with pore structure evolution. The reactions among minerals and aqueous species are calculated through IPhreeqc used to update component concentration. The calculation process of the two-scale continuum model using UTCOMP-IPhreeqc is described in Figure 4.1 in Chapter 4. The mathematical model is introduced briefly in this chapter with more details included in Chapter 4.

### 7.2.2 Parallelized IPhreeqc

IPhreeqc was designed intelligently to facilitate parallelization (Charlton and Parkhurst 2011). When running UTCOMP-IPhreeqc with parallelized IPhreeqc, each processor has its own IPhreeqc module and performs its own tasks of geochemical calculations (Korrani 2014). The master processor is responsible for flow and transport calculations, and distribution of geochemical data among the slave processors. The geochemical calculations are distributed among all the processors including the master processor and slave processors.

### 7.2.3 Speedup methods

Two types of speedup methods are used to improve the computational efficiency for UTCOMP-IPhreeqc. The two methods are both based on a defined tolerance for the relative amount change of geochemical components. When the relative amount change of all the geochemical components is less than the tolerance, geochemical calculations can be skipped without calling IPhreeqc at the current time-step. If the relative amount change of any geochemical component is above the tolerance, geochemical calculations are required to be performed at the current time-step. In the first method, the relative concentration change of geochemical components is compared between two consecutive time-steps (Sanaei 2019):

$$100 \times \left| \frac{N_i^{'n} - N_i^{'n-1}}{N_i^{'n-1}} \right| > \varepsilon \,, \tag{7.1}$$

where $N_i^{'n}$ is the mole number of the geochemical component $i$ at the $n^{th}$ time-step; $N_i^{'n-1}$ is the mole number of the geochemical component $i$ at the $n-1^{th}$ time-step; $\varepsilon$ is the defined tolerance.

In the second method, the relative concentration change of geochemical components is compared between the current time-step and the last time-step when the IPhreeqc was called:

$$100 \times \left| \frac{N_i^{'n} - N_i^{'m}}{N_i^{'m}} \right| > \varepsilon \,, \tag{7.2}$$

where $N_i^{'m}$ is the mole number of the geochemical component $i$ at the last time-step when IPhreeqc was called before the $n^{th}$ time-step.

## 7.3 VALIDATION

The UTCOMP-IPhreeqc model for acidizing process was validated in the previous work (Wei et al. 2019). In this chapter, the simulation results using multiple

processors to do geochemical calculations are validated through comparison with the case using a single processor. Two cases with different core sizes and different grid numbers are used to do validation and performance analysis. All simulations in this chapter were run on Lonestar 5 of TACC (Texas Advanced Computing Center), which is a high performance computing system deployed at TACC sponsored by The University of Texas System. Lonestar 5 has 1252 computer nodes each with two 12-core processing cores. The maximum time limit for jobs on TACC is 48 hours (Lonestar 5 User Guide). One of the following simulation runs in Case 2 was not able to be finished due to the time limit.

### 7.3.1 Case 1

Geochemical calculations in the UTCOMP-IPhreeqc model are parallelized. Parallel performance is investigated through the comparison of simulation cases using different processor numbers. The parameters used in Case 1 are listed in Table 7.1. The grid information in simulation of Case 1 is listed in Table 7.2. Before investigating the parallel performance, the acidizing breakthrough curves in Case 1 using different processor numbers are compared in Figure 7.1. The overlapping curves indicate the result accuracy when using multiple processors.

| Parameter | Value | Unit | Parameter | Value | Unit |
|---|---|---|---|---|---|
| $x_l$ | 1.97 | in | $\gamma$ | 1.0 | - |
| $y_l$ | 0.79 | in | $\beta$ | 1.0 | - |
| $z_l$ | 0.6 | in | $r_{p0}$ | 1.0 | μm |
| $\varphi_0$ | 0.20 | - | $D_m$ | $3.6\times10^{-9}$ | $m^2/s$ |
| $\Delta\varphi_0$ | ±0.15 | - | $\alpha_{os}$ | 0.5 | - |
| $K_0$ | 1.0 | mD | $\lambda_L$ | 0.5 | - |
| $p_i$ | 14.7 | psi | $\lambda_T$ | 0.1 | - |
| $\mu_w$ | 1.0 | cp | $T$ | 100 | °F |
| $C_{a0}$ | 4.1 | mol/L | - | - | - |

Table 7.1: Parameters used in simulation of Case 1.

| Parameter | | Value | Unit |
|---|---|---|---|
| No. of gridblocks | | 8000 (40×20×10) | - |
| $\Delta x$ | | 0.04925 | in |
| $\Delta y$ | | 0.0395 | in |
| $\Delta z$ | | 0.06 | in |
| Permeability | $x$ direction | Heterogeneous | - |
| | $y$ direction | Heterogeneous | |
| | $z$ direction | Heterogeneous | |
| Porosity | | Heterogeneous | - |

Table 7.2: Grid information in simulation of Case 1.

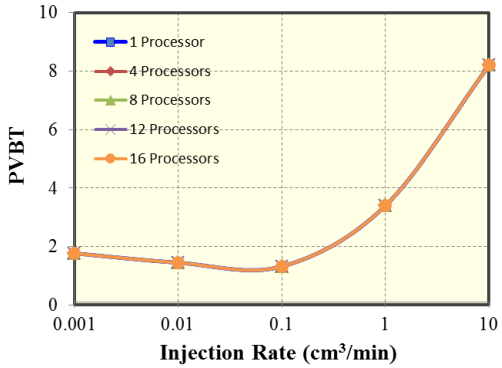


Figure 7.1: Acid breakthrough curves using different processor numbers in Case 1.

### 7.3.2 Case 2

The parameters used in Case 2 are listed in Table 7.3. The grid information in simulation of Case 2 is listed in Table 7.4. The acidizing breakthrough curves in Case 2 using different processor numbers are compared in Figure 7.2. The breakthrough pore volumes are almost the same when using different processor numbers. Simulation run under the injection rate of 0.01 $cm^3$/min using a single processor took more than 48 hours and was not able to be finished due to the time limit on TACC.

| Parameter | Value | Unit | Parameter | Value | Unit |
|---|---|---|---|---|---|
| $x_l$ | 3.94 | in | $\gamma$ | 1.0 | - |
| $y_l$ | 1.57 | in | $\beta$ | 1.0 | - |
| $z_l$ | 1.57 | in | $r_{p0}$ | 1.0 | μm |
| $\varphi_0$ | 0.20 | - | $D_m$ | $3.6\times10^{-9}$ | $m^2/s$ |
| $\Delta\varphi_0$ | ±0.15 | - | $\alpha_{os}$ | 0.5 | - |
| $K_0$ | 1.0 | mD | $\lambda_L$ | 0.5 | - |
| $p_i$ | 14.7 | psi | $\lambda_T$ | 0.1 | - |
| $\mu_w$ | 1.0 | cp | $T$ | 100 | °F |
| $C_{a0}$ | 4.1 | mol/L | - | - | - |

Table 7.3: Parameters used in simulation of Case 2.

| Parameter | | Value | Unit |
|---|---|---|---|
| No. of gridblocks | | 16000 (40×20×20) | - |
| $\Delta x$ | | 0.0985 | in |
| $\Delta y$ | | 0.0785 | in |
| $\Delta z$ | | 0.0785 | in |
| Permeability | $x$ direction | Heterogeneous | - |
| | $y$ direction | Heterogeneous | |
| | $z$ direction | Heterogeneous | |
| Porosity | | Heterogeneous | - |

Table 7.4: Grid information in simulation of Case 2.

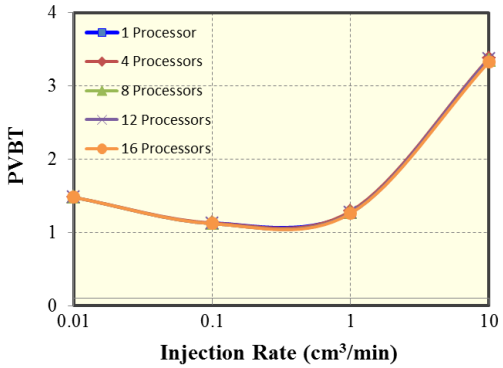


Figure 7.2: Acid breakthrough curves using different processor numbers in Case 2.

## 7.4 SIMULATION STUDIES

In the following analysis, parallel performance is analyzed based on the comparison of total CPU time, CPU time spent on geochemical calculations, and speedup ratios for simulation cases using different processor numbers. The speedup ratio is defined as the ratio of the serial running time using the sequential algorithm for solving a problem to the time taken using the parallel algorithm for solving the same problem. The equation of speedup is expressed as

$$S = \frac{T_s}{T_p}, \tag{7.3}$$

where $S$ is the speedup ratio; $T_s$ is the computational time using a single processor; $T_p$ is the computational time with the number of processors as $p$.

### 7.4.1 Simulation cases using a single processor

***Case 1***

In this section, 3D simulation cases are presented for carbonate acidizing using a single processor. The matrix is heterogeneous with a uniform distribution of porosity ranging from 0.05 to 0.35. The parameters used in the simulation of Case 1 are listed in

Table 7.1. The grid number in Case 1 is 8000 (40×20×10). Different PVBT (Pore Volume Breakthrough) values are required under different injection rates as shown on the acidizing breakthrough curve when using a single processor as shown in Figure 7.3. There is a minimum point on the curve corresponding to the optimal injection rate which requires the least amount of acid. Dissolution structure under the optimal injection rate is wormhole pattern shown in Figure 7.4. When the injection rate is higher than 0.1 $cm^3$/min, PVBT increases considerably due to the change of dissolution patterns. Dissolution pattern under the injection rate of 10 $cm^3$/min is shown in Figure 7.5. The dissolution is very uniform with porosity ranging from 0.5 to 0.84 in most regions as shown Figure 7.5(b).

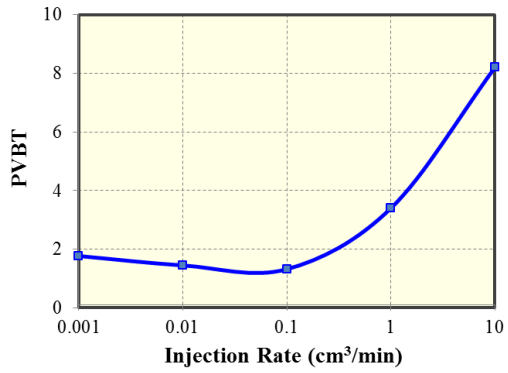


Figure 7.3: Acid breakthrough curve using a single processor in Case 1.

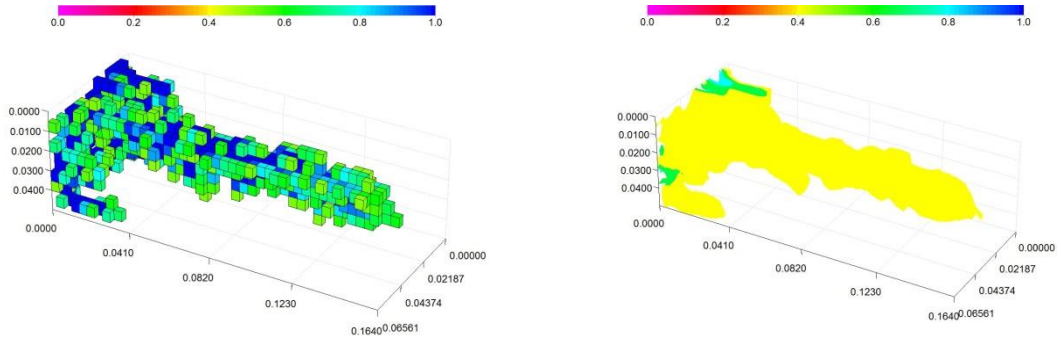


(a) Regions with porosity above 0.5 (b) Porosity iso surface

Figure 7.4: Dissolution structure under the injection rate of 0.1 $cm^3$/min in Case 1.

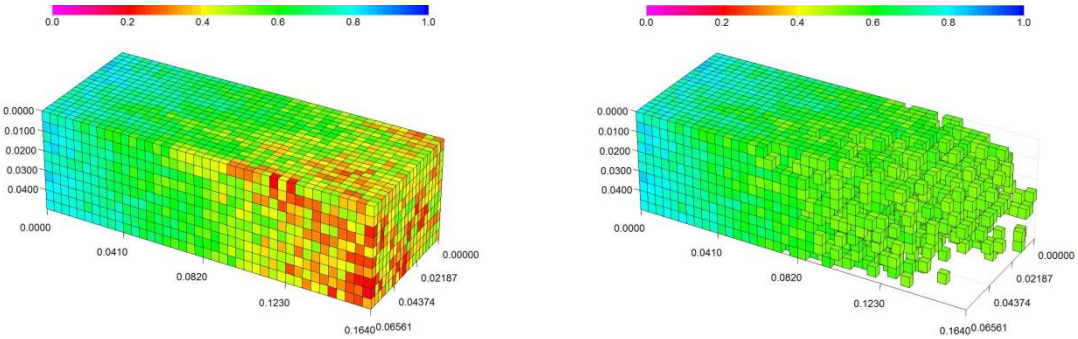


(a) Porosity distribution in the entire region (b) Regions with porosity between 0.5 and 0.84

Figure 7.5: Dissolution structure under the injection rate of 10 $cm^3$/min in Case 1.

***Case 2***

The parameters used in the simulation of Case 2 are listed in Table 7.2. The grid number in Case 2 is 16000 (40×20×20), which is two times of that in Case 1. Different PVBT values are required under different injection rates as shown on the acidizing breakthrough curve when using a single processor shown in Figure 7.6. The simulation run under the injection rate of 0.01 $cm^3$/min using a single processor took more than 48 hours and was not able to be finished due to the time limit on TACC. The point for the injection rate of 0.01 $cm^3$/min is replaced with the PVBT value using 4 processors. There is a minimum point on the curve corresponding to the optimal injection rate which

requires the least amount of acid. Dissolution structures under different injection rates are presented in Figures 7.7-7.10. The ramified wormhole pattern is generated at 10 $cm^3$/min. The dominant wormhole pattern is generated at 1 $cm^3$/min and 0.1 $cm^3$/min. Near the injection face, several wormholes are generated. But as wormholes propagate, only a dominant wormhole propagates from inlet to outlet until breakthrough. Other wormholes except for the dominant one stop propagation earlier for the case at injection rate of 0.1 $cm^3$/min than that at injection rate of 1 $cm^3$/min, leading to a smaller PVBT at 0.1 $cm^3$/min. A conical wormhole is generated at 0.01 $cm^3$/min, which requires larger acid consumption compared with the dominant wormhole pattern.

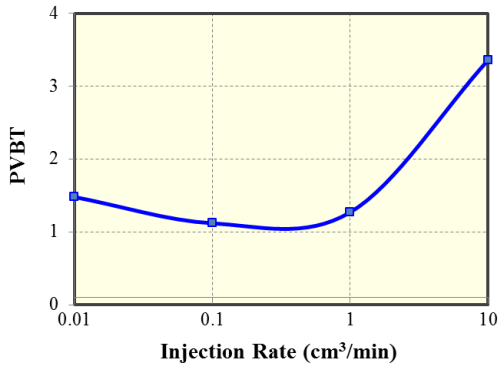


Figure 7.6: Acid breakthrough curve using a single processor in Case 2.

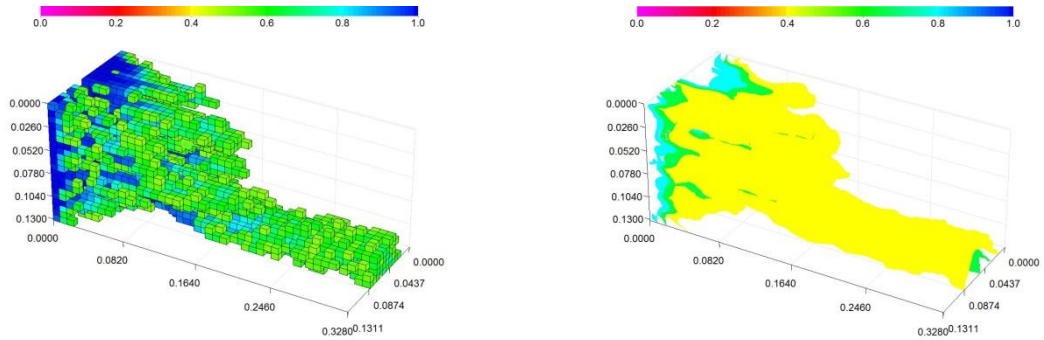


(a) Regions with porosity above 0.5 (b) Porosity iso surface

Figure 7.7: Dissolution structure under the injection rate of 10 $cm^3$/min in Case 2.

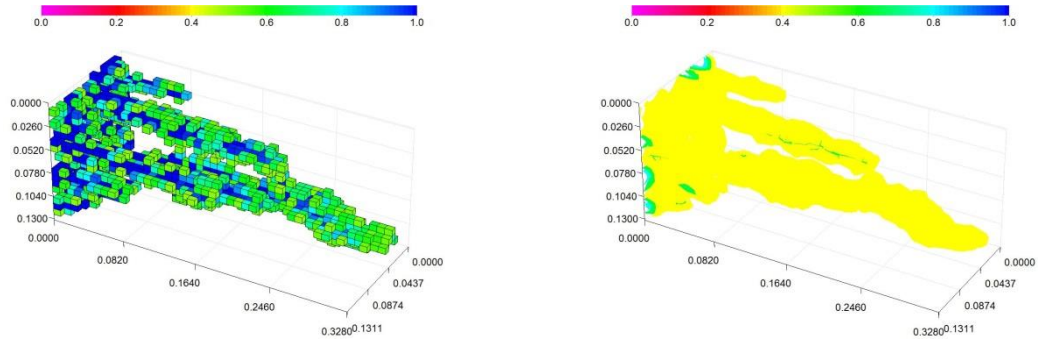


(a) Regions with porosity above 0.5 (b) Porosity iso surface

Figure 7.8: Dissolution structure under the injection rate of 1 $cm^3$/min in Case 2.

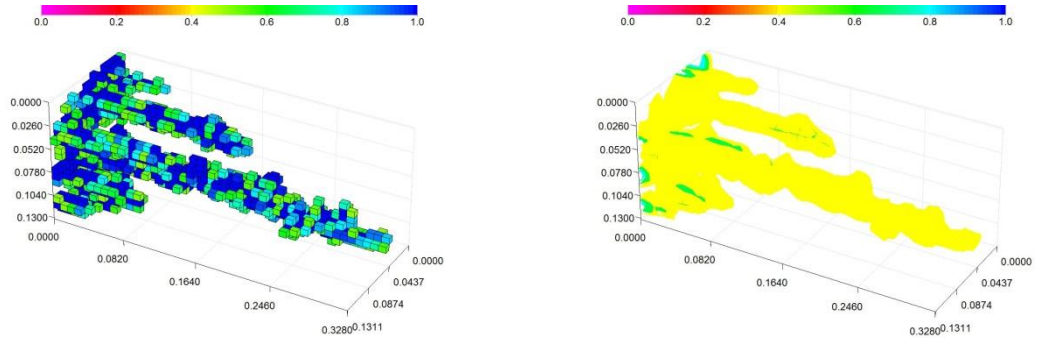


(a) Regions with porosity above 0.5 (b) Porosity iso surface

Figure 7.9: Dissolution structure under the injection rate of 0.1 $cm^3$/min in Case 2.

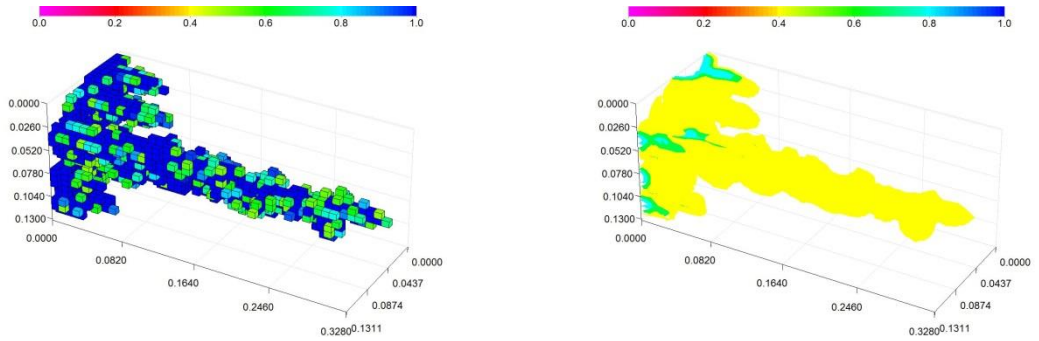


(a) Regions with porosity above 0.5 (b) Porosity iso surface

Figure 7.10: Dissolution structure under the injection rate of 0.01 $cm^3$/min in Case 2.

### 7.4.2 Simulation cases using multiple processors

***Case 1***

In Case 1, the total grid number is 8000 (40×20×10). The CPU time and the speedup ratio are used to measure the parallel performance. Total CPU time and speedup ratios are compared at injection rate of 10 $cm^3$/min in Figure 7.11. The processor number ranges from 1 to 16. The speedup ratio is 3.32 when the processor number is 4, which implies about 30.1% of CPU time is needed compared with the case using a single processor. As the processor number increases from 4 up to 16, the curve of speedup ratio starts to deviate from the linear speedup curve, which represents the ideal parallel performance as the dashed line in Figure 7.11(b). The speedup ratio is 4.91 when the processor number is 8, which implies about 20.4% of CPU time is needed compared with the case using a single processor. The speedup ratio is 5.79 when the processor number is 12, which implies about 17.3% of CPU time is needed compared with the case using a single processor. The speedup ratio is 6.52 when the processor number is 16, which implies about 15.3% of CPU time is needed compared with the case using a single processor. CPU time spent on geochemical calculations and corresponding speedup ratios are also compared in Figure 7.12 since geochemical calculations are the parallelized part. For the case using a single processor, geochemical calculations take up about 92% of the total CPU time. As the processor number increases, CPU time of geochemical calculations decreases to about 44% of the total CPU time when using 16 processors. Compared with the overall speedup curve in Figure 7.11(b), the deviation point occurs later and the deviation amount is smaller on the speedup curve regarding geochemical calculations in Figure 7.12(b). The speedup ratio is 4.13 when the processor number is 4, which implies about 24.2% of CPU time is needed for geochemical calculations

compared with the case using a single processor. The speedup ratio is 7.67 when the processor number is 8, which implies about 13.0% of CPU time is needed for geochemical calculations compared with the case using a single processor. The speedup ratio is 10.55 when the processor number is 12, which implies about 9.5% of CPU time is needed for geochemical calculations compared with the case using a single processor. The speedup ratio is 13.57 when the processor number is 16, which implies about 7.4% of CPU time is needed for geochemical calculations compared with the case using a single processor.

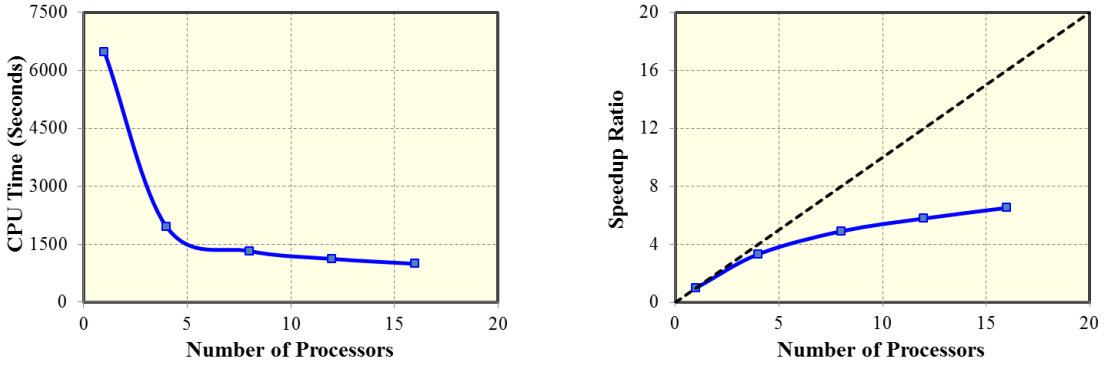


(a) CPU time (b) Speedup ratio

Figure 7.11: Parallel performance regarding total computational time at 10 $cm^3$/min in Case 1.

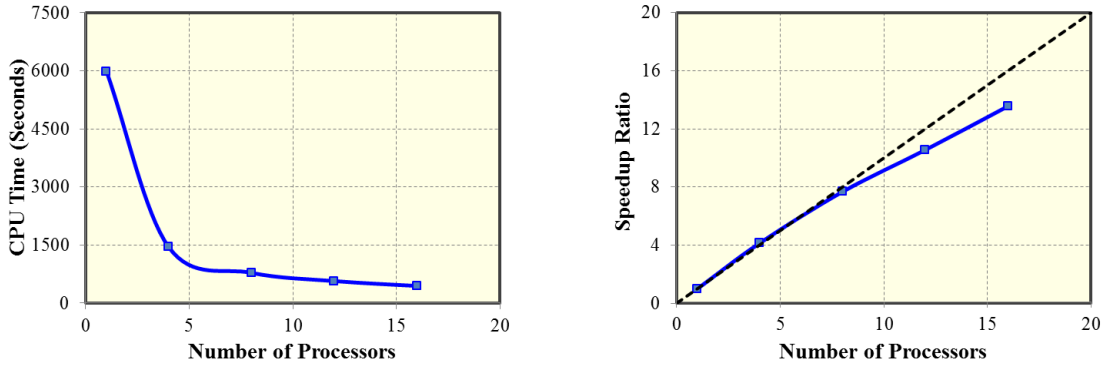


(a) CPU time (b) Speedup ratio

Figure 7.12: Parallel performance regarding computational time spent on geochemical calculations at 10 $cm^3$/min in Case 1.

For other cases with different injection rates, parallel performance is analyzed similarly. Total CPU time and speedup ratios are compared at injection rate of 1 $cm^3$/min in Figure 7.13. The speedup ratio is 3.45 when the processor number is 4, implying about 29.0% of CPU time is needed compared with the case using a single processor. The speedup ratio is 5.0 when the processor number is 8, implying about 19.9% of CPU time is needed compared with the case using a single processor. The speedup ratio is 5.88 when the processor number is 12, implying about 17.0% of CPU time is needed compared with the case using a single processor. The speedup ratio is 6.69 when the processor number is 16, implying about 15.0% of CPU time is needed compared with the case using a single processor. For the case using a single processor, geochemical calculations take up about 92% of the total CPU time. The CPU time spent on geochemical calculations and corresponding speedup ratios are compared in Figure 7.14. The speedup ratio is 4.35 when the processor number is 4, implying about 23.0% of CPU time is needed for geochemical calculations compared with the case using a single processor. The speedup ratio is 7.93 when the processor number is 8, implying about 12.6% of CPU time is needed for geochemical calculations compared with the case using

a single processor. The speedup ratio is 10.82 when the processor number is 12, implying about 9.24% of CPU time is needed for geochemical calculations compared with the case using a single processor. The speedup ratio is 14.21 when the processor number is 16, implying about 7.0% of CPU time is needed for geochemical calculations compared with the case using a single processor. The total CPU time and the proportion used on geochemical calculations using a single processor at 1 $cm^3$/min are very similar as the case with injection rate of 10 $cm^3$/min, resulting in comparable parallel performance when using multiple processors.

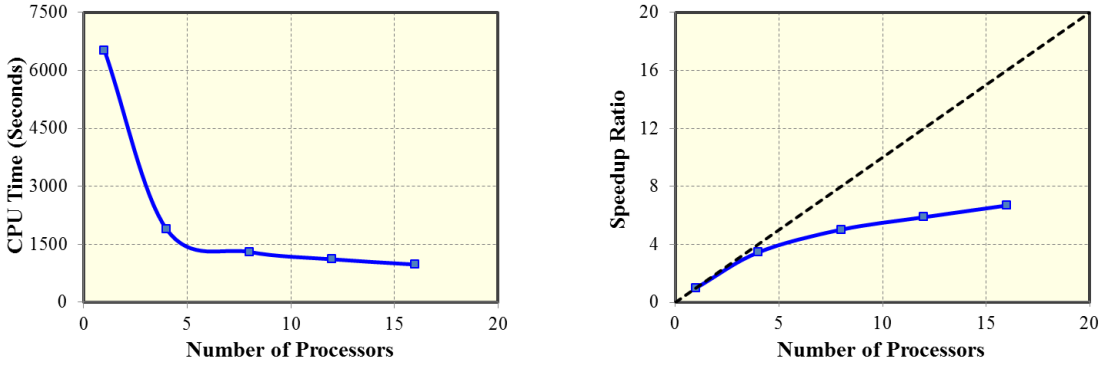


(a) CPU time (b) Speedup ratio

Figure 7.13: Parallel performance regarding total computational time at 1 $cm^3$/min in Case 1.

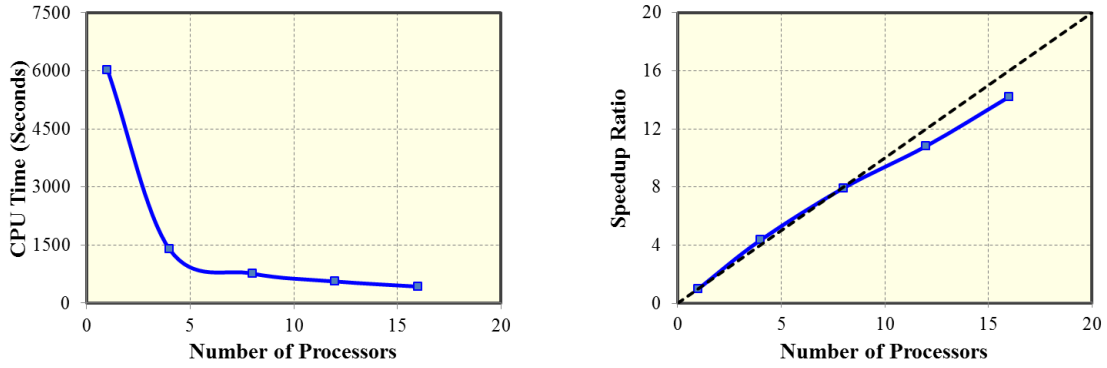


(a) CPU time (b) Speedup ratio

Figure 7.14: Parallel performance regarding computational time spent on geochemical calculations at 1 $cm^3$/min in Case 1.

The cases with other injection rates are investigated for the parallel performance in the same manner. The total computational time varies with injection rates and is proportional to the total number of time-steps, which depends on the average time-step size and the total injection time. The speedup ratio based on the total computational time deviates earlier and further compared with that based on the computational time spent on geochemical calculations. Total CPU time and speedup ratios are compared at injection rate of 0.1 $cm^3$/min in Figure 7.15. The speedup ratio is 2.95 when the processor number is 4, implying about 33.9% of CPU time is needed compared with the case using a single processor. The speedup ratio is 4.03 when the processor number is 8, implying about 24.8% of CPU time is needed compared with the case using a single processor. The speedup ratio is 4.72 when the processor number is 12, implying about 21.2% of CPU time is needed compared with the case using a single processor. The speedup ratio is 5.18 when the processor number is 16, implying about 19.3% of CPU time is needed compared with the case using a single processor. For the case using a single processor, geochemical calculations take up about 90% of the total CPU time. The CPU time spent on geochemical calculations and corresponding speedup ratios are compared in Figure

7.16. The speedup ratio is 3.83 when the processor number is 4, implying about 26.1% of CPU time is needed for geochemical calculations compared with the case using a single processor. The speedup ratio is 6.65 when the processor number is 8, implying about 15.0% of CPU time is needed for geochemical calculations compared with the case using a single processor. The speedup ratio is 9.35 when the processor number is 12, implying about 10.7% of CPU time is needed for geochemical calculations compared with the case using a single processor. The speedup ratio is 11.67 when the processor number is 16, implying about 8.6% of CPU time is needed for geochemical calculations compared with the case using a single processor.

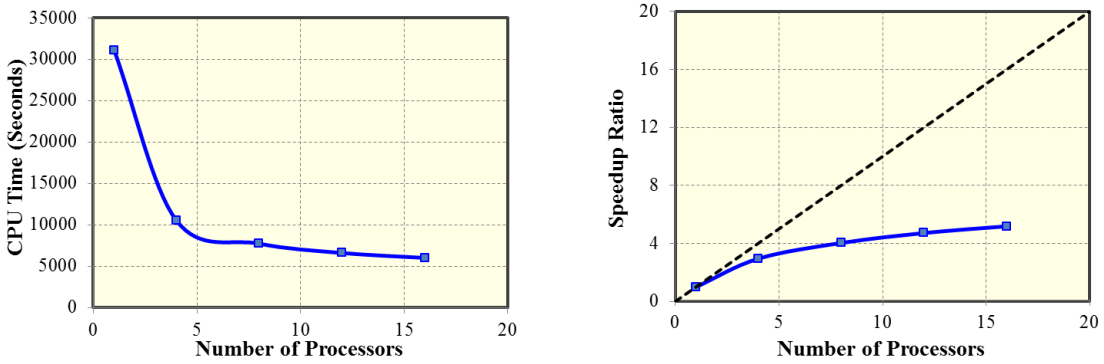


(a) CPU time (b) Speedup ratio

Figure 7.15: Parallel performance regarding total computational time at 0.1 $cm^3$/min in Case 1.

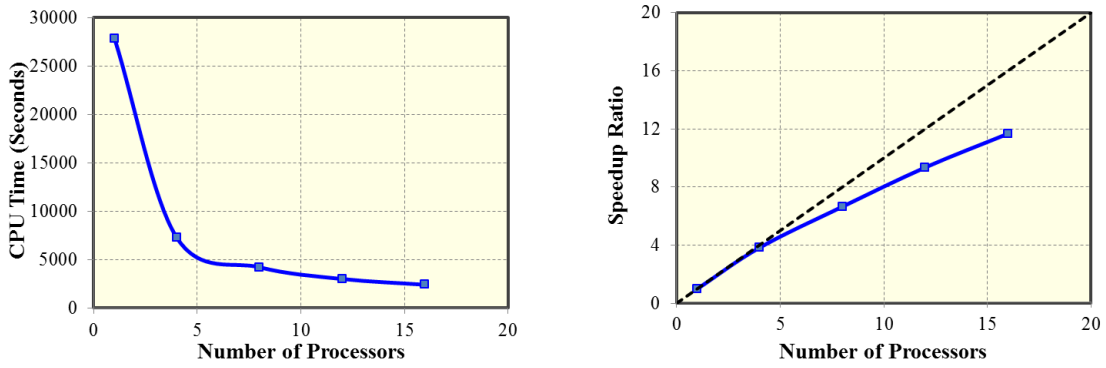


(a) CPU time (b) Speedup ratio

Figure 7.16: Parallel performance regarding computational time spent on geochemical calculations at 0.1 $cm^3$/min in Case 1.

Total CPU time and speedup ratios are compared at injection rate of 0.01 $cm^3$/min in Figure 7.17. The speedup ratio is 2.96 when the processor number is 4, implying about 33.8% of CPU time is needed compared with the case using a single processor. The speedup ratio is 4.15 when the processor number is 8, implying about 24.1% of CPU time is needed compared with the case using a single processor. The speedup ratio is 4.85 when the processor number is 12, implying about 20.6% of CPU time is needed compared with the case using a single processor. The speedup ratio is 5.35 when the processor number is 16, implying about 18.7% of CPU time is needed compared with the case using a single processor. For the case using a single processor, geochemical calculations take up about 90% of the total CPU time. The CPU time spent on geochemical calculations and corresponding speedup ratios are compared in Figure 7.18. The speedup ratio is 3.76 when the processor number is 4, implying about 26.6% of CPU time is needed for geochemical calculations compared with the case using a single processor. The speedup ratio is 6.66 when the processor number is 8, implying about 15.0% of CPU time is needed for geochemical calculations compared with the case using a single processor. The speedup ratio is 9.20 when the processor number is 12, implying

about 10.9% of CPU time is needed for geochemical calculations compared with the case using a single processor. The speedup ratio is 11.45 when the processor number is 16, implying about 8.7% of CPU time is needed for geochemical calculations compared with the case using a single processor.

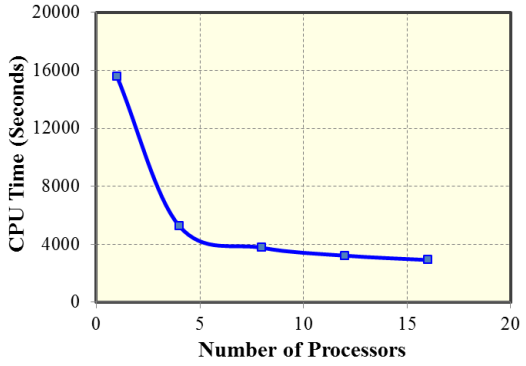


(a) CPU time

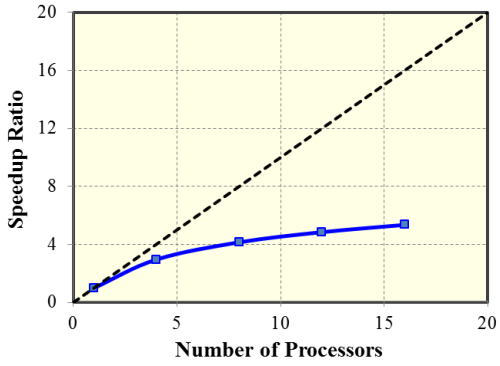


(b) Speedup ratio

Figure 7.17: Parallel performance regarding total computational time at 0.01 $cm^3$/min in Case 1.

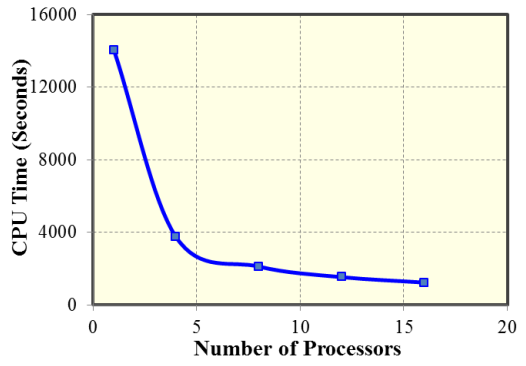


(a) CPU time

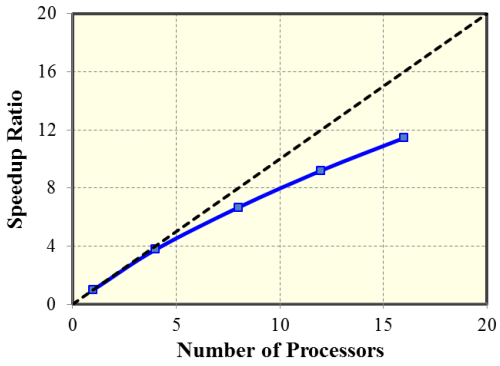


(b) Speedup ratio

Figure 7.18: Parallel performance regarding computational time spent on geochemical calculations at 0.01 $cm^3$/min in Case 1.

Total CPU time and speedup ratios are compared at injection rate of 0.001 $cm^3$/min in Figure 7.19. The speedup ratio is 3.07 when the processor number is 4,

implying about 32.6% of CPU time is needed compared with the case using a single processor. The speedup ratio is 4.05 when the processor number is 8, implying about 24.7% of CPU time is needed compared with the case using a single processor. The speedup ratio is 4.63 when the processor number is 12, implying about 21.6% of CPU time is needed compared with the case using a single processor. The speedup ratio is 5.00 when the processor number is 16, implying about 20.0% of CPU time is needed compared with the case using a single processor. For the case using a single processor, geochemical calculations take up about 88% of the total CPU time. The CPU time spent on geochemical calculations and corresponding speedup ratios are compared in Figure 7.20. The speedup ratio is 4.23 when the processor number is 4, implying about 23.7% of CPU time is needed for geochemical calculations compared with the case using a single processor. The speedup ratio is 7.33 when the processor number is 8, implying about 13.6% of CPU time is needed for geochemical calculations compared with the case using a single processor. The speedup ratio is 10.10 when the processor number is 12, implying about 9.9% of CPU time is needed for geochemical calculations compared with the case using a single processor. The speedup ratio is 12.45 when the processor number is 16, implying about 8.0% of CPU time is needed for geochemical calculations compared with the case using a single processor.

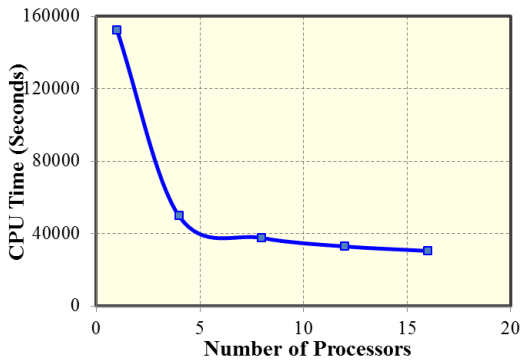


(a) CPU time

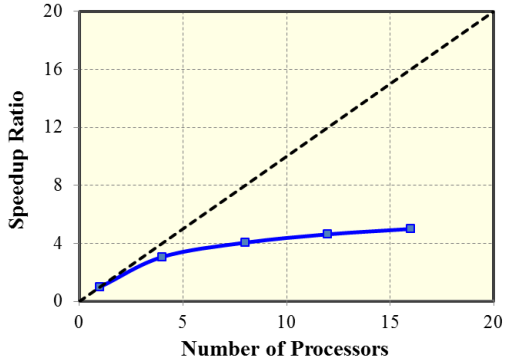


(b) Speedup ratio

Figure 7.19: Parallel performance regarding total computational time at 0.001 $cm^3$/min in Case 1.

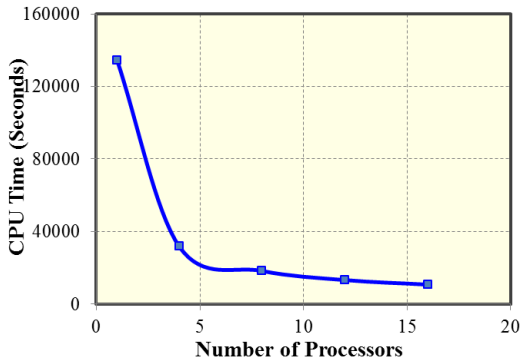


(a) CPU time

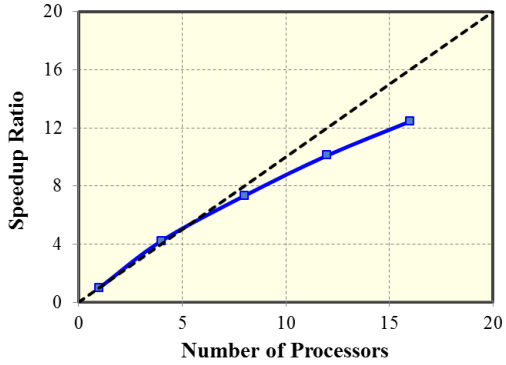


(b) Speedup ratio

Figure 7.20: Parallel performance regarding computational time spent on geochemical calculations at 0.001 $cm^3$/min in Case 1.

Among cases with different injection rates in Case 1, the case with the injection rate of 1 $cm^3$/min obtains the highest parallel efficiency. When using 16 processors, 85.0% of the total computational time is saved with the speedup ratio of 6.69, while 93.0% of the computational time spent on geochemical calculations is reduced with the speedup ratio of 14.21.

***Case 2***

In Case 2, the total grid number is 16000 (40×20×20), which is two times of case 1. A larger number of total grids needs more computational time compared with Case 1. The processor numbers range from 1 to 20. Total CPU time and speedup ratios are compared at injection rate of 10 $cm^3$/min in Figure 7.21. The speedup ratio is 2.31 when the processor number is 4, which implies about 43.4% of CPU time is needed compared with the case using a single processor. The speedup ratio is 2.69 when the processor number is 8, which implies about 37.2% of CPU time is needed compared with the case using a single processor. The speedup ratio is 2.82 when the processor number is 12, which implies about 35.4% of CPU time is needed compared with the case using a single processor. The speedup ratio is 3.04 when the processor number is 16, which implies about 32.9% of CPU time is needed compared with the case using a single processor. The speedup ratio is 2.97 when the processor number is 20, which implies about 33.7% of CPU time is needed compared with the case using a single processor. CPU time spent on geochemical calculations and corresponding speedup ratios are also compared in Figure 7.22. For the case using a single processor, geochemical calculations take up about 73% of the total CPU time. The speedup ratio is 4.68 when the processor number is 4, which implies about 21.4% of CPU time is needed for geochemical calculations compared with the case using a single processor. The speedup ratio is 8.66 when the processor number is 8, which implies about 11.5% of CPU time is needed for geochemical calculations compared with the case using a single processor. The speedup ratio is 11.9 when the processor number is 12, which implies about 8.4% of CPU time is needed for geochemical calculations compared with the case using a single processor. The speedup ratio is 16.04 when the processor number is 16, which implies about 6.2% of CPU time is needed for geochemical calculations compared with the case using a single processor.

The speedup ratio is 18.19 when the processor number is 20, which implies about 5.5% of CPU time is needed for geochemical calculations compared with the case using a single processor.

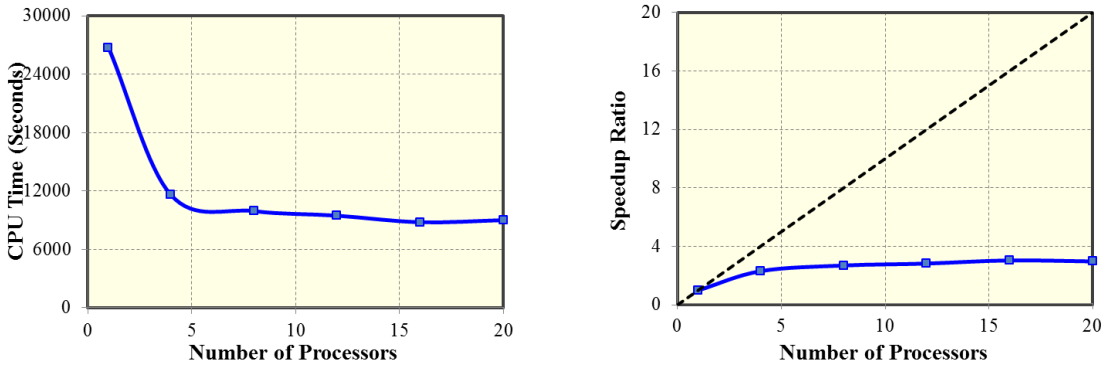


(a) CPU time (b) Speedup ratio

Figure 7.21: Parallel performance regarding total computational time at 10 $cm^3$/min in Case 2.

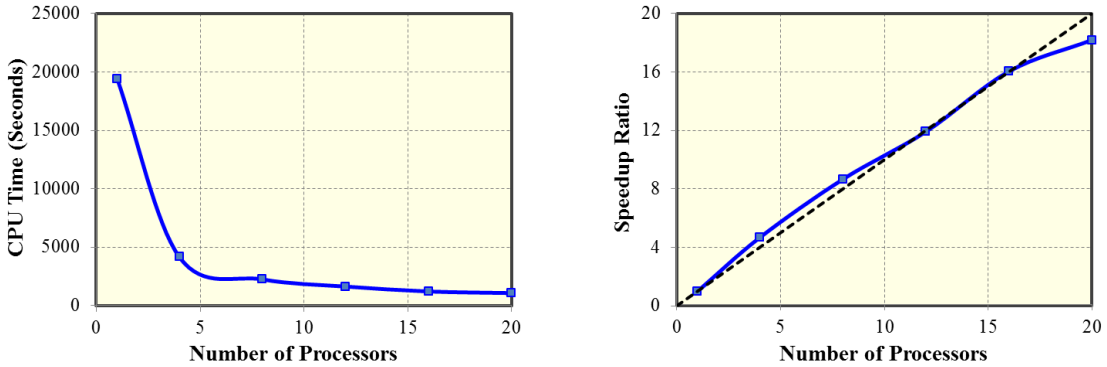


(a) CPU time (b) Speedup ratio

Figure 7.22: Parallel performance regarding computational time spent on geochemical calculations at 10 $cm^3$/min in Case 2.

Total CPU time and speedup ratios are compared at injection rate of 1 $cm^3$/min in Figure 7.23. The speedup ratio is 2.12 when the processor number is 4, which implies about 47.2% of CPU time is needed compared with the case using a single processor. The

speedup ratio is 2.39 when the processor number is 8, which implies about 41.8% of CPU time is needed compared with the case using a single processor. The speedup ratio is 2.50 when the processor number is 12, which implies about 40.0% of CPU time is needed compared with the case using a single processor. The speedup ratio is 2.58 when the processor number is 16, which implies about 38.7% of CPU time is needed compared with the case using a single processor. The speedup ratio is 2.62 when the processor number is 20, which implies about 38.2% of CPU time is needed compared with the case using a single processor. CPU time spent on geochemical calculations and corresponding speedup ratios are also compared in Figure 7.24. For the case using a single processor, geochemical calculations take up about 68% of the total CPU time. The speedup ratio is 4.48 when the processor number is 4, which implies about 22.3% of CPU time is needed for geochemical calculations compared with the case using a single processor. The speedup ratio is 8.03 when the processor number is 8, which implies about 12.5% of CPU time is needed for geochemical calculations compared with the case using a single processor. The speedup ratio is 11.16 when the processor number is 12, which implies about 9.0% of CPU time is needed for geochemical calculations compared with the case using a single processor. The speedup ratio is 14.34 when the processor number is 16, which implies about 7.0% of CPU time is needed for geochemical calculations compared with the case using a single processor. The speedup ratio is 16.75 when the processor number is 20, which implies about 6.0% of CPU time is needed for geochemical calculations compared with the case using a single processor.

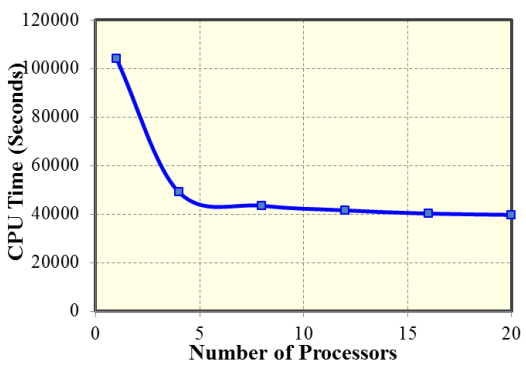


(a) CPU time

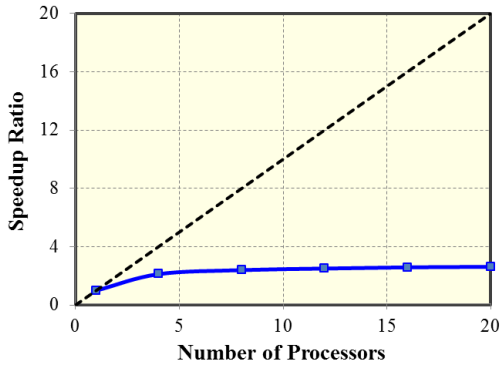


(b) Speedup ratio

Figure 7.23: Parallel performance regarding total computational time at 1 $cm^3$/min in Case 2.

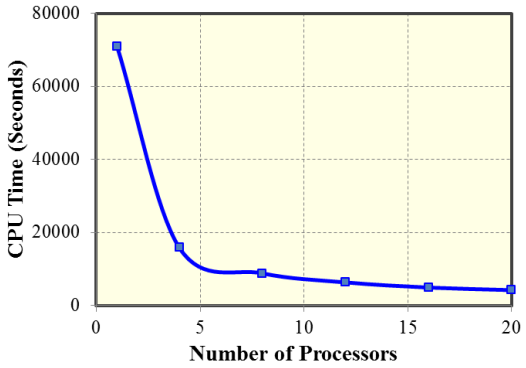


(a) CPU time

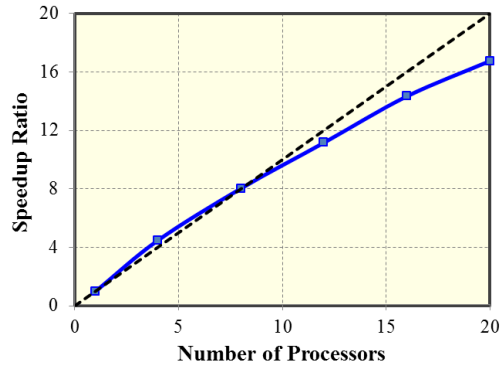


(b) Speedup ratio

Figure 7.24: Parallel performance regarding computational time spent on geochemical calculations at 1 $cm^3$/min in Case 2.

Total CPU time and speedup ratios are compared at injection rate of 0.1 $cm^3$/min in Figure 7.25. The speedup ratio is 2.19 when the processor number is 4, which implies about 45.6% of CPU time is needed compared with the case using a single processor. The speedup ratio is 2.43 when the processor number is 8, which implies about 41.1% of CPU time is needed compared with the case using a single processor. The speedup ratio is 2.57 when the processor number is 12, which implies about 39.0% of CPU time is needed compared with the case using a single processor. The speedup ratio is 2.66 when the

processor number is 16, which implies about 37.6% of CPU time is needed compared with the case using a single processor. The speedup ratio is 2.68 when the processor number is 20, which implies about 37.3% of CPU time is needed compared with the case using a single processor. CPU time spent on geochemical calculations and corresponding speedup ratios are also compared in Figure 7.26. For the case using a single processor, geochemical calculations take up about 69% of the total CPU time. The speedup ratio is 4.47 when the processor number is 4, which implies about 22.3% of CPU time is needed for geochemical calculations compared with the case using a single processor. The speedup ratio is 7.84 when the processor number is 8, which implies about 12.8% of CPU time is needed for geochemical calculations compared with the case using a single processor. The speedup ratio is 10.97 when the processor number is 12, which implies about 9.1% of CPU time is needed for geochemical calculations compared with the case using a single processor. The speedup ratio is 13.97 when the processor number is 16, which implies about 7.2% of CPU time is needed for geochemical calculations compared with the case using a single processor. The speedup ratio is 16.12 when the processor number is 20, which implies about 6.2% of CPU time is needed for geochemical calculations compared with the case using a single processor.

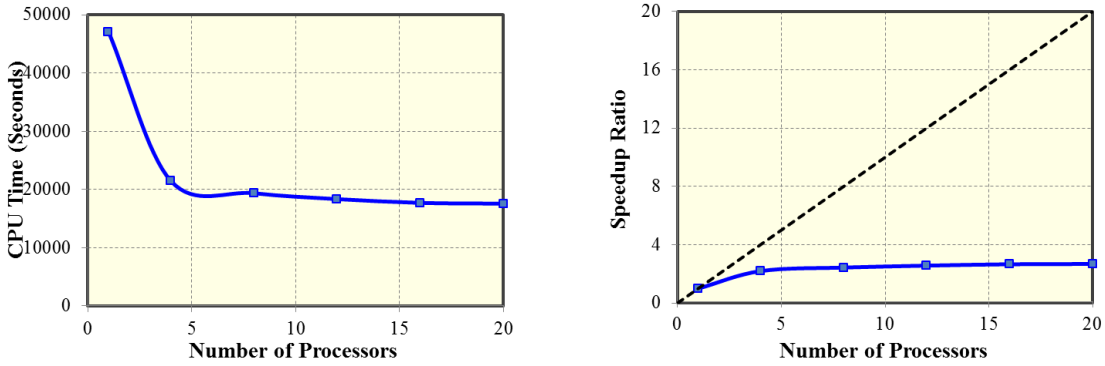


(a) CPU time (b) Speedup ratio

Figure 7.25: Parallel performance regarding total computational time at 0.1 $cm^3$/min in Case 2.

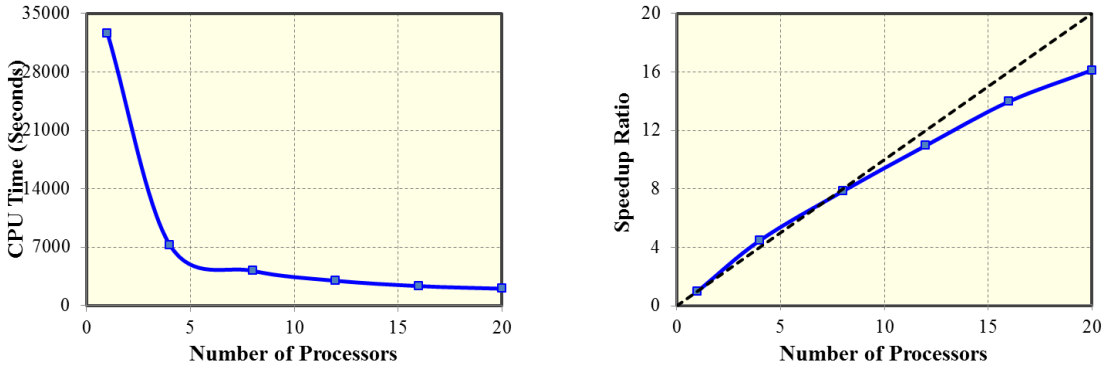


(a) CPU time (b) Speedup ratio

Figure 7.26: Parallel performance regarding computational time spent on geochemical calculations at 0.1 $cm^3$/min in Case 2.

Total CPU time and speedup ratios are compared at injection rate of 0.01 $cm^3$/min in Figure 7.27. The running time when using a single processor is longer than 48 hours which is the limit for jobs on TACC. So the processor number ranges from 4 to 20 and the reference case for calculation of the speedup ratio is the case using 4 processors. The speedup ratio is 4.46 when the processor number is 8, which implies about 89.6% of CPU time is needed compared with the case using 4 processors. The speedup ratio is 4.65 when the processor number is 12, which implies about 86.0% of CPU time is needed

compared with the case using 4 processors. The speedup ratio is 4.76 when the processor number is 16, which implies about 84.0% of CPU time is needed compared with the case using 4 processors. The speedup ratio is 4.82 when the processor number is 20, which implies about 82.9% of CPU time is needed compared with the case using 4 processors. CPU time spent on geochemical calculations and corresponding speedup ratios are also compared in Figure 7.28. For the case using 4 processors, geochemical calculations take up about 30% of the total CPU time. The speedup ratio is 7.35 when the processor number is 8, which implies about 54.4% of CPU time is needed for geochemical calculations compared with the case using 4 processors. The speedup ratio is 10.13 when the processor number is 12, which implies about 39.5% of CPU time is needed for geochemical calculations compared with the case using 4 processors. The speedup ratio is 12.91 when the processor number is 16, which implies about 31.0% of CPU time is needed for geochemical calculations compared with the case using 4 processors. The speedup ratio is 14.95 when the processor number is 20, which implies about 26.8% of CPU time is needed for geochemical calculations compared with the case using 4 processors.

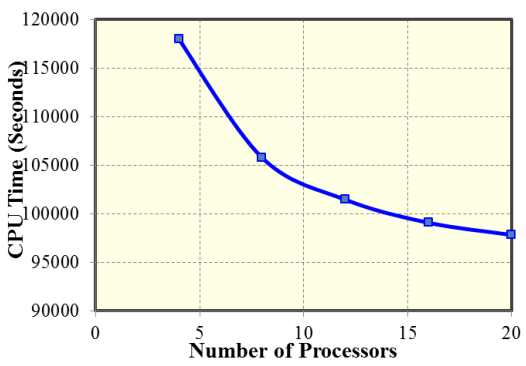


(a) CPU time

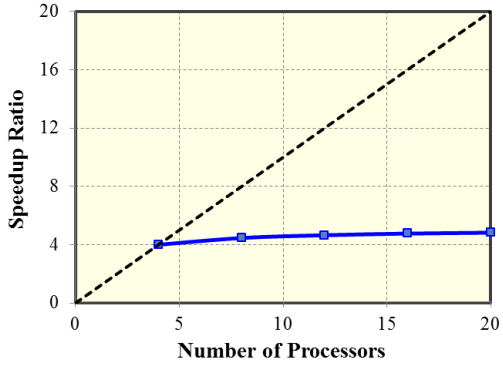


(b) Speedup ratio

Figure 7.27: Parallel performance regarding total computational time at 0.01 $cm^3$/min in Case 2.

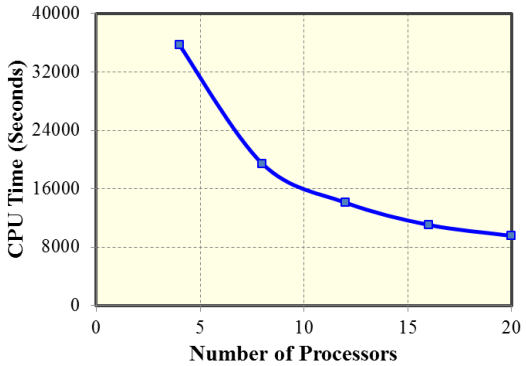


(a) CPU time

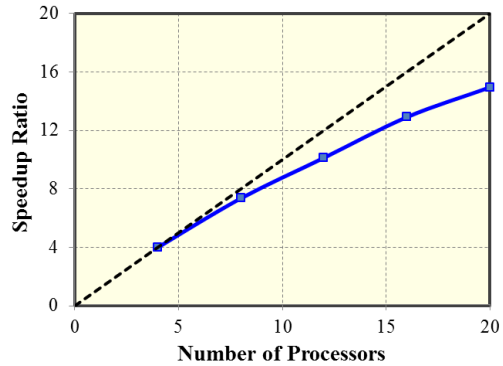


(b) Speedup ratio

Figure 7.28: Parallel performance regarding computational time spent on geochemical calculations at 0.01 $cm^3$/min in Case 2.

Among cases with different injection rates, the case with the injection rate of 10 $cm^3$/min obtains the highest parallel efficiency. When using 20 processors, 66.3% of the total computational time is saved with the speedup ratio of 2.97. Regarding the computational time spent on geochemical calculations, 94.5% of CPU time is saved with the speedup ratio of 18.19. Here we did not include the case under the injection rate of 0.01 $cm^3$/min, since CPU time when using 4 processors is used as a reference, which is different from other cases.

### 7.4.3 Speedup techniques

Two methods are used to reduce the number of IPhreeqc calls through defining a tolerance as mentioned above. When the relative amount change of all the geochemical elements in a certain grid is less than the tolerance, the geochemical calculations are neglected. The relative amount change of each geochemical component is monitored at every time-step to label each grid to determine whether an IPhreeqc call is necessary. In the first method, the relative change of each geochemical component is measured between the two consecutive time-steps. In the second method, the amount of each geochemical element at the current time-step is compared with that from the last time-step when the IPhreeqc was invoked previously. The total CPU time is plotted against the tolerance for cases using different processor numbers at the injection rate of 1 $cm^3$/min in Figure 7.29. For the cases with a single processor, the total CPU time reduces to 73.7% using the tolerance of 0.01% and to 49.3% using the tolerance of 0.4%. The CPU time spent on geochemical calculations is plotted against the tolerance for cases using different processor numbers at the injection rate of 1 $cm^3$/min in Figure 7.30. For the cases with a single processor, the CPU time spent on geochemical calculations reduces to 71.6% using the tolerance of 0.01% and to 44.4% using the tolerance of 0.4%. However, for cases with multiple processors, the speedup method does not improve much when using different tolerances. As shown in Figure 7.31, the number of active grids follows the same trend with the increasing tolerance when using different processor numbers. The reason is that through parallelization each processor is assigned a certain number of grids. If the grids for one processor are all active, other processors need to wait for it to perform geochemical calculations. The computational time is dependent on the largest active grid number among all the processors. In this way, the computational time is not reduced compared with the case with zero tolerance. The similar phenomena have been observed

in speedup performance for low salinity water injection cases (Sanaei 2019). The acidizing PVBT values for the cases using different processors and different tolerances at the injection rate of 1 $cm^3$/min are shown in Figure 7.32. The PVBT values are exactly the same when using different processor numbers with tolerance of 0 which means no speedup techniques are used. There are some differences in PVBT values when using multiple processors and speedup techniques. The largest difference is 4.1% compared with the PVBT value when using a single processor without using any speedup techniques.

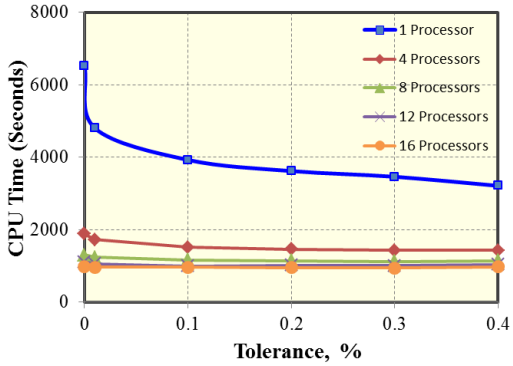


Figure 7.29: Comparison of total CPU time using the first speedup method at 1 $cm^3$/min.

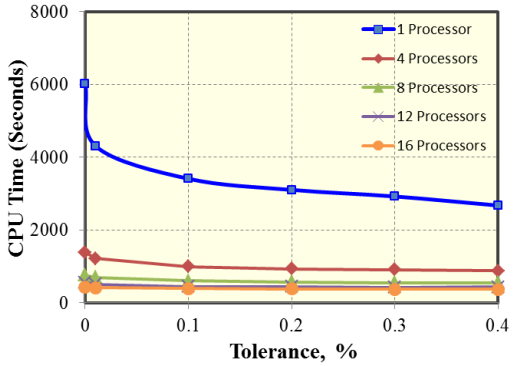


Figure 7.30: Comparison of CPU time spent on geochemical calculations using the first speedup method at 1 $cm^3$/min.

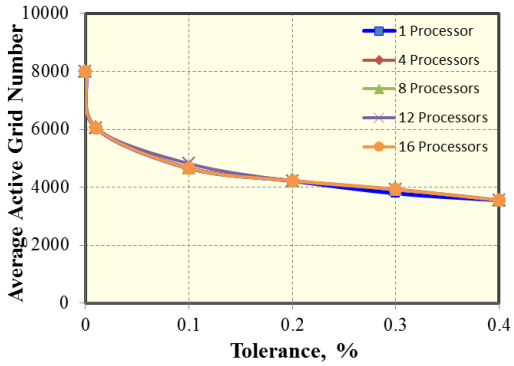


Figure 7.31: Comparison of average active grid number using the first speedup method at 1 $cm^3$/min.

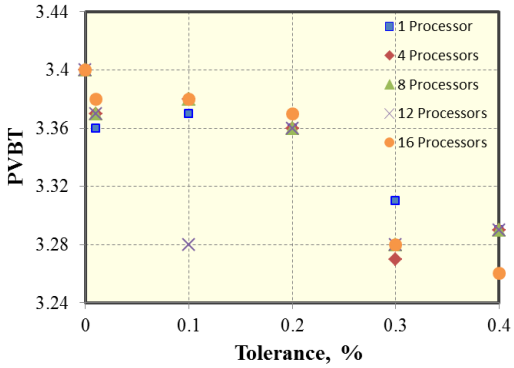


Figure 7.32: Comparison of PVBT values using the first speedup method at 1 $cm^3$/min.

The second speedup method is also applied for the case at the injection rate of 1 $cm^3$/min. The total CPU time and CPU time spent on geochemical calculations are compared in Figure 7.33 and Figure 7.34, respectively. The PVBT values are compared in Figure 7.35. The speedup performance is very similar for this case when either the first or the second speedup method is applied. For the single-processor cases, the total CPU time reduces to 76.7% with the tolerance of 0.01% and reduces to 54.2% with the tolerance of 0.4%, CPU time spent on geochemical calculations reduces to 74.8% with the tolerance of 0.01% and reduces to 50.0% with the tolerance of 0.4%. The PVBT

maintains the accuracy above 96.1% among the cases using different processor numbers and different tolerances.

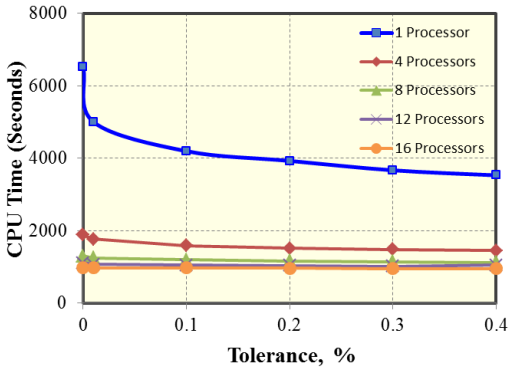


Figure 7.33: Comparison of total CPU time using the second speedup method at 1 $cm^3$/min.

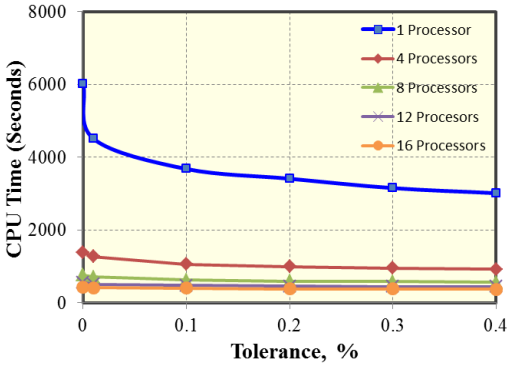


Figure 7.34: Comparison of CPU time spent on geochemical calculations using the second speedup method at 1 $cm^3$/min.

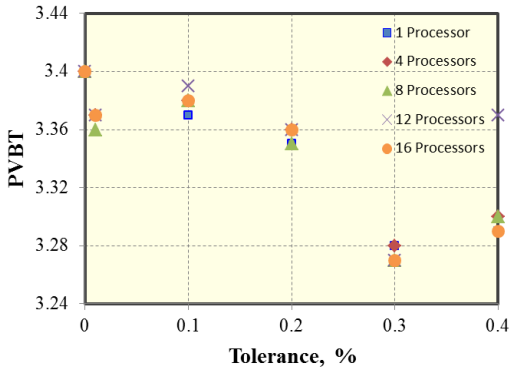


Figure 7.35: Comparison of PVBT values using the second speedup method at 1 $cm^3$/min.

When the IPhreeqc call is necessary in a grid, the grid is defined as an active grid. The number of active grids represents the geochemical computational amount which is proportional to the computational time. The active grid numbers are compared when using a single processor and different tolerances using the first speedup method in Figure 7.36. For the case without using the speedup technique, the active grid number remains the same as shown in Figure 7.36(a). When using a non-zero tolerance, as shown in Figure 7.36(b)-(f), the active grid number changes as the injected acid flows into the domain. The number of active grids is initialized to be equal to the total grid number and adjusted in every time-step based on the relative amount change of geochemical components. During the initial period, as acid spreads into the domain, the active grid number increases until IPhreeqc calls are required for every grid based on the defined tolerance. After the initial buildup period, there is a stable period during which the active grid number remains the same as the total grid number. After the stable period, the active grid number starts to decrease until the breakthrough time. Taking the tolerance of 0.01% for example, active grid distributions at different periods are presented in Figure 7.37. In the initial periods shown in Figure 7.37(a)-(b), the active grid number changes as acid

injection is accumulated. In the stable period shown in Figure 7.37(c), the active grid number remains the same as the total grid number. From the point as shown in Figure 7.37(d), the active grid number starts to shrink as the wormhole propagates from the inlet to the outlet. The corresponding porosity distributions from this point are shown in Figure 7.38. The active grid distributions for the breakthrough time are compared for the tolerance of 0.01% and 0.1% in Figure 7.39. The distribution of active grids is consistent with the dissolution structure as shown in Figure 7.38. The larger tolerance neglects more geochemical calculations in the transitional region between wormhole and the remaining parts of the domain.

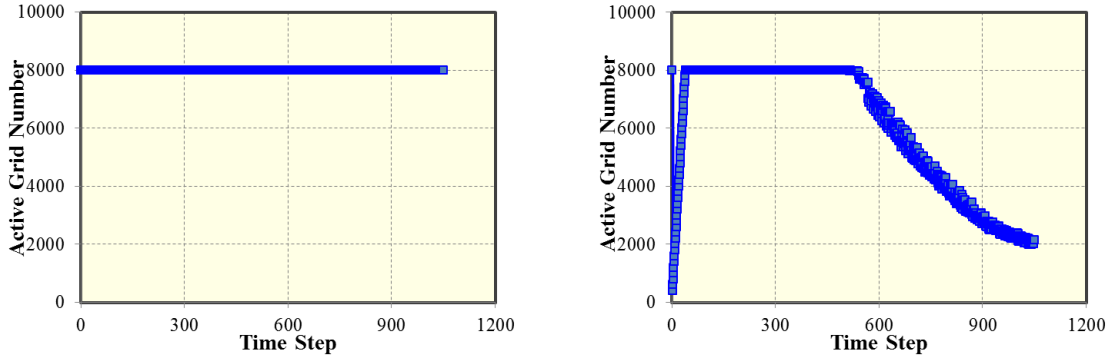


(a) Tolerance of 0




(b) Tolerance of 0.01%

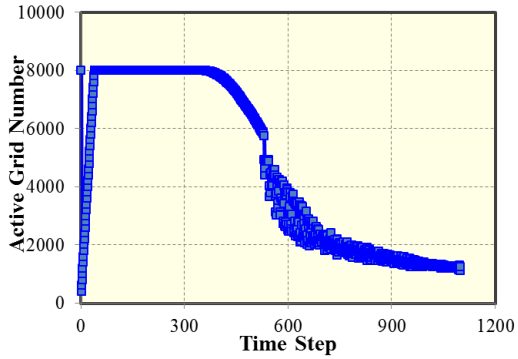


(c) Tolerance of 0.1%

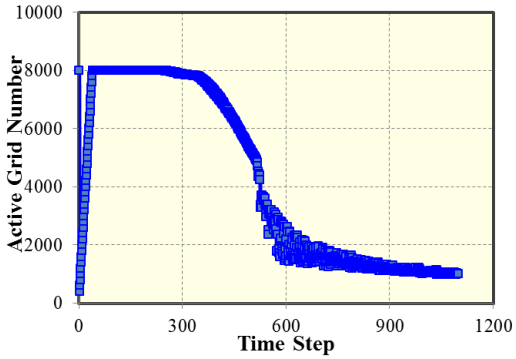


(d) Tolerance of 0.2%

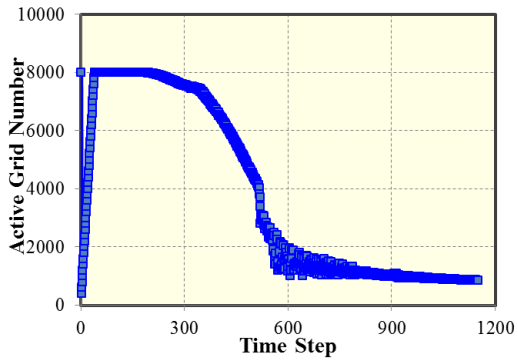


(e) Tolerance of 0.3%

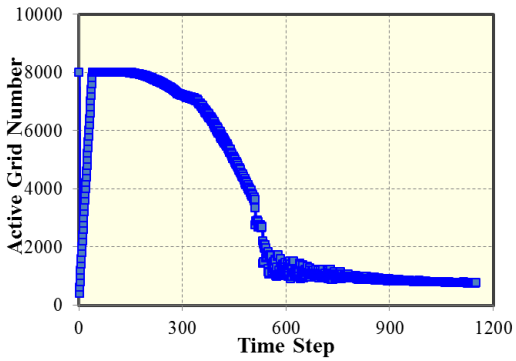


(f) Tolerance of 0.4%

Figure 7.36: Comparison of active grid numbers using a single processor and different tolerances using the first speedup method at 1 $cm^3$/min.

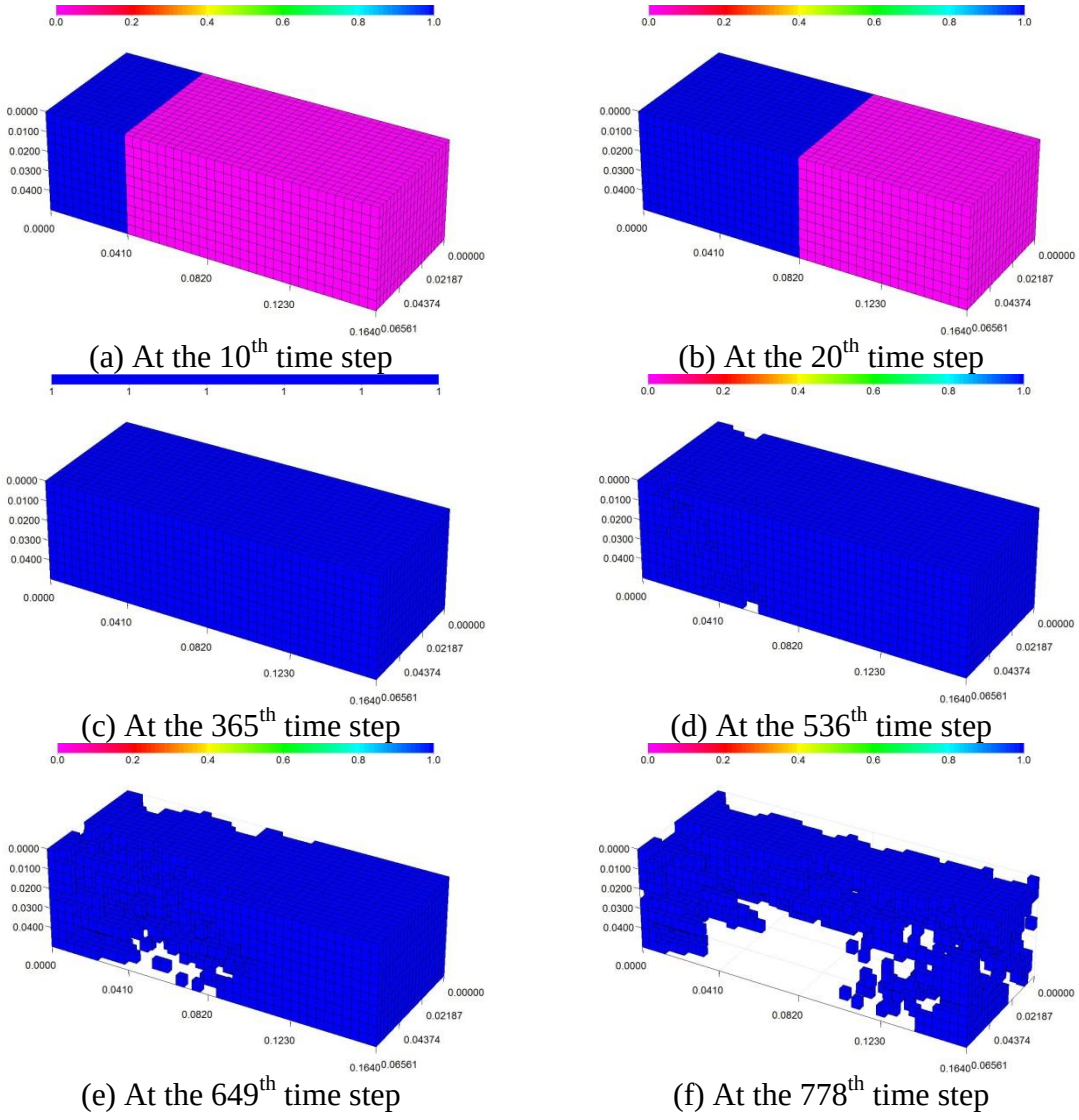


(a) At the 10th time step

(b) At the 20th time step

(c) At the 365th time step

(d) At the 536th time step

(e) At the 649th time step

(f) At the 778th time step

Figure 7.37: Active grids at different times using a single processor and tolerance of 0.01% at 1 $cm^3$/min.

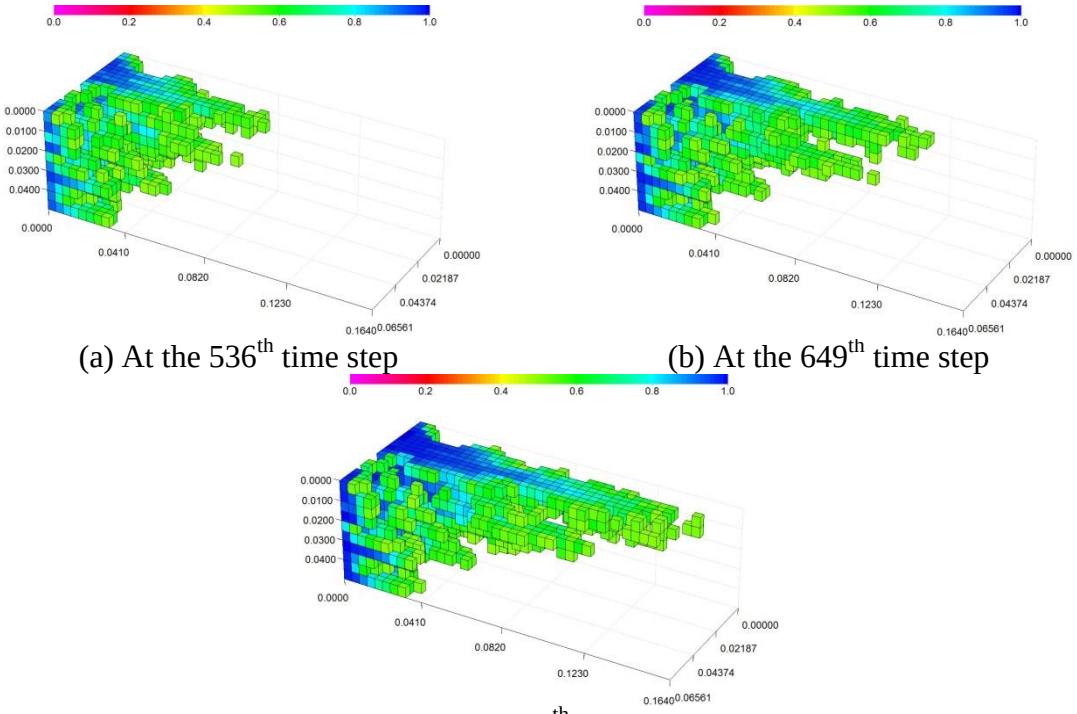


(a) At the 536th time step (b) At the 649th time step

(c) At the 778th time step

Figure 7.38: Porosity distributions at different times using a single processor and tolerance of 0.01% at 1 $cm^3$/min.

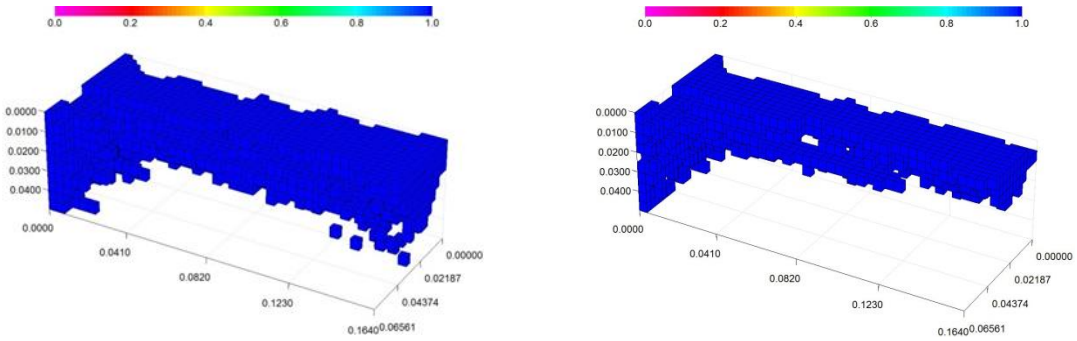


(a) Tolerance of 0.01% (b) Tolerance of 0.1%

Figure 7.39: Active grids at breakthrough using a single processor and different tolerances at 1 $cm^3$/min.

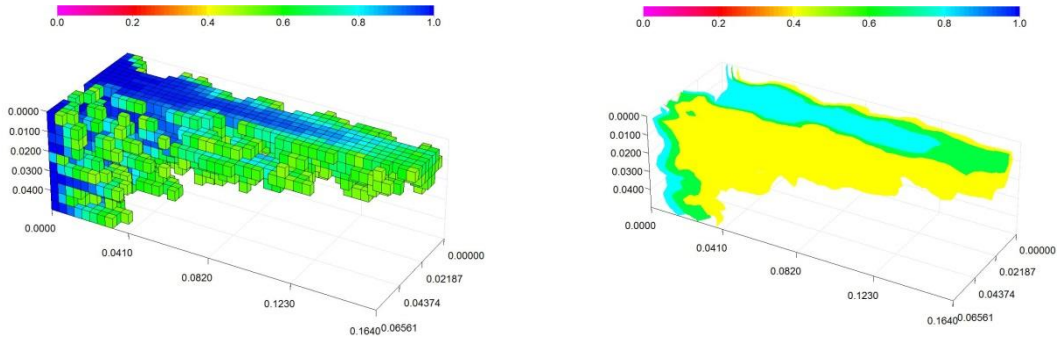


(a) Porosity above 0.5 (b) Porosity iso surface

Figure 7.40: Dissolution structure under the injection rate of 1 $cm^3$/min.

For the heterogeneous matrix, under some optimal injection rates, acid chooses to flow into high-perm region and the dissolution happens in a localized volume. This leads to the situation where the amount change of geochemical components is relatively large in the localized volume while that in the other parts of the domain is negligible. However, when the injection rate is large enough to generate the uniform pattern, acid flows everywhere and dissolves the minerals in the whole domain, and the amount change of geochemical components is hard to distinguish by regions using a tolerance. The speedup performance is unsatisfactory under such circumstances. The total CPU time and CPU time spent on geochemical calculations are compared using a single processor and different tolerances at the injection rate of 10 $cm^3$/min in Figure 7.41. The total CPU time only reduces 2.3% using the tolerance of 0.06% compared with the case without using speedup techniques. The CPU time spent on geochemical calculations only reduces 2.5% using the tolerance of 0.06% compared with the case without using speedup techniques. When the tolerance is increased further, the computational time increases due to the difference in total injection time until breakthrough. The tolerance above 0.06% causes a discrepancy on the acidizing PVBT values as shown in Figure 7.42. When the tolerance is increased to 0.08%, the accuracy decreases to 92% compared with the case using

tolerance of zero. The active grid numbers are shown for the case using the tolerance of 0.06% in Figure 7.43. There are only buildup period and stable period on the curve of active grid number. The number smaller than the total grid number near the breakthrough time is due to the reason that a smaller time-step size is forced to be used to generate distribution data at a specified time. The small time-step size changes the amount of geochemical components in some grids slightly enough to escape some calculations.

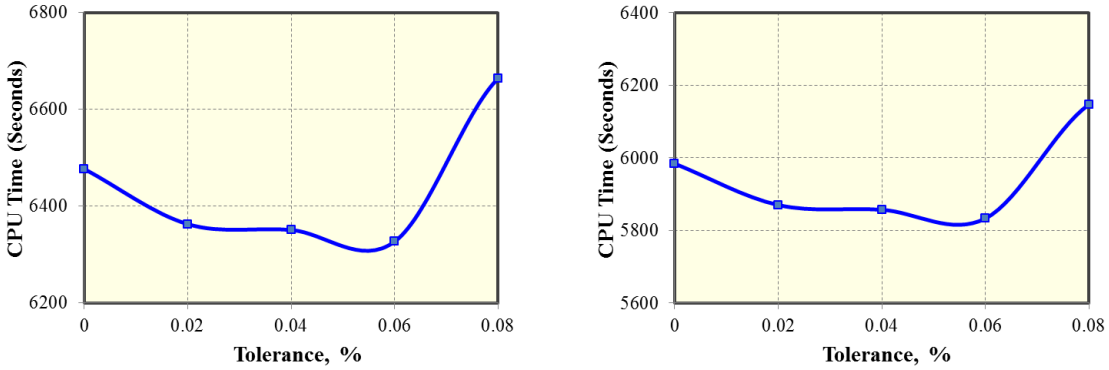


(a) Total CPU time

(b) CPU time spent on geochemical calculations

Figure 7.41: Comparison of CPU time using the first speedup method at 10 $cm^3$/min.

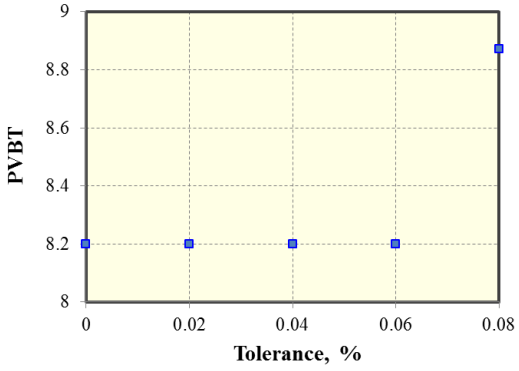


Figure 7.42: Comparison of PVBT values using the first speedup method at 10 $cm^3$/min.

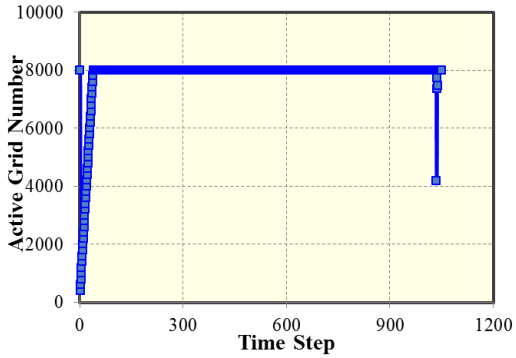


Figure 7.43: Active grid numbers using a single processor and tolerance of 0.06% using the first speedup method at 10 $cm^3$/min.

## 7.5 CONCLUSIONS

The main objective of this chapter is to evaluate computational efficiency of acidizing simulation using UTCOMP-IPhreeqc with the parallelized geochemical calculations (Korrani 2014) and speedup methods (Sanaei 2019). The parallel performance is evaluated through running acidizing simulation cases using a single processor and using multiple processors on TACC. The speedup performance is evaluated and analyzed through running acidizing simulation cases using different tolerances. Based on the simulation studies, the following conclusions can be drawn:

- The semi-parallel version of UTCOMP-IPhreeqc model improves the computational efficiency when using multiple processors compared with using a single processor. The parallel performance shows sub-linear speedup when comparing total CPU time for cases using different injection rates. The speedup ratio is closer to linear speedup for the CPU time spent on geochemical calculations than the total CPU time.
- Among cases with different injection rates in Case 1, the case with the injection rate of 1 $cm^3$/min obtains the highest parallel efficiency. When using 16

processors, 85.0% of the total computational time is saved with the speedup ratio of 6.69, while 93.0% of the computational time spent on geochemical calculations is reduced with the speedup ratio of 14.21.

- Among cases with different injection rates in Case 2, the case with the injection rate of 10 $cm^3$/min obtains the highest parallel efficiency. When using 20 processors, 66.3% of the total computational time is saved with the speedup ratio of 2.97. Regarding the computational time spent on geochemical calculations, 94.5% of CPU time is saved with the speedup ratio of 18.19.
- Overall, parallel performance is better regarding CPU time spent on geochemical calculations for the case with a larger number of total grids. However, the parallel performance regarding total CPU time is not guaranteed to be better because it is also dependent on the time proportion of geochemical calculations in total computational time.
- When using a single processor, the speedup methods achieve best speedup performance for wormhole pattern and very poor speedup performance for uniform pattern. The two types of speedup methods achieve similar speedup performance for wormhole pattern.
- When using multiple processors, the speedup methods achieve poor speedup performance. It indicates combining parallel processing and speedup methods do not lead to superposition effects on computational efficiency in acidizing cases.

# CHAPTER 8: SANDSTONE ACIDIZING SIMULATION BASED ON UTCOMP-IPHREEQC

Similar as carbonate acidizing, sandstone acidizing aims at improving productivity to minimize the near-wellbore damage through mineral dissolution. The mineral compositions in sandstone formation may include quartz, clays, feldspars, carbonates, and ion-based minerals (Nasr-El-Din et al. 2007). In normal practice, mud acid composed of hydrochloric acid (HCl) and hydrofluoric acid (HF) is used in sandstone acidizing. Compared with carbonate acidizing, sandstone acidizing involves more complex reactions, including both dissolution and precipitation. Mineral dissolution increases porosity and permeability, while mineral precipitation decreases porosity and permeability. Mineral compositions and the injected acid solution are defined through IPhreeqc input file, while kinetic reactions of mineral dissolution and mineral precipitation are defined through IPhreeqc database. In this chapter, sandstone acidizing process is simulated using UTCOMP-IPhreeqc.

## 8.1 INTRODUCTION

Reactions between mud acid and minerals in sandstone are complex. There are different models developed mathematically to simulate sandstone acidizing, including lumped-parameter model, two-parameter model, four-parameter model, and detailed geochemistry model.

The lumped-parameter model simplifies all the reactions into a single reaction. Williams and Whiteley (1971) developed a model to predict porosity distribution during sandstone acidizing. The reaction rate used in the model was obtained from core-flood experiments. The reaction rate was found to be first-order with HF concentration and vary with temperature. McCune et al. (1975) developed a practical procedure to apply

laboratory results to acidizing field designs. They described the method on how to identify the reaction front through laboratory tests, establish a mathematical model describing the front, and then apply the model to the radial flow geometry around the wellbore. Based on the procedure, parameter values in radial flow modeling were determined through laboratory data of linear flow to facilitate acidizing field design near the wellbore. Fogler et al. (1976) conducted theoretical and experimental analyses in acidizing, based on sandstone cores. They used a lumped-parameter model to predict acid movement and permeability changes in sandstone cores as a function of acid concentration and flow rate.

In the two-parameter model, minerals are grouped into two types including fast-reacting types (feldspar and clay) and slow-reacting types (quartz), based on the difference on dissolution rates. Hekim et al. (1982) developed a distributed parameter model for radial flow to consider different reaction rates of minerals. The model was used to describe the separation of reaction fronts between more soluble minerals and less soluble quartz. Taha et al. (1986) developed a numerical simulator to predict the change of well productivity during sandstone acidizing. They took into consideration the permeability contrast between non-communicating layers. They also modeled the effect of organic resin diverting agents on vertical fluid distribution. Lea et al. (1992) applied the two-parameter model to simulate sandstone acidizing in a single perforation. They modeled the single-phase flow through a perforation in the sandstone formation which is composed of two pseudo-chemical minerals with different dissolution rates.

In the four-parameter model, a secondary reaction which generates hydrated silica is considered. The model gives a better prediction of porosity change compared with the lumped-parameter model and the two-parameter model. Bryant (1991) introduced an improved model to include the reaction between $H_2SiF_6$ and aluminosilicates. The

improved model was more reliable to extrapolate laboratory data to different operating conditions and simulate well treatments. Hsi et al. (1993) validated the improved model with more laboratory core-flood tests using different sandstone cores, different acid injection rates, and different acid concentrations. Li et al. (2005) developed a model to simulate sandstone acidizing in order to investigate the effect of fine-scale heterogeneities considering both dissolution and precipitation. The acid penetration was found to be much deeper with the presence of small-scale heterogeneities compared with the homogeneous matrix.

In the detailed geochemistry model, mineral compositions are considered more comprehensively. Sevougian et al. (1995) developed a geochemical simulator to model the reactive transport process which involves any number of chemical species. The model included kinetic and equilibrium reactions and was used to predict the optimal acid injection rate in sandstone acidizing. Liu et al. (1997) developed a two-dimensional geochemical simulator with built-in thermodynamic and kinetic database. They obtained good agreement with laboratory sandstone acidizing results. Li et al. (1998) developed a geochemical model considering two types of acids and eight types of minerals. All the possible reactions were solved simultaneously to consider mineral dissolution and precipitation. Ziauddin et al. (1999) developed a geochemical model and resolved the sandstone mineralogy into eight minerals. The model was validated against several sandstone experiments with different injection rates and temperatures.

In this chapter, the application of UTCOMP-IPhreeqc is extended from carbonate acidizing to sandstone acidizing. PHREEQC database includes a wide range of equilibrium reactions among minerals and species in the aqueous phase. It also provides a kinetic formulation that facilitates modeling of non-equilibrium mineral dissolution and precipitation. The mineral compositions of sandstone include quartz, clays such as

kaolinite and illite, alkaline aluminosilicates such as feldspars and zeolites, carbonates such as calcite and dolomite, iron-based minerals such as hematite and pyrite (Nasr-El-Din et al. 2007). All these minerals react with acid with different reaction rates. Besides mineral dissolution, precipitation occurs in the secondary reaction and in the tertiary reaction. In the secondary reaction, fluorosilicic acid reacts with aluminosilicates to generate hydrated silica. In the tertiary reaction, aluminum fluoride reacts with aluminosilicates to generate silica gel. However, due to lack of detailed kinetic data for reactions between acid and each type of minerals, in current work, only two representative minerals (slow-reacting quartz and fast-reacting kaolinite) are considered in the sandstone mineralogy. Dissolution of quartz and kaolinite mineral from primary reactions and precipitation of hydrated silica from secondary reaction are included.

## 8.2 METHODOLOGY

### 8.2.1 Model description

Sandstone acidizing is simulated through UTCOMP-IPhreeqc based on the two-scale continuum model. In Darcy-scale model, pressure equation, mass conservation equation of each geochemical element, and pore evolution equation need to be solved. In pore-scale correlations, Darcy-scale parameters vary with the porosity change. The difference is that more complex reactions are involved due to different mineral compositions and different acids used compared with carbonate acidizing.

### 8.2.2 Permeability-porosity correlations

Different permeability-porosity correlations have been used to predict the permeability based on porosity change for sandstones. Labrid (1975) proposed a correlation relating permeability with porosity:

$$\frac{K}{K_0} = \left( \frac{\varphi}{\varphi_0} \right)^b , \tag{8.1}$$

where $b$ is close to 3 for the acidizing process.

McCune et al. (1975) suggested a correlation between permeability and porosity with an experimentally determined constant $n$ :

$$\frac{K}{K_0} = \exp\left[ n\left(\varphi - \varphi_0\right) \right]. \tag{8.2}$$

Walsh and Brace (1984) proposed the correlation

$$\frac{K}{K_0} = \frac{s_0{}^2 \varphi^2}{s^2 \varphi_0{}^2}, \tag{8.3}$$

where $s_0$ is the specific surface area at the initial condition, $s$ is the specific surface area at the predicted time.

Mou et al. (2019) used the following correlation in the simulation:

$$\frac{K}{K_0} = \frac{\varphi}{\varphi_0} \left( \frac{\varphi\left(1-\varphi_0\right)}{\varphi_0\left(1-\varphi\right)} \right)^{2\beta} . \tag{8.4}$$

In the following simulation cases, Eq. 8.4 is used to update permeability during sandstone acidizing. Using different correlations will affect the permeability estimation and the productivity prediction. The permeability-porosity correlation is a characteristic of rocks and needs to be matched with experimental data for a specific sandstone formation.

## 8.3 SIMULATION STUDIES OF CORE-SCALE SAMPLES

In this section, simulation cases for sandstone acidizing of core-scale samples are presented. The sandstone samples are assumed to be homogeneous and 1D simulation results along the core length are presented. The parameters used in the simulation of core-scale sandstone acidizing are listed in Table 8.1. The grid information is listed in Table 8.2. The commonly used acid is mud acid which is a mixture of HF and HCl.

| Parameter | Value | Unit | Parameter | Value | Unit |
|---|---|---|---|---|---|
| $x_l$ | 2.04 | in | $T$ | 180.0 | °F |
| $y_l$ | 0.89 | in | $\beta$ | 1.0 | - |
| $z_l$ | 0.89 | in | $r_{p0}$ | 1.0 | μm |
| $\varphi_0$ | 0.08 | - | $D_m$ | $3.6\times10^{-9}$ | $m^2/s$ |
| $K_0$ | 51.0 | mD | $\alpha_{os}$ | 0.5 | - |
| $p_i$ | 1000.0 | psi | $\lambda_L$ | 0.5 | - |
| $\mu_w$ | 1.0 | cp | $\lambda_T$ | 0.1 | - |

Table 8.1: Parameters used in the simulation of core-scale sandstone acidizing.

| Parameter | | Value | Unit |
|---|---|---|---|
| No. of gridblocks | | 100 (100×1×1) | - |
| $\Delta x$ | | 0.0204 | in |
| Permeability | $x$ direction | 51 | mD |
| Porosity | | 0.08 | - |

Table 8.2: Grid information in the simulation of core-scale sandstone acidizing.

### 8.3.1 Base case

The acid injected in the base case is mud acid which is composed of 3% HF and 12% HCl. The mineral compositions in the sandstone sample in the base case include quartz with a volume ratio of 89% and kaolinite with a volume ratio of 11%. The porosity profile after injecting 10 PVs (pore volumes) of mud acid is shown in Figure 8.1. For the whole length of the sandstone sample, porosity increases due to rock dissolution. Major constituents of a sandstone sample include quartz and clays. Kaolinite is one of the clay minerals in sandstone formations and is used to represent clays in the following simulation cases. After supplementing kinetic reactions between acid and each type of clay minerals in the PHREEQC database, more comprehensive modeling of sandstone

acidizing may be realized. Dissolution of kaolinite with HF is much faster than dissolution of quartz with HF. Compared with HF, HCl is considered not to react with clays. However, HCl is necessary since some sandstone formations may contain calcite and HCl is also used to maintain a low pH value improving the dissolution power of HF.

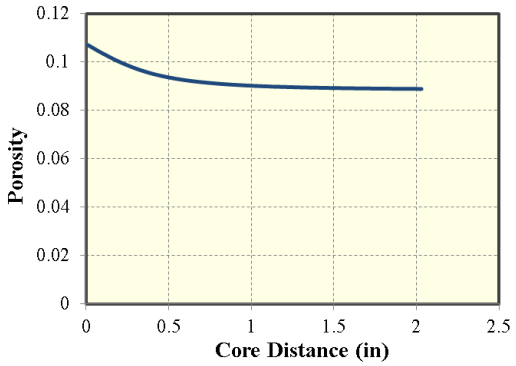


Figure 8.1: Porosity profile after injecting 10 PVs of mud acid in the base case.

Volume fractions of minerals in the whole volume of the sandstone matrix are presented in Figure 8.2. The volume fraction of quartz is not included in the figure since no significant amount of quartz is dissolved during sandstone acidizing. Mostly the porosity increase is due to dissolution of clays. During sandstone acidizing, secondary reaction produces precipitation of hydrated silica, which decreases porosity.

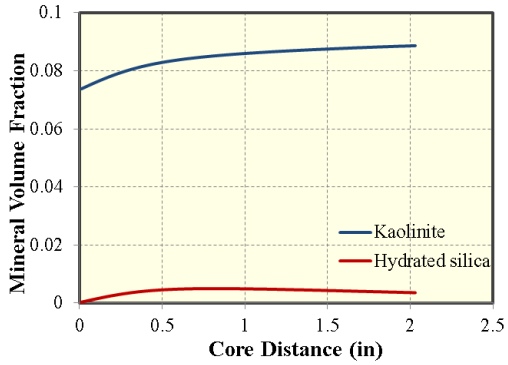


Figure 8.2: Mineral volume fraction profile after injecting 10 PVs of mud acid in the base case.

The permeability is calculated based on pore-scale correlations which relate permeability with porosity. The permeability profile is shown in Figure 8.3. The permeability improvement increases the productivity/injectivity of the sandstone sample.

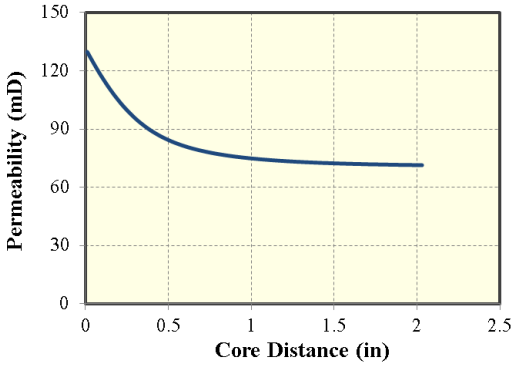


Figure 8.3: Permeability profile after injecting 10 PVs of mud acid in the base case.

The productivity/injectivity improvement will reduce the pressure drop between inlet and outlet of the sandstone sample. The dimensionless BHP (bottomhole pressure) is shown in Figure 8.4. The pressure drop decreases after 10 PVs of acid injection due to rock dissolution.

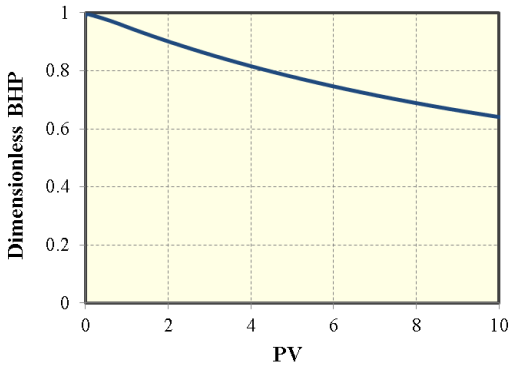


Figure 8.4: Dimensionless BHP profile after injecting 10 PVs of mud acid in the base case.

### 8.3.2 Effect of mineral compositions

In this section, sandstone samples with different mineral compositions are compared. The mineral compositions in three cases are 78% quartz and 22% kaolinite, 83% quartz and 17% kaolinite, 89% quartz and 11% kaolinite, respectively. The comparison of porosity profiles is shown in Figure 8.5. The sandstone sample with a larger volume ratio of kaolinite obtains better porosity improvement along the entire core length.

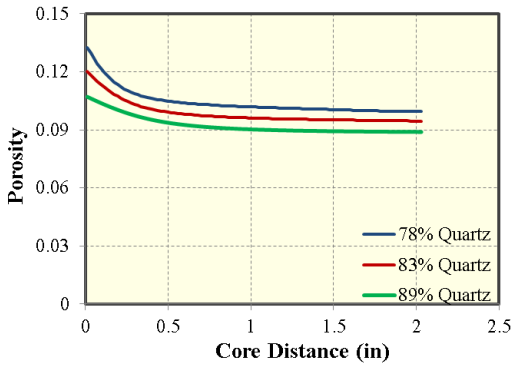


Figure 8.5: Comparison of porosity profiles after injecting 10 PVs of mud acid regarding mineral compositions.

The comparison of kaolinite volume fraction profiles is shown in Figure 8.6. For the sandstone sample with 78% quartz, the initial volume fraction of kaolinite in the entire matrix volume is 0.2024. For the sandstone sample with 83% quartz, the initial volume fraction of kaolinite in the entire matrix volume is 0.1564. For the sandstone sample with 89% quartz, the initial volume fraction of kaolinite in the entire matrix volume is 0.1012. The dissolution of kaolinite occurs along the entire core length, with more dissolution near the inlet. For sandstone samples with a larger volume ratio of kaolinite, the dissolution is faster, especially near the inlet.

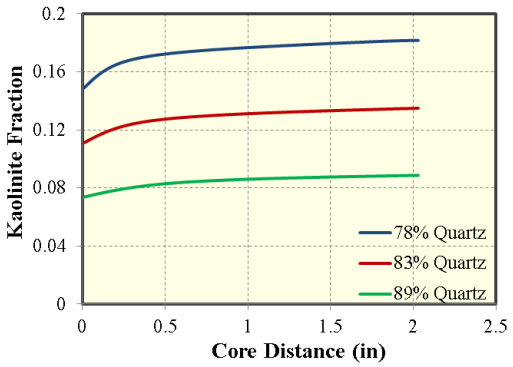


Figure 8.6: Comparison of kaolinite volume fraction profiles after injecting 10 PVs of mud acid regarding mineral compositions.

The comparison of hydrated silica volume fraction profiles is shown in Figure 8.7. Hydrated silica is precipitated during acidizing since there is no hydrated silica before acidizing. There is a peak of hydrated silica after a distance from the inlet of the sandstone sample. For sandstone samples with a smaller proportion of kaolinite, the peak of precipitation is deeper and the peak value is smaller. However, after the peak point, there is more precipitation for sandstone samples with 89% quartz.

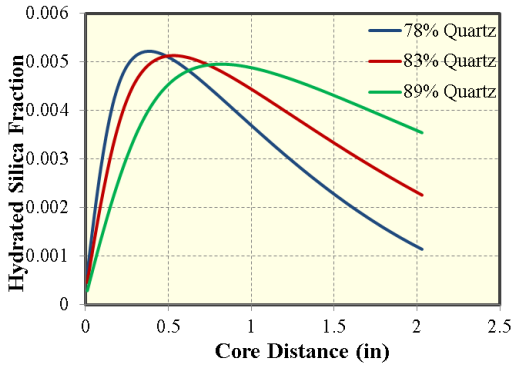


Figure 8.7: Comparison of hydrated silica volume fraction profiles after injecting 10 PVs of mud acid regarding mineral compositions.

The comparison of permeability profiles is shown in Figure 8.8. For sandstone samples with more clays, a larger proportion of mineral is able to be dissolved, the improvement of permeability and productivity/injectivity is better.

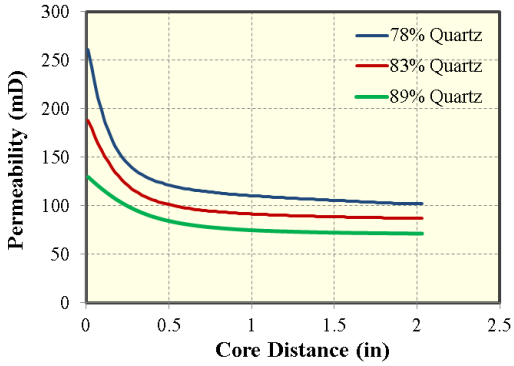


Figure 8.8: Comparison of permeability profiles after injecting 10 PVs of mud acid regarding mineral compositions.

To compare the productivity increase, the comparison of dimensionless bottomhole pressure profiles is shown in Figure 8.9.

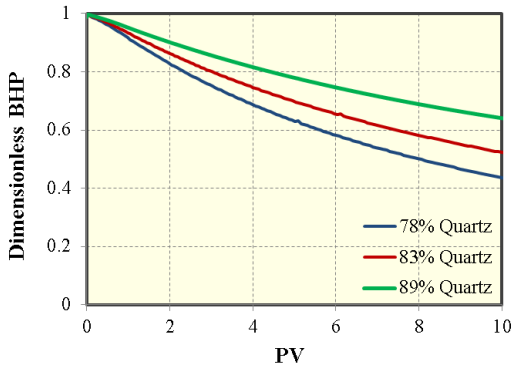


Figure 8.9: Comparison of dimensionless BHP profiles after injecting 10 PVs of mud acid regarding mineral compositions.

### 8.3.3 Effect of HF concentration

In this section, different HF concentrations are used in the sandstone sample with 89% quartz. HF concentration varies from 3% to 5% while HCl concentration remains the same as 12%. The comparison of porosity profiles is shown in Figure 8.10. The porosity improvement is better in the part near inlet but worse in the part near outlet when using a larger concentration of HF.

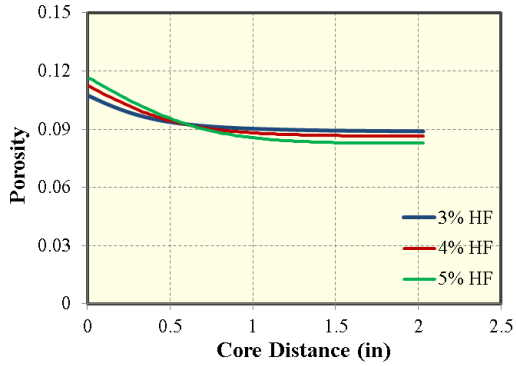


Figure 8.10: Comparison of porosity profiles after injecting 10 PVs of mud acid regarding HF concentrations.

The comparison of kaolinite volume fractions for different HF concentrations is presented in Figure 8.11. The reaction between kaolinite and HF is dependent on HF concentration. For a larger HF concentration, the kaolinite dissolution is faster along the entire core length, especially near inlet where HF concentration is the largest. This can explain the difference in the part near inlet in the porosity profile when using different HF concentrations.

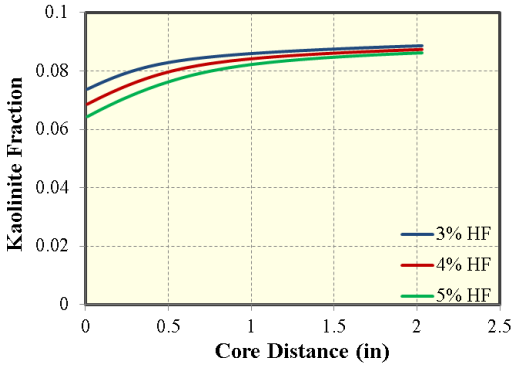


Figure 8.11: Comparison of kaolinite volume fraction profiles after injecting 10 PVs of mud acid regarding HF concentrations.

The difference in the part near outlet in the porosity profile is due to precipitation. The comparison of hydrated silica volume fractions for different HF concentrations is presented in Figure 8.12. For a larger HF concentration, reaction between kaolinite and HF generates more fluorosilicic acid which is the reactant for the secondary reaction. There is more hydrated silica precipitated when using 5% HF which leads to porosity decrease.

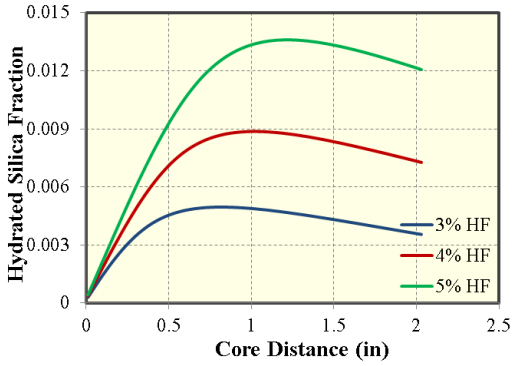


Figure 8.12: Comparison of hydrated silica volume fraction profiles after injecting 10 PVs of mud acid regarding HF concentrations.

The comparison of permeability profiles for different HF concentrations is presented in Figure 8.13. The permeability distribution is similar to the porosity profile since permeability is calculated based on porosity change.

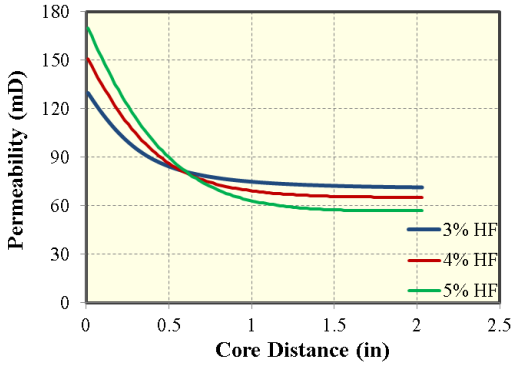


Figure 8.13: Comparison of permeability profiles after injecting 10 PVs of mud acid regarding HF concentrations.

When using a larger HF concentration, better performance is obtained near inlet and worse performance is obtained near outlet. To compare the overall performance, the comparison of dimensionless BHP is presented in Figure 8.14. For the entire length of the core, the pressure drop between inlet and outlet decreases more when using 3% HF. It

indicates for the sandstone with 89% quartz and 11% kaolinite, using 3% HF gives best acidizing performance.

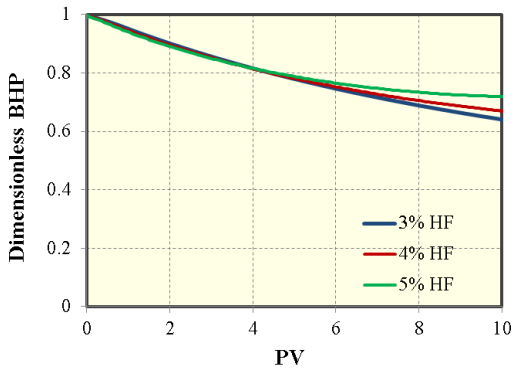


Figure 8.14: Comparison of dimensionless BHP profiles after injecting 10 PVs of mud acid regarding HF concentrations.

### 8.3.4 Effect of acid injection rate

In this section, different acid injection rates are used for the sandstone sample with 89% quartz. The comparison of porosity profiles with different acid injection rates is presented in Figure 8.15. The porosity improvement is best when using 3.3 ml/min. This is because for the same amount of acid injection, longer injection time is required when using a smaller injection rate. The longer residence time increases reaction time resulting in more dissolution.

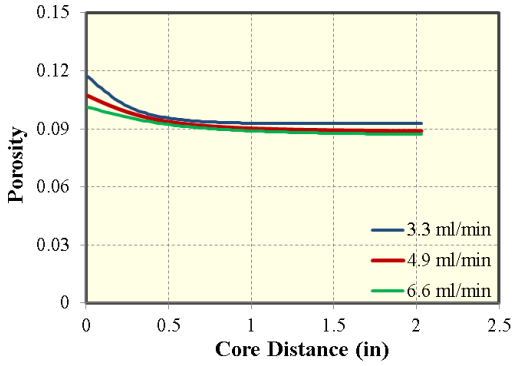


Figure 8.15: Comparison of porosity profiles after injecting 10 PVs of mud acid regarding acid injection rates.

The kaolinite volume fractions are compared for different acid injection rates in Figure 8.16. When using 3.3 ml/min, the residence time is the longest among the three cases. The longer residence time increases mineral dissolution.

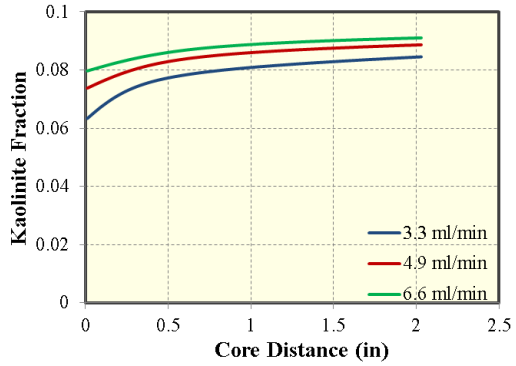


Figure 8.16: Comparison of kaolinite volume fraction profiles after injecting 10 PVs of mud acid regarding acid injection rates.

The longer residence time not only increases mineral dissolution, but also increases mineral precipitation. The hydrated silica volume fractions are compared for different acid injection rates in Figure 8.17. The peak value of precipitation occurs at a

similar position along the core, but a smaller injection time leads to more precipitation of hydrated silica.

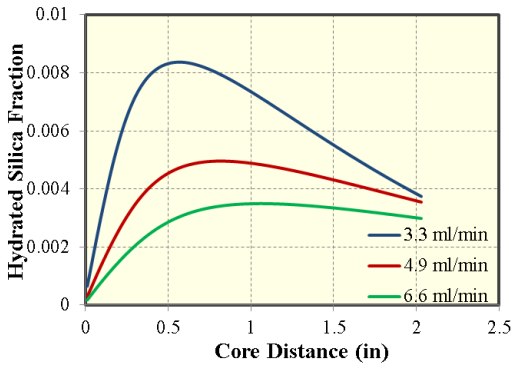


Figure 8.17: Comparison of hydrated silica volume fraction profiles after injecting 10 PVs of mud acid regarding acid injection rates.

Permeability profiles are compared for different acid injection rates in Figure 8.18. On one hand, when acid injection rate is small, acid has more time to dissolve minerals near inlet before it penetrates into the matrix further. On the other hand, a smaller injection rate leads to more precipitation of hydrated silica. So the permeability improvement near inlet is better than the part near outlet when the injection rate is 3.3 ml/min.

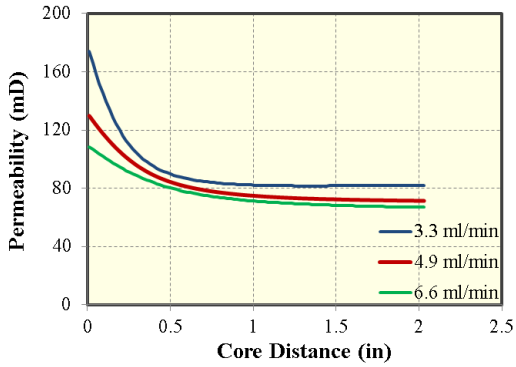


Figure 8.18: Comparison of permeability profiles after injecting 10 PVs of mud acid regarding acid injection rates.

The comparison of dimensionless BHP is presented in Figure 8.19. Based on the better improvement of porosity and permeability, 3.3 ml/min gives best productivity/injectivity improvement for the sandstone sample with 89% quartz and 11% kaolinite after 10 PVs of injection.

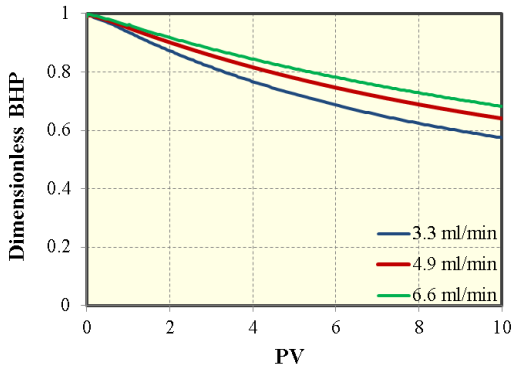


Figure 8.19: Comparison of dimensionless BHP profiles after injecting 10 PVs of mud acid regarding acid injection rates.

To further improve the productivity/injectivity, more PVs of acid needs to be injected. As more acid is injected, more dissolution and more precipitation may occur. The comparison of porosity profiles after 40 PVs of injection for different acid injection

rates is presented in Figure 8.20. After 40 PVs of injection, there is an obvious minimum point on the porosity profile when using 3.3 ml/min.

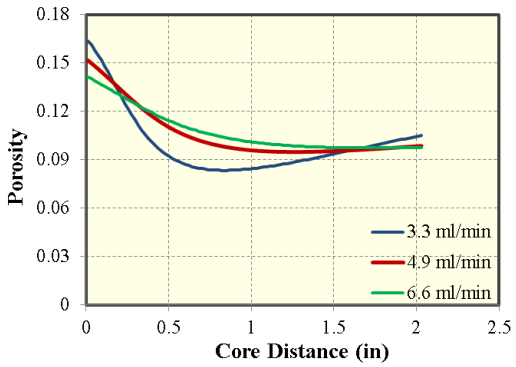


Figure 8.20: Comparison of porosity profiles after injecting 40 PVs of mud acid regarding acid injection rates.

The comparison of kaolinite volume fractions after 40 PVs of injection is presented in Figure 8.21. Compared with kaolinite dissolution after 10 PVs of injection in Figure 8.16, more kaolinite has been dissolved for different injection rates.

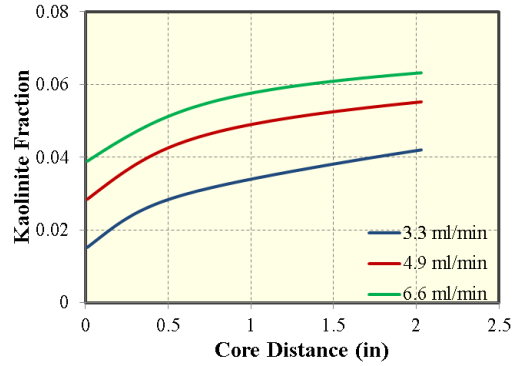


Figure 8.21: Comparison of kaolinite volume fraction profiles after injecting 40 PVs of mud acid regarding acid injection rates.

The comparison of hydrated silica volume fractions after 40 PVs of injection is presented in Figure 8.22. More dissolution of kaolinite generates more fluorosilicic acid leading to more precipitation of hydrated silica. The peak value of precipitation corresponds to the minimum value on the porosity profile in Figure 8.20 for the injection rate of 3.3 ml/min.

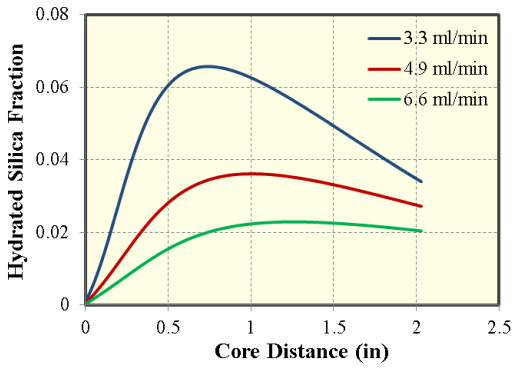


Figure 8.22: Comparison of hydrated silica volume fraction profiles after injecting 40 PVs of mud acid regarding acid injection rates.

The comparison of permeability profiles after 40 PVs of injection is presented in Figure 8.23. The permeability profile is consistent with the porosity profile.

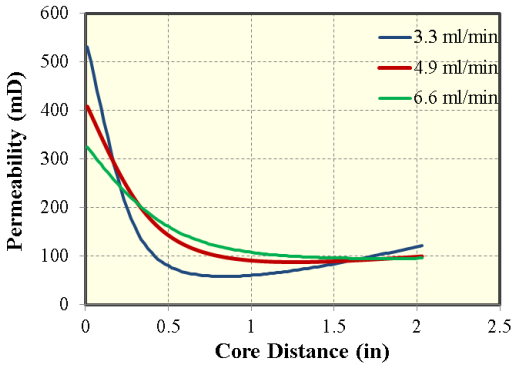


Figure 8.23: Comparison of permeability profiles after injecting 40 PVs of mud acid regarding acid injection rates.

To compare the improvement of productivity/injectivity, the comparison of dimensionless BHP after 40 PVs of injection is presented in Figure 8.24. When the injection rate is 3.3 ml/min, the dimensionless BHP decreases first, and then increases as the precipitation accumulates. The optimal injection pore volume is about 23 PVs; after 23 PVs of acid injection, the productivity/injectivity decreases instead of increasing. However, the optimum injection rate for this case is 6.6 ml/min under which the final productivity/injectivity improvement is best after 40 PVs of injection.

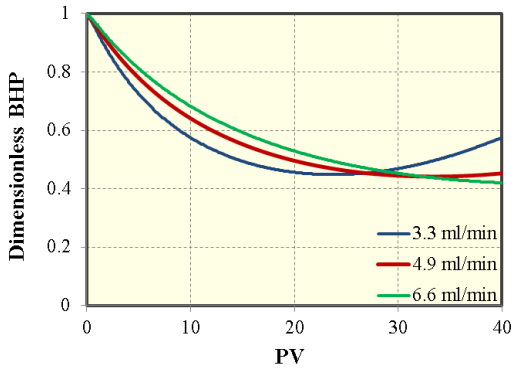


Figure 8.24: Comparison of dimensionless BHP profiles after injecting 40 PVs of mud acid regarding acid injection rates.

## 8.4 SIMULATION STUDIES OF 2D NEAR-WELLBORE SANDSTONE ACIDIZING

In this section, simulation cases for near-wellbore sandstone acidizing are presented. Parameters used in the simulation are listed in Table 8.3. The grid information is listed in Table 8.4. The injected acid is mud acid with 3% HF and 12% HCl. The sandstone formation is assumed to be composed of 89% quartz and 11% kaolinite.

| Parameter | Value | Unit | Parameter | Value | Unit |
|---|---|---|---|---|---|
| $x_l$ | 3.15 | ft | $T$ | 180.0 | °F |
| $y_l$ | 3.15 | ft | $\beta$ | 1.0 | - |
| $z_l$ | 0.15 | ft | $r_{p0}$ | 1.0 | μm |
| $\varphi_0$ | 0.08 | - | $D_m$ | $3.6\times10^{-9}$ | $m^2/s$ |
| $K_0$ | 51.0 | mD | $\alpha_{os}$ | 0.5 | - |
| $p_i$ | 1000.0 | psi | $\lambda_L$ | 0.5 | - |
| $\mu_w$ | 1.0 | cp | $\lambda_T$ | 0.1 | - |

Table 8.3: Parameters used in the simulation of near-wellbore sandstone acidizing.

| Parameter | | Value | Unit |
|---|---|---|---|
| No. of gridblocks | | 400 (20×20) | - |
| $\Delta x$ | | 0.1575 | ft |
| $\Delta y$ | | 0.1575 | ft |
| Permeability | $x$ direction | 51.0 | mD |
| | $y$ direction | 51.0 | |
| Porosity | | 0.08 | - |

Table 8.4: Grid information in the simulation of near-wellbore sandstone acidizing.

### 8.4.1 Injection rate of 70 bbl/day

The porosity and permeability distributions after 50 minutes of injection are shown in Figure 8.25, respectively. The volume ratios of kaolinite and hydrated silica in the volume of the whole matrix are presented, respectively, in Figure 8.26.

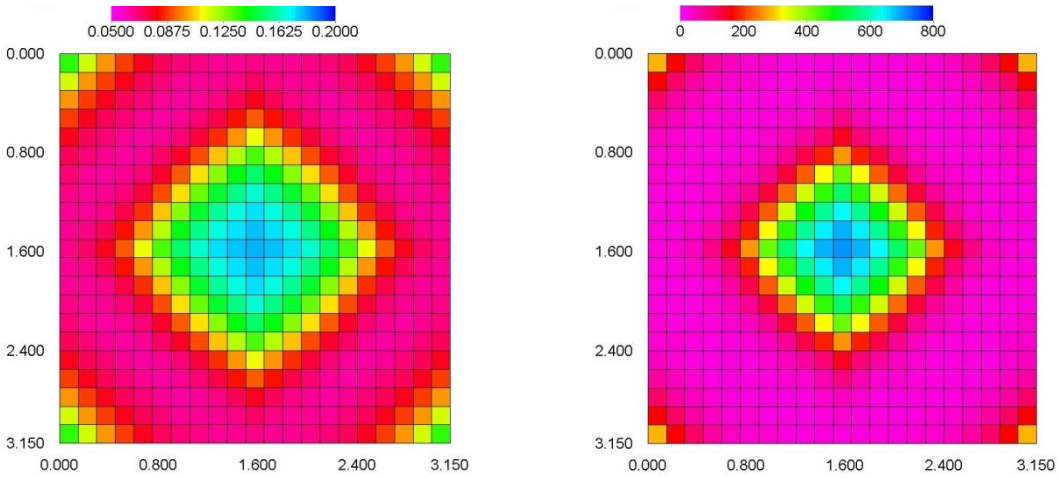


(a) Porosity (b) Permeability

Figure 8.25: Porosity and permeability distributions after injecting mud acid for 50 minutes at injection rate of 70 bbl/day.

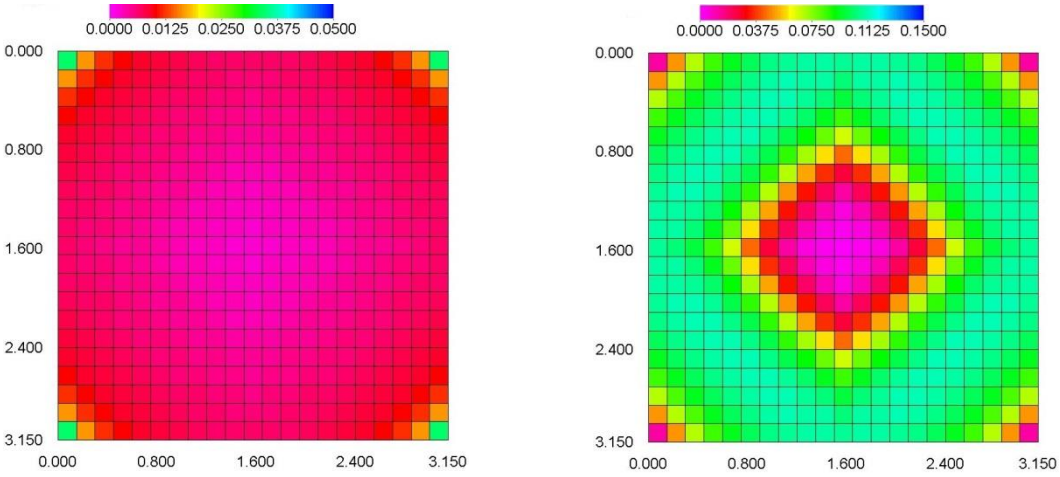


(a) Kaolinite (b) Hydrated silica

Figure 8.26: Mineral volume ratio distributions after injecting mud acid for 50 minutes at injection rate of 70 bbl/day.

### 8.4.2 Injection rate of 80 bbl/day

To inject the same acid volume, mud acid is injected for 44 minutes at an injection rate of 80 bbl/day. The porosity and permeability distributions after 44 minutes

of injection are shown in Figure 8.27. The volume ratios of kaolinite and hydrated silica in the volume of the whole matrix are presented in Figure 8.28.

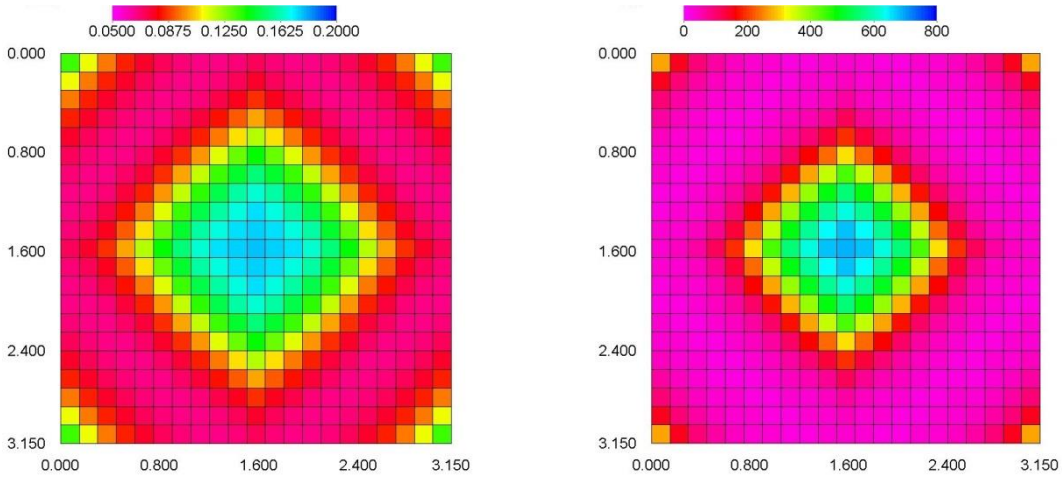


(a) Porosity (b) Permeability

Figure 8.27: Porosity and permeability distributions after injecting mud acid for 44 minutes at injection rate of 80 bbl/day.

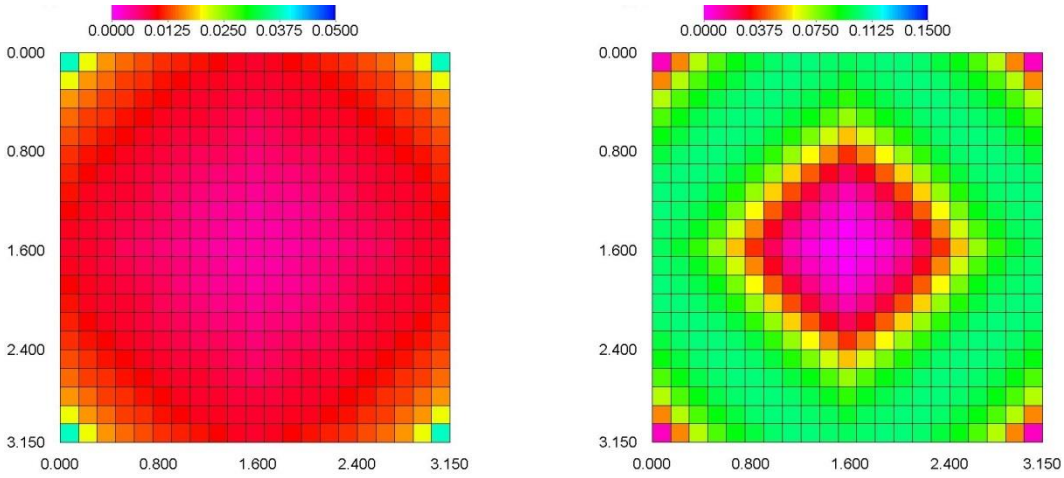


(a) Kaolinite (b) Hydrated silica

Figure 8.28: Mineral volume ratio distributions after injecting mud acid for 44 minutes at injection rate of 80 bbl/day.

### 8.4.3 Injection rate of 90 bbl/day

To inject the same acid volume, mud acid is injected for 39 minutes at an injection rate of 90 bbl/day. The porosity and permeability distributions after 39 minutes of injection are shown in Figure 8.29. The volume ratios of kaolinite and hydrated silica in the volume of the whole matrix are presented in Figure 8.30.

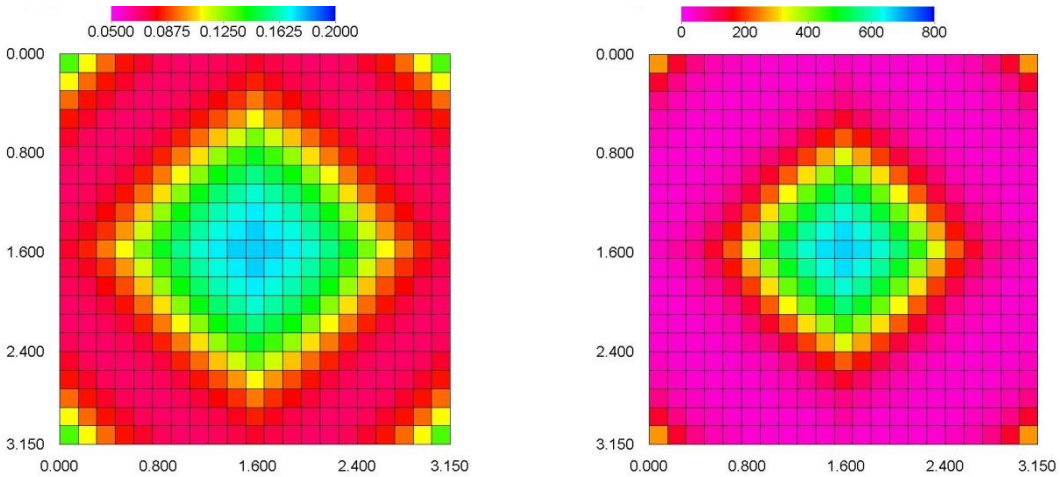


(a) Porosity (b) Permeability

Figure 8.29: Porosity and permeability distributions after injecting mud acid for 39 minutes at injection rate of 90 bbl/day.

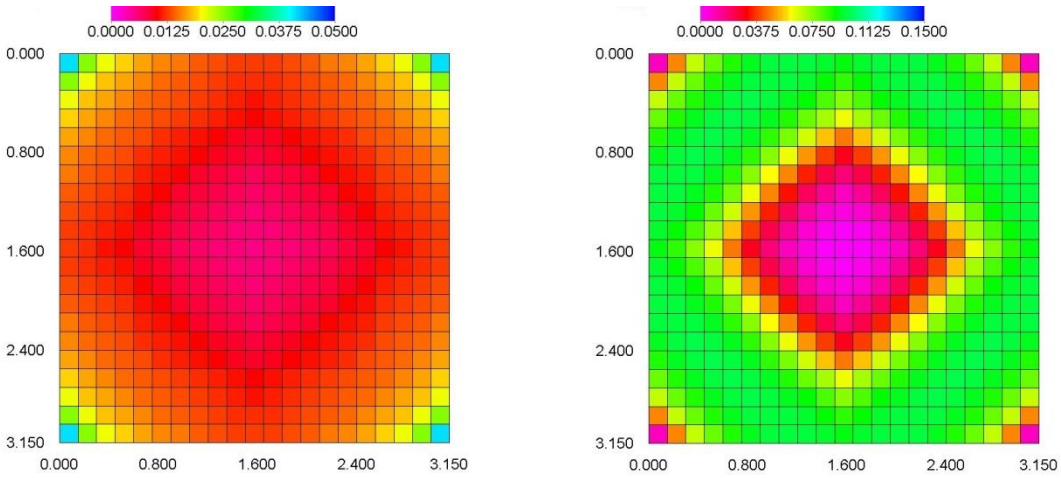


(a) Kaolinite (b) Hydrated silica

Figure 8.30: Mineral volume ratio distributions after injecting mud acid for 39 minutes at injection rate of 90 bbl/day.

### 8.4.4 Injection rate of 100 bbl/day

To inject the same acid volume, mud acid is injected for 35 minutes at an injection rate of 100 bbl/day. The porosity and permeability distributions after 35 minutes of injection are shown in Figure 8.31. The volume ratios of kaolinite and hydrated silica in the volume of the whole matrix are presented in Figure 8.32.

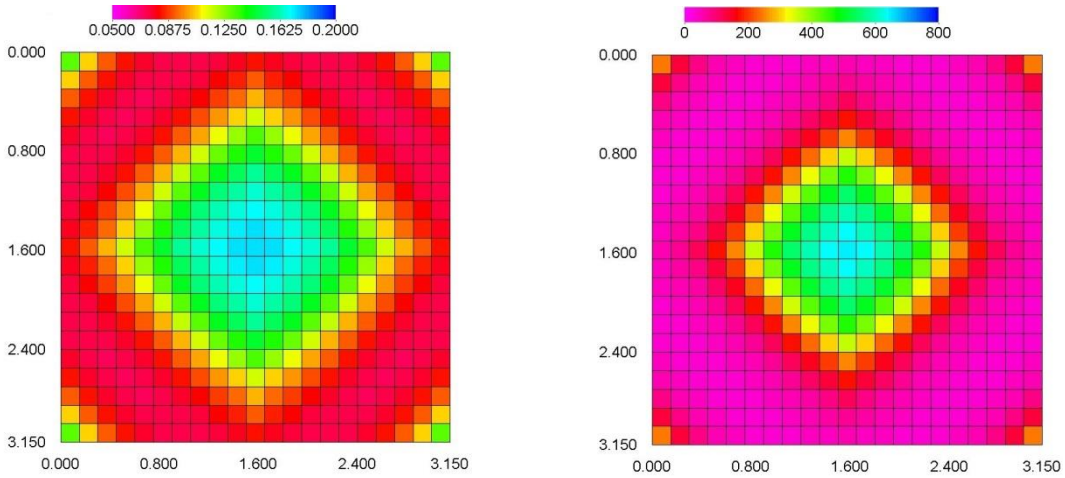


(a) Porosity (b) Permeability

Figure 8.31: Porosity and permeability distributions after injecting mud acid for 35 minutes at injection rate of 100 bbl/day.

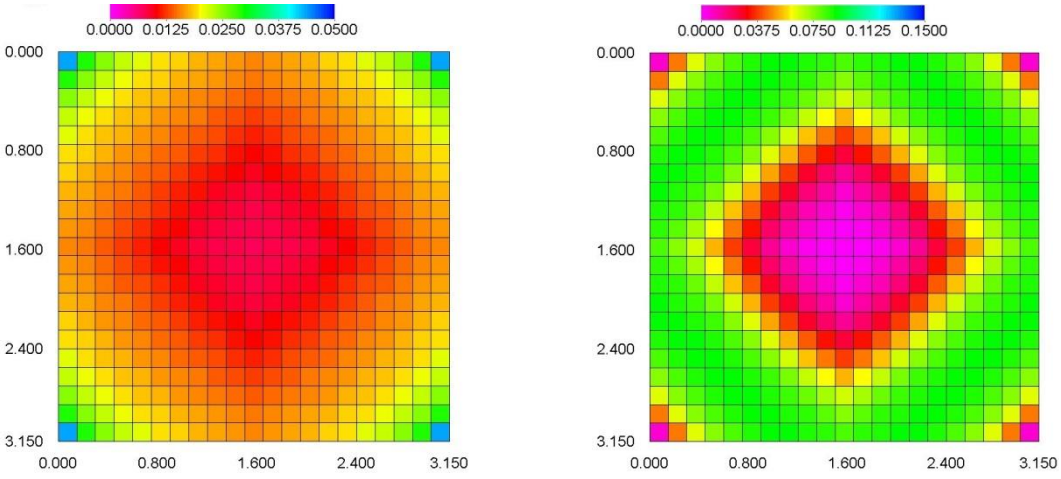


(a) Kaolinite (b) Hydrated silica

Figure 8.32: Mineral volume ratio distributions after injecting mud acid for 35 minutes at injection rate of 100 bbl/day.

### 8.4.5 Comparison of different injection rates

The bottomhole pressure when using different injection rates is compared in Figure 8.33. BHP decreases first and then increases a little as precipitation causes formation damage. To compare productivity improvement using different injection rates,

productivity is compared in Figure 8.34. The best productivity improvement can be achieved using 100 bbl/day. But the total injection volume should be optimized. After injecting about 73 gallons of acid, the productivity starts to decrease. Using a larger injection rate leads to better acidizing performance, but should be limited to avoid fracturing the matrix.

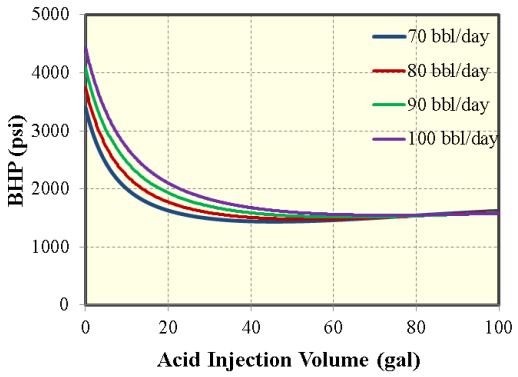


Figure 8.33: Comparison of BHP for different injection rates.

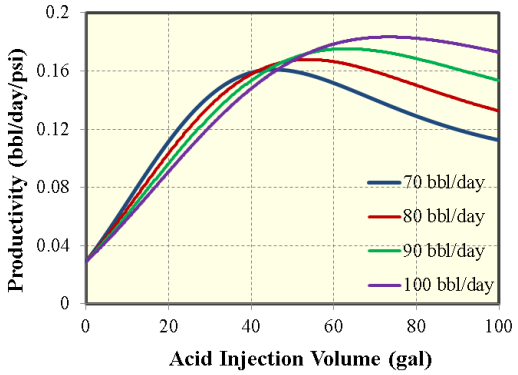


Figure 8.34: Comparison of productivity for different injection rates.

## 8.5 CONCLUSIONS

The main objective of this chapter is to apply UTCOMP-IPhreeqc in sandstone acidizing. The UTCOMP-IPhreeqc is used in simulation of core-scale samples and near-wellbore cases. Based on the simulation studies, the following conclusions can be drawn:

- The acidizing performance is different for sandstone samples with different mineral compositions and is dependent on the volume ratio of clays. Since quartz is almost insoluble compared with clay, a larger volume ratio of clay content leads to a better acidizing performance.
- More dissolution is obtained when using a higher concentration of HF but precipitation also accumulates more in the matrix. In the sandstone sample with 89% quartz and 11% kaolinite, 3% HF obtains best acidizing performance.
- Acid injection rate determines residence time when injecting the same amount of acid. Smaller acid injection rate leads to more dissolution and precipitation due to longer residence time. Using a larger acid injection rate is beneficial for obtaining better acidizing performance by reducing formation damage caused by precipitation. In near-wellbore simulation cases, a largest possible injection rate avoiding fracturing the formation should be used to obtain best acidizing performance.

# CHAPTER 9: SUMMARY, CONCLUSIONS, AND FUTURE WORK

This chapter summarizes the research work in this dissertation. The acidizing model is developed and implemented based on the two-scale continuum method. The model is implemented in a radial coordinate system and in a Cartesian coordinate system separately. The model in the Cartesian coordinate system is implemented in UTCOMP-IPhreeqc coupled software to extend acidizing application in both carbonates and sandstones with different mineral compositions. The model is also coupled with EDFM model to simulate acidizing process in carbonates with fractures. To improve computational efficiency, the acidizing model is also implemented in the semi-parallel version of UTCOMP-IPhreeqc and speedup techniques have been applied.

## 9.1 SUMMARY AND CONCLUSIONS

### 9.1.1 Acidizing modeling in radial coordinates

The acidizing simulation model has been implemented in radial coordinates and extended from single-phase to two-phase based on the two-scale continuum model. In addition, a new criterion to determine acid breakthrough has been proposed for two-phase flow (water and oil) based on overall mobility variation in the domain. Based on the pressure drop analysis, pressure difference between inner and outer boundary is affected by overall mobility; it changes with the variation of phase saturation in the domain. Based on simulation studies on the effect of the two-phase flow on wormhole propagation in carbonate acidizing, the following conclusions can be drawn:

- If rocks are preferentially oil-wet, higher efficiency can be obtained compared with water-wet rocks. It is due to the difference in relative permeability curves. In other words, adverse mobility ratio improves acidizing efficiency, and the larger water-oil mobility ratio is, the higher efficiency can be achieved.

- Higher oil viscosity leads to earlier acid breakthrough compared with lower oil viscosity. The reason behind is also the effect of mobility ratio on water-oil displacement.
- A higher saturation of oil before acidizing treatment reduces acid volume consumption compared with the case with residual oil saturation. This can give a hint for field acidizing treatment that maintaining a high saturation of oil can enhance acidizing efficiency at near or below optimal injection rate.

### 9.1.2 Geochemical modeling of wormhole propagation in UTCOMP-IPhreeqc

The two-scale continuum model is implemented in UTCOMP-IPhreeqc coupled software to realize acidizing process with complex geochemical reactions. With the aid of the UTCOMP-IPhreeqc coupled model, mineral compositions of carbonate rocks are taken into consideration. Based on the simulation studies, the following conclusions are presented:

- Pure dolomite requires larger amount of acid than pure calcite. The difference in acidizing efficiency between pure calcite and pure dolomite increases as the injection rate increases, which is due to the change of dissolution structures.
- Acidizing efficiency for the mixture of calcite and dolomite is smaller than pure calcite, but larger than pure dolomite. Compared with pure calcite, thicker wormhole is generated for the mixture at certain injection rates which correspond to wormhole pattern.
- For partially dolomitized carbonate rocks, as the degree of dolomitization increases, acidizing efficiency decreases. At very low injection rates, larger amount of acid is required for partially dolomitized carbonates than pure dolomite.

### 9.1.3 Geochemical modeling of wormhole propagation in UTCOMP-IPhreeqc considering fractures based on EDFM

The two-scale continuum model is coupled with EDFM to realize acidizing process with consideration of fractures. In this process, IPhreeqc is used to calculate all the reactions occurring in the matrix and in the fracture. All the transmissibility factors are modified during acidizing process based on the mineral dissolution results calculated from IPhreeqc. Based on the simulation studies, the following conclusions can be drawn:

- For a homogeneous matrix with a single fracture, the wormhole is generated along the fracture. For a homogeneous matrix with two parallel fractures, the dissolution structure is symmetric with two wormholes propagating along the fractures.
- For a heterogeneous matrix with a single fracture, the initiation of the wormhole is dependent on the initial permeability distribution in the matrix, and the wormhole propagation is dependent on the fracture position. For a heterogeneous matrix with two parallel fractures, the dominant channel propagates along one of the fractures while the other fracture receives much less acid.
- The presence of the fracture retards wormhole propagation in the matrix. For a partially penetrated fracture in the vertical direction, wormhole propagation is slowed down for the entire matrix.

### 9.1.4 High performance computing and speedup techniques in geochemical modeling of matrix acidizing

To improve computational efficiency, the acidizing model is implemented into the semi-parallel version of UTCOMP-IPhreeqc with the parallelized geochemical calculations and speedup techniques are applied. The parallel performance is evaluated through running acidizing simulation cases using a single processor and multiple

processors on TACC. The speedup performance is evaluated and analyzed through running acidizing simulation cases using different tolerances. Based on the simulation studies, the following conclusions can be drawn:

- The UTCOMP-IPhreeqc model improves the computational efficiency when using multiple processors compared with using a single processor. The parallel performance shows sub-linear speedup when comparing total CPU time for cases using different injection rates. The speedup ratio is closer to linear speedup for the CPU time spent on geochemical calculations than the total CPU time.
- Among cases with different injection rates in Case 1 with 8000 grids in Chapter 7, the case with the injection rate of 1 $cm^3$/min obtains the highest parallel efficiency. When using 16 processors, 85.0% of the total computational time is saved with the speedup ratio of 6.69, while 93.0% of the computational time spent on geochemical calculations is reduced with the speedup ratio of 14.21.
- Among cases with different injection rates in Case 2 with 16000 grids in Chapter 7, the case with the injection rate of 10 $cm^3$/min obtains the highest parallel efficiency. When using 20 processors, 66.3% of the total computational time is saved with the speedup ratio of 2.97. Regarding the computational time spent on geochemical calculations, 94.5% of CPU time is saved with the speedup ratio of 18.19.
- Overall, parallel performance is better regarding CPU time spent on geochemical calculations for the case with a larger number of total grids. However, the parallel performance regarding total CPU time is not guaranteed to be better because it is also dependent on the time proportion of geochemical calculations in total computational time.

- When using a single processor, the speedup methods achieve best performance for wormhole pattern and very poor performance for uniform pattern. The two types of speedup methods achieve similar speedup performance for wormhole pattern.
- When using multiple processors, the speedup methods achieve poor performance. It indicates combining parallel processing and speedup methods do not lead to superposition effects on computational efficiency in acidizing cases.

### 9.1.5 Sandstone acidizing modeling based on UTCOMP-IPhreeqc

The application of UTCOMP-IPhreeqc is extended from carbonate acidizing to sandstone acidizing through modifying PHREEQC database. The UTCOMP-IPhreeqc is used in simulation of core-scale samples and near-wellbore cases. Based on the simulation studies, the following conclusions can be drawn:

- The acidizing performance is different for sandstone samples with different mineral compositions and is dependent on the volume ratio of clays. Since quartz is almost insoluble compared with clay, a larger volume ratio of clays leads to a better acidizing performance.
- More dissolution is obtained when using a higher concentration of HF but precipitation also accumulates more in the matrix. In the sandstone sample with 89% quartz and 11% kaolinite, 3% HF obtains best acidizing performance compared with 4% HF and 5% HF.
- Acid injection rate determines residence time when injecting the same amount of acid. Smaller acid injection rate leads to more dissolution and precipitation due to longer residence time. In sandstone core-scale samples, using a larger acid injection rate is beneficial for obtaining better acidizing performance by reducing formation damage caused by precipitation. In near-wellbore simulation cases, a

largest possible injection rate avoiding fracturing the formation should be used to obtain best acidizing performance.

## 9.2 FUTURE WORK

For the acidizing model development, the following future research can be considered:

- The two-scale continuum model in radial coordinates can be extended to 3D cylindrical model with consideration of gravity.
- The two-scale continuum model can be extended to three phases including water, oil, and gas; and $CO_2$ generation during carbonate acidizing can be considered.
- The diversion property of gelled acid can be modeled for acidizing in multi-layer reservoirs and reservoirs with natural fractures.
- The energy conservation equation can be modeled to consider heat transfer during acidizing.
- The acidizing model can be implemented into the parallel version of UTCOMP-IPhreeqc to further improve the computational efficiency.
- The fluid flow and solute transport can be modeled in carbonates with consideration of vugs.
- The non-Darcy flow can be considered when the velocity is high as porosity and permeability increase during acidizing.
- In carbonates with fractures, the change of the fracture length due to fracture propagation during acidizing can be considered.
- The acidizing model can be implemented into UTCOMPP, a parallel version of UTCOMP developed by Ghasemi Doroh (2012) to further improve computational

efficiency. And higher level of grid refinement can be done to capture dissolution patterns under lower injection rates more accurately.

For the application based on the current acidizing model, the following future research can be considered:

- The complex natural fractures can be constructed to study the effect of natural fractures in carbonate acidizing.
- The PHREEQC database can be supplemented to include kinetic reactions between more minerals and acid. And detailed reactions including primary reaction, secondary reaction, and tertiary reaction can be considered in sandstone acidizing. The pre-flush and post-flush of HCl can be optimized to minimize precipitation.
- Different mineral compositions and permeabilities in and beyond the damaged zone can be considered.
- Different compositions of the injection solution can be considered since the injection solution may contain acid, additives, and other chemical species. And using fresh water or produced water can cause difference in chemical compositions in the injection solution.

# References


Ahusborde, E., Amaziane, B., and El Ossmani, M. 2018. Improvement of Numerical Approximation of Coupled Multiphase Multicomponent Flow With Reactive Geochemical Transport in Porous Media. *Oil & Gas Science and Technology–Revue d'IFP Energies nouvelles* **73**: 1-15. https://doi.org/10.2516/ogst/2018033.

Akanni, O. O. and Nasr-El-Din, H. A. 2016. Modeling of Wormhole Propagation During Matrix Acidizing of Carbonate Reservoirs By Organic Acids and Chelating Agents. Presented at SPE Annual Technical Conference and Exhibition, Dubai, UAE, 26-28 September. SPE-181348-MS. https://doi.org/10.2118/181348-MS.

Akanni, O. O., Nasr-El-Din, H. A., and Gusain, D. 2017. A Computational Navier-Stokes Fluid-Dynamics-Simulation Study of Wormhole Propagation in Carbonate-Matrix Acidizing and Analysis of Factors Influencing the Dissolution Process. *SPE J.* **22** (06): 2049-2066. https://doi.org/10.2118/187962-PA.

Al-harbi, B. G., Dahlan, A., Nasser, M. et al. 2012. Aluminum and Iron Precipitation During Sandstone Acidizing Using Organic-HF Acids. Presented at SPE International Symposium and Exhibition on Formation Damage Control, Lafayette, Louisiana, 15-17 February. SPE-151781-MS. https://doi.org/10.2118/151781-MS.

Ali, M. T. and Nasr-El-Din, H. A. 2018. A Robust Model To Simulate Dolomite-Matrix Acidizing. *SPE Production & Operations*. https://doi.org/10.2118/191136-PA.

Baghel, V. S. and Pravesh, J. 2016. A Semi-Empirical Carbonate Acidizing Model for Chelating-Agent-Based Fluids. Presented at IADC/SPE Asia Pacific Drilling Technology Conference, Singapore, 22-24 August. SPE-180590-MS. https://doi.org/10.2118/180590-MS.

Balakotaiah, V. and West, D. H. 2002. Shape normalization and analysis of the mass transfer controlled regime in catalytic monoliths. *Chemical Engineering Science* **57**(8): 1269-1286. http://doi.org/10.1016/S0009-2509(02)00059-3.

Bazin, B. 2001. From Matrix Acidizing to Acid Fracturing: A Laboratory Evaluation of Acid/Rock Interactions. *SPE Prod &Fac* **16** (01): 22-29. SPE-66566-PA. http://dx.doi.org/10.2118/66566-PA.

Beisman, J. J., Maxwell, R. M., Navarre-Sitchler, A. K. et al. 2015. ParCrunchFlow: an Efficient, Parallel Reactive Transport Simulation Tool for Physically and Chemically Heterogeneous Saturated Subsurface Environments. *Computational Geosciences* **19**(2): 403-422.

Bennion, D. B. 2002. An Overview of Formation Damage Mechanisms Causing a Reduction in the Productivity and Injectivity of Oil and Gas Producing Formations. *Journal of Canadian Petroleum Technology* **41**(11): 29-36. https://doi.org/10.2118/02-11-DAS.

Bryant, S. L. 1991. An Improved Model of Mud Acid/Sandstone Chemistry. Presented at SPE Annual Technical Conference and Exhibition, Dallas, Texas, 6-9 October. SPE-22855-MS. https://doi.org/10.2118/22855-MS.

Buijse, M. A. 1997. Understanding Wormholing Mechanisms Can Improve Acid Treatments in Carbonate Formations. Presented at SPE European Formation Damage Conference, The Hague, Netherlands, 2-3 June. SPE-38166-MS. https://doi.org/10.2118/38166-MS.

Buijse, M. A. and Glasbergen, G. 2005. A Semi-Empirical Model To Calculate Wormhole Growth in Carbonate Acidizing. Society of Petroleum Engineers. Presented at SPE Annual Technical Conference and Exhibition , Dallas, Texas, 9-12 October. SPE-96892-MS. https://doi.org/10.2118/96892-MS.

Busenberg, E. and Plummer, L. N. 1982. The Kinetics of Dissolution of Dolomite in $CO_2$-$H_2O$ Systems at 1.5 to 65°C and 0 to 1 atm $P_{CO_2}$. *American Journal of Science* **282** (1): 45-78. https://pubs.er.usgs.gov/publication/70011818.

Carman, P. C. 1956. *Flow of Gases Through Porous Media*, first edition. New York: Academic Press.

Chabert, M., Morvan, M., and Tabary, R. 2010. Fractured Carbonates: A Methodology to Evaluate Surfactant Performances. Society of Petroleum Engineers. Presented at SPE Improved Oil Recovery Symposium, Tulsa, Oklahoma, 24-28 April. SPE-129178-MS. http://dx.doi.org/10.2118/129178-MS.

Chang, Y. B. 1990. Development and Application of an Equation of State Compositional Simulator (Doctoral dissertation, University of Texas at Austin).

Chang, F., Qu, Q., and Frenier, W. 2001. A Novel Self-diverting-acid Developed for Matrix Stimulation of Carbonate Reservoirs. Presented at SPE International Symposium on Oilfield Chemistry, Houston, Texas, 13-16 February. SPE-65033-MS. https://doi.org/10.2118/65033-MS.

Charlton, S. R. and Parkhurst, D. L. 2011. Modules Based on the Geochemical Model PHREEQC for Use in Scripting and Programming Languages. *Computers & Geosciences* **37**(10): 1653-1663. Doi:10.1016/j.cageo.2011.02.005.

Chilingar, G. V. and Yen, T. F. 1983. Some Notes on Wettability and Relative Permeabilities of Carbonate Reservoir Rocks, II. *Energy Sources* **7**(1): 67-75. http://dx.doi.org/10.1080/00908318308908076.

Corbella, M., Gomez-Rivas, E., Martín-Martín, J. D. et al. 2014. Insights to Controls on Dolomitization by means of Reactive Transport Models Applied to the Benicàssim Case Study (Maestrat Basin, eastern Spain). *Petroleum Geoscience* **20**(1): 41–54. https://doi.org/10.1144/petgeo2012-095.

Crowe, C., Masmonteil, J., and Thomas, R. 1992. Trends in matrix acidizing. *Oilfield Review* **4**(4): 22-40.

Daccord, G. 1987. Chemical Dissolution of a Porous Medium by a Reactive Fluid. *Physical review letters* **58**(5): 479-482. http://dx.doi.org/10.1103/PhysRevLett.58.479.

De Oliveira, T. J. L., De Melo, A. R., Oliveira, J. A. A. et al. 2012. Numerical Simulation of the Acidizing Process and PVBT Extraction Methodology Including Porosity/Permeability and Mineralogy Heterogeneity. Society of Petroleum Engineers. Presented at SPE International Symposium and Exhibition on Formation Damage Control, Lafayette, Louisiana, 15-17 February. SPE-151823-MS. https://doi.org/10.2118/151823-MS.

Dong, C., Hill, A. D. and Zhu, D. 1999. Acid Etching Patterns in Naturally-Fractured Formations. Presented at SPE Annual Technical Conference and Exhibition, Houston, Texas, 3-6 October. SPE-56531-MS. https://doi.org/10.2118/56531-MS.

Dong, C., Zhu, D. and Hill, A. D. 2001. Acid Penetration in Natural Fracture Networks. Presented at SPE European Formation Damage Conference, The Hague, Netherlands, 21-22 May. SPE-68927-MS. https://doi.org/10.2118/68927-MS.

Dong, C., Zhu, D., and Hill, A. D. 2002. Acidizing in Naturally Fractured Carbonate Reservoirs. Presented In SPE/DOE Improved Oil Recovery Symposium, Tulsa, Oklahoma, 13-17 April. https://doi.org/10.2118/75252-MS.

Dong, K., Zhu, D., and Hill, A. D. 2017. Theoretical and Experimental Study on Optimal Injection Rates in Carbonate Acidizing. *SPE J.* **22**(03): 892-901. http://doi.org/10.2118/178961-PA.

Dong, K., Zhu, D., and Hill, A. D. 2018. The Role of Temperature on Optimal Conditions in Dolomite Acidizing: An Experimental Study And Its Applications. *Journal of Petroleum Science and Engineering* **165**: 736-742. http://doi.org/10.1016/j.petrol.2018.03.018.

Dong, R., Lee, S., and Wheeler, M. 2019. Numerical Simulation of Matrix Acidizing in Fractured Carbonate Reservoirs Using Adaptive Enriched Galerkin Method. Presented at SPE Reservoir Simulation Conference, Galveston, Texas, 10-11 April. SPE-193862-MS. https://doi.org/10.2118/193862-MS.

Economides M. J. and Nolte, K. G. 1989. *Reservoir Stimulation* (Vol. 2). Englewood Cliffs, NJ: Prentice Hall.

El-Hisnawi, A. A., Duduković, M. P., and Mills, P. L. 1982. Trickle-bed reactors: dynamic tracer tests, reaction studies, and modeling of reactor performance. *ACS Symposium Series* **196**(34): 421-220. 10.1021/bk-1982-0196.ch034.

Fitch, P. J. R. 2011. Heterogeneity in the Petrophysical Properties of Carbonate Reservoirs. Doctoral dissertation, University of Leicester.

Fogler, H. S., Lund, K., and McCune, C. C. 1976. Predicting the Flow and Reaction of HCl/HF Acid Mixtures in Porous Sandstone Cores. *Society of Petroleum Engineers Journal* **16**(05): 248-260. https://doi.org/10.2118/5646-PA.

Fredd, C. N. 2000. Dynamic Model of Wormhole Formation Demonstrates Conditions for Effective Skin Reduction During Carbonate Matrix Acidizing. Society of Petroleum Engineers. Presented at SPE Permian Basin Oil and Gas Recovery Conference, Midland, Texas, 21-23 March. SPE-59537-MS. doi:10.2118/59537-MS.

Fredd C. N. and Fogler H. S. 1998. Influence of Transport and Reaction on Wormhole Formation in Porous Media. *AIChE Journal* **44**(9): 1933-1949. 10.1002/aic.690440902.

Fredd C. N. and Fogler H. S. 1999. Optimum Conditions for Wormhole Formation in Carbonate Porous Media: Influence of Transport and Reaction. *SPE J.* **4**(03): 196-205. SPE-56995-PA. http://dx.doi.org/10.2118/56995-PA.

Garcia, E. A. R., LaBlanc, A., Beuterbaugh, A. et al. 2016. Developments in Sandstone HF Acidizing: HF Fluid Compatible with Na or K Brines and Carbonate-laden Mineralogy for High Temperatures (360 F). Presented at SPE International Conference and Exhibition on Formation Damage Control, Lafayette, Louisiana, 24-26 February. SPE-178999-MS. https://doi.org/10.2118/178999-MS.

Garland, J., Horbury, A., Vincent, B. et al. 2018. Natural Fracture Systems in Carbonate Reservoirs. Presented at The Geology of Fractured Reservoirs, Piccadilly, London, 24-25 October.

Gdanski, R. 1996. Kinetics of Tertiary Reaction of HF on Alumino-Silicates. Presented at SPE Formation Damage Control Symposium, Lafayette, Louisiana, 14-15 February. SPE-31076-MS. https://doi.org/10.2118/31076-MS.

Gdanski, R. D. 1999. Kinetics of the Secondary Reaction of HF on Alumino-Silicates. *SPE Production & Facilities* **14**(04): 260-268. SPE-59094-PA. https://doi.org/10.2118/59094-PA.

Gdanski, R. D. 2000. Kinetics of the Primary Reaction of HF on Alumino-Silicates. *SPE Production & Facilities* **15**(04): 279-287. SPE-66564-PA. https://doi.org/10.2118/66564-PA.

Geffen, T. M., Owens, W. W., Parrish, D. R. et al. 1951. Experimental Investigation of Factors Affecting Laboratory Relative Permeability Measurements. *J Pet Technol* **3**(04): 99-110. SPE-951099-G. http://dx.doi.org/10.2118/951099-G.

Ghasemi Doroh, M. 2012. Development and Application of a Parallel Compositional Reservoir Simulator (MS thesis, University of Texas at Austin).

Ghommem, M. and Brady, D. 2016. Multifidelity Modeling and Analysis of Matrix Acidizing Under Radial Flow Conditions. Presented at SPE Kingdom of Saudi Arabia Annual Technical Symposium and Exhibition, Dammam, Saudi Arabia, 25-28 April. SPE-182743-MS. https://doi.org/10.2118/182743-MS.

Ghommem, M., Zhao, W., Dyer, S. et al. 2015. Carbonate Acidizing: Modeling, Analysis, and Characterization of Wormhole Formation and Propagation. *Journal of Petroleum Science and Engineering* **131**: 18-33. http://dx.doi.org/10.1016/j.petrol.2015.04.021.

Gidley, J. L. 1985. Acidizing Sandstone Formations: A Detailed Examination of Recent Experience. Presented at SPE Annual Technical Conference and Exhibition, Las Vegas, Nevada, 22-26 September. SPE-14164-MS. https://doi.org/10.2118/14164-MS.

Golfier, F., Zarcone, C., Bazin, B. et al. 2002. On the Ability of a Darcy-scale Model to Capture Wormhole Formation During the Dissolution of a Porous Medium. *Journal of Fluid Mechanics* **457**: 213-254. http://dx.doi.org/10.2118/132535-MS.

Gomaa, A. M., Mahmoud, M. A., and Nasr-El-Din, H. 2010. A Study of Diversion Using Polymer-Based In-Situ Gelled Acids Systems. Presented at Trinidad and Tobago Energy Resources Conference, Port of Spain, Trinidad, 27-30 June. SPE-132535-MS. 10.1007/s11242-010-9543-6.

Gong, M. and El-Rabaa, A. M. 1999. Quantitative Model of Wormholing Process in Carbonate Acidizing. Presented at SPE Mid-Continent Operations Symposium, Oklahoma City, Oklahoma, 28-31 March. SPE-52165-MS. https://doi.org/10.2118/52165-MS.

Gray, F., Anabaraonye, B., Shah, S. et al. 2018. Chemical Mechanisms of Dissolution of Calcite by HCl in Porous Media: Simulations and Experiment. *Advances in water resources* **121**:369-387. https://doi.org/10.1016/j.advwatres.2018.09.007.

Hajibeygi, H., Karvounis, D. and Jenny, P. 2011. A Hierarchical Fracture Model for the Iterative Multiscale Finite Volume Method. *Journal of Computational Physics* **230**(24): 8729-8743. https://doi.org/10.1016/j.jcp.2011.08.021.

Ham, W. E. and Pray, L. C. 1962. Modern Concepts and Classification of Carbonate Rocks. *AAPG* **1**: 2-19.

Hammond, G. E., Lichtner, P. C., and Mills, R. T. 2014. Evaluating the Performance of Parallel Subsurface Simulators: An Illustrative Example with PFLOTRAN. *Water resources research* **50**(1): 208-228. https://doi.org/10.1002/2012WR013483.

Hartman, R. L., Lecerf, B., Frenier, W. et al. 2003. Acid Sensitive Aluminosilicates: Dissolution Kinetics and Fluid Selection for Matrix Stimulation Treatments. Presented at SPE European Formation Damage Conference, The Hague, Netherlands, 13-14 May. SPE-82267-MS. https://doi.org/10.2118/82267-MS.

He, W., Beyer, C., Fleckenstein, J. H. et al. 2015. A Parallelization Scheme to Simulate Reactive Transport in the Subsurface Environment with OGS# IPhreeqc 5.5. 7-3.1. 2. *Geoscientific Model Development* **8**(10): 3333-3348. doi:10.5194/gmd-8-3333-2015.

Hekim, Y., Fogler, H. S., and McCune, C. C. 1982. The Radial Movement of Permeability Fronts and Multiple Reaction Zones in Porous Media (includes associated papers 11284 and 11590). *Society of Petroleum Engineers Journal* **22**(01): 99-107. https://doi.org/10.2118/9495-PA.

Hill, A. D., Lindsay, D. M., Silberberg, I. H. et al. 1981. Theoretical and Experimental Studies of Sandstone Acidizing. *Society of Petroleum Engineers Journal* **21**(01):30-42. SPE-6607-PA. https://doi.org/10.2118/6607-PA.

Hiorth, A., Cathles, L. M., and Madland, M. V. 2010. The Impact of Pore Water Chemistry on Carbonate Surface Charge and Oil Wettability. *Transport in Porous Media* **85**(1): 1-21. 10.1007/s11242-010-9543-6.

Hoefner, M. L. and Fogler, H. S. 1988. Pore Evolution and Channel Formation During Flow and Reaction in Porous Media. *AIChE Journal* **34**(1): 45-54. 10.1002/aic.690340107.

Hsi, C. D., Bryant, S. L. and Neira, R. D. 1993. Experimental Validation of Sandstone Acidization Models. Presented at SPE International Symposium on Oilfield Chemistry, New Orleans, Louisiana, 2-5 March. SPE-25212-MS. https://doi.org/10.2118/25212-MS.

Hung, K. M., Hill, A. D., and Sepehrnoori, K. 1989. A Mechanistic Model of Wormhole Growth in Carbonate Matrix Acidizing and Acid Fracturing. *J Pet Technol* **41**(01): 59-66. SPE-16886-PA. http://dx.doi.org/10.2118/16886-PA.

Jarrahian, Kh., Seiedi, O., Sheykhan M. et al. 2012. Wettability Alteration of Carbonate Rocks by Surfactants: A Mechanistic Study. *Colloids and Surfaces A: Physicochemical and Engineering Aspects* **410**: 1-10. http://dx.doi.org/10.1016/j.colsurfa.2012.06.007.

Jatnieks, J., De Lucia, M., Dransch, D. et al. 2016. Data-driven Surrogate Model Approach for Improving the Performance of Reactive Transport Simulations. *Energy Procedia* **97**: 447-453.

Ji, Q., Zhou, L., and Nasr-El-Din, H. A. 2014. Acidizing Sandstone Reservoirs Using Fines Control Acid. Presented at SPE Latin America and Caribbean Petroleum Engineering Conference, Maracaibo, Venezuela, 21-23 May. SPE-169395-MS. https://doi.org/10.2118/169395-MS.

Kalia, N. and Balakotaiah, V. 2007. Modeling and Analysis of Wormhole Formation in Reactive Dissolution of Carbonate Rocks. *Chemical Engineering Science* **62**(4): 919-928. http://dx.doi.org/10.1016/j.ces.2006.10.021.

Karimi-Fard, M., Durlofsky, L. J., and Aziz, K. 2003. An Efficient Discrete Fracture Model Applicable for General Purpose Reservoir Simulators. Presented at SPE Reservoir Simulation Symposium, Houston, Texas, 3-5 February. SPE-79699-MS. https://doi.org/10.2118/79699-MS.

Korrani, A. K. N. 2014. Mechanistic Modeling of Low Salinity Water Injection (Doctoral dissertation, University of Texas at Austin).

Kunze, K. R. and Shaughnessy, C. M. 1983. Acidizing Sandstone Formations with Fluoboric Acid. *Society of Petroleum Engineers Journal* **23**(01), 65-72. SPE-9387-PA. https://doi.org/10.2118/9387-PA.

Labrid, J. C. 1975. Thermodynamic and Kinetic Aspects of Argillaceous Sandstone Acidizing. *Society of Petroleum Engineers Journal* **15**(02): 117-128. https://doi.org/10.2118/5156-PA.

Lea, C., Hill, A. K., and Sepehrnoori, K. 1992. Simulation of Sandstone Acidizing of a Damaged Perforation. *SPE production engineering* **7**(02): 212-218. SPE-19419-PA. https://doi.org/10.2118/19419-PA.

Lee, S. H., Lough, M. F. and Jensen, C. L. 2001. Hierarchical Modeling of Flow in Naturally Fractured Formations with Multiple Length Scales. *Water Resources Research* **37**(3): 443-455. https://doi.org/10.1029/2000WR900340.

Legemah, M. U., Gomaa, A., Bilden, D. et al. 2015. Sequential Injection Process Enhances Acidizing Treatment of High-Temperature Wells. Presented at SPE Production and Operations Symposium, Oklahoma City, Oklahoma, 1-5 March. SPE-173626-MS. https://doi.org/10.2118/173626-MS.

Leong, V. H., Mahmud, H. B., Law, M. C. et al. 2018. A Comparison and Assessment of the Modelling and Simulation of the Sandstone Matrix Acidizing Process: a Critical Methodology Study. *Journal of Natural Gas Science and Engineering* **57**: 52-67. https://doi.org/10.1016/j.jngse.2018.06.044.

Leong, V. H., Mahmud, H. B., Law, M. C. et al. 2019. A Numerical Modelling and Simulation of Core-scale Sandstone Acidizing Process: a Study on the Effect of Temperature. *Journal of Petroleum Exploration and Production Technology* **9**(1), 483-516. DOI: 10.1007/s13202-018-0522-8.

Li, L. and Lee, S. H. 2008. Efficient Field-Scale Simulation of Black Oil in a Naturally Fractured Reservoir Through Discrete Fracture Networks and Homogenized Media. *SPE Reservoir Evaluation & Engineering* **11**(04): 750-758. SPE-103901-PA. https://doi.org/10.2118/103901-PA.

Li, C., Xie, T., Pournik, M. et al. 2005. Fine-scale Simulation of Sandstone Acidizing. *Journal of Energy Resources Technology* **127**(3): 225-232. https://doi.org/10.1115/1.1944027.

Li, Y. H., Fambrough, J. D., and Montgomery, C. T. 1998. Mathematical Modeling of Secondary Precipitation From Sandstone Acidizing. *SPE Journal* **3**(04): 393-401. https://doi.org/10.2118/53001-PA.

Liang, C., Cui, M., Xue, H. et al. 2015. Simulation and Analysis of Wormhole Structure Affected by Mineralogy Heterogeneity in Carbonate Rocks. *EJGE* **20**(26): 12811-12831.

Liu, P., Yao, J., Couples, G. D. et al. 2017. Modeling and Simulation of Wormhole Formation During Acidization of Fractured Carbonate Rocks. *Journal of Petroleum Science and Engineering* **154**: 284-301.

Liu, M., Zhang, S., Mou, J. et al. 2013. Wormhole Propagation Behavior Under Reservoir Condition in Carbonate Acidizing. *Transport in porous media* **96**(1): 203-220. 10.1007/s11242-012-0084-z.

Liu, X., Ormond, A., Bartko, K. et al. 1997. A Geochemical Reaction-Transport Simulator for Matrix Acidizing Analysis and Design. *Journal of Petroleum Science and Engineering* **17**(1-2):181-196. https://doi.org/10.1016/S0920-4105(96)00064-2.

Lund, K., Fogler, H. S., and McCune, C. C. 1973. Acidization—I. The Dissolution of Dolomite in Hydrochloric Acid. *Chemical Engineering Science* **28**(3): 691-700. https://doi.org/10.1016/0009-2509(77)80003-1.

Lund, K., Fogler, H. S., McCune, C. C. et al. 1975. Acidization—II. The Dissolution of Calcite in Hydrochloric Acid. *Chemical Engineering Science* **30**(8): 825-835. https://doi.org/10.1016/0009-2509(75)80047-9.

Lynn, J. D. and Nasr-El-Din, H. A. 2001. A Core Based Comparison of the Reaction Characteristics of Emulsified and In-situ Gelled Acids in Low Permeability, High Temperature, Gas Bearing Carbonates. Presented at SPE International Symposium on Oilfield Chemistry, Houston, Texas, 13-16 February. SPE-65386-MS. https://doi.org/10.2118/65386-MS.

MaGee, J., Buijse, M. A., and Pongratz, R. 1997. Method for Effective Fluid Diversion when Performing a Matrix Acid Stimulation in Carbonate Formations. Presented at Middle East Oil Show and Conference, Bahrain, 15-18 March. SPE-37736-MS. https://doi.org/10.2118/37736-MS.

Maheshwari, P. and Balakotaiah, V. 2013. 3D Simulation of Carbonate Acidization with HCl: Comparison with Experiments. Presented at SPE Production and Operations Symposium, Oklahoma City, Oklahoma, 23-26 March. SPE-164517-MS. http://dx.doi.org/10.2118/164517-MS.

Maheshwari, P., Ratnakar, R. R., Kalia, N. et al. 2013. 3-D Simulation and Analysis of Reactive Dissolution and Wormhole Formation in Carbonate Rocks. *Chemical Engineering Science* **90**: 258-274. http://dx.doi.org/10.1016/j.ces.2012.12.032.

Maheshwari, P., Maxey, J., and Balakotaiah, V. 2016. Reactive-dissolution Modeling and Experimental Comparison of Wormhole Formation in Carbonates with Gelled and

Emulsified Acids. *SPE Production & Operations* **31**(02): 103-119. https://doi.org/10.2118/171731-PA.

Mahmoud, M. A., Nasr-El-Din, H. A., De Wolf, C. et al. 2011. Sandstone Acidizing Using a New Class of Chelating Agents. Presented at SPE International Symposium on Oilfield Chemistry, The Woodlands, Texas, 11-13 April. SPE-139815-MS. https://doi.org/10.2118/139815-MS.

Mahrous, M., Sultan, A., and Sonnenthal, E. 2017. Towards Geochemically Accurate Modeling of Carbonate Acidizing with HCl Acid. Presented at SPE Annual Technical Conference and Exhibition, San Antonio, Texas, 9-11 October. SPE-187183-MS. https://doi.org/10.2118/187183-MS.

McCune, C. C., Fogler, H. S., and Cunningham, J. R. 1975. A New Model of the Physical and Chemical Changes in Sandstone During Acidizing. *Society of Petroleum Engineers Journal* **15**(05): 361-370. https://doi.org/10.2118/5157-PA.

McDuff, D., Shuchart, C. E., Jackson, S. et al. 2010. Understanding Wormholes in Carbonates: Unprecedented Experimental Scale and 3-D Visualization. Presented at SPE Annual Technical Conference and Exhibition, Florence, Italy, 19-22 September. SPE-134379-MS. http://dx.doi.org/10.2118/134379-MS.

Mohammed A. K. 2016. Well Stimulation and Sand Production Management.

Moinfar, A., Varavei, A., Sepehrnoori, K. et al. 2012. Development of a Novel and Computationally-Efficient Discrete-Fracture Model to Study IOR Processes in Naturally Fractured Reservoirs. Presented at SPE Improved Oil Recovery Symposium, Tulsa, Oklahoma, 14-18 April. SPE-154246-MS. https://doi.org/10.2118/154246-MS.

Moinfar, A. 2013. Development of an Efficient Embedded Discrete Fracture Model for 3D Compositional Reservoir Simulation in Fractured Reservoirs. PhD Dissertation. The University of Texas at Austin.

Moinfar, A., Varavei, A., Sepehrnoori, K. et al. 2014. Development of an Efficient Embedded Discrete Fracture Model for 3D Compositional Reservoir Simulation in Fractured Reservoirs. *SPE Journal* **19**(02): 289-303. SPE-154246-PA. https://doi.org/10.2118/154246-PA.

Moore, C. H. and Wade, W. J. 2013. Carbonate reservoirs: Porosity and diagenesis in a sequence stratigraphic framework. **67**. Newnes.

Mou, J., Wang, L., Zhang, S. et al. 2019. A Research on the Effect of Heterogeneities on Sandstone Matrix Acidizing Performance. *Geofluids* **2019**. https://doi.org/10.1155/2019/6328909.

Muller, M., Parkhurst, D. L. and Charlton, S. R. 2011. Programming PHREEQC Calculations with C++ and Python A Comparative Study. *EXCHANGE* **1**(40): 632-636.

Ziauddin, M., Berndt, O., and Robert, J. 1999. An Improved Sandstone Acidizing Model: The Importance of Secondary and Tertiary Reactions. Presented at SPE European Formation Damage Conference, The Hague, Netherlands, 31 May-1 June. SPE-54728-MS. https://doi.org/10.2118/54728-MS.

Nasr-El-Din, H. A., Samuel, M. M., and Kelkar, S. K. 2007. Investigation of a New Single-Stage Sandstone Acidizing Fluid for High Temperature Formations. Presented at European Formation Damage Conference, Scheveningen, The Netherlands, 30 May-1 June. SPE-107636-MS. https://doi.org/10.2118/107636-MS.

Nelson, R. A. 1979. Natural Fracture Systems: Description and Classification: Geologic Notes. *AAPG Bulletin* **63**(12): 2214-2221.

Nelson, R. 2001. *Geologic Analysis of Naturally Fractured Reservoirs*. Elsevier.

Nierode, D. E. and Williams, B. B. 1971. Characteristics of Acid Reaction in Limestone Formations. *SPE J.* **11**(04): 406-418. SPE-3101-PA. http://dx.doi.org/10.2118/3101-PA.

Schwalbert, M. P., 2019. Comprehensive Analysis of Acid Stimulation in Carbonates (Doctoral dissertation, Texas A&M University).

Panga, M. K. R., Ziauddin, M., and Balakotaiah, V. 2005. Two-scale Continuum Model for Simulation of Wormholes in Carbonate Acidization. *AIChE Journal* **51**(12): 3231-3248. 10.1002/aic.10574.

Parkhurst, D. L. and Appelo, C. A. J. 1999. User's Guide to PHREEQC (Version 2): A Computer Program for Speciation, Batch-Reaction, One-Dimensional Transport, and Inverse Geochemical Calculations.

Parkhurst, D. L. and Appelo, C. A. J. 2013. Description of Input and Examples for PHREEQC Version 3-a Computer Program for Speciation, Batch-reaction, One-dimensional Transport, and Inverse Geochemical Calculations.

Parlar, M., Parris, M. D., Jasinski, R. J. et al. 1995. An Experimental Study of Foam Flow Through Berea Sandstone with Applications to Foam Diversion in Matrix Acidizing. Presented at SPE Western Regional Meeting, Bakersfield, California, 8-10 March. SPE-29678-MS. https://doi.org/10.2118/29678-MS.

Peaceman, D. W. 1983. Interpretation of Well-Block Pressures in Numerical Reservoir Simulation With Nonsquare Grid Blocks and Anisotropic Permeability. *Society of Petroleum Engineers Journal* **23**(03): 531-543. https://doi.org/10.2118/10528-PA.

Plummer, L. N., Wigley, T. M. L., and Parkhurst, D. L. 1978. The Kinetics of Calcite Dissolution in $CO_2$-Water Systems at 5°C to 60°C and 0.0 to 1.0 atm $CO_2$. *American journal of science* **278**(2): 179-216. doi:10.2475/ajs.278.2.179.

Qiu, X. W., Zhao, W., Dyer, S. J. et al. 2014. Revisiting Reaction Kinetics and Wormholing Phenomena During Carbonate Acidising. Presented at International Petroleum Technology Conference, Doha, Qatar, 19-22 January. IPTC-17285-MS. https://doi.org/10.2523/IPTC-17285-MS.

Rao, V. G. and Drinkenburg, A. A. H. 1985. Solid-liquid mass transfer in packed beds with cocurrent gas-liquid downflow. *AIChE journal* **31**(7): 1059-1068. 10.1002/aic.690310703.

Ratnakar, R., Kalia, N., and Balakotaiah, V. 2012. Carbonate Matrix Acidizing with Gelled Acids: An Experiment-Based Modeling Study. Presented at SPE International Production and Operations Conference & Exhibition, Doha, Qatar, 14-16 May. SPE-154936-MS. http://dx.doi.org/10.2118/154936-MS.

Ratnakar, R. R., Kalia, N., and Balakotaiah, V. 2013. Modeling, Analysis and Simulation of Wormhole Formation in Carbonate Rocks with in situ Cross-linked Acids. *Chemical Engineering Science* **90**: 179-199. https://doi.org/10.1016/j.ces.2012.12.019.

Salimi, S., Ghalambor, A. and Hayer, H. 2014. Insights Into the Process of Effectively Acidizing Naturally Fractured Reservoirs. Presented at SPE International Symposium and Exhibition on Formation Damage Control, Lafayette, Louisiana, 26-28 February. SPE-168126-MS. https://doi.org/10.2118/168126-MS.

Sanaei, A. 2019. Compositional Reactive-Transport Modeling of Engineering Waterflooding (Doctoral dissertation, University of Texas at Austin).

Saroha, A. K. 2010. Solid–Liquid Mass Transfer Studies in Trickle Bed Reactors. *Chemical Engineering Research and Design* **88**(5): 744-747. http://doi.org/10.1016/j.cherd.2009.11.015.

Satterfield, C. N., Van Eek, M. W., and Bliss, G. S. 1978. Liquid-solid mass transfer in packed beds with downward concurrent gas-liquid flow. *AIChE Journal* **24**(4): 709-717. 10.1002/aic.690240421.

Schechter, R. S. 1992. *Oil Well Stimulation*. New York. Prentice Hall. Chap. 17: 512-517.

Schlumberger 2007. Carbonate Reservoirs.

Schlumberger 2008. Characterization of fractured reservoirs.

Sevougian, S. D., Lake, L. W., and Schechter, R. S. 1995. KGEOFLOW: A New Reactive Transport Simulator for Sandstone Matrix Acidizing. *SPE Production and Facilities* **10**(1). DOI: 10.2118/24780-PA.

Shafiq, M. U., Kyaw, A., and Shuker, M. T. 2013. Performance Prediction of Acids on Sandstone Acidizing. *ASJ International Journal of Advances in Scientific Research and Reviews* **1**(2): 07-12.

Shafiq, M. U., Mahmud, H. K. B., and Rezaee, R. 2017. New Acid Combination for a Successful Sandstone Acidizing. *IOP Conference Series: Materials Science and Engineering* **206**(1).

Shakiba, M. 2014. Modeling and Simulation of Fluid Flow in Naturally and Hydraulically Fractured Reservoirs Using Embedded Discrete Fracture Model (EDFM) (MS Thesis, The University of Texas at Austin).

Shuchart, C. E. 1995. HF Acidizing Returns Analyses Provide Understanding of HF Reactions. Presented at SPE European Formation Damage Conference, The Hague, Netherlands, 15-16 May. SPE-30099-MS. https://doi.org/10.2118/30099-MS.

Shuchart, C. E. and Buster, D. C. 1995. Determination of the Chemistry of HF Acidizing with the Use of F NMR Spectroscopy. Presented at SPE International Symposium on Oilfield Chemistry, San Antonio, Texas, 14-17 February. SPE-28975-MS. https://doi.org/10.2118/28975-MS.

Shukla, S., Zhu, D., and Hill, A. D. 2006. The Effect of Phase Saturation Conditions on Wormhole Propagation in Carbonate Acidizing. *SPE J.* **11**(03): 273-281. SPE-82273-PA. http://dx.doi.org/10.2118/82273-PA.

Smith, C. F. and Hendrickson, A. R. 1965. Hydrofluoric Acid Stimulation of Sandstone Reservoirs. *Journal of Petroleum Technology* **17**(02): 215-222. SPE-980-PA. https://doi.org/10.2118/980-PA.

Taha, R., Hill, A. D., and Sepehrnoori, K. 1986. Simulation of Sandstone-Matrix Acidizing in Heterogeneous Reservoirs. *Journal of Petroleum Technology* **38**(07), 753-767. SPE-13218-PA. https://doi.org/10.2118/13218-PA.

Talbot, M. S. and Gdanski, R. D. 2008. Beyond the Damkohler Number: A New Interpretation of Carbonate Wormholing. Presented at Europec/EAGE Conference and Exhibition, Rome, Italy, 9-12 June. SPE-113042-MS. https://doi.org/10.2118/113042-MS.

Tansey, J. 2014. Pore-Network Modeling of Carbonate Acidization. Presented at SPE Annual Technical Conference and Exhibition, Amsterdam, The Netherlands, 27-29 October. SPE-173472-STU. http://dx.doi.org/10.2118/173472-STU.

Tansey, J. and Balhoff, M. T. 2016. Pore Network Modeling of Reactive Transport and Dissolution in Porous Media. *Transport in Porous Media* **113**(2): 303-327. https://doi.org/10.1007/s11242-016-0695-x.

Tansey, J. F. 2016. Multiscale Pore Network Modeling of Carbonate Acidization (Doctoral dissertation, University of Texas at Austin).

Tardy, P. M. J., Lecerf, B., and Christanti, Y. 2007. An Experimentally Validated Wormhole Model for Self-diverting and Conventional Acids in Carbonate Rocks Under Radial Flow Conditions. Presented at European Formation Damage Conference, Scheveningen, The Netherlands, 30 May-1 June. SPE-107854-MS. http://dx.doi.org/10.2118/107854-MS.

Taylor, K. C. and Nasr-El-Din, H. A. 2003. Laboratory Evaluation of In-Situ Gelled Acids for Carbonate Reservoirs. *SPE J.* **8**(04): 426-434. SPE-87331-PA. http://dx.doi.org/10.2118/87331-PA.

Thomas, R. L., Nasr-El-Din, H. A., Lynn, J. D. et al. 2001. Precipitation During the Acidizing of a HT/HP Illitic Sandstone Reservoir in Eastern Saudi Arabia: A Laboratory Study. Presented at SPE Annual Technical Conference and Exhibition, New Orleans, Louisiana, 30 September-3 October. SPE-71690-MS. https://doi.org/10.2118/71690-MS.

Treiber, L. E. and Owens, W. W. 1972. A Laboratory Evaluation of the Wettability of Fifty Oil-producing Reservoirs. *SPE J.* **12**(06): 531-540. SPE-3526-PA. http://dx.doi.org/10.2118/3526-PA.

Walsh, J. B. and Brace, W. F. 1984. The Effect of Pressure on Porosity and the Transport Properties of Rock. *Journal of Geophysical Research: Solid Earth* **89**(B11): 9425-9431. https://doi.org/10.1029/JB089iB11p09425.

Wang, Y., Hill, A. D., and Schechter, R. S. 1993. The Optimum Injection Rate for Matrix Acidizing of Carbonate Formations. Presented at SPE Annual Technical Conference and Exhibition, Houston, Texas, 3-6 October. SPE-26578-MS. http://dx.doi.org/10.2118/26578-MS.

Wei, W., Varavei, A., and Sepehrnoori, K. 2017. Modeling and Analysis on the Effect of Two-Phase Flow on Wormhole Propagation in Carbonate Acidizing. *SPE Journal* **22**(06): 2067-2083. https://doi.org/10.2118/186111-PA.

Wei, W., Varavei, A., Sanaei, A. et al. 2019. Geochemical Modeling of Wormhole Propagation in Carbonate Acidizing Considering Mineralogy Heterogeneity. *SPE Journal* **24**(05): 2163-2181. https://doi.org/10.2118/195593-PA.

Williams, B. B., Gidley, J. L., and Schechter, R. S. 1979. *Acidizing Fundamentals*, first edition. Texas/Dallas: SPE Monograph Series.

Williams, B. B. and Whiteley, M. E. 1971. Hydrofluoric Acid Reaction with a Porous Sandstone. *Society of Petroleum Engineers Journal* **11**(03): 306-314. SPE-3112-PA. https://doi.org/10.2118/3112-PA.

Witherspoon, P. A., Wang, J. S., Iwai, K. et al. 1980. Validity of Cubic Law for Fluid Flow in a Deformable Rock Fracture. *Water Resource Research* **16**(6): 1016-1024. https://doi.org/10.1029/WR016i006p01016.

Wu, Y., Salama, A., and Sun, S. 2015. Parallel Simulation of Wormhole Propagation With the Darcy–Brinkman–Forchheimer Framework. *Computers and Geotechnics* **69**: 564-577. https://doi.org/10.1016/j.compgeo.2015.06.021.

Xiong, H. 1994. Prediction of Effective Acid Penetration and Acid Volume for Matrix Acidizing Treatments in Naturally Fractured Carbonates. *SPE Production & Facilities* **9**(03): 188-194. https://doi.org/10.2118/25410-PA.

Xu, Y. 2015. Implementation and Application of the Embedded Discrete Fracture Model (EDFM) for Reservoir Simulation in Fractured Reservoirs (Thesis, The University of Texas at Austin).

Xu, Y., de Araujo Cavalcante Filho, J. S., Yu, W. et al. 2016. Discrete-Fracture Modeling of Complex Hydraulic-Fracture Geometries in Reservoir Simulators. *SPE Reservoir*

*Evaluation & Engineering* **20**(02): 403-422. SPE-183647-PA. https://doi.org/10.2118/183647-PA.

Xu, Y., Cavalcante Filho, J. S. A., Yu, W. et al. 2017. Discrete-Fracture Modeling of Complex Hydraulic-Fracture Geometries in Reservoir Simulators. *SPE Reservoir Evaluation & Engineering* **20**(02): 403-422. doi:10.2118/183647-PA.

Xu, Y., Yu, W., and Sepehrnoori, K. 2019. Modeling Dynamic Behaviors of Complex Fractures in Conventional Reservoir Simulators. *SPE Reservoir Evaluation & Engineering* **22**(03): 1110-1130. doi:10.2118/194498-PA.

Yang, F., Nasr-El-Din, H. A., and Al-Harbi, B. M. 2012. Acidizing Sandstone Reservoirs Using HF and Formic Acids. Presented at SPE International Symposium and Exhibition on Formation Damage Control, Lafayette, Louisiana, 15-17 February. SPE-150899-MS. https://doi.org/10.2118/150899-MS.

Yu, W. and Sepehrnoori, K. 2014. Development of a Semi-analytical Model for Simulation of Gas Production in Shale Gas Reservoirs. Presented at Unconventional Resources Technology Conference, Denver, Colorado, 25-27 August. https://doi.org/10.15530/urtec-2014-1922945.

Zhou, W., Banerjee, R., Poe, B. D. et al. 2013. Semianalytical Production Simulation of Complex Hydraulic-Fracture Networks. *SPE Journal* **19**(01): 6-18. https://doi.org/10.2118/157367-PA.